The ARGOS Wavefront Sensor Detector and Computer

and

The Black Hole Growth of Narrow-Line Seyfert 1 Galaxies

Gilles Orban de Xivry

München 2013

The ARGOS Wavefront Sensor Detector and Computer

and

The Black Hole Growth of Narrow-Line Seyfert 1 Galaxies

Gilles Orban de Xivry

Dissertation
an der Fakultät für Physik
der Ludwig–Maximilians–Universität
München

vorgelegt von
Gilles Orban de Xivry
aus Uccle

München, den 17.12.2013

On m'a dit:
"Tu n'es que cendres et poussières."
On a oublié de me dire qu'il s'agissait de poussières d'étoiles.

A READER OF "PATIENCE DANS L'AZUR" (HUBERT REEVES).

ZUSAMMENFASSUNG

In dieser Doktorarbeit geht es um die Entwicklung einer einmaligen Adaptiven Optik und die Anwendung von hochauflösenden Beobachtungsverfahren auf astrophysikalische Probleme. Der erste Teil handelt von der Entwicklung, Validierung und Implementation des Wellenfrontsensor-Detektors und -Computers für das Laserleitstern-gestützte Adaptive Optik System (Argos) des Large Binocular Telescope (LBT). Im zweite Teil dieser Arbeit geht es um Galaxien, die sich ohne große Galaxien-Verschmelzungen entwickeln ("secular evolution") und welche Rolle eine derartige Entwicklung für das Wachstum von Schwarzen Löchern in Seyfert-1-Galaxien mit schmalen Emissionslinien (NLS1) hat. Dazu untersuche ich deren zentrale Verdickung und vergleichen diese mit typischen Seyfert-1-Galaxien. Außerdem studiere ich den zentralen Bereich der NLS1-Galaxie NGC 1365.

Argos ist das Laserleitstern-gestützte Adaptive Optik (AO) System für das LBT. Es dient dazu, die Auflösung über ein großes Gesichtsfeld von vier Bogenminuten um den Faktor zwei bis drei zu verbessern und wird zusammen mit dem Instrument Luci eingesetzt. Luci ist ein Nahinfrarot Instrument, welches eine Kamera, ein Langspalt- und Multi-Objekt-Spektrometer vereint. Die Kombination beider Systeme stellt das erste Weitfeld Ground-Layer Adaptive Optik System dar, die im wissenschaftlichen Betrieb verwendet werden wird. Argos ist ein gemeinsames Projekt von europäischen und amerikanischen Instituten unter der Führung des Max-Planck-Instituts für extraterrestrische Physik.

Der erste Teil behandelt eine detaillierte Analyse des Wellenfrontsensor-Detektors und -Computers, dem Nervenzentrum von Argos. Um eine Weitfeld-Korrektur zu erbringen, verwendet Argos drei Laserleitsterne, die die atmosphärische Turbulenz bodennaher Schichten messen. Der verbleibende Wellenfront-Fehler der drei Leitsterne wird vom Wellenfront bestimmt, welches drei Shack-Hartmann-Muster auf einer einzelnen PN-CCD-Kamera produziert. Insgesamt werden so 525 Punkte erzeugt, die sich jeweils in 8×8 Pixel großen Regionen bewegen können. Im Rahmen dieser Arbeit entwickele ich in Kollaboration mit der Firma pnSensor diese Kamera mit einem PN-CCD auf dem neuesten Stand der Technik. Mein Beiträge finden sich in allen Bereichen des Systems: bei der Integration der gesamten Kontroll-Elektronik, in der Entwicklung der Kamera-Steuerungs-Software sowie bei der Durchführung zahlreicher Tests des Kameragehäuses, des PN-CCDs und der Erfassungs-Elektronik in verschiedenen Phasen des Projekts. Insbesondere führe ich ausführliche Tests durch und unterstütze die Entwicklung von neuen Netzteilen durch die MPE-Elektronik-Abteilung, um das Rauschen der PN-CCD zu vermindern. In diesem Zusammenhang führe ich verschiedene Rausch-Analysen durch, sowohl mit optischen Aufbauten als auch mit AO-Simulationen in geschlossenen Regelkreisen. Die finalen Eigenschaften der Kamera sind hervorragend und werden vorgeführt. Mit einer Bildwiederholrate von 1 kHz, einem Ausleserauschen von 3,5

Elektronen und einem kompakten wartungsfreundlichen Gehäuse, erfüllt das fertiggestellte System alle Anforderungen von Argos. Parallel zur Arbeit am Detektor definiere ich die benötigte Architektur des Argos-Wellenfrontsensor-Computers. Dieser DSP-basierte Computer verarbeitet die Detektorbilder, berechnet die lokalen Gradienten der Wellenfronten der Laserleitsterne und sammelt die Tip-Tilt Terme des natürlichen Leitsterns und die Daten eines möglichen dritten Wellenfrontsensors. Dieser dritte Wellenfrontsensor kann mit dem natürlichen Leitstern oder einem zukünftigen Natrium Laser-Leitstern zur Messung der Turbulenz hoher Atmosphärenschichten genutzt werden. Ich unterstütze die Entwicklung durch Microgate, entwickle die ersten Konfigurations-Hilfsprogramme, beseitige Fehler in den Hardware-Schnittstellen und zeige die Funktion im Echtzeit-Betrieb.

Als Teil dieser Arbeit zeige ich den Weg für die Integration des Wellenfrontsensor-Systems auf, indem ich den Wellenfrontsensor-Detektor, das Taktungs-System und den Wellenfront-Computer vorläufig installiere. Die Einheiten sind mittlerweile vollständig in den Wellenfrontsensor integriert und werden nun systemweiten Tests unterzogen, bevor sie am LBT zusammengebaut werden.

Im zweiten Teil dieser Arbeit untersuche ich die Koevolution der zentralen sehr massereichen Schwarzen Löcher und ihrer Wirtsgalaxien. Ich konzentriere mich dabei auf Seyfert-1-Galaxien mit schmalen Linien (NLS1) und zeige die bedeutende Rolle auf, die eine Galaxien-Entwicklung ohne große Verschmelzungen für die Entwicklung des Schwarze-Loch-Wachstums in diesen Galaxien spielt. Ich gebe einen umfangreichen Überblick über die Literatur zu solchen Prozessen im lokalen Universum. Ich nutze Archiv-Bilder des Hubble-Weltraum-Teleskops, um die Eigenschaften der zentralen Verdickung von einer Stichprobe aus NLS1-Galaxien zu untersuchen. Außerdem vergleiche ich diese mit typischeren Seyfert-1-Galaxien. Damit zeige ich die Entwicklung von nicht-Verschmelzungs-getriebener Galaxien-Evolution in NLS1-Galaxien und diskutiere, wie dies in einem kosmologischen Kontext der Galaxienevolution verstanden werden kann.

Aufbauend auf dieser Arbeit analysiere ich die zentralen einhundert Parsec von NGC 1365, einer nahegelegenen NLS1-Galaxie. Dazu benutze ich Daten von SINFONI, einem AO-unterstützten Integralfeldspektrometer am VLT. Ich untersuche die verschiedenen Phasen des interstellaren Mediums und finde, dass die Sterne zu einem großen Teil jünger sind als zehn Millionen Jahre. Zusammen mit der Stern- und Gas-Kinematik und den Literaturstudien zeigt das, welch bedeutende Rolle Prozesse, die nicht mit der Verschmelzung von Galaxien zusammenhängen, in dieser Galaxie spielen : Die Galaxie zeigt eine ungestörte Struktur von großen Skalen bis hinunter zum zentralen Schwarzen Loch. Dieselben Prozesse können verantwortlich sein für die Ansammlung von Gas in einem nuklearen Ring und dazu führen, dass derzeit nicht mehr Gas akkretiert werden kann, obwohl es sich in einem Gas-Reservoir ansammelt. Dies erklärt auch die relativ geringe Leuchtkraft dieses aktiven Galaxienkerns und die schwache Emission durch molekulares Gas.

ABSTRACT

This thesis addresses both the development of a unique adaptive optics system and the application of high resolution observations to astrophysics. The first part describes the development, validation and implementation of the wavefront sensor detector and computer of the laser guide star adaptive optics system for the Large Binocular Telescope (LBT), ARGOS. The second part demonstrates the important role of secular evolution in the black hole growth of narrow-line Seyfert Type 1 galaxies by studying their bulges and comparing it to more typical Seyfert type 1 galaxies, and by studying the inner regions of one NLS1, NGC1365.

ARGOS is the laser guided ground-layer adaptive optics system for the LBT. It aims to provide a factor 2-3 improvement in resolution over a wide field of view of 4×4 arcminutes^2, and is intended for LUCI, the near-infrared imager, longslit, and multi-object spectrograph. As such it will be the first wide-field Ground-Layer Adaptive Optics facility dedicated for science operation. This instrument is a joint project of European and American institutes lead by the Max-Planck-Institut für extraterrestrische Physik.

Part I provides a detailed analysis of the wavefront sensor detector and the wavefront computer, the nerve center of the ARGOS wavefront sensing capability. In order to perform its wide-field correction, ARGOS uses three laser guide stars to sample the atmospheric turbulence. The residual wavefront error of these three guide stars is measured by the wavefront sensing system that creates three Shack-Hartmann patterns on a single PNCCD camera, *i.e.* a total of 525 spots each allowed to move in its 8×8 pixels region. In the framework of this thesis, I develop in collaboration with the company PNSENSOR this state-of-the-art camera implementing a PNCCD. My contribution covers all aspects of the system : integrating the entire control electronics, developing the camera control software, and performing extensive tests of the camera housing, the PNCCD, and the acquisition electronics at the various stages of the project. In particular, I also carry out an extensive test campaign and support the development of new power supplies by the MPE electronics department to tackle the PNCCD characteristic noise. In that frame, I perform several noise analyses, from optical setups to closed-loop adaptive optics simulations. The final excellent characteristics of the camera are demonstrated. With its 1kHz framerate, 3.5e$^-$ readout noise, and its compact, low-maintenance housing, the integrated system fully answers the ARGOS requirements. In parallel to the detector work, I define the required architecture of the ARGOS wavefront computer at the center of the wavefront sensing. This DSP-based computer processes the detector images, computes the LGS local wavefront gradients, and collects the measurements of the natural guide star tip-tilt sensor and of a possible third wavefront sensor. The latter wavefront sensor can probe higher layer turbulence with either a natural or a future Sodium laser guide star. I support its development by MICROGATE, develop the initial configuration tools,

debug its different hardware interfaces and demonstrate its real-time functionality.

As part of this thesis, I pave the way for the wavefront sensor system integration by preliminarily integrating the wavefront sensor detector, the gating system, and the wavefront computer. The units are now fully integrated into the wavefront sensor and are undergoing system tests before being assembled at LBT.

In Part II, I study the co-evolution of central super-massive black holes and their host galaxies. I focus on narrow-line Seyfert type 1 galaxies (NLS1), revealing the major role played by secular evolution in driving the black hole growth in those galaxies. I extensively review the literature for signs of present day secular processes. I then use high-resolution HST archive images to study the bulge properties in a sample of NLS1s and compare them to more typical Seyfert type 1 galaxies. By doing so I show the importance of secular processes in NLS1s and discuss how this can be understood in a cosmological context of galaxy evolution. Building on this work, I analyze the inner hundreds of parsecs region of NGC1365, a nearby NLS1s, with data from the adaptive optics integral field spectrometer SINFONI at VLT. I study the different phases of the interstellar medium and find that a large fraction of the stellar population consists of young stars of less than 10Myr. This reveals, together with the stellar and gas kinematics and the broader context found in the literature, the major role of secular processes in this galaxy, displaying an unperturbed alignment from large scales down to the central black hole. Those same secular processes may be responsible for the gas settling in a nuclear ring, currently preventing more gas from being accreted while the gas reservoir is replenished, and explain the relatively low luminosity of the AGN and the faintness of the molecular gas.

TABLE OF CONTENTS

PREAMBLE

This manuscript is organized in two parts : the instrumentation and the astronomy part.

We start by introducing in CHAP.1 the main concepts and motivations behind adaptive optics in general, and wide field ground layer correction in particular. In CHAP.2, we introduce the ARGOS project, review its main design characteristics, and overview the system design. In that context our contribution is the ARGOS wavefront sensor detector and computer. Those two systems allow ARGOS to sample the atmospheric turbulence with three laser guide stars, projecting respectively three Shack-Hartmann patterns on the PNCCD, and to measure the respective wavefront gradients with the ARGOS computer. In CHAP.3, we discuss the requirements, the concept, the development, the testing and the challenges tackled of the ARGOS wavefront sensor detector. In the following chapter 4, we essentially keep the same structure and motivate the design requirements, present the hardware, the tests, the validation and integration of the ARGOS wavefront sensor computer. Those two systems are successfully working together, and have been integrated to the wavefront sensor system.

In the second part, we discuss the role of secular evolution in narrow-line Seyfert Type 1 galaxies. Chapter 5 is, to a large extent, a re-print of Orban de Xivry et al. (2011) and discusses the bulges properties in NLS1 and in BLS1 galaxies using HST archive images. A literature review and the detailed analysis of those high resolution images allow us to propose that NLS1 are, and have always been, dominated by secular evolution. This in turn has implications on their black hole growth, discussed at the end of the chapter. In CHAP.6, we study a single NLS1 object, NGC1365. We use adaptive optics integral field spectroscopy, with SINFONI, to study the central region of the galaxy. We discuss the different phases of the interstellar medium and constrain the stellar population. Those results, together with the larger context provided in the literature, reveal the major role of secular processes in this galaxy.

The conclusions of this work can be found at the end of the respective chapters.

ADAPTIVE OPTICS AND WAVEFRONT SENSING PRINCIPLES

Light propagating to a ground-based telescope passes through a region of varying refractive index, the turbulent atmosphere. The incoming flat wavefront of astronomical objects becomes perturbed, which limits optical and near-infrared resolutions achievable by ground-based telescopes. As an example, the seeing limit is of order one arcsecond whereas a 10m class telescope could in principle reach an angular resolution down to ten milli-arcseconds at 500nm wavelength.

The effect stated, the question is why would we want to correct the atmospheric turbulence? Because we are interested in high spatial resolution and sensitivity. This drives a lot of progress in understanding complex objects and their morphology. And as the telescopes grow in diameter, we want to benefit from their capabilities rather than being limited by the atmosphere. In the seeing limited case, the detectivity, *i.e.* the inverse of the time needed to reach a given signal-to-noise ratio, grows with the square of the diameter as more light can be collected. At the diffraction limit however, it increases with the fourth power of the diameter as the light is additionally concentrated to a smaller area proportional to the square of the resolution, *i.e.* the inverse square of the diameter. This difference amounts to a factor of a hundred for a 10m telescope for background limited observations. This allows one to observe fainter details and to reduce the observing time. Spatial resolution and sensitivity are essential and, for example, have allowed us to constrain accurately the bulge properties of NLS1s and the nuclear region of NGC1365 presented in this work (Chap.5 and 6). The complementary option to turbulence correction is space observation. While space telescopes are naturally only limited by their optics and essentially do not suffer from atmospheric background radiation and transmission, they are however extremely expensive, only limited in size, and difficult to maintain.

In that context, adaptive optics (AO) is a technique that flattens the distorted wavefront by measuring the residual errors and by controlling a deformable mirror. It improves the performance of ground-based telescopes up to the diffraction limit. In this chapter, we discuss in section 1.1 the atmospheric turbulence to introduce the main characteristic parameters of interest to us. In section 1.2 we present the general AO concepts with more emphasis on the wavefront sensing and the Shack-Hartmann sensor. We discuss the limitation of conventional adaptive optics[1], *i.e.* the sky coverage and the anisoplanatism. This allows us to introduce the concept of laser guide star ground-layer adaptive optics in section 1.3. We discuss the

---

[1] using a single natural guide star to perform the correction.

advantages of the concepts, but as well their own limitations, *i.e.* the increased complexity, the unsampled turbulence, and the LGS lack of sensitivity to tip-tilt. Finally, we present a short description of the laser guided ground-layer adaptive optics facilities, existing and forthcoming. In that context, ARGOS would be the first wide-field ground layer adaptive optics system dedicated for science operation.

Extensive discussions on atmospheric turbulence and adaptive optics can be found for example in Fried (1994), Parenti & Sasiela (1994), Hardy (1998), Glindemann et al. (2000), Davies & Kasper (2012).

1.1 Atmospheric turbulence effects on image formation

The optical effects of atmospheric turbulence are driven by atmospheric temperature and their associated refractive index variations. From the statistics of the atmospheric temperature variation, we can calculate the statistics of the effects of the atmosphere on optical propagation. However we are not interested in a complete understanding of the atmospheric variations, as large scales have essentially no impact on the optical propagation statistics. Including for example the diurnal variations, the variance and covariance of turbulence fluctuations are very large and of no interest to us. Rather the local differences of these perturbations govern the optical propagation statistics. Hence, in practice one works with the structure function instead of the covariance.

Based on dimensional analysis and simple physical arguments, Kolmogorov (1962) and Tatarskii (1961) described the statistics of turbulent velocity, temperature and refractive index. In particular the refractive index structure function, defined by

$$D_n(\mathbf{r}_1, \mathbf{r}_2) = \left\langle |n(\mathbf{r}_1) - n(\mathbf{r}_2)|^2 \right\rangle, \tag{1.1}$$

can be written as

$$D_n(\mathbf{r}) = C_n^2 \mathbf{r}^{2/3}, \tag{1.2}$$

with n the refractive index, $\mathbf{r}_1$ and $\mathbf{r}_2$ the position vectors where n is measured, and $\mathbf{r} \equiv |\mathbf{r}_1 - \mathbf{r}_2|$. The quantity C_n^2 is referred to as the refractive index structure constant. Its value has to be determined by measurements and, as we will see, is of key interest. Interestingly, the two-thirds power law on the distance separation $\mathbf{r}$ is at the origin of all the peculiar fractional powers appearing in turbulence and optical propagation results. This expression is essentially valid in the so-called *inertial range*, a regime almost entirely governed by inertial forces between the outer scale L_0 at which energy is introduced into the turbulent flow, and the inner l_0 at which viscous dissipation becomes significant.

The refractive index fluctuations produce a phase shift ϕ as the wavefront propagates through the atmosphere. Hence the fluctuations will be integrated along the propagation path and the phase structure function can be calculated and is given by

$$
\begin{aligned}
D_\phi(\mathbf{r}) \quad &= \left\langle |\phi(\mathbf{x}) - \phi(\mathbf{x} + \mathbf{r})|^2 \right\rangle \\
&= 2.914 k^2 |\mathbf{r}|^{5/3} \sec \zeta \int_0^\infty C_n^2(h) dh \\
&= 6.88 \left(\frac{|\mathbf{r}|}{r_0} \right)^{5/3},
\end{aligned}
\tag{1.3}
$$

where h designates the altitude, $k = 2\pi/\lambda$, ζ is the zenith angle, and r_0 is the fundamental Fried parameter then defined by

$$r_0 = \left[0.423 k^2 \sec \zeta \int_{\text{path}} C_n^2(z) dz \right]^{-3/5}. \tag{1.4}$$

The apparently arbitrary factor of 6.88 introduced in equation 1.3 is chosen to give r_0 the following significance : the resolution of seeing-limited images obtained through a turbulent atmosphere characterized by a Fried parameter r_0 is the same as the resolution of diffraction-limited images taken with a telescope diameter r_0. As such, observations with telescope much larger than r_0 are seeing-limited, and telescope smaller than r_0 are diffraction-limited.

The same structure function can be used to introduce the concept of *angular anisoplanatism*. The light separated by an angle of θ on the sky passes through different patches of the atmosphere and hence experiences different phase variations. Replacing $r = \theta h \sec \zeta$, the angular anisoplanatic error in radian can be written as

$$\sigma_{aniso}^2 = \left(\frac{\theta}{\theta_0} \right)^{5/3}, \tag{1.5}$$

where we have introduced the *anisoplanatic angle* θ_0

$$\theta_0 = \left[2.914 k^2 \sec \zeta^{8/3} \int_{\text{path}} C_n^2(h) h^{5/3} dh \right]^{-3/5}. \tag{1.6}$$

This parameter governs the field of view over which the wavefront compensation is considered valid (for which $\sigma_{aniso} < 1$rad within θ_0).

Finally, by expressing the structure functions in terms of two covariance functions, the spatial power spectrum of phase fluctuations can be derived (Noll, 1976)

$$\Phi_\phi(\boldsymbol{\kappa}) = 0.023 \frac{\boldsymbol{\kappa}^{-11/3}}{r_0^{5/3}}, \tag{1.7}$$

where κ is the spatial frequency vector. The phase variance, integral of the power spectral density, is infinite due to the divergence at low spatial frequencies. This divergence is not physical. In reality the outer scale will truncate the large scale and is modeled by the von Kármán spectrum[2]

So far we have only discussed the spatial variation by considering, in effect, time averaged values. The time dependence of the turbulence induced refractive index variations is usually modeled by the Taylor hypothesis of "frozen" turbulence. According to it, the refractive index variations are considered to be fixed forming a "frozen" pattern and are transported by wind, responsible for the time dependence. Obviously the turbulence is not only being transported but is evolving continuously. However, this hypothesis is usually reasonable if

---

[2]this model is a generalization of the Kolmogorov spectrum and introduces an outer scale L_0 in the spatial phase power spectrum, thus written as

$$\Phi_\phi(\boldsymbol{\kappa}) = 0.023 r_0^{-5/3} \left(\boldsymbol{\kappa}^2 + \left(\frac{1}{L_0} \right)^2 \right)^{-11/6}.$$

one realizes that the small scale turbulence is derived from the energy in the overall wind pattern. Consequently we can expect the wind to transport the entire pattern faster than the smaller scale fluctuations can rearrange that pattern. If the Taylor's hypothesis is valid, we can convert the spatial structure function into a temporal structure introducing the time constant $\tau_0 = \dfrac{r_0}{\bar{v}}$ with $\bar{v}$ the average wind velocity. The temporal power spectrum of phase fluctuations can be calculated from the spatial power spectrum (equation 1.7) by integration over k_y and with $k_x = f/\bar{v}$ (Conan et al., 1995, Glindemann et al., 2000)

$$\Phi_\phi(f) = 0.077\tau_0^{-5/3}f^{-8/3}, \tag{1.8}$$

with f the temporal frequency. In their temporal analysis, Conan et al. (1995) describe the temporal power spectra of the Zernike polynomials defined over the pupil. In Fig. 1.1, we reproduce one of their plots. Two domains are distinguished : a slowly varying regime at low frequencies (f^0 or $f^{-2/3}$) and a fast drop above the cutoff frequencies ($f^{-17/3}$). The high frequency power law is characteristic of circular pupil filtering of the wavefront phase. An interesting aspect at high frequencies is that the power of atmospheric turbulence is almost equally distributed among the modes (the high frequency contributions increase only very slowly with the radial degree n). The practical consequence of that is that low-order modes (and tip-tilt) should be corrected with the same bandwidth as higher order in order to achieve a good compensation.

From the above considerations, we can highlight the following wavelength dependences :

$$r_0, \theta_0, \tau_0 \propto \lambda^{6/5} \qquad \theta_{\text{seeing}} \propto \lambda^{-1/5} \qquad S \propto (r_0)^2\tau_0 \propto \lambda^{18/5}. \tag{1.9}$$

The last dependence S is the sensitivity of the wavefront control loop. Similarly, to preserve a given sensitivity, the photon flux must increase following that relation, *i.e.* visible adaptive optics requires a much larger amount of photons than near-infrared AO and illustrates why visible AO is much more complex.

In the following paragraph, we give typical numbers associated to those parameters.
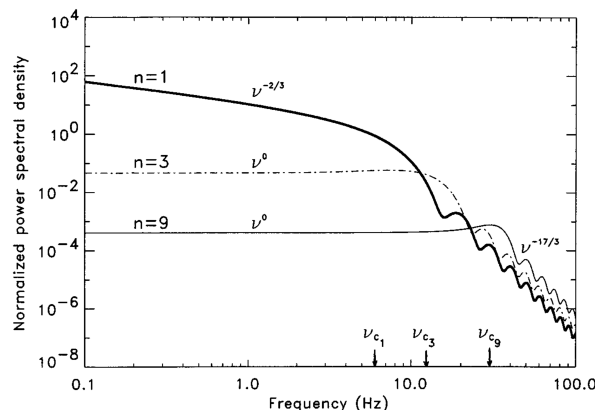
Figure 1.1: Zernike polynomial mean temporal power spectra in a given radial degree n for $n = 1, 3, 9$. The asymptotic power laws and the cutoff frequencies (here noted by ν instead of f in the text) are indicated. Credit: Conan et al. (1995).

Atmospheric profiles and characteristic parameters

To attach numerical values to these important parameters, it is necessary to establish baseline turbulence and wind velocity profiles. A commonly used C_n^2 profile is based on the Hufnagel-Valley turbulence models. Their modification allows a good representation of average nighttime turbulence. In Fig. 1.2 we give the median C_n^2 profile measured on Mt. Graham (at the LBT, Masciadri et al., 2010), and three simulated profiles based on modified Hufnagel-Valley models (see e.g. Parenti & Sasiela, 1994, Hardy, 1998, for the model parameters) that we construct and use to compute r_0, θ_0, and τ_0.
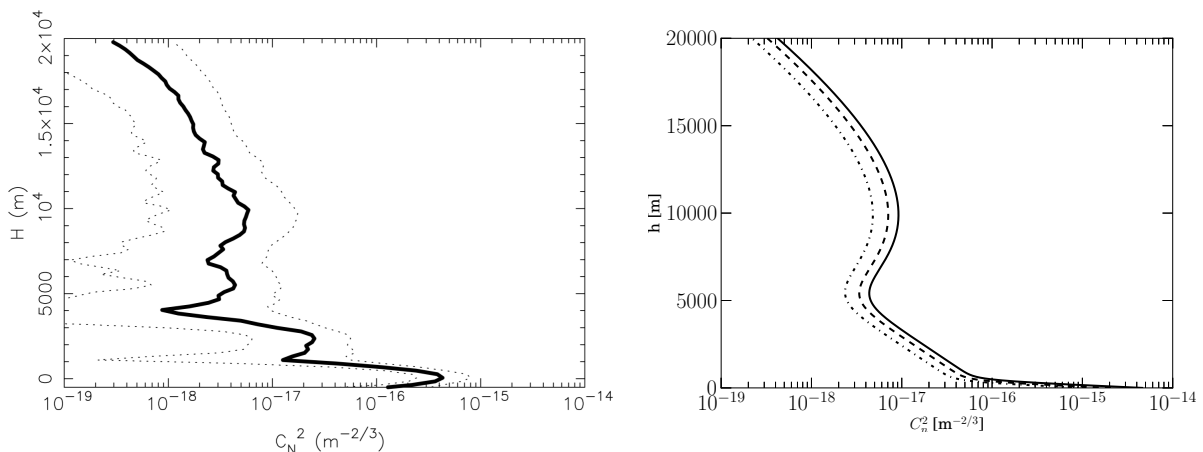
Figure 1.2: (Left) Median C_n^2 profile at Mt. Graham (at the LBT) based on data of 43 nights. The dotted lines indicate the standard deviation. Credit: Masciadri et al. (2010). (Right) Three general atmospheric models based on modified Hufnagel-Valley models. We distinguish three different regimes and use them to compute r_0, θ_0 and f_G. See Fig. 1.3.

To be able to characterize the temporal behavior, we also need a wind profile description. A standard form has been proposed by Bufton (1973) and is in [m/s]

$$v_W(h) = 5 + 30e^{-((h-9400)/4800)^2}. \tag{1.10}$$

Finally, instead of τ_0, one often uses the so-called Greenwood frequency as it is directly related to the required AO closed-loop bandwith requirement for a given temporal error. This is directly related to τ_0 by $f_G = 0.1344/\tau_0$. The Greenwood frequency is a measure of the rate at which the Kolmogorov atmospheric turbulence changes with time and is written as follows

$$f_G = 2.31\lambda^{-6/5}\left[\sec\zeta \int_{\text{path}} C_n^2(z)v_W^{5/3}(z)dz\right]^{3/5}, \tag{1.11}$$

where v_W is the atmospheric wind profile.

In Fig. 1.3, we integrate and plot as a function of wavelength the typical atmospheric parameters, r_0, θ_0, and f_G. In the near-infrared, we typically have $r_0 \sim 40\text{-}80$cm, and $\theta_0 \sim 7\text{-}15''$. This illustrates well the interest in adaptive optics even for telescopes as small as 1m diameter. The small isoplanatic patch illustrates the small portion of sky around a guide star that is well corrected. As we will discuss, it motivates wide-field adaptive optics concepts. Finally,
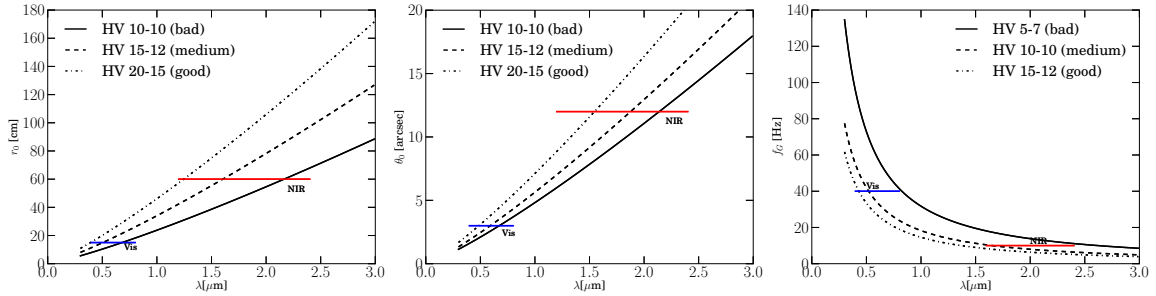
Figure 1.3: Typical parameters computed by using our C_n^2 model in function of wavelength. From left to right : the Fried parameter r_0, the anisoplanatic angle θ_0, and the Greenwood frequency f_G. In blue and red, the typical visible and near-IR wavelength ranges.

the Greenwood frequency is around 10Hz in the near-infrared. This then sets requirements on the closed-loop bandwith requirements. As mentioned before, those values are strongly dependent on λ, and visible wavelengths have much more stringent characteristic parameters, *i.e.* $r_0, \theta_0, f_G \sim 15$cm, $4''$, 40Hz.

1.2   Adaptive optics concepts

The basic goal of adaptive optics is easily stated: to measure the aberrations of an incoming wavefront and then cancel these out by applying compensation aberrations in real time.

     In the context of our previous discussion, a conventional adaptive optics system can only achieve near diffraction limit performances in the limit that the astronomical object of interest and the bright turbulence probe are of $< \theta_0$ separation, that the spacing between the control elements – and so of the wavefront sensing sampling – is better than the turbulence coherence length $< r_0$, and the closed-loop operates at a sufficiently high update rate providing a bandwidth $> f_G$. Those requirements are then mitigated in light of the technological limitations and the desired performances.

     The essential components of an adaptive optics system operating in closed-loop are represented in Fig. 1.4. The perturbed wavefront enters the system and is corrected by a fast tip-tilt mirror and a deformable mirror. The residual errors are measured by a tip-tilt sensor and a phase sensor. This is then used to compute appropriate commands to control the tip-tilt and the deformable mirrors. The distinction between tip-tilt and phase corrections is not a necessity but is often preferred due to the large stroke required for the tip-tilt correction.

     The overall performance of an adaptive optics system is estimated by summing the individual errors. The residual wavefront phase error is then given by

$$\sigma_{\text{system}}^2 \quad = \quad \sum_i \sigma_i^2 \tag{1.12}$$

$$\simeq \quad \sigma_{\text{temporal}}^2 + \sigma_{\text{fitting}}^2 + \sigma_{\text{measurements}}^2, \tag{1.13}$$

which is essentially dominated by three terms describing how well the correction is performed spatially, σ_{fitting}, and temporally, σ_{temporal}, and how well we are able to measure the wavefront, $\sigma_{\text{measurements}}$. This formulation is strictly valid if the different contributions are not correlated. In practice, it tends to overestimate the errors but is a conservative measure as it can compensate other unconsidered error contributions. We discuss the temporal and spatial
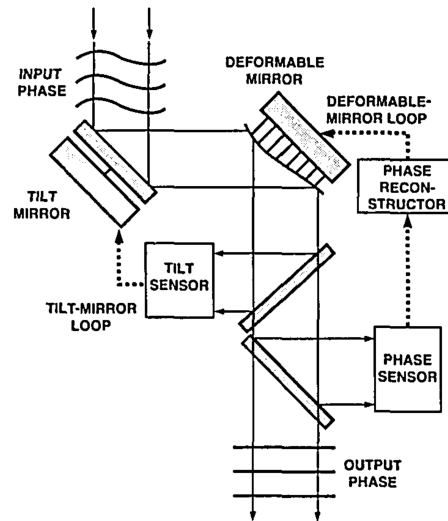
Figure 1.4: Essential components of an adaptive-optics system. The phase sensor measures the phase difference between the incoming wavefront and the surface of the deformable mirror. A separate tip-tilt sensor is used to correct for the image motion. Credit : Parenti & Sasiela (1994).

errors in the context of ARGOS in CHAP.2. The measurement error is discussed in the context of the Shack-Hartmann WFS here below.

1.2.1 Wavefront measurement

As the name implies, the wavefront sensor measures the aberrations of an incoming wavefront. Conceptually, the "wavefront sensing" converts a wavefront phase surface into a uniquely defined intensity distribution measurable on a detector. In turn this becomes an inversion problem to recover the original phase, *i.e.* the role of the wavefront reconstruction that we shortly describe in the next section.

Hence, the wavefront sensing involves manipulation of the original wavefront to facilitate the subsequent inversion. This manipulation can be done in the pupil plane (e.g. the insertion of a lenslet array in the Shack-Hartmann procedure), or the image plane (e.g. inserting a pyramid for pyramid wavefront sensing). The three most common AO wavefront sensors are : the Shack-Hartmann, the pyramid, and the curvature wavefront sensors. We discuss their principles and provide more details for the Shack-Hartmann.

Pyramid wavefront sensing. Instead of sampling the pupil, the PWFS focuses the wavefront onto the vertex of a four faces pyramidal prism. The four sides of the pyramid deflect the light in different directions, a lens relay is placed after that pyramid and creates four images of the pupil on a detector (Ragazzoni, 1996).

The two-dimensional principle is represented in Fig. 1.5. A flat wavefront is focused on the pyramid vertex and produces four identical pupil images. Aberrated rays (such as from a local gradient), will miss the vertex and be re-imaged only in one of the two images. Hence, the difference between the illuminations of the four pupil images recorded by the PWFS detector is proportional to the wavefront local derivative.
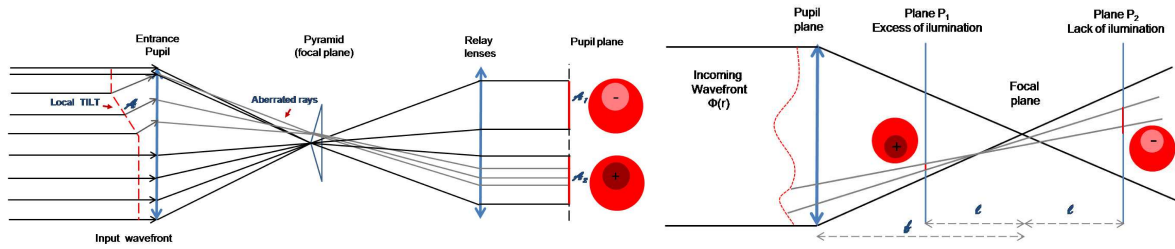
Figure 1.5: (Left) Pyramid WFS concept sketch (2D). A local phase tilt causes the aberrated rays to hit one side only of the pyramid causing pupil images non-uniformity between the four images. See text for more description. (Right) Principle of the curvature wavefront sensor. An local aberration (curvature) leads to a difference of illumination between the intra- and extra- focal plane $P1$ and $P2$. See text for more description. Credit : both sketches are from Aller Carpentier (2011).

However, as such, the PWFS quickly saturates for small aberrations : all the aberrated rays fall in one side of the pyramid and there is no information of the gradient strength. Hence, the PWFS are usually modulated to increase their sensitivity : the beam is circularly modulated around the pyramid vertex. Over one modulation cycle, the time spent on each face, and hence the intensity at the corresponding points in each of the four pupil images, will depend on the modulus of the aberration slope. The modulation of the pyramid is also one of its strengths : the possibility to easily adjust the sensitivity of the wavefront sensor with smaller modulation amplitude (*i.e.* smaller circle) more sensitive to smaller aberrations and vice-versa.

The First Light Adaptive Optics at LBT, commissioned in 2010, uses a pyramid wavefront sensor (Esposito et al., 2010). Its excellent performance has been demonstrated with high Strehl ratio[3] of ∼85% with bright ($m_r = 8.0$) guide stars and partial correction with guide star of $m_r = 17.5$ and Strehl of ∼5%.

Curvature sensor. This technique was introduced by Roddier (1988). It relies on the measurements of the intensity distributions in two different planes on either side of the focus, using the normalized difference between the two distributions. This difference is a measure of the curvature of the wavefront in the telescope pupil (and of the wavefront tilt at the aperture edge). A schematic principle is represented in Fig. 1.5. Two intensity distributions are recorded in the plane $P1$ and $P2$ at a distance l from the focal plane. The curved wavefront leads to a local excess of illumination in plane $P1$ and a lack of illumination in $P2$ as the light is spread out.

The adjustment of the distance l (and the CCD pixel size) modifies the sensitivity and the degree of correction. Larger l allows smaller aberrations to be measured. It can also be used with extended sources, for which for the same correction, l must be larger than for point sources.

As an example, the AO-module of SINFONI at VLT uses a 60-element curvature sensor system. A membrane mirror moves the pupil back and forth along the optical axis allowing

---

[3]the Strehl ratio is a measure of the optical quality of an imaging system. It is defined as the ratio of the observed peak intensity generated by a point-like object on the image plane compared to the theoretical maximum peak intensity of an imaging system working at the diffraction limit.

a lenslet array to intercept alternatively the intra and extra- focal regions. An aberration in the wavefront would decollimate the beam locally, causing the flux density to vary along the optical axis. The detectors are read out synchronously with the oscillation and used for the correction. Typically the Strehl ratio ranges from 20% to $> 60\%$ for guide star magnitude of $m_V \sim 16 - 11$ (Bonnet et al., 2004).

Shack-Hartmann sensor

The Shack-Hartmann sensor divides the telescope aperture into a set of small subapertures. It uses a lenslet array to produced multiple images and measures the wavefront aberrations. This is illustrated in Fig. 1.6. The angular displacement α_x of each of those sub-images with respect to their reference position gives an estimate of the average wavefront gradient in the x-direction over the subaperture. This can be expressed as (Primot et al., 1990)

$$\alpha_x = \frac{c_x}{fm} = \frac{\lambda}{2\pi A_{sa}} \int_{sa} \frac{\partial \phi(x,y)}{\partial x} dx dy, \qquad (1.14)$$

where c_x is the spot displacement, f is the lenslet array focal length, $m = f_{telescope}/f_{collimator}$ is the magnification between the telescope and the lenslet array, A_{sa} is the area of the subaperture, and ϕ is the wavefront phase. This equation also expresses the linear relation between the SH wavefront measurement and the first derivative of the wavefront. In practice, the spot position (x, y) measurements are often performed by a center of gravity estimation. More complex algorithms are also sometimes considered but they can require a priori knowledge, are less general, and can be slower. We discuss in CHAP.4 the algorithm implemented in the ARGOS wavefront computer, variation of the center of gravity.
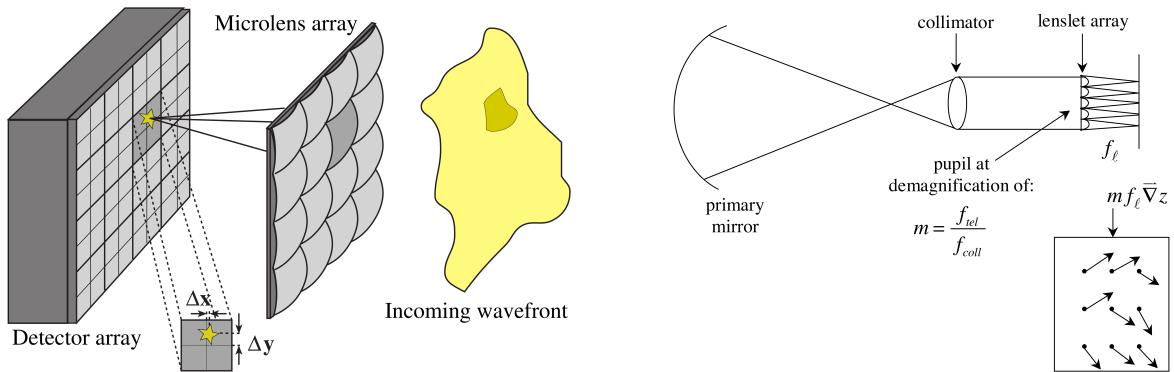
Figure 1.6: Shack-Hartmann concept sketchs. (Left) The incoming wavefront is subdivided by the microlens array, and image centroids are shifted according to average local wavefront slopes. Credit: Glindemann et al. (2000). (Right) The inset indicates typical displacement of the subimages proportional to the phase derivative. Credit: Chanan (2000).

The angle of arrival fluctuation σ_α over a subaperture of diameter d_{sa} can be approximated from the phase structure function (Kasper 2000, see also Primot et al. 1990 for an other

derivation)

$$\begin{aligned}
\sigma_\alpha \quad &= \frac{\lambda}{2\pi}\frac{\sqrt{D_\phi(d_{sa})}}{d_{sa}} \\
&= 0.42\frac{\lambda}{r_0}\left(\frac{d_{sa}}{r_0}\right)^{-1/6}.
\end{aligned} \tag{1.15}$$

From this expression, we see that the SH is achromatic (independent of λ since $r_0 \propto \lambda^{6/5}$), and σ_α is typically $\sim$0.4 times the seeing (if $d_{sa} = r_0$).

To evaluate the performance of the AO system, we need a measure of the wavefront sensor error. The accuracy of the spot position measurements will depend on two contributions : photon noise and detector noise. The one-axis measurement error in SH sensors, in radians RMS of phase difference per subaperture is (derived by Hardy, 1998)

$$\begin{aligned}
\sigma_{meas.} \quad &= \frac{\pi^2}{4SNR}\left[\left(\frac{3}{2}\right)^2 + \left(\frac{\theta d_{sa}}{\lambda}\right)^2\right]^{1/2} \qquad r_0 > d \\
\sigma_{meas.} \quad &= \frac{\pi^2}{4SNR}\left[\left(\frac{3d}{2r_0}\right)^2 + \left(\frac{\theta d_{sa}}{\lambda}\right)^2\right]^{1/2} \qquad r_0 < d
\end{aligned} \tag{1.16}$$

with θ the angular diameter of the reference source. For random perturbations, the total two axis error is $\sqrt{2}$ times this value. The SNR of the CCD detector depends on the photon noise, any background and the electronic readout noise. The SNR is described by

$$SNR = \frac{N}{\left[N + n_{pix}(\sigma_{ron}^2 + \sigma_{bckg}^2)\right]^{1/2}}, \tag{1.17}$$

where N is the number of photo-electrons per subaperture, σ_{ron} is the read-out noise, σ_{bckg} is the background flux in photo-electron per subaperture, and n_{pix} is the number of pixels in a subaperture.

1.2.2 Wavefront reconstruction

Having performed local measurements of the wavefront gradients (or curvature), this is now an inverse problem : converting the wavefront gradient measurements (for a SH) back in a wavefront to control a deformable mirror (DM), see Fig. 1.7. A common approach is to reconstruct the phase perturbation in a set of modal functions such as Zernike polynomials, and use this representation of the phase perturbation to calculate the appropriate command of each actuator. This modal approach is usually preferred to the zonal approach[4].

The starting point of the modal control is the modal decomposition of the wavefront into a set of functions

$$\phi(\mathbf{r}, t) = \sum_{i=1}^{\infty} a_i(t)F_i(\mathbf{r}), \tag{1.18}$$

---

[4]in the case of a "zonal" approach, the error associated to a SH subimage is minimised by tilting the respective(s) DM elements. This requires precise opto-mechanical alignement to ensure precise correspondence between the wavefront sensor elements and the deformable mirror. Also modal approach allows easier filtering and anti-aliasing to improve the performances.
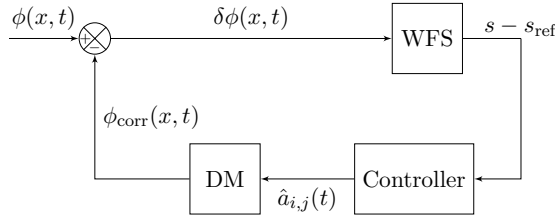
Figure 1.7: Block sketch of an adaptive optics system. A WFS measures the phase error residual $\delta\phi$, in the form of local gradient $s - s_{ref}$. A controller reconstruct the wavefront based on those measurements and command a DM with the command $\hat{a}$.

with F_i the basis functions describing the wavefront spatial characteristics, and the modal coefficients $a_i(t)$ describing the dynamics. The most commonly used bases are the Zernike polynomials – widely used to describe optical aberrations – and the Karhunen-Loève polynomials. The latter display lower residual phase variance as a function of the number of corrected modes compared to Zernike polynomials (Kasper, 2000).

Following this approach, two matrices are needed, the first transforming the values of the wavefront distortion measured values by the subapertures into the modal coefficients and the second relating the modal coefficients of the chosen basis to the zonal actuator displacements. The first depends on the response of the AO system as a whole and needs to be calibrated, and the second is dependent on the deformable mirror specificity. Hence, the static response of an AO system is characterized by its interaction matrix. It provides the mapping between the modal space and the WFS space, hence can be expressed by

$$\mathbf{s} = \mathbf{Ma},$$

with $\mathbf{a}$ the modal coefficients, $\mathbf{M}$ the interaction matrix, and $\mathbf{s}$ the wavefront measurements. This matrix $\mathbf{M}$ is typically measured experimentally. Its inversion allows the wavefront reconstruction, in a simple expression

$$\mathbf{a} = \mathbf{Rs},$$

thus performing the spatial reconstruction of the wavefront.

A second step is related to the temporal control and filtering of this command to ensure a good rejection and stability of the AO system. The simplest controller is a proportional integrator. This filtered commands are then passed to the DM and use to produce mirror commands, as sketched in Fig. 1.7.

1.2.3 Conventional adaptive optics limitation: sky coverage & anisoplanatism

Performing the AO correction at a sufficiently high wavefront spatial and temporal sampling requires a wealth of photons. This leads us to the issue of sky coverage or the probability to find a sufficiently bright star in the vicinity of the astronomical object.

Sky coverage estimation can make use of an analytical model of star densities. Parenti & Sasiela (1994) fit analytical functions of surface star densities and derive for the galactic pole (valid for $m_V < 20$),

$$D_p = 1.27 \times 10^{-4} (m_{V;0})^{8.2} \quad \text{stars per sq. rad with } m_V \geq m_{V;0}. \tag{1.19}$$

Using the above formula, the sky coverage (for low values)[5] is readily estimated by $Sc \approx \pi\theta_0^2 D_p$, *i.e.* the star density times the sky area within the isoplanatic patch θ_0. Natural guide star single conjugated adaptive optics (SCAO) systems have typically sky coverage of below 1%[6].

This poor sky coverage is the prime motivation for the use of artificial guide stars as generated with lasers, as we discuss in the next paragraph.

The second issue associated to SCAO is the angular anisoplanatism. Indeed, a SCAO system measures a cylinder of turbulence in the direction of the bright star used for correction. An increasing distance between this guide star and the astronomical target will cause their wavefronts to be uncorrelated, thus the performance will decrease. This is the angular anisoplanatism and is typically around $\theta_0 \sim 10''$ in the near-IR.

To increase the FoV of the AO correction, more advanced concepts are required, with more WFS and correctors. To perform a full compensation of the 3D turbulence, one requires several DMs in the optical path, conjugated to different layers. This is the concept of multi-conjugated AO. In the case of a single DM, the turbulence compensation can be performed over a wide field but only partially. In this case the DM is conjugated to the ground where the turbulence is the strongest, hence the term "Ground Layer" AO systems.

1.3   Laser guided ground layer adaptive optics

The angular anisoplanatism arises because what we correct in a SCAO system is effectively occuring in a volume, and not in a single plane. From this observation, and because the dominant layer in most astronomical sites is the boundary layer, ground layer compensation has been proposed as a "seeing enhancer", where only this layer common to all points in a finite field of view is compensated (Rigaut, 2002).

The principle is then as follows. Several guide stars at typically the edge of the FoV are used to sense the wavefront and extract the ground layer turbulence by averaging their contribution and cancelling out non-common aberrations from higher layers. In this concept, the higher layers usually dominate the error budget and the correction is only partial. In particular the PSF does not possess a diffraction core, but is uniform over a large FoV. The gain in FWHM size is typically a factor 2 to 3. This leads to a factor > 4 in integration time, equivalent to an increase of telescope diameter by a factor 2.

While this can be performed in principle with natural guide stars, it requires a sufficient number of bright stars in the required geometry, further reducing the sky coverage. Hence, GLAO systems normally use artificial guide stars to perform the wavefront measurements, and have virtually full sky coverage. Sky coverage is also the prime driver for laser guided adaptive optics sytem in general. Two regimes should be distinguished : "Sodium" laser guide star using a laser to excite Sodium atoms present at an altitude of $\sim$100km; and "Rayleigh"

---

[5]the spatial distribution of the stars on the sky follows a Poisson law (assuming clustering is negligible). Hence the probability to get k stars in an area S is $P\{k, S\} = \left((D_p S)^k / k!\right) e^{-D_p S}$. Thus the probability of getting at least one star in a field of view of $\pi\theta_0^2$ is

$$Sc = P\{k = 1, 2, 3, ...; S = \pi\theta_0^2\} = 1 - P\{k = 0, S = \pi\theta_0^2\} = 1 - e^{-D_p \pi\theta_0^2},$$

where Sc is the sky coverage. In the low value limit $Sc \approx D_p \pi\theta_0^2$. See also e.g. Rigaut (1994).

[6]applying this star density to the First Light Adaptive Optics (LBT) results leads to $\sim$0.7% sky coverage for a partial correction of Strehl ratio$\sim$5% assuming $m_r \simeq m_V$ ($m_V = 17.5$, $\theta_0 = 7''$).
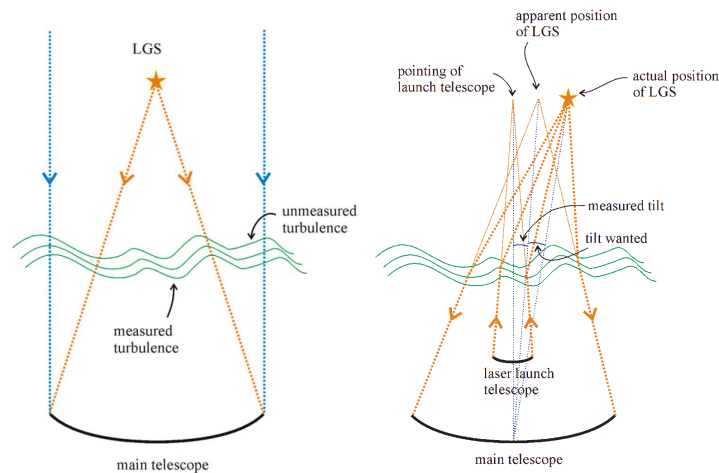
Figure 1.8: (Left) Illustration of the cone effect for a guide star at a finite height. This is also referred as "focus anisoplanatism". (Right) Illustration of the LGS lack of sensitivity to tip-tilt due to the round trip of the laser beam through the atmosphere. Credit : both illustrations are from Davies et al. (2005a),

guide star based on the scattering of air molecules and usually aimed for 10-20km heights. For GLAO operation, "Rayleigh" guide stars are normally preferred as the non-common aberrations have a smaller contribution, allowing a better ground-layer reconstruction. Rayleigh scattering is the elastic scattering of optical radiation for which the wavelength is much larger than the physical size of the scatterers, *i.e.* in our case the atmospheric molecules. A well known result is that the Rayleigh scattering is larger for shorter wavelength, $\propto \lambda^{-4}$, and that it decreases with the density of air molecules, itself decreasing exponentially with altitude. Those two considerations favor lower altitude guide stars (10-20km) and shorter wavelengths. This scattering also presents a downside effect : since a large amount of light is backscattered by the lower atmosphere, the useful signal is generally diluted. Hence, pulsed lasers are usually preferred to reduce the light pollution effects, which implies the coupling of the pulsation with a temporal range gating system.

As we have seen, the use of laser guide stars allows us to resolve the sky coverage and possibly the angular anisoplanatism issues. However LGS-AO does not come without problem, and a number of laser guide star peculiarities can be identified :

Complexity. A large increase in complexity and cost is needed to create those dedicated lasers, to control them and maintain them. Necessary launch optics is required and if pulsed lasers are chosen, a gating system is also required.

Cone effect and unsampled turbulence. As those guide stars are generated at a finite height, they do not sample the entire cylinder of turbulence, but only their respective cone. This is also illustrated in Fig. 1.8. The effect is referred to as cone effect or focus anisoplanatism. Two separate effects can be distinguished : the upper unsampled turbulence, and the lower incorrectly sampled turbulence. These two effects are described

analytically by Parenti & Sasiela (1994). In a multi-guide stars GLAO, the cone effect is averaged out at the price of higher unsampled upper turbulence.

Spot elongation. As the sensed backscattered light is from a finite altitude depth, the star will be elongated[7] generating additional measurement errors. This results in a lower accuracy of the SH measurements along the elongation axis (see equation 1.16).

LGS jitter. The positioning of the laser is dependent on the telescope pointing capability, the internal jitter, but as well from the upper propagation, and requires an additional dedicated stabilizing mirror. Since the width of the launch aperture is usually close to r_0, considering equation 1.15, the LGS jitter on sky is about half the seeing size λ/r_0. The jitter from the downward propagation is smaller considering the larger diameter of the telescope.

LGS tip-tilt. Another conceptual limitation is the LGS lack of sensitivity to tip-tilt. This is illustrated in Fig. 1.8. Basically the overall tip-tilt is hardly measurable with the LGS due to the round trip of the laser beam through the atmosphere leaving its absolute position on the sky uncertain. A few techniques have been proposed, e.g. : using auxiliary telescopes to measure the upward jitter (Ragazzoni & Esposito, 1999), or using a polychromatic laser so that the tip-tilt can be measured from diffferential dispersion in the atmosphere (Foy et al., 1995). Because those are complex solutions, and usually only provide partial correction, they essentially have not been implemented so far leaving the LGS tip-tilt determination challenge open. This conceptual limitation imposes a requirement to use a NGS for tip-tilt sensing even for LGS operation. Having to measure only two slopes relaxes the flux constraint and allows one to greatly increase the sky coverage. This is further supported by a somewhat larger tip-tilt isoplanatic patch due to the slower decorrelation of the tip-tilt with angular distance. However, as the tip-tilt needs to be sampled as fast as any other mode, large enough fluxes are still required. Typically LGS-AO systems have sky coverage in the range of >70% with NGS magnitude of $m_V > 18$.

In appendix A, we explore this LGS tip-tilt further, discussing how partial upward tip-tilt recovery could be possible based on spatial and temporal decorrelation considerations.

Despite their complexity and the challenges we have described, LGS AO systems have become more common by their sky coverage attractiveness, in particular also allowing extra-galactic research to benefit from it (see e.g. Davies & Kasper, 2012, Wizinowich, 2013, for a review of the astronomical impact of adaptive optics).

GLAO LGS, by enlarging the FoV and providing an uniform PSF, increases the range of applications of AO to astronomical research. In the next section, we shortly present the existing and forthcoming GLAO facilities.

---

[7]From simple geometry, the spot elongation θ_{el} can be approximated by

$$\theta_{el} \simeq \frac{\Delta h x}{h^2},$$

whit h the altitude, Δh the layer slab used for the wavefront sensing, and x the radial distance in the telescope plane. For a 8-m telescope, and $h = 12 km$ and $\Delta h = 300m$ (ARGOS conditions), we get a maximum spot elongation of $\theta_{el} \simeq 1.7''$, so about $2 \times$ the seeing size. This problem becomes much more significant for ELT sizes.

1.3.1   GLAO facilities

In the more recent past a number of experiments and projects have been triggered first to prove the on-sky feasibility of (LGS-)GLAO and to offer it as future facilities. Two pathfinder experiments are : the MAD bench installed at one of the VLT telescopes, and the GLAO system at the MMT. Past, current and foreseen GLAO facilities are : the GLAS at WHT, the SAM at SOAR, GRAAL for the VLT, and of course Argos at LBT. A comparison of a few essential parameters is summarized in Tab. 1.1.

The MAD system is a multi-conjugate adaptive optics demonstrator to prove the feasibility of different MCAO concepts. It was mounted on one Unit Telescope of the VLT to perform on-sky tests. In that context they demonstrated the feasibility of the GLAO concept using three natural guide stars on circles of $1'$ or $2'$, providing an improvement under various seeing conditions and a relatively uniform PSF (Marchetti et al., 2007).

The MMT GLAO system has demonstrated the feasibility of GLAO with laser guide stars. It generates a five stars asterism launched on-axis behind the secondary for a total of 24W power. On the sensing part, instead of using a gating system, it employs a refocusing mechanism while the pulse propagates. This allows it to integrate the scattered light over a larger altitude range and thus to collect more photons, for a sensing range of 20 to 29km altitude. The adaptive secondary mirror (ASM) is based on the same technology as the LBT ASM and has 335 voice coil actuators. The demonstrated performances are a gain of >2 for a FoV of $\sim 2'^2$ (Hart et al., 2010).

The GLAS system at the WHT observatory created an artificial star at 15km. The laser was launched on-axis behind the secondary. A gating was performed with Pockels cells similarly to Argos. The AO correction was performed with a 8-segments deformable mirror for a 4.2m telescope diameter. The scientific driver was essentially the increased sky coverage. GLAS essentially improved the capabilities of the near-infrared camera INGRID. GLAS has shown a gain of > 2 for a moderate wide field of view of $\sim 40''^2$. The system is now decommissioned.

SAM is the SOAR Adaptive Module and has been recently offered to the community. It is a single laser GLAO, using a UV laser thus increasing the Rayleigh scattering efficiency. This has required dedicated optics and full enclosure to the launch telescope mounted behind the secondary. It also uses a Shack-Hartmann WFS, with Pockels cells, and APDs for the tip-tilt measurements. This comes with a visible and infrared imaging camera for a $3'$ FoV. At the time of writing, the system is in scientific demonstration before being offered to the community.

Finally, GRAAL will feed the HAWK-I instrument, a large near-infrared imager already in operation at VLT. The science field of view is 7.5 arcmin square. The correction will be provided by a new adaptive secondary mirror, similar to the LBT one. It will use four Sodium lasers, thus generating guide stars at 80-100km altitude outside the scientific FoV. The expected gain factor is between 1.5-2 in resolution. It is currently planned for 2015. At the current time it is however not clear whether HAWK-I will be kept for science operations once it has been used to commission GRAAL. The somewhat smaller gain factor resolution is due to the trade-off between FoV and corrected turbulence. Indeed the larger the FoV one wants to correct, the thinner the compensated effective layer.

In the next chapter, we describe the Argos system and the concepts and designs allowing it to provide its wide-field ground layer correction.

Table 1.1: Parameters comparison of LGS GLAO systems. The MMT GLAO, and GLAS are considered apart. The first is so far only a demonstrator and is not offered as a facility. The second is now decommissioned.

	SAM [SOAR]	GRAAL [VLT]	ARGOS [LBT]	MMT [MMT]	GLAS [WHT]
FoV	$3'^2$	$7.5'^2$	$4'^2$	$2'^2$	$40''^2$
NIR Instrument	SAM (I)	HAWK-I (I)	Luci (I,S,MOS)	PISCES (I)	INGRID (I)
LGS numbers	1	4	3	5	1
Laser λ [nm]	335	589	532	532	515
Laser altitude	10km	90km	12km	20-29km	15km
Telescope D	4.1	8.2	2×8.4	6.5m	4.2
Gain FWHM	2 (y, I)	1.5-2	2-3 (K)	2-3	> 2
Date	2013	2015	2014	2010	2008

ARGOS ADVANCED RAYLEIGH GUIDED GROUND LAYER ADAPTIVE OPTICS SYSTEM

In the following chapter, we present the motivation, the general design and the overview of ARGOS. We try to emphasize the concepts and related designs that will enable ARGOS to have a strong scientific impact. More detailed information can be found in the many design documents (Phase A study, PDR, and FDR ARGOS consortium, 2008, 2009, 2010), as well as a number of proceeding papers. The contribution of this thesis to the ARGOS project concerns the wavefront sensing part, in particular the wavefront sensor detector and its associated computer and are covered in more details in the two following chapters CHAP.3 and CHAP.4. These have also been partly reported in (ARGOS consortium, 2010, FDR 016) and in Orban de Xivry et al. (2010, 2011), and Orban de Xivry & Rabien (2012).

2.1 Motivation & goals

ARGOS is the acronym of Advanced Rayleigh Guided Ground Layer Adaptive Optics System for the LBT. The scientific motivation of ARGOS can be simply stated: the ground layer adaptive optics system will strongly increase the scientific capabilities of LUCI at LBT, a wide field imager and multi-object spectrograph (MOS).

We shall set the scene first, presenting shortly the LBT, the LUCI instrument, and the benefit brought by ARGOS.

The Large Binocular Telescope The LBT is an 8m-class telescope in Arizona that includes an AO system by design. The mechanical structure is a single alt-azimuth mount supporting its two 8.4m diameter mirrors. Its fast primary optics (with a focal number[1] $f_{1.142}$) allows a Gregorian configuration with two adaptive secondary mirrors (ASM) of 0.91m diameter producing f_{15} beams. Each ASM features a single 1.6 mm thin shell made of Zerodur and has 672 actuators, and is operated at tens of kHz (allowing 1kHz closed-loop). These ASMs therefore provide AO possibilities for any focal station, hence decreasing the number of optics placed before any instruments. As a potential interferometric facility, the LBT provides an equivalent 22.8m baseline. Instruments can be placed at the prime focii (LBC, the wide field cameras), at the direct Gregorian focii under the primary mirrors (MODS, the visible

---

[1]the ratio of the focal length to the aperture diameter

imaging and MOS), and at bent Gregorian focii (Luci, the near-IR imaging and MOS ; LBTI, the mid infrared coronograph and interferometer in nulling configuration; LINC-NIRVANA, the near-IR interferometer; and PEPSI, the fiber fed high-resolution echelle spectrograph).

LUCI The instrument is one of the main "science-enabler" LBT instruments. It provides near-infrared imaging, long-slit spectroscopy in seeing and diffraction limited mode, and multi-object spectroscopy in seeing-limited mode. The first Luci has been in operation for a few years now, so far only in seeing-limited operation, and the second Luci and the AO optics integration is on-going. The strength of Luci resides in its versatility and its field-of-view. Indeed, it provides a $4' \times 4'$ ($30'' \times 30''$ in diffraction limited operation) FoV for imaging, and $4' \times 2.8'$ for multi-object spectroscopy, allowing large multiplexing of 20 slits or more in one shot.

It covers a large wavelength range of 1.0-2.4μm with a set of broad (J, H, K, $H + K$) and narrow filters (e.g. Brγ, FeII 1.64μm, H$_2$ 2.12μm, etc.). The instrument will offer three resolution configurations with f-numbers of $f_{1.8}$, $f_{3.75}$, and f_{30} or in pixel scale 0.25$''$, 0.12$''$ for seeing limited, and 0.015$''$ for diffraction limited operations. Depending on the grating and the camera, the spectral resolution ranges from $\sim$2000 to 40000. More details can be found in e.g., Buschkamp (2012).

The Luci dichroic entrance window is tilted by 15 degrees and reflects light with $\lambda < 0.87\mu m$ towards the natural guide star wavefront sensor unit (also called First Light Adaptive Optics unit). Light with $\lambda > 0.87\mu m$ passes into the instrument. The useful unvignetted FOV of the telescope has a diameter of $\sim$7$'$. This FOV is stopped down to a usable FOV of $4' \times 4'$ in the instrument focal plane where longslit and multi-object slitmask can be placed for spectroscopy.

ARGOS The prime driver for Argos is to be a "seeing enhancer" for Luci, taking advantage of the LBT instrument and enhancing the FWHM by a factor 2-3 over the Luci wide field of view. The key to success is to develop a reliable and robust system that greatly enhances the science "throughput" of the instrument by allowing faster observations and transforming good nights into excellent seeing conditions (demanding observing programmes could therefore be carried out most of the nights).

From this broad definition, early simulations have shaped the conceptual design : a constellation of three laser guide stars at 12km distance placed on a circle of $2'$ radius allows to effectively sense the ground-layer and correct for it. The behavior with various seeing conditions has also been demonstrated, casting on average a gain of 2-3 in FWHM (equivalently 4-9 in a square of 0.25$''$ width), see Fig. 2.1. More recent work has refined the simulations by incorporating realistic optics (FDR, using directly the Argos optical design), and realistic end-to-end simulation (Bonaglia, 2012). They confirm the previously predicted gain presented Fig. 2.1.

The bottom line here is that 1) observations can be done much faster, saving a significant amount of time, 2) science programmes that would require the best seeing conditions could instead be performed most of the time.

Following this expectation, the improvements brought by the LGS-GLAO on an instrument such as Luci can be described in a number of ways,

- *Increased Point Source Sensitivity.* For point sources, the improvement in the PSF FWHM allows one to reduce the aperture size and hence reduce the background noise

contribution, or vice-versa, reduce the integration time. Indeed, the SNR in background limited regime scales as

$$
\begin{aligned}
S/N &\propto \frac{f_{\text{aper}}t}{\sqrt{d_{\text{aper}}^2 t}} \\
t &\propto \left(\frac{d_{\text{aper}}}{f_{\text{aper}}}\right)^2 \qquad \text{at constant S/N}
\end{aligned}
\tag{2.1}
$$

where f_{aper} is the fraction of the point source flux within the aperture, d_{aper} is the aperture diameter, and t the integration time. We can readily see that for a constant f_{aper} the aperture diameter can be reduced by a factor 2-3, hence the integration time by 4-9 times. This is therefore a large gain in observing efficiency.

- *Increased Slit Coupling Efficiency.* In a similar fashion to what we have just described, for a fixed spectral resolution, compact sources (such as high-redshift galaxies) will be better coupled to the slits. This effect will be particularly important at small slit width (hence high resolution) and the gain in integration time would be similar, *i.e.* estimated to ~ 5.

- *Reduced Crowding Noise.* In dense field, crowding becomes the limiting factor. Wide field correction is especially interesting for crowded field that can be larger than the isoplanatic patch of a SCAO system. Hence Argos will also improve the depth of dense star cluster fields with a gain in magnitude of a few.

- *Enhanced Spatial Resolution.* For extended sources, the gain does not reside in SNR (as the pixel size is also decreased), but as a gain in morphological and kinematical information. Galaxy structures and their rotation curves may be acquired in greater details and this over the large FoV of $4'$ of Luci.

2.2 General design considerations

The Argos science requirements as a seeing-enhancer is to improve the seeing by a factor 2 for 75% of the observable nights, and to reach $0.25''$ on a significant fraction of them. In the following we detail a few key aspects of the Argos design that will allow us to meet these requirements. We discuss the LGS constellation geometry, the sky coverage, the LGS photon return, the wavefront reconstruction and the overall error budget.

Geometry & wavefront sampling The Phase A study and PDR have shown that 4 LGS only marginally improve the correction compared to 3 LGS in term of energy concentration. Different radius sizes ($2'$, $4'$, $6'$) of the constellation have been simulated. A larger radius leads to better uniformity but lower correction. As the correction non-uniformity was still relatively small, the smaller configuration of $2'$ radius constellation has been chosen.

The geometry drives in fact indirectly the sampled and possibly corrected turbulence above the telescope, thus also the spatial wavefront sampling. The maximum altitude at which the LGS light cone overlap for a single subaperture is given by

$$
h = \frac{d_{\text{subap}}}{2}\frac{1}{\tan\theta/2},
$$
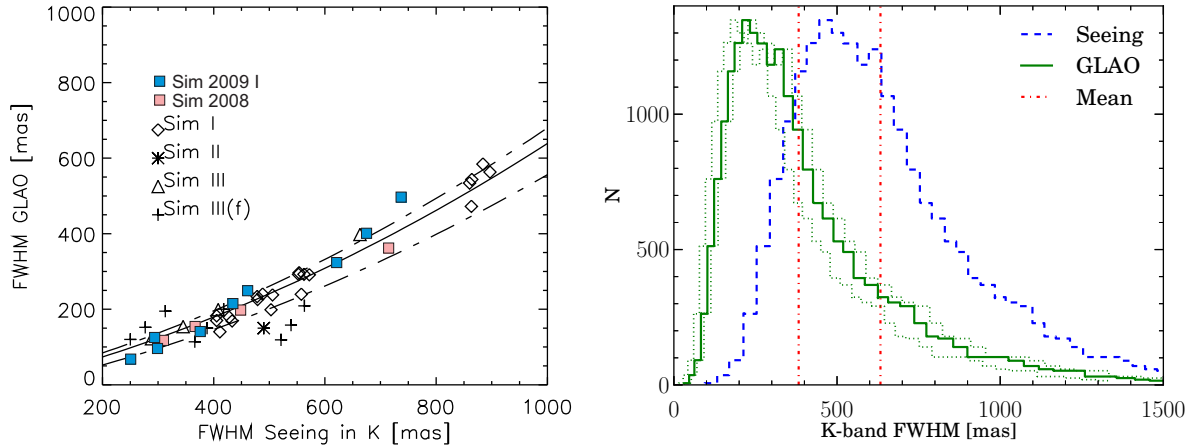
Figure 2.1: (Left) Argos performances evaluation based on closed-loop and Argos optics simulations. We can observe the factor of 2-3 improvement in the PSF FWHM. (Right) Predicted reduction of the PSF size in the K-band based on seeing statistics as derived at the MMT in Arizona. The mean of the distribution before and after GLAO ($0.63''$ and $0.34''$ respectively), correction are indicated in red. Credit: Argos consortium (2009, 2010).

where θ is the angular distance between the LGS beams, *i.e.* $\theta \sim 3.5'^2$, and so the maximum altitude is $h \sim 550m$. As a first approximation any turbulence above this altitude can be considered uncorrected. We discuss in the last paragraph of this section how it translates in term of error budget.

Sky Coverage As a LGS system, the observable fraction of the sky is limited by the probability to find a suitable natural tip-tilt star. The constraints for Argos are relatively relaxed. First, the tip-tilt sensor will sit on the on-axis natural guide star wavefront sensor unit in front of Luci, hence the typical field available to find a tip-tilt star is similar to the Luci FoV, *i.e.* a circle of $\sim 2'$ radius. Second, the star can be relatively faint due to a larger error budget – translating into a larger pixel scale (120mas for the finest pixel scale that preserve the $4' \times 4'$ wide field) – than typical diffraction limited system. Indeed, constraining the tip-tilt error to not broaden the PSF by more than 10% results in a maximum jitter of 100mas, considering a PSF width of 200-240mas.

The science case study (at PDR) cast a requirement of $> 80\%$ sky coverage – even for the deep fields. In order to estimate the required tip-tilt star limiting magnitude this requirement translates into, we can use the simple model of star density for the galactic pole as given by equation 1.19, and use Poisson statistics to estimate the sky coverage. Assuming an available FoV of $2'$ circle radius, we find that a magnitude of $V \sim 18$ would provide $> 90\%$ and

---

[2]assuming $4'$ diameter FoV, the distance of 3 LGS distributed in an equi-triangle is $\theta^2 = 2 \times 2^2 - 2 \times 2 \times 2\cos(lgs1, lgs2)$.

A slightly more accurate expression for h would be:

$$h = \frac{d_{\text{subap}}}{2} \frac{1}{\tan\theta/2} \frac{1}{1 + \frac{d_{\text{subap}}}{2H} \frac{1}{\tan\theta/2}},$$

with H the LGS altitude. From the same numbers, $h \sim 525m$.

a $V \sim 19$ would provide $\sim 98\%$, almost full sky coverage. More details considerations of particular deep-fields (see PDR Argos consortium, 2009) show in fact that a $V \sim 19$ should provide $>80\%$ of sky coverage in those field.

This magnitude is approximately equivalent to $R \sim 18 - 18.5$ and is therefore the required limiting magnitude for Argos. More details about the NGS tip-tilt is given below in section 2.3. See also Fig. 2.6.

LGS Photon Return   An essential parameter of a LGS system is the number of photons it has to generate for a given photon return on the wavefront sensor detector. Based on Rayleigh scattering theory, and a careful transmission budget, the expected number of photons returned back to the WFS detector have been calculated by subaperture and by integration for a laser power of 18W at 10kHz and an altitude of 12km and 15 subapertures on the pupil diameter. The overall transmission efficiency including atmospheric transmission has been estimated at PDR (Argos consortium, 2009). The values are given in Tab. 2.1 for three different gating heights and two different transmissions. The baseline for Argos is a gating over 300m ensuring $\sim$1800 photons/subaperture/frame. This is further used as a requirement in Chap.3, where we see that those return fluxes give an ample margin for the wavefront measurement.

Table 2.1: Number of returned photons on the WFS detector per subaperture per frame (1ms). Assuming 18W laser power at 10kHz and 532nm, 1kHz detector rate, 15×15 subapertures, an altitude of 12km above the telescope altitude. See Argos consortium (2009).

Gating height ΔH [m]	$\eta_{tr} = 0.25$	$\eta_{tr} = 0.1$
200	1220	488
300	1830	731
400	2440	975

Wavefront sensing & reconstruction   As discussed in our crude error budget in the next paragraph, the main residual wavefront error contribution is the uncorrected higher layer turbulence. Hence the wavefront spatial sampling is not required to fully sample r_0, but the subaperture size should be chosen as a compromise between low fitting error and high flux per subaperture. The Argos concept is to use 15 subapertures on the pupil diameter for a total of $\sim$175 subapertures[3] over the entire pupil and to correct for $\sim$150 modes. The Argos wavefront sensing computation definition and implementation is part of this thesis and is presented in Chap.4. On the other hand, the Argos reconstructor is implemented in the ASM electronics (see Xompero et al., 2008, for a complete description).

The baseline control loop is in fact a proportional integration,

$$\mathbf{m}_f = \mathbf{g}\mathbf{B}_0\mathbf{s}_f + \mathbf{e}_{f-1}, \tag{2.2}$$

where $\mathbf{m}_f$ are the modes to be computed for the frame f, $\mathbf{g}$ is the gain vector, $\mathbf{B}_0$ the reconstructor, s_f the slope vector (wavefront measurements), and $\mathbf{e}_{f-1}$ are the pre-computed

---

[3]the exact number depends on how useful are the subapertures that are partially vignetted and that receive less flux.

modes based on the previous frame (or iteration) $f - 1$ that are added to the differential modal command. Once computed, the modes are then projected on the command space of the ASM (from modal to zonal space) by a simple matrix multiplication $\mathbf{c}_f = \mathbf{M}\mathbf{m}_f$, which is then directly used by the internal control of the ASM. An additional disturbance vector $\mathbf{c}_{\mathrm{noise};f}$ can be added to this command vector, which is typically used for calibration.

The main element of equation 2.2 is the reconstruction matrix $\mathbf{B}_0$ allowing the mapping from wavefront measurements to modal commands. The reconstruction matrix is typically obtained by pseudo-inversion[4] of the interaction matrix $\mathbf{IM}$. The later is part of the calibration of the ARGOS AO loop, and is obtained as follows. Modes are successively applied to the ASM (e.g. by using the disturbance vector $\mathbf{c}_{\mathrm{noise}}$) and for each of them the wavefront measurements are recorded therefore constructing the matrix $\mathbf{IM}$ of dimension $(N_{slopes} \times N_{modes})$. The ARGOS interaction matrix is made of three blocks : the three LGS Shack-Hartmann sensors $\mathbf{IM_{LGS;1-3}}$, the natural tip-tilt sensor $\mathbf{IM_{TT}}$, and an optional third wavefront sensor $\mathbf{IM_{Na/FLAO}}$ (either the natural guide star wavefront sensor unit or from an ARGOS upgrade including a Sodium laser guide star) and can thus be written as follows,

$$\mathbf{IM} = \begin{bmatrix} 0 & 0 & \mathbf{IM_{LGS;1}} \\ 0 & 0 & \mathbf{IM_{LGS;2}} \\ 0 & 0 & \mathbf{IM_{LGS;3}} \\ \mathbf{IM_{TT}} & 0 & 0 \\ 0 & \mathbf{IM_{Na/FLAO}} & 0 \end{bmatrix}, \tag{2.3}$$

In case the optional wavefront sensor is not used, all modes are sensed by the ARGOS LGS wavefront sensor except for the first two tip-tilt modes, and the matrix above is simplified accordingly. This is also the ARGOS baseline. A detailed description of the ARGOS AO calibration is given in Busoni & Puglisi (2013).

In addition to those wavefront measurements and the modal reconstruction, ARGOS will use the natural guide star wavefront sensing unit to measure slowly changing non-common path aberrations between the LGS optical beam and the near-infrared light going to LUCI. This "truth sensing" will be projected back to slopes and offloaded as new slope offsets in the ARGOS wavefront sensing computer.

The collection of all those measurements has been foreseen at the ARGOS slope computer level, as discussed in CHAP.4.

A crude error budget   A GLAO system has, by definition, a large spatial wavefront error from unsampled turbulence. By design ARGOS should minimize any other contribution.

The main contributors to the error budget are:

- *Unsampled turbulence.* To estimate the spatial wavefront error from unsampled turbulence, we can make the following simplification. Let us assume that the turbulence below $\sim$500m (as the maximum altitude where the subaperture beams overlap, see above) is perfectly corrected, and higher altitude turbulence is uncorrected. We can compute[5]

---

[4]The pseudo-inversion is based on Singular Value Decomposition, and is also the least square minimization of a linear system. In a way this pseudo-inversion will thus optimize the respective weighting of each LGS wavefront measurements. Indeed in practice, the different LGS measurements are not identical but have different orientation on sky for which the telescope aberrations may be different, and the secondary mirror is not exactly conjugated to 0km but to $\sim$100m (hence the three LGS "see" the DM slightly differently).

[5]either by integration of a modified C_n^2 profile or by use of $r_0 = (\sum_i r_{0,i}^{-5/3})^{(-3/5)}$ if the layer contributions have been previously identified for simulation.

a r_0^{new}, and estimate the error by $\sigma_{GLAO}^2 \sim \left(\dfrac{D}{r_0^{new}}\right)^{5/3}$. This is a similar formula to the wavefront variance due to the cone effect. For example an initial $r_0 = 0.2$m would become $r_0^{new} \gtrsim 0.5$m, hence the seeing would improve from $0.56''$ down to $\sim 0.25''$. The corresponding residual contribution would be $\sigma_{GLAO} \lesssim 1000$nm at 500nm.

- *Fitting error.* This represents the accuracy with which the WFS samples the wavefront and how well the DM can be shaped to the reconstructed wavefront. The wavefront sampling, by the ARGOS small number of subapertures, is here driving the fitting error. This error can be either expressed in a "zonal" form:

$$\sigma_f^2 = c_f \left(\frac{d_s}{r_0}\right)^{5/3} \quad [\text{rad}^2],$$

with $c_f \approx 0.34$ (Parenti & Sasiela, 1994)[6] and d_s the subaperture size projected on the primary mirror, or in a "modal" form (Noll, 1976):

$$\sigma_f^2 = 0.2944 N_m^{-\sqrt{3}/2} \left(\frac{D}{r_0}\right)^{5/3} \quad [\text{rad}^2].$$

with N_m the number of Zernike corrected modes. ARGOS has subaperture sizes projected on the primary of $d_s = 0.56$m and intends to correct for ~ 150 modes. Both estimates lead to a wavefront error of ~ 110 nm for $r_0 = 0.2$m at 500nm.

- *Temporal error.* The temporal error is a function of how well the system can keep up with the changing turbulence. This depends on the sampling rate of the wavefront and the time delay between the measurement and the correction. This is globally described by the closed-loop bandwidth f_{BW}. Hence the error can be expressed by

$$\sigma_{temp}^2 = C \left(\frac{f_G}{f_{BW}}\right)^{5/3} \quad [\text{rad}^2], \tag{2.4}$$

where f_G is the Greenwood frequency giving the changing rate of the turbulence, and $C = 1$ for a typical servo-loop (*i.e.* a proportional integrator). The typical Greenwood frequency at 500nm is $f_G \sim 40$Hz, and the ARGOS f_{BW} will be around 70-100Hz thanks to its high sampling rate (1kHz) and small delay $\tau < 2$ms. Hence the temporal error is foreseen to be ~ 40-60nm. We discuss in more details the ARGOS closed-loop bandwidth in relation with the ARGOS slope computer, part of this thesis work, in CHAP.4 section 4.5.

- *Centroiding or measurement error.* The measurement accuracy of the sampled wavefront is another potential error source. Ultimately, the error performed on individual subapertures should be propagated through the reconstruction. For simplicity, however we will stick to the phase error within one subaperture and use equation 1.16. Considering a readout noise of $4e^-$, and ~ 1800 photons/subaperture/frame, we get an approximate measurement error <50nm at 500nm, $r_0 = 0.2$m, and for a subaperture pixel size of $0.56''$. This value will also be used as a requirement in CHAP.3.

---

[6]as calculated for a continuous-mirror structure with one actuator per subaperture with perfect matching.

From those various estimates, we clearly see that the unsampled turbulence is the dominant factor as intended by design.

The design phases of ARGOS have actually provided more detailed error budgets, given here in Tab. 2.2, by means of various simulations (we refer to the PDR, ARGOS consortium 2009, for detailed information). More recent system simulations have also confirmed those numbers (Bonaglia, 2012). Nevertheless, we can see that our crude estimation captures correctly the various contributions.

Table 2.2: Error budget for the main contributors for different atmospheric conditions (given in percentile of the expected LBT conditions). Values are given in [nm] at 500nm wavelength.

Atmosphere	25 %	50%	75%	bad
Unsampled turbulence and fitting error	380	460	540	850
Temporal error	90	106	124	170
Centroiding error and reconstruction error	38	39	40	50

2.3   System overview

Following its wide field correction objective, the ARGOS baseline, sketched in Fig. 2.2, is as follows for each LBT eye. Three Rayleigh pulsed LGS are projected at 12km on a circle of $2'$ radius. All three lasers are triggered upon command at a 10kHz repetition rate, firing ∼40ns pulses. The beams are expanded, first by the laser system and then by the launch optics, and launched on-axis above the secondary mirror by two large flat mirrors and focussed at 12km distance. As the beams propagate through the atmosphere, photons are scattered back by air molecules. After ∼80μs, the light from 12km distance returns back to the telescope allowing us to probe the atmospheric turbulence.

The backscattered light is directed in front of the LUCI rotator structure and a dichroic setup reflects the laser beams towards the ARGOS wavefront sensor system (WFS). The latter collimates the beams coming from 12km distance, brings them together, stabilizes them (i.e. LGS tip-tilt and vibration compensations), centers the pupils, and optically gates the light over an equivalent height of 300m around 12km altitude. The gated beams fall then on a lenslet array creating three image arrays on the detector, i.e. a large, high speed and low readout noise PNCCD. The lasers and the optical gating units are typically synchronized at 10kHz, creating 10 snapshots before the readout of the PNCCD at 1kHz. The frames are collected by the ARGOS slope computer, which then computes the local wavefront gradients of 15×15 subapertures of all three Shack-Hartmann patterns.

In parallel, at the dichroic, wavelengths > 600nm are transmitted. The 600-1000nm range is used for natural guide star tip-tilt and truth sensing, where wavelengths > 1000nm are dedicated for scientific observation with LUCI. The tip-tilt sensing is performed by a quad-cell based on four Avalanche Photo-Diodes (APDs) allowing faint natural guide star magnitudes to be used and thus ensuring a large sky coverage. After computation, the tip-tilt slopes are then sent to the ARGOS slope computer. A small fraction of the light is also directed to the pyramid wavefront sensor to sense a few low order modes to take into account non-common

path aberrations, imperfect calibration, and slight differences introduced by the LGS spot elongations.

After collection of the different wavefront measurements, the ARGOS slope computer transmits the local wavefront gradients to the ASM computer, reconstructing the wavefront and projecting it on the ASM actuators, as we have described in the previous section 2.2.

ARGOS is a fairly distributed system as represented in Fig. 2.3 in a CAD model. In the following paragraphs, we review the key sub-system functionalities and designs, in particular the laser system, the LGS wavefront sensor, the natural guide star tip-tilt sensor, and the calibration unit.

My contribution to the project, in the framework of this thesis, concerns the design, testing and integration of the PNCCD wavefront sensor detector and the ARGOS slope computer, described in more details in CHAP.3 and in CHAP.4.

Laser system

The laser systems are mounted on two support platforms between the two C-ring extensions (between the two primary mirrors, see also Fig. 2.3). The two laser boxes are essentially mirror copies. Each unit contains three green pulsed lasers with possible room for a fourth laser (in case of diffraction limited system upgrade). The beams are pre-expanded, adjusted to the required polarization for proper optical gating in the WFS, and stabilized for internal flexure and vibration. The three laser beams are brought to a single pupil mirror controlling the global pointing direction on sky, and directing the beams to the launch optics system. This latter one consists of a refractive beam expander integrated in the LBT windbrace structure (the vertical structure between the two primary mirrors, see Fig. 2.3) and two flat mirrors. The system expands the pupil from 8mm to 40cm, launching the three beams on-axis to focus them at 12km distance. The first flat mirror also implements a vibration compensation system to correct for telescope vibrations. The lasers themselves consist of frequency doubled Nd:YAG lasers emitting at 532nm. They emit 18W at a nominal 10kHz rate, with pulse width of ∼40ns.

Most of the development was carried by MPE. At the time of writing, the laser systems have been successfully installed, and partly commissioned as a sub-unit at the LBT.

Wavefront sensor system

Coming from a 12km distance, the backscattered light from the laser beacons of ARGOS will be picked up in front of the LUCI instrument rotator structure by a dichroic reflector and directed to the wavefront sensor optical setup. The revised dichroic setup features an actual dichroic and a mirror directing the green laser light to the WFS, see Fig. 2.4.

Fig. 2.5 gives an overview of the arrangement of the WFS with its three beam arms. Past the entrance window and the collimating lenses, periscope mirrors bring the light of the three laser beacons closer to the symmetry axis. The second mirrors of these periscopes, located at the pupil planes, are mounted on fast piezo tip-tilt stages. These fast tip-tilt mirrors stabilize the Shack-Hartmann patterns, removing the overall LGS tip-tilt as originating from residual laser beam jitter, and up and down propagation in the atmosphere. Following the periscope mirrors, optical shutters, based on Pockels cells, gate out the desired slice of the atmosphere from the backscattered light, *i.e.* a 300m height around 12km altitude. These Pockels cells
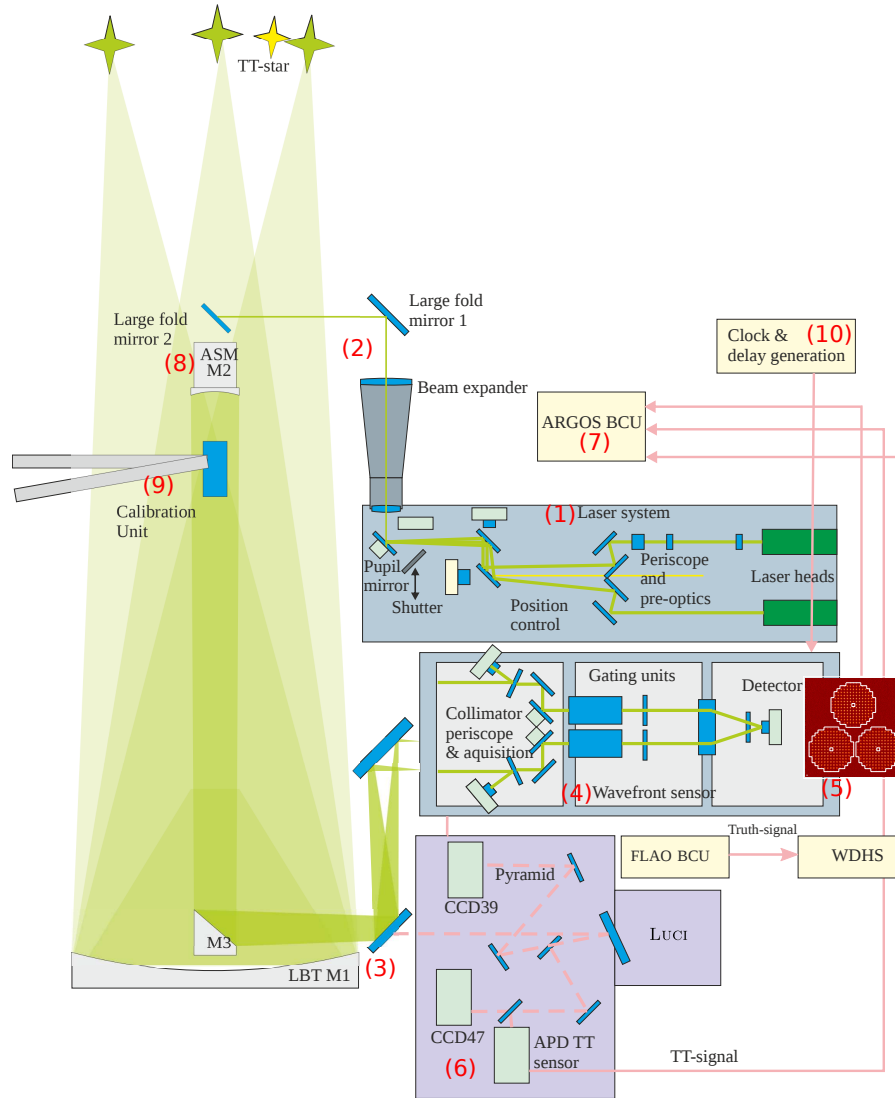
Figure 2.2: Functional sketch of the ARGOS system for one LBT side. The laser system (1) generates the three beacons, controls their position and the polarization, and pre-expands them. The launch beam expander (2) brings the beam size to ∼40cm, launchs them on-axis and focusses them at 12km. The backscattered light is directed to the wavefront sensor unit by a dichroic (3) in front of Luci. The WFS (4) brings the beams closer together, controls the pupil centers and the field positions, gates the beams and re-images the pupils on a lenslet array, generating three Shack-Hartmann patterns on the pnCCD (5). In parallel, natural guide star tip-tilt sensing (*i.e.* using APD TT sensor) and truth sensing (*i.e.* using a pyramid WFS) is performed inside the natural guide star wavefront sensor unit (6), itself inside the rotator structure of Luci. The sampled turbulence images (LGS, NGS tip-tilt, and truth sensing) are treated by the ARGOS slope computer (ARGOS BCU, (7)) which computation is used by the adaptive secondary mirror (ASM, (8)) to compensate for the ground-layer turbulence. The system is calibrated thanks to the unit (9) attached to a deployable arm that can be placed just below the ASM (as shown in the sketch). A common clock (10) synchronizes the lasers firing, the gating, and the detector readout. Credit: S. Rabien.
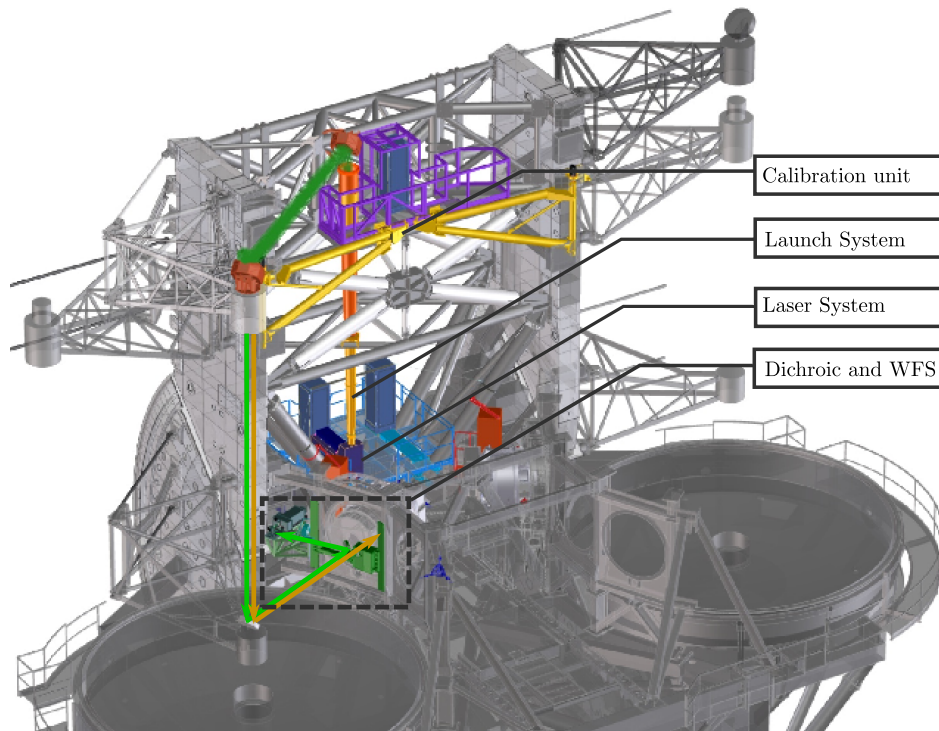
Figure 2.3: CAD model of LBT with the ARGOS hardware (complete for one side). As it can be seen the system is very distributed and the final integration can only be done at LBT. This figure can be read in parallel to Fig. 2.2. The main sub-systems are annotated. The dashed grey box is also represented in Fig. 2.4. The light rays are indicated by arrows from the ASM down to the WFS (green) and to LUCI (orange). Credit: modified from image of M. Deysenroth and H. Gemperlein.
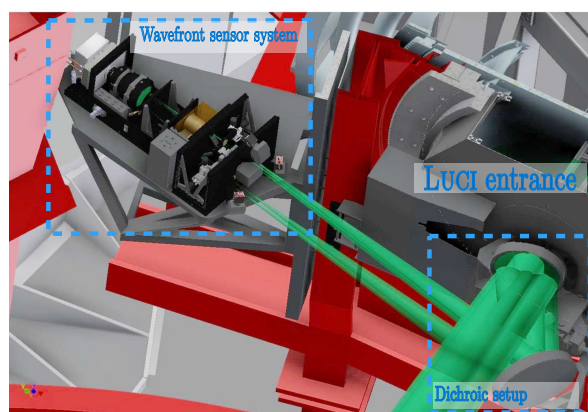
Figure 2.4: CAD layout of the dichroic setup in front of the LUCI rotator structure directing the laser beams to the WFS. The laser beams are represented in green. Courtesy: figure annotated from L. Busoni and M. Bonaglia.

Table 2.3: Summary of ARGOS Pockels cell characteristics and application.

| Parameter	Value
Risetime	<10ns
Output pulse jitter	<2ns
Suppression over ±4°	1:1000
Pockels cell suppression over the required ±0.8°FoV	1:5000
Transmission over ±0.8°	>97%
No ringing present	
Typical on-time	2 μs
Typical repetition rate	10kHz

are therefore synchronized with the laser pulses at 10kHz. Finally, re-focussing lenses, field lenses and a common collimator will re-image the pupil onto a lenslet array in front of the PNCCD, thus creating 3 Shack-Hartmann patterns on the PNCCD detector. Additionally, three cameras (called patrol cameras) will be used to find the laser spot in a field of view of one arcminute in order to help the acquisition process.

The optical gating, *i.e.* Pockels cell, is essential here to avoid dilution of the 12km guide stars by Rayleigh scattering throughout the laser propagation. Hence, the gating units are synchronized with each laser to the desired time duration, *i.e.* 2μs for a 300m slice of the atmosphere. This is a compromise between spot elongation and the number of collected photons, both influencing the accuracy of the wavefront gradient measurements. The Pockels cell basic principle is as follows. An electro-optic active crystal is placed between two polarizers. Applying a large electric field to the crystal modifies linearly its birefringence properties. Hence upon appropriate voltage the crystal can introduce, e.g., a $\lambda/2$ phase shift, and the transmission of a beam through a Pockels cell can be suppressed upon command. To obtain an optimized suppression and transmission over a large FoV[7], the designed unit consists on the following elements : a first polarizer, an electro-optical modulator (BBO crystal), a polarization rotator, a second BBO crystal, and a last polarizer[8]. The aforementioned scheme allows a high transmission/suppression rate and relatively large field of view with few artifacts and high uniformity. The key characteristics are summarized in Tab. 2.3.

The end part being the detector, the PNCCD simultaneously senses the three Shack-Hartmann patterns per LBT eye. With a laser pulse rate of 10kHz and the Pockels cells opening after the appropriate delay, the detector integrates ten backscattered pulses before reading out at a frame rate of 1kHz. Each Shack-Hartmann pattern provides ~175 subapertures leading to 350 slopes and allows ARGOS to correct for approximately 150 modes. In addition to this large number of subapertures, each of them is 8-by-8 pixels wide allowing large offsets of the spot positions. Finally, the large pixel size, *i.e.* 48 μm, of the pnCCD together with the WFS optical setup provide a pixel scale of 0.56″/px which leads to a good signal-to-noise ratio while correctly sampling the spots, considering the non-diffraction limited laser spot. Because the PNCCD is split in two half frames at the readout, and that those

---

[7]as the incoming beam from < 12km will be convergent.

[8]BBO, Beta Barium Borate, crystals are negative uniaxial crystal, where the polarization rotator used is a positive uniaxial crystal, hence allowing to compensate for the phase delays when the appropriate voltages are applied to the BBO crystals.
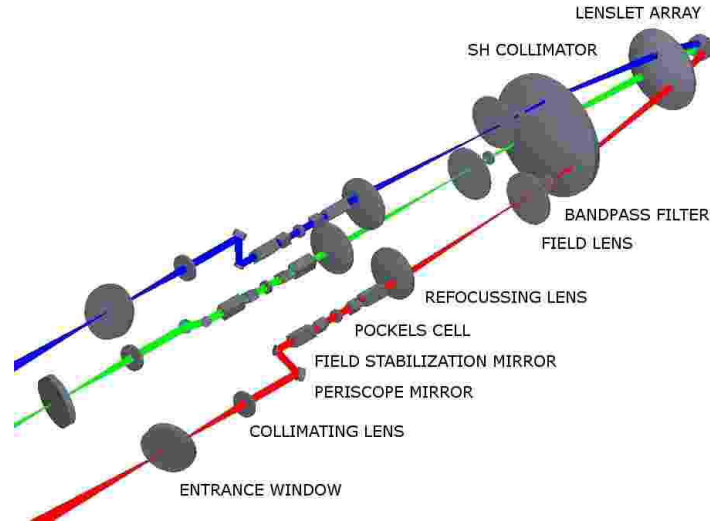
Figure 2.5: Arrangement of the three laser guide stars inside the WFS. Each optical element is annotated and the light paths of the three beams is shown in different colors. The light enters from the right and falls onto the detector on the extreme right. Credit: M. Bonaglia.

are treated separately at the computational level, the triangular symmetry of the on-sky beams had to be broken by the optical design. Hence, one of the Shack-Hartmann pattern is de-centered by 4 pixels on the PNCCD plane.

The PNCCD wavefront detector and the ARGOS slope computer have been successfully integrated to the rest of the WFS system at INAF in Italy. The WFS is currently undergoing system test, calibration, and further software development before being shipped to LBT.

Natural guide star tip-tilt wavefront sensing

The necessary NGS tip-tilt wavefront sensor is a key element of ARGOS as the limiting magnitude of the NGS tip-tilt star directly drives the sky coverage and thus the science opportunities offered by ARGOS.

In this perspective, a quad-cell APD-based tip-tilt tracker has been chosen. In this configuration, a lenslet array is directly glued to optical fibers after a proper positioning adjustment for an optimum coupling. Those four fibers bring the light to four commercial APD units. This concept allows the lowest limiting magnitude down to $R \sim 18.5$mag.

As it has to be within the isoplanatic patch, the unit is placed on the natural guide star wavefront sensor unit (*i.e.* FLAO unit). In order to avoid modification of the AO beam train, the tip-tilt quad-cell is placed in the focal plane of the technical arm. The FLAO unit receives light in the range $600 - 870$nm, where it is split for ARGOS as follows: 10% goes to the natural guide star wavefront sensor (*i.e.* pyramid WFS) to allow for slow "truth sensing" of low order modes to account for slowly changing non-common path aberrations and focus error, 90% goes to the technical arms. Of these, 95% is directed to the quad-cell for tip-tilt sensing and 5% to the technical camera to be able to quickly center the star on the quad-cell. The FoV of the lenslet array is 2.3″ but an adjustable aperture stop is also placed in front of the quad-cell to filtered out any scattered laser light possibly contaminating the tip-tilt signal.
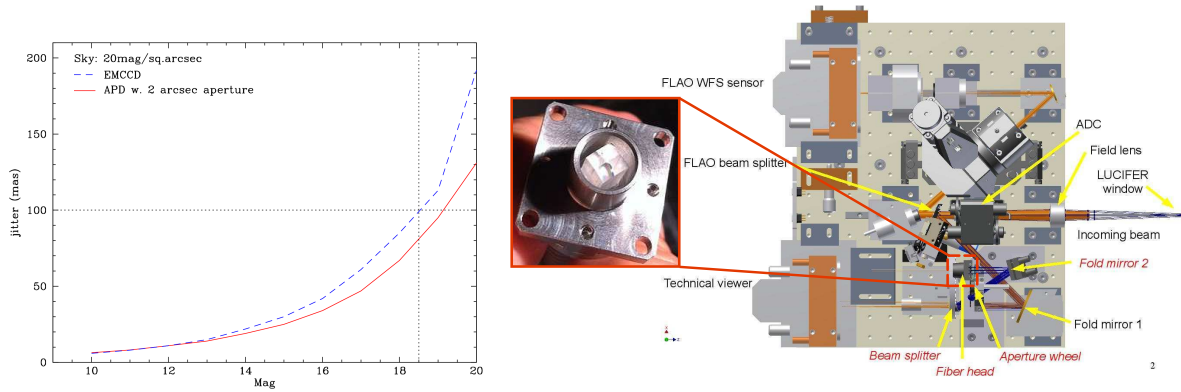
Figure 2.6: (Left) Simulated performances of two NGS sensing concepts : 1) using a quad-cell APD-based sensor, 2) replacing the "FLAO WFS" sensor by a EMCCD. The APD offers the best performances with a limiting magnitude of $R \sim 18.5$ for a residual jitter of 100mas. See also ARGOS consortium (2010). (Right) The natural guide star wavefront sensor unit (FLAO unit) including the pyramid wavefront sensor. The main elements of the crowded board are annotated. The new elements mounted for ARGOS are indicated in red. The zoom image shows the quad-cell glued on the fibers that direct the light to the APD for the tip-tilt sensing. Modified images from FDR (ARGOS consortium, 2010) and J. Storm.

The APD counts the photons in the four quadrants, and a dedicated FPGA-based computer – the so-called MPIfR Bonn-unit – performs the data calibration, centroiding, and de-rotation and then sends the vector to the ARGOS slope computer.

The tip-tilt acquisition is performed asynchronously to the LGS wavefront sensing but at the same rate of 1kHz. This allows to properly sample in time the more slowly varying but higher power contribution of the tip-tilt modes.

Calibration Unit

The good behavior of a closed-loop AO system relies on its calibration, *i.e.* on the correct acquisition of the interaction matrix (see also section 2.2) between the ASM and the WFS, allowing the transformation from local wavefront gradients to modal coefficients and ASM commands. While on-sky calibration is in principle an option, it requires night time observation and is thus restricted. AO systems therefore usually use internal calibration sources to perform the interaction matrix acquisition, which thus can be done in day-time. Having an ASM, the situation is more complex at LBT. Hence, the calibration is done using an optical deployable unit that generates artificial light sources at the prime focus, see Fig. 2.2 and Fig. 2.3. In addition to this challenging solution, the multi-LGS beacons are substantially off-axis with respect to the telescope FoV, hence the LGS beacons suffer important aberrations that need to be replicated to allow a good calibration. Hence the deployable arm provides off axis fibres mimicking the 12km distance LGS on sky with the help of an hologram that reproduces the off-axis aberrations. This swing-arm is foreseen to be easily deployable to allow robust and efficient calibration operation.

Currently the deployable arms are already mounted at the LBT. The finalization of the optics is currently on-going.
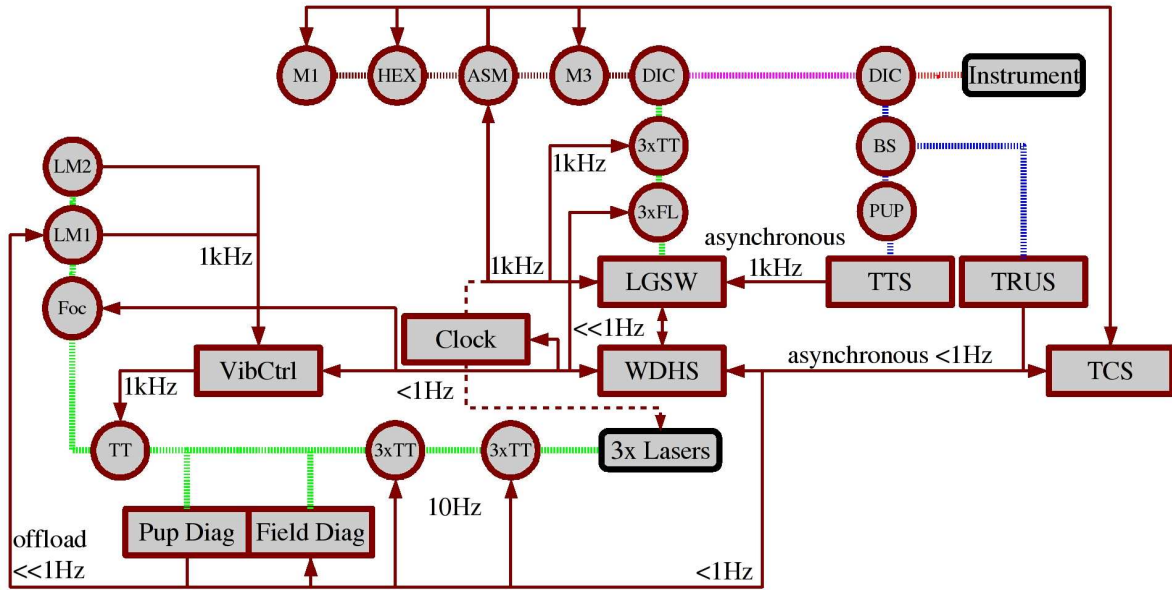
Figure 2.7: ARGOS control architecture. Circles are optical components, rectangles are control units (red) or hardware (black). The optical path is represented in fine dense dashed line with different colors indicating the wavelengths. Control interactions are represented by solid and dash red lines and arrows. The elements are : M1 primary, HEX hexapod, ASM adaptive secondary, M3 tertirary, Dic dichroic, TT tip tilt mirror, BS beam splitter, LM launch mirror, PUP pickup mirror, TCS telescope control software, TTS tip-tilt Software, TRUS truth sensing, LGSW LGS WFS, and WDHS wavefront data handling system. The LGSW system includes operating the PNCCD camera, and the ARGOS slope computer. Credit: FDR ARGOS consortium (2010).

Final system considerations

ARGOS is a highly distributed system over the telescope. Eventually it is the control software that ties the sub-systems together. In that respect, each ARGOS device is controlled by a service part of a general property tree. The control software has the critical task of operating this large number of devices, including the already existing natural guide star adaptive optics system and the telescope control software. It also implements a large number of control loops for vibration compensations, laser and WFS synchronization, etc.. The general control architecture is represented in Fig. 2.7 and illustrates the overall ARGOS complexity. In the framework of this thesis we implement the PNCCD control software part of the LGSW, a standalone software that monitors the PNCCD and allows remote and safe operations through the standarized communication agreement. This is further described in CHAP.3 section 3.2.4.

A correct synchronization is also a key element to ensure a good wavefront measurement and subsequent correction. We present in Fig. 2.8 the general timing from firing the laser down to the ASM control. We include numbers that are also inferred in this thesis, *i.e.* the delays introduced by the PNCCD readout and the ARGOS slope computation, see section 3.2.2 and section 4.5.

As already mentioned, ARGOS is highly distributed over the telescope and uses hardware
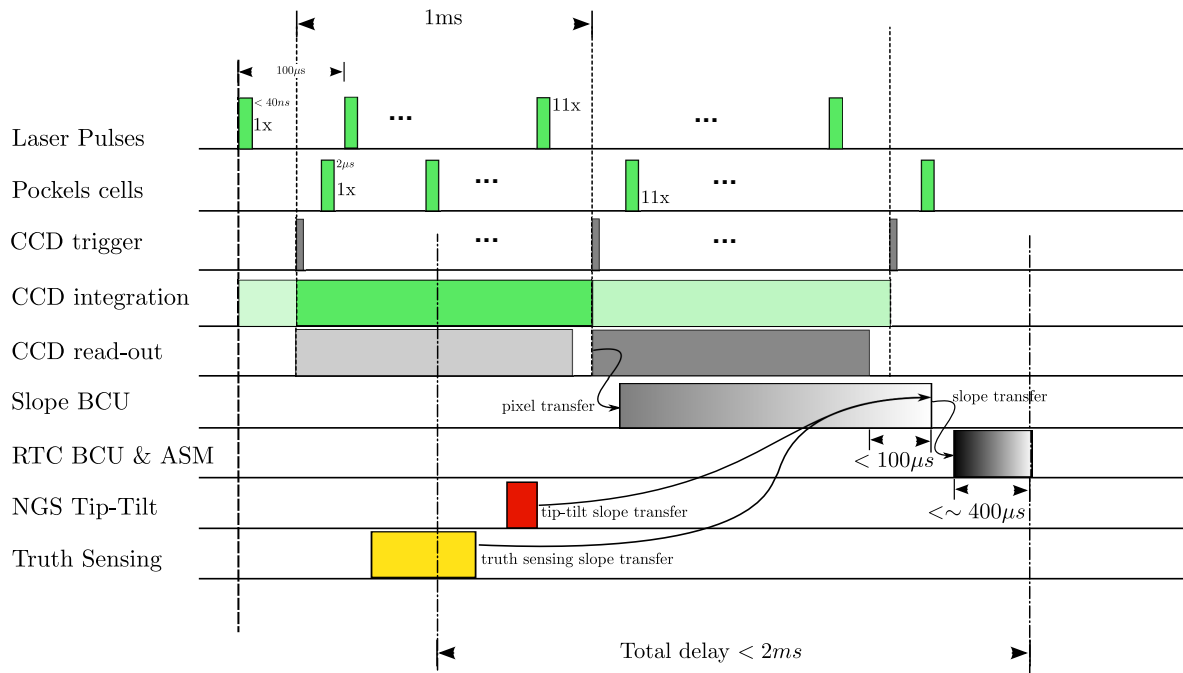
Figure 2.8: ARGOS AO closed-loop timing diagram. It illustrates the nominal timing from laser firing down to deformable mirror control as foreseen by design and estimated in CHAP.3 and in CHAP.4. The total delay between the wavefront measurement and its correction is estimated to $< 2ms$. The NGS tip-tilt an the "truth sensing" are asynchronous.

already in place such as the natural guide star wavefront sensing unit platform in the instrument rotator and the ASM. This prevents the integration of all units in a laboratory (including the ASM), and hence full system test can only be performed at the telescope. It also increases the risks and challenges at the telescope. In particular, the calibration unit and the NGS tip-tilt – both essential for the overall performances – depend strongly on their proper integration to the telescope and with the rest of ARGOS.

In addition to that, the structure of the consortium also implies that hardware units are developped at different places. Hence the approach has been step-wise, performing as far as possible acceptance tests for sub-systems before their shipment to LBT. The same applies to the software.

The development of such a system sees lots of challenges along the way which need to be aggresively tackled for the project to stay on time. We illustrate this by two examples which have been tackled in the framework of this thesis. First, the PNCCD early characterization showed problematic correlated noise (later referred to as "common-mode" noise) which has lead to a dedicated test campaign, development of new PNCCD power supplies, and impact studies on the AO performances. Second, the procurement of the PNCCD analog-to-digital converters readout electronics has been exceedingly long and at first arrival was shown to be out of specifications. Hence to speed up the electronics development and avoid any bottleneck a parallel development has been ordered from another company. Other examples from which one can learn important lessons are given in Gässler et al. (2012). They require a constant testing of the hardware and re-evaluation of the system performances.

ARGOS is now entering its assembly phase at the telescope. While some parts are already installed and functional as sub-system units (e.g. the laser system), others are being integrated and tested in the laboratory in Europe (e.g. the wavefront sensor) and are planned for installation in early 2014. System commissionning should start in 2014.

In the next two chapters, we describe the development, testing and validation of the PNCCD wavefront sensor detector and of the ARGOS slope computer performed in the framework of this thesis.

WAVEFRONT SENSOR PNCCD CAMERA

At the heart of the wavefront sensing system, the detector of ARGOS has to sense the sampled wavefront errors of the three laser guide stars. This same detection allows the wavefront computation and its correction. The detector being a critical part of an AO system, it drives in part the design and the limitation of the system.

In this chapter, we present the ARGOS wavefront sensor PNCCD camera, from the PNCCD chip to the fully integrated ARGOS AO camera. We start by describing the ARGOS requirements that the camera should fullfill. In section 3.2, we then present the various aspects of the unit : from the chip characteristics developed by HLL/PNSENSOR, to the final electronics, the final camera housing, and the control software. In section 3.3, we describe the performances of the detector, most of which have been tested in the framework of this thesis. In section 3.4, we focus on the main challenge we have faced with the PNCCD chip : a correlated noise, or so-called "common-mode" noise. In particular, we present our staged analysis : first, the frequency analysis of the frames and their evolution with the different camera versions; second, the impact on centroiding creating first a Shack-Hartmann pattern on the detector by implementing a dedicated test setup, and then combining simulations and measurements; finally the closed-loop AO simulations performed to understand the global impact of this common-mode. From these various analysis tools, we summarize the learnings, present how we tackle the problem, and show how this noise will not influence the ARGOS operations. We end by comparing the PNCCD with other possible AO cameras. Finally, we conclude on the successfull integration to the wavefront sensor system.

From the early camera version to the final system, my role in this development is 1) the constant testing and validation of the chip characteristics, the camera housing, and the electronics, 2) the integration of the electronics with the camera, 3) the optimization of the PNCCD (e.g., clocks and voltages) together with PNSENSOR, and 4) the development of the control software. I have also lead the effort in solving two major problems the units had : the "common-mode" noise hampering the aimed AO operations (section 3.4), and the procurement, debugging and integration of functional, noise-free PNCCD ADC electronics (section 3.2.2).
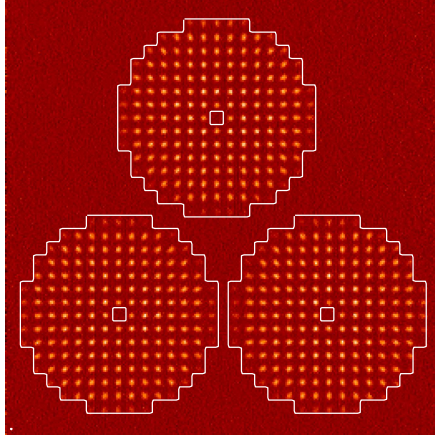
Figure 3.1: The three Shack-Hartmann patterns as it will be sensed by the pnCCD at a frame rate of 1kHz. The white contours define the telescope pupil as sampled by each Shack-Hartmann. The WFS samples the telescope pupil by 15 subapertures across the diameter, hence a projected size of $d_s = 0.56$m. Each subaperture is 8×8 pixels wide to allow large spot wandering. The telescope pupil is sampled by the three LGS. The top SH pattern is shifted by 4 pixels to the left to not split a subaperture in the two halves of the CCD, see section 3.2 and Fig. 3.2.

3.1   Argos wavefront detector requirements

Before discussing the Argos specific requirements, a few general ones can be emphasized. We can summarize them in a few points (see also Downing et al., 2008, for further discussion) :

- The detector number of pixels and the frame rate : both should be large to allow the required spatial and temporal wavefront sampling. The combination of both is of course one of the main challenges. Larger pixel size also eases the optical design.

- High signal-to-noise ratio for precise wavefront measurements : high quantum efficiency (QE), low noise, low dark current, and no defect (e.g. dead pixels). This is directly related to the accuracy of the measurements, see also equation 1.16 in the case of Shack-Hartmann wavefront sensing.

- Good spatial characteristics : the ability to detect the photons where they fall down on the detector, *i.e.* typically FWHM PSF response of ≤ 0.8 pixel is required, which gives a 3σ width of ~ 1pixel, or a $> 97\%$ probability the photon is detected at the right location.

- An easy-to-use and compact camera with a minimum of required maintenance.

While those general criteria are valid for Argos, we shall details the requiremets in our specific context. As we have discussed in Chap.2, Argos requires the simultaneous detection of the backscattered light from its three laser beacons, each one with a relatively large number of sub-apertures, as illustrated in Fig. 3.1.

Following our description of the wavefront sensor system in section 2.3, the main specific requirements and constraints for the Argos wavefront detector are as follows (see also e.g.

Argos consortium, 2010)

- Simultaneous detection of 3 Shack-Hartmann (SH) patterns arranged on a triangle, each having 15 sub-apertures on the pupil diameter, each one 8-by-8 pixels large. This ensures a compact optical design, and the large number of pixels allows both a proper sampling of the FWHM PSF and a large spot motion dynamic range (both of which also depend on the pixel scale driven by the optics). Based on those considerations and the PNCCD pixel size (48μm), the pixel scale is 0.56″/pixel for a total subaperture size of 4.48″.

- The accepted LGS spot FWHM is 0.5 to 2.5 arcseconds to support various weather conditions. See also Fig. 2.1.

- The WFS detector is fed with monochromatic light at 532nm, the Argos laser "light".

- The AO update rate is 1kHz (see the temporal error budget, e.g. Tab. 2.2), as should be the detector frame rate. It must be synchronized with the pulses of the lasers and the Pockels cells, *i.e.* the optical gating unit.

- The typical LGS flux in photons per milli-seconds per subaperture is ~ 1800, and in the worst case $\sim$700, see Tab. 2.1.

- The measurement accuracy requirements of the wavefront is 50nm (see also Tab. 2.2) which translates to approximately 50mas for one axis in the centroiding measurement. This is calculated as follows. The 50nm is a maximum wavefront phase error allowed at 532nm, *i.e.* in radian of phase: 0.59rad. To relate it to the PNCCD, we convert it to an angular tilt error along one axis :

$$\sigma_\alpha = 0.59 \frac{4}{k d_{subap}} \frac{1}{\sqrt{2}}, \tag{3.1}$$

  where $d_{subap}/2 = 0.28$m, the half sub-aperture size projected on the pupil, and $k = 2\pi/\lambda$. The factor $1/\sqrt{2}$ allows the conversion to single-axis error, and the factor two converts the wavefront standard deviation in a slope angle. Therefore $\sigma_\alpha \sim 53$mas, or $\sim$0.1pixel for a pixel scale of 0.56″/pixel.

Following those requirements, the PNCCD chip from HLL/PNSENSOR has been selected at PDR. Nevertheless, while being a state-of-the-art detector, the PNCCD was not a mature "wavefront sensor" camera. Hence, this work presents the development of the Argos AO camera.

3.2   The Argos pnCCD camera

We describe in this section the final Argos PNCCD camera and its related development : the Argos control electronics, data acquisition, camera housing, and finally the control software. Originally developed for X-ray detection, the PNCCD can be used for fast optical application (e.g. Strüder et al., 1987, 2001, Ihle et al., 2008). Indeed, the PNCCD features split frame transfer, frame store operation and column-parallel readout, and therefore it reaches frame rates up to 1kHz. Its frame rate together with its high quantum efficiency (QE), large imaging area and low readout noise make it a technological solution for different AO applications.
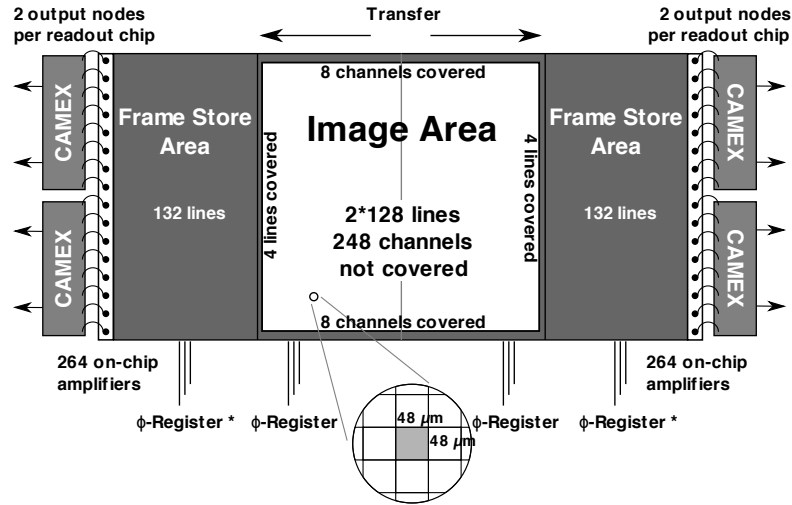
Figure 3.2: Schematic layout of the PNCCD. The image area (264×264px, the light sensitive area plus 8 covered lines and 16 covered channels) is split in two halves. The charges are transferred to their respective frame store area. The covered lines and channels, and the frame stores are covered by an aluminium layer. At the end of the frame store areas, each channel has an on-chip JFET amplifier which is then wire-bonded to the CAMEX chips performing the column-parallel amplification and producing 8 analog outputs. Credit: Ihle et al. (2008).

Fig. 3.2 shows the schematic PNCCD design for fast application composed of an image area, two frame store areas and four multi-channel readout ASIC, named CAMEX, that amplify the signal and multiplex it on eight analog outputs.

The specificities of the chip are its combined high QE, low readout noise, excellent cosmetic, and high frame rate for a large image area. The key specifications of the PNCCD, as used for ARGOS, are summarized in Tab. 3.1. More details and camera specific characteristics are given in section 3.3.7 at the end of our performance analysis.

In the following section, we present the PNCCD principle, the control and readout electronics, the compact camera housing, and the developed control software.

3.2.1   The pnCCD principle

The design of the PNCCD chip has been carried by HLL/PNSENSOR for X-ray applications first (e.g. Strüder et al., 2001) and then adapted for fast optical applications (e.g. Ihle et al., 2008). It sets the performances and limitations of the camera. It is therefore appropriate to present here its concept, which we try to summarize hereafter.

Fully depleted, backside illuminated pnCCD

The main difference from the PNCCD to a standard buried channel CCD (BCCD) is its full depletion over a large thickness. As for the BCCD however the electron potential minimum is close to one side of the wafer and the readout is the typical three-phase transfer registers. The thick full depletion gives the PNCCD a few advantages, namely a good QE and, in particular,

Table 3.1: Summary of the key PNCCD specifications.

Parameter	Value
CCD type	column-parallel, split frame readout
Pixel in image area	248 × 256 pixels
Light shielded pixels for dark correction (incl. common-mode correction)	2×8 channels + 2×4 lines
Pixel size	48 × 48 μm
Frame rate	up to 1000Hz
Frame transfer duration	$\leq 40\ \mu$s
Quantum Efficiency at 532nm	~ 98 %
Readout noise (RON)	3.5-4e$^-$ (depending on the gain setting)
Dark current	~ 0.2e$^-$/px/s at 100Hz and -50°C.

an improved red response and no fringing (essentially no reflection back into the substrate thanks to the thickness).

The PNCCD is based on the principle of sideward depletion[1] (Gatti & Rehak, 1984) of a n-type silicon bulk. It follows a pnp-structure (see Fig. 3.3) : the backside, used as the entrance window, consists of a very thin p$^+$ implantation; a fully depleted thick n substrate[2]; and p$^+$ implantations on the frontside to allow charge transfer, *i.e.* by use of the transfer registers.

The basic principle comes as follow (see also, e.g., Strüder et al., 2001) : the interaction of photons with the silicon atoms will generate electron-hole pairs. The latter are separated by the strong electric field before they recombine. The holes move to the negatively biased back side, where they are "absorbed". The electrons drift to the potential wells inside the low resistivity layer, and are stored under the transfer registers that define the pixels allowing the charge transfer upon command.

The transfer is performed by a 3-phase set of registers, applying clocked periodic voltages, towards the readout anode. Each CCD channel is terminated by an on-chip JFET amplifier which in its turn is connected to the input stage of a multi-channel analog signal processor, *i.e.* the CAMEX, see Fig. 3.3 and Fig. 3.4.

pnCCD on-chip and CAMEX readout electronics

Each readout anode is equipped with a front-end amplifier directly on the detector, see Fig. 3.4 and Fig. 3.3. The main elements are (see also Pinotti et al., 1993, for more details) : 1) a storage capacitor C_d where the electrons are collected, 2) the first FET (FF), used as a source

---

[1]full depletion is reached by applying reverse biased voltages between the two pn-junctions of both front and back sides of the wafer and a small contact somewhere at the edge of the wafer. This concept lead to a small capacitance of the contact anode, minimizing the effect of amplifier series noise. This also allows the superposition of a second electric field to transport the charges (Gatti & Rehak, 1984).

[2]effectively two "regions" should be distinguished: the "fully depleted volume n$^-$ (lightly doped) -Si (2.5kOhm)" and the epitaxial layer n (highly doped) with low resistance. The latter hosts the potential minimum and serves as the channel guide (necessary for the good charge transfer properties of the CCD). This layer is also depleted.
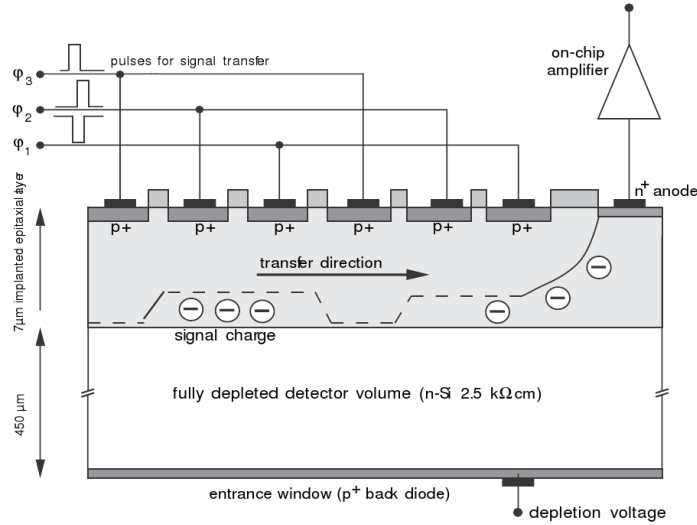
Figure 3.3: Schematic cross-section of the PNCCD. The full volume is depleted and the charges are collected in the potential minimum defined by the three ϕ voltages, which after collection allow, by appropriate clocking, the charge transfer to a readout anode and a first on-chip amplifier. Credit: Hartmann et al. (2005).

follower, matching the high input impedance (low C_d) to the lower one at the subsequent stages, 3) the reset FET (RF) that, when the readout is terminated, switches in conduction state resetting the signal charge on the anode, 4) the current generator F2-Rs that imposes the drain current of the FF and is adjusted for optimized noise properties, 5) the readout electronics, schematized by "A", is the CAMEX unit.

The CAMEX (CMOS Amplifier and MultiplEX) performs the amplification, signal filtering and multiplexing of all its 132 channels in parallel. Its building blocks are represented in Fig. 3.5.

It uses the multi-correlated double sampling (MCDS) concept for the signal amplification and filtering. Correlated double sampling (CDS) is a standard technique in CCD operation allowing the removal of reset noise. This technique consists essentially in taking the difference between the signal voltage level and the baseline, or reset, voltage level. The reset voltage being "frozen" during the two samples[3], the offset in each sample is essentially the same or "correlated". The CAMEX can perform up to 8 times this sampling operation to minimize the noise contribution, *i.e.* a multi-CDS. The sequence of the MCDS is also optimized for the ARGOS high speed operation and is as follows (ARGOS consortium, 2010, Hartmann et al., 2006). Since the first amplifier is not resetted after each signal evaluation, the signal samples of the previous cycle are regarded as the baseline samples for the current cycle instead of the reset voltage level, see Fig. 3.6. Following this scheme, the first amplifier signal input is reset only after a full frame. Hence the input at the first amplifier increases at each pixels and thus limit the maximum number of photons per column and frame above which the amplifier saturates. In conclusion, in the case of ARGOS, the saturation and "dynamic range" will not depend on the full-well capacity but on the first amplifier dynamic range.

---

[3]the reset noise time constant being much longer than the time between the two samples.
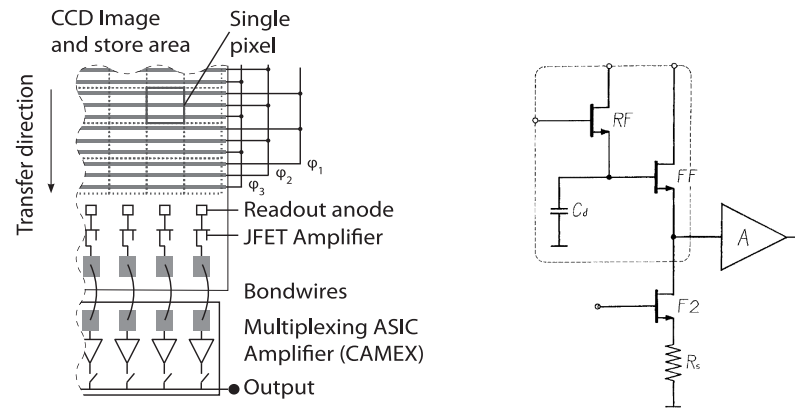
Figure 3.4: (Left) Schematic top view of the PNCCD. The pixels are defined in dashed lines. There are defined by the three ϕ voltage connections in the readout direction and by channel stops perpendicular to it (not represented). The charges are collected at a readout anode, and pre-amplified. The signal is then processed by the so-called CAMEX units, capacitively decoupled from the chip. The output of one CAMEX unit is multiplexed in two nodes, for a total of 8 analog outputs. The signal is later digitized by appropriate ADCs. Credit: Ordavo et al. (2011). (Right) On-chip electronics schematics at the readout anode. The components in the dashed box are integrated on the CCD chip and are wire-bonded to the channel signal processor, *i.e.* the CAMEX. Credit: Pinotti et al. (1993).

After the MCDS, the output is finally stored on a sample and hold (S&H) capacitance and then multiplexed to one of the two analog output nodes per CAMEX chip. The analog signal is then sent to analog-to-digital converters located in the electronics crate. The CAMEX chip performs the output multiplexing at the same time as the amplification and filtering of the following line. In addition to this parallelization, the shaping and amplification are also reduced. Those modifications bring the CAMEX pixel signal processing time from $\sim 15\mu s$ down to $7.2\mu s$, allowing the fast operation.

3.2.2 Control electronics and data acquisition

With the PNCCD chip and its four CAMEX units come a set of control electronics to power the chip, to clock the CCD and program the CAMEX, to control the CCD temperature, and to acquire the analog signals. The integration and testing of the control electronics have been performed in the framework of this thesis.

In Fig. 3.7, we give an overview of the interfaces of the ARGOS PNCCD and its control electronics. The key elements are :

1. A computer to control and monitor the various pieces of hardware. It hosts a newly developed control software allowing remote operation and standalone monitoring of the camera, and is described in section 3.2.4.

2. A pattern generator, or "sequencer", that generates all the digital signals for the ADCs, the PNCCD electronics outer board and for programmation of the CAMEX configuration registers.
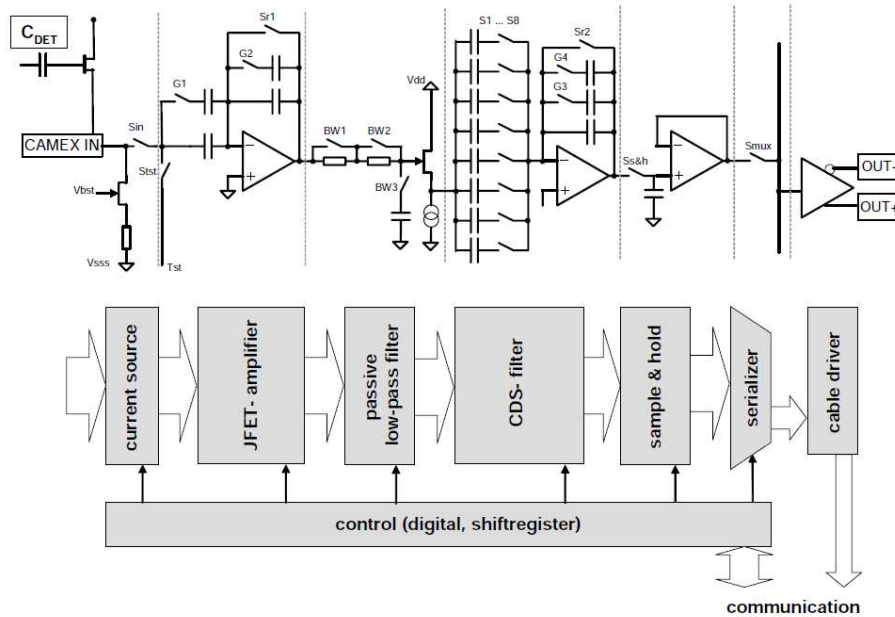
Figure 3.5: Block diagram overview of the CAMEX showing the operation flow. The on-chip signal enters in the left and the amplified signal is multiplexed on the extreme right. The current source on the left is the same as represented in Fig. 3.4. The signal is amplified, filtered by a correlated double sampling CDS filter, then stored on a sample & hold capacitance, to be finally multiplexed. While this happens, the subsequent row of the CCD is transferred to the CAMEX input. The sequence of operation are given by the digital control, *i.e.* on-chip configuration registers that are configured at the startup of the PNCCD. The operation flow and timing is configurable, and depends on the application. See text for more details. Credit: Meidinger et al. (2012).
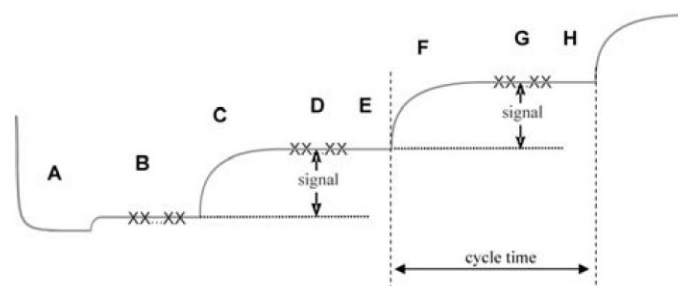
Figure 3.6: "High-speed" timing for the MCDS-filter. (A) is the initial reset of the amplifier and (B) the first baseline. Following this scheme, the amplifier is only reseted at the end of a frame and not after each "cycle time". See also text for more details. Credit: FDR ARGOS consortium (2010), Hartmann et al. (e.g. 2008).
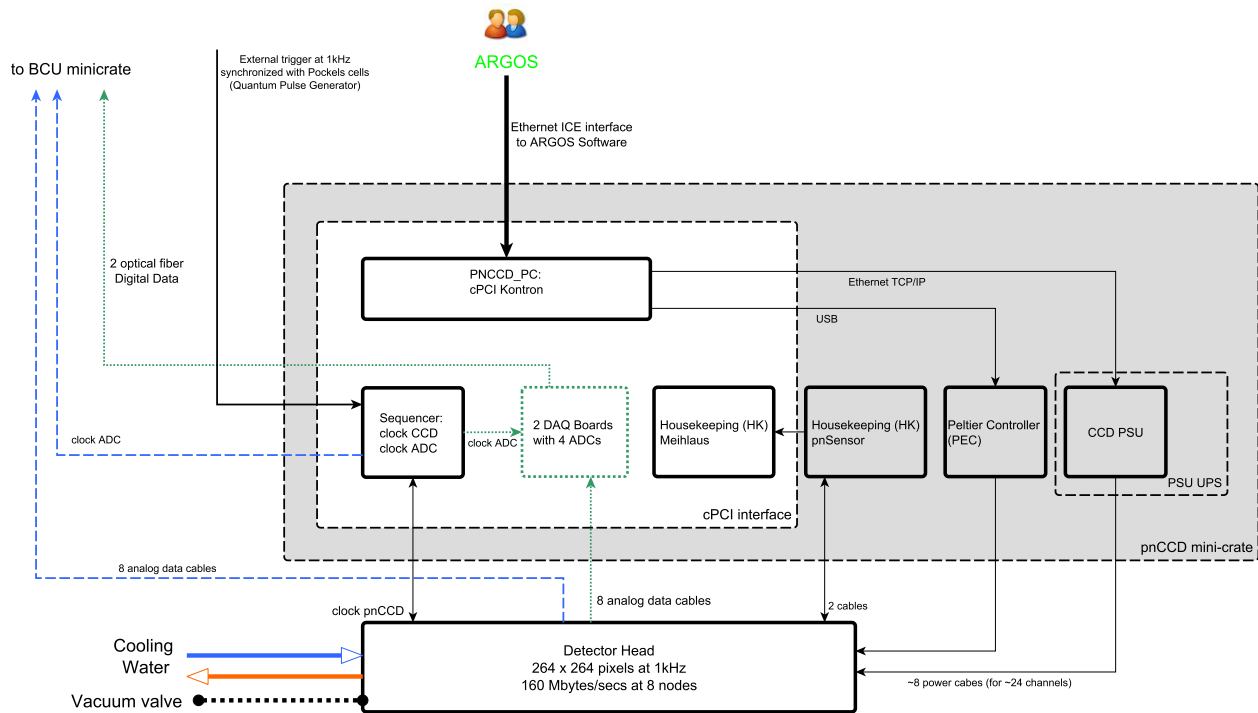
Figure 3.7: Interface scheme of the Argos pnCCD unit. It displays all interfaces between the pnCCD mini-crate and the pnCCD camera head. The two ADC possibilites are also represented : (dotted green) using the optical ADCs; (dashed blue) the BCU built-in ADCs. See text for more details.

3. Analog-to-digital converters transforming the analog signal, collected from the eight analog outputs of the CAMEX, in 14 or 16 bits.

4. Housekeeping hardware comprising a Peltier controller to cool down the camera, and two boards for housekeeping data acquisition.

5. Dedicated power supplies providing the 23 different voltages for the camera.

We describe in the following paragraphs the main features of this control electronics and the associated development.

The final pnCCD mini-crate: smaller and smarter

The initial pnCCD control system – as in mid 2009 – was filling more than a full rack with some bulky power supplies, a large computer, a cryogenic cooler, and a vacuum pump. We represent it in Fig. 3.8 for illustration. This was far too large for our application, and subsequent work followed to optimize the system, in collaboration with pnSensor.

The first motivation was obviously to bring the system to a reasonable size, and to a fully robust and remotely controllable system for Argos. An additional motivation to the development of a new power supply unit was to tackle the pnCCD correlated noise, *i.e.* the common-mode. We discuss this issue in further details in section 3.4.
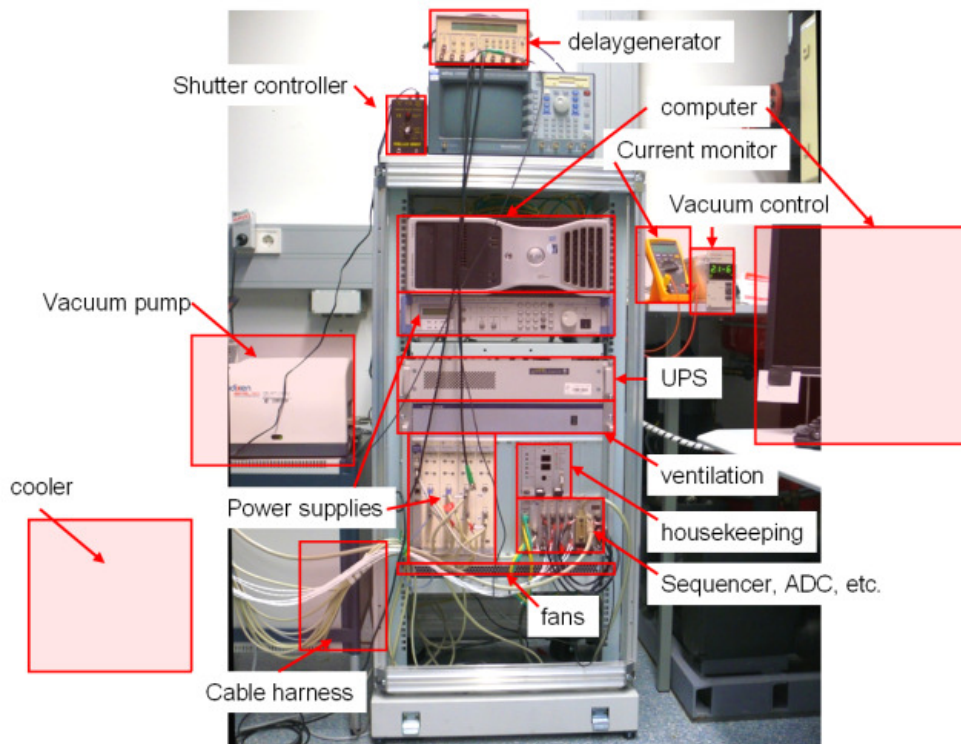
Figure 3.8: Initial PNCCD rack illustrating the bulky and very distributed devices needed to operated the PNCCD, four to five times larger than the final system represented in Fig. 3.9.

The final electronics mini-crate fits in a 19″ rack and uses 6 height units (the total size is then 48.26×26.67cm); this is four or five times more compact than the original design. The rack composition is represented in Fig. 3.9. The key components, *i.e.* the ADCs, the sequencer, and the camera power supplies are described in more details hereafter. They drive, for a large part, the performance of the system and have been subject to dedicated optimization.

Analog to Digital Converters

As mentioned earlier, the PNCCD CAMEX outputs are multiplexed through 8 analog nodes. Therefore the PNCCD requires 8 ADC units working simultaneously to digitize the signal. The digitisation has to be done following the analog "data rate" of 264×264 pixels in 1ms and with a digitisation of 14 to 16 bits per pixels (discussed next paragraph).[4] This gives a typical total data rate output of the ADCs of 130-140MBytes/seconds, including the data headers of 4 × 32-bits words. Finally the CAMEX voltage output ranges can vary approximately between −0.2 to 1.2 volts, which should then be translated in the full ADC voltage range to benefit at best of the digitisation.

---

[4]The analog "data rate" is given by : the pixel duration of 80ns, with $\sim 2\mu s$ interline pause and $< 40\mu s$ interframe delay due to charge transfer from the image to the framestore area. The total amounts to only marginally smaller than 1ms. Hence, the maximum frame rate of 1kHz.
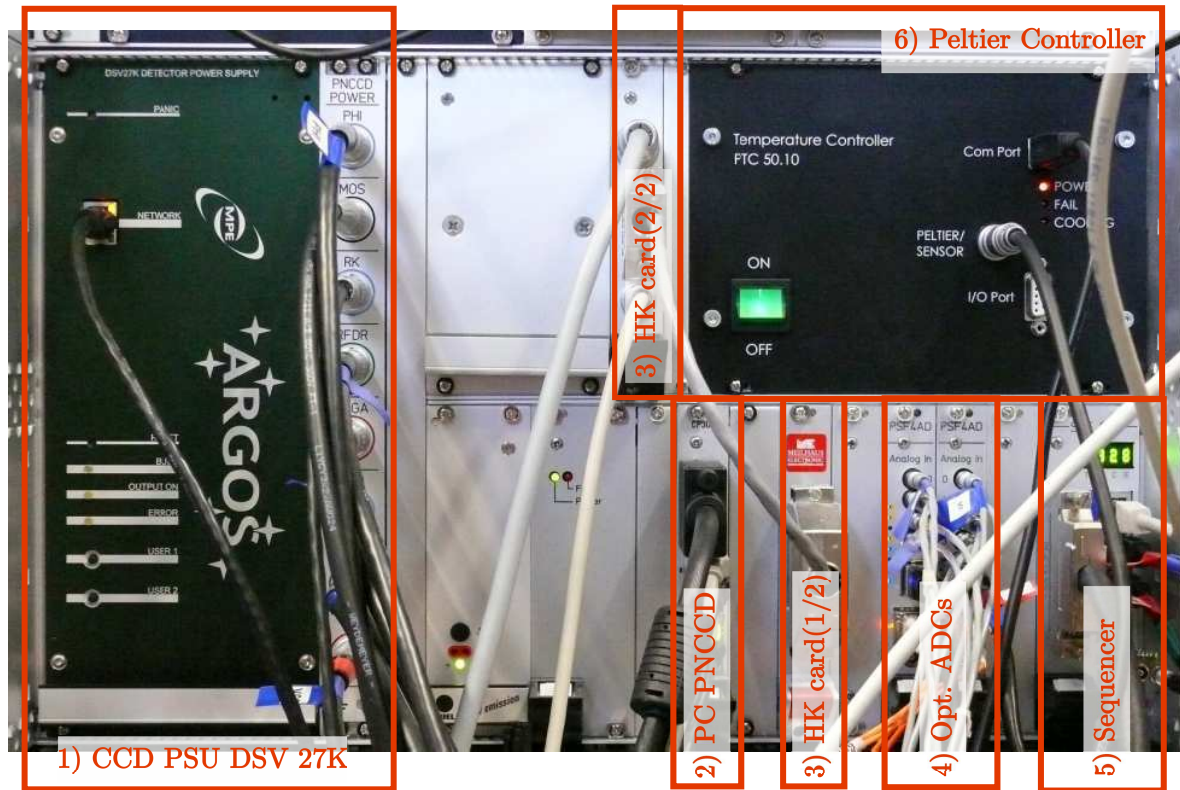
Figure 3.9: Final Argos pnCCD minicrate. This includes essentially 1) the CCD power supplies, 2) a cPCI computer hosting the software for remote operation, , 3) 2 housekeeping boards, 4) two ADCs with optical output, 5) a pattern generator (or sequencer), and 6) the Peltier controller for the camera cooling.

This project has seen three different sets of ADCs. We discuss them in chronological order.

In the initial electronics system, the ADCs were mounted on four data acquisition boards, each featuring two ADC units, developed previously at MPE. The digitized data were then transmitted through a PCI-bus and routed to an external computer through dedicated Ethernet interfaces, by four RJ45 cables. That configuration, although reliable, was not optimized for our application, *i.e.* fast and high data rate with a minimum of latency allowed and in a compact configuration. The constant data flow, 140 MBytes/seconds, could not easily be maintained over long period on the cPCI-bus. In addition, the acquisition, including a Ethernet receiving board integrated to a PC, was not adapted.

The solution proposed by pnSensor is two data acquisition boards, featuring each four ADCs, with one optical fiber interface each and designed by the Jülich Forschungszentrum. This solution is more compact, has no limitation in term of data rate, and allows for minimum latencies. The procurement of these has been however problematic : two years delay and flawed hardware at delivery. Indeed the boards were introducing extra noise and the communication to the receiver, the Argos BCU (Chap.4), was not working. The noise behavior has been solved one year later by firmware update and hardware redesign by FZ Jülich. The

communication to the receiver disagreement[5] was identified by us, and later solved.

To avoid a potential bottleneck, we have investigated another parallel possibility in collaboration with MICROGATE (already under contract with us for the development of the wavefront sensor computer, see next chapter CHAP.4). A fast track development was contracted and ADCs integrated to the BCU DSP board were finally delivered in winter 2012.

At present, the ARGOS PNCCD wavefront sensor has two working sets of ADCs with similar performances. We discuss in the next paragraphs ("ADC clocking", "Digital noise", and "General Considerations") how the ADCs are synchronized with the rest of the system and how the two possibilities affect differently the system.

ADC clocking and data flow.   Three clocks delivered by the sequencer define the ADC timing : 1) the frame clock, 2) the ADC clock, and 3) the pixel clock. The first simply marks the beginning of a new frame and is a delayed version of the external trigger (e.g. for synchronization with the laser trigger) or of the internal end-of-exposure trigger. The second has a frequency of 50MHz and is intended to clock the ADC themselves. Finally, the pixel clock triggers the FPGA of the data acquisition board to get the current acquired pixel (from the ADC clock), and is a 12.5MHz clock. In that scheme, the optical ADCs acquire four pixel samples, from which one is selected and sent by optical fiber to the ARGOS slope computer. The BCU built-in ADCs behaves slightly differently : it disregards the ADC clock and uses only a 12.5MHz to clock the ADCs. The data are then directly transferred through a built-in bus to the BCU DSP for computation.

Fig. 3.10 represents the important "hand-shake" produced by the sequencer between the CAMEX clocking and the ADC clocks as designated by "pixel start delay". The last clock of a CAMEX cycle triggers the multiplexing of the analog signal to the output of the CAMEX. Following this clock, the signal is transferred and should be acquired after the appropriate delay. Whence the start of the pixel clock has an important impact on the data quality, as it sets the pixel acquisition time (or which pixel sample is selected).

This last clock fixes the timing of the pixel acquisition during its 80ns analog length. Wrong values lead to increased noise as the signal might not be settled yet or the transition between two pixels occur. Hence the delay between the multiplexing clock and the pixel clock need to be optimized depending on the cable lengths and the electronics delays. With the optical ADCs, changing this delay in the sequencer programmation is satisfying and allow delta of 20ns. For the BCU built-in ADC, the firmware of the unit needs to be modified, which makes it not as easily configurable.

Digital noise.   One of the differences between the two "final" ADC sets are their digitisation. Indeed, the "optical ADC" boards feature 14bits ADCs with essentially no analog pre-amplification gain. The "BCU built-in ADCs" boards feature 16bits ADCs with an analog pre-amplification of approximately $1/2.5$ [ADU/e$^-$]. This brings the digitisation gain (ADU/e$^-$) ratio between the two boards to $\sim 4/2.5 = 1.6$ in favor of the BCU built-in ADCs. Assuming that both boards do not introduce any analog noise before digitisation, the only difference is the digitisation noise depending on the gain. Indeed, the digitisation noise in e$^-$

---

[5]the communication agreement was not identical between the framegenerator board, used to develop the ARGOS BCU optical interfaces, and those data acquisition boards. A different special char was used for the synchronization between the emitter and the receiver.
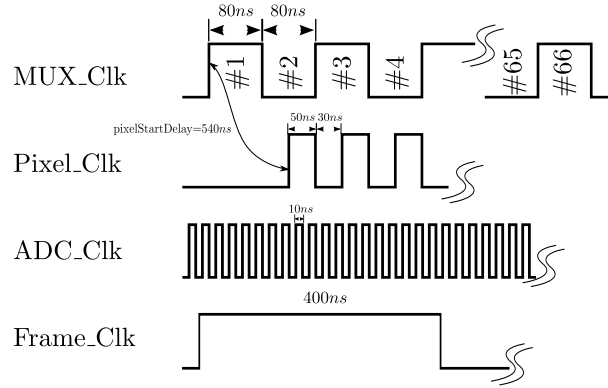
Figure 3.10: "Hand-shake" between CAMEX and ADC clocks. The MUX clock designates the multiplexing clock of the analog pixels at the output of the CAMEX. The other 3 clocks are ADC clocking, with the frame clock marking the start of frame, the ADC clock triggering the ADC acquisition, and the pixel clock selecting the appropriate ADC sample. The delay between the MUX clock and the start of pixel clock has an important effect on the noise quality.

is given by $\sigma_{digit} \sim 0.289g$ with g the gain in $[\mathrm{e}^-/\mathrm{ADU}]$.[6] The typical gain using the "optical ADCs" is 2.4ADU/e$^-$, leading to $\sigma_{digit} \sim 0.12$. Using the "BCU built-in ADCs", one gets $\sigma_{digit} \sim 0.07$. Adding in quadrature this noise contribution to a 3e$^-$ readout noise, we get respectively ~ 3.0024 and ~ 3.0008, *i.e.* a completely negligible contribution from the digital noise in both case.

We can therefore state, that in term of digital noise, both ADC units are essentially the same and the use of 14 or 16 bits do not make any differences.[7]

General considerations. As we have seen, the differences between the two ADC sets are relatively minor and should not affect the Argos operation either ways. A detailed characterization in term of additional readout noise contribution has been performed to compare the BCU built-in ADCs to the optical ADCs. The results are a slightly higher readout noise ($\sim$0.1-0.2e$^-$) with the BCU built-in ADCs. On one hand, the optical ADC are well suited for laboratory work with their dedicated receiver board and the pnSensor software for data acquisition. On the other hand, the BCU built-in ADC has been more quickly in operation with the BCU (due to the high degree of integration) and is already in extensive use in the wavefront sensor integration. It is also easier to use and do not required any dedicated configuration (once the clock handshake has been correctly implemented in the firmware).

---

[6]The digitisation noise can be quickly derived as follows: assuming any analog value f around the ADU value $\bar{f}$ is equiprobable, the quantification error $\Delta f = f - \bar{f}$ is uniformily distributed, and $\Delta f \in [-1/2, 1/2]$, the error is thus given by

$$\sigma_{digit}^2 = \int_{\bar{f}-1/2}^{\bar{f}+1/2} (f - \bar{f})^2 df = \left[\frac{1}{3}\Delta f^3\right]_{-1/2}^{1/2} = \frac{1}{12},$$

therefore the standard deviation is $\sqrt{\frac{1}{12}} \sim 0.289$ [ADU].

[7]this short analysis performed is a fortiori true for the highest gain, $\sim 4\times$ the one discussed here. This overspecified digitisation is foreseen for lower gain available with the CAMEX, not for our low-light level.

Pattern generator: the CCD and ADC clocks

The sequencer (or pattern generator) provides all digital timing to the PNCCD and to the ADCs. It is therefore the master clock of the PNCCD camera and the "hand-shake" between the CAMEX and the ADCs, as just discussed above.

The device is freely programmable and is based on a FPGA. It needs to be programmed at every start of the device.

In summary, the sequencer performs the following tasks:

1. programmation of the CAMEX registers when powering the PNCCD,

2. during the exposure, it keeps the voltages constant, in particular the ϕ registers in a defined "confining" state,

3. after an external trigger or the end of the CCD integration time, it performs the transfer of charges from the image to the storage region,

4. readout of the CCD by simultaneously synchronizing the charge transfer, the CAMEX operations, the multiplexing of the outputs of the CAMEX, and the clocking of the ADCs.

Those operation are done with an accuracy of 10ns, the sequencer running at 100MHz.

Most of the clocking and synchronization, in particular for what concerns the CAMEX, is the expertise of PNSENSOR and their description is outside this framework. We discuss here however an important feature. The central two lines of the ARGOS PNCCD are effectively larger, collecting more light. This is explained by the arrangement of the ϕ voltages and is explained as follows. The ϕ voltages in "collecting mode" are schematized in Fig. 3.11. The ϕ_1 and ϕ_2 are in their high state and define the potential minimum in the n-type silicon (in the epitaxial layer, see also Fig. 3.2). Using two out of the three ϕ voltages instead of only one defines better the potential minimum and lead to a more uniform pixel response. However, this scheme has a side effect. It creates larger pixels in the center of the PNCCD[8], as represented in Fig. 3.11. The SH pattern shared between the two PNCCD halves (see also Fig. 3.1) has 29 subapertures containing such central line. This potentially biases the centroiding measurements by the coordinate shift (1/6 of a pixel) and the larger collecting area. This can be compensated by adapting the pixel coordinates and the pixel weights at the computational level in the ARGOS slope BCU, see CHAP.4.

Timing for an image acquisition. The timing is a key elements of the ARGOS wavefront sensor. Indeed the PNCCD must be correctly synchronized with the laser pulses and the Pockels cells opening time in order to avoid any overlap between light exposure and charge transfer.

We compute here the full time delay between external trigger and "ready for next integration", relevant for the synchronization, and "frame fully read", relevant for the ARGOS closed-loop bandwidth. We give our computed values in Tab. B.1.

To summarize, the full frame reading time is $\sim984\mu s$, and the image to the framestore area shift is $\sim33\mu s$ during which the CCD should not be exposed.

---

[8]this is linked to the split frame transfer scheme.
[9]derived from the "pixelStartDelay" clock.
[10]for the BCU built-in ADCs.
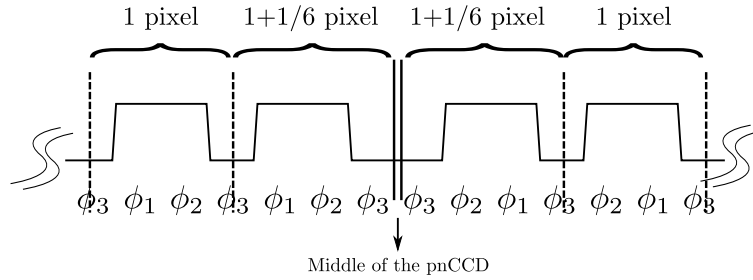
Figure 3.11: ϕ registers in "collecting", or storage, mode along one channel in the middle of the PNCCD. The double middle lines define the middle of the PNCCD, where the left side is readout to the left, and vice-versa for the right. The dashed line defines the separation between pixels along the channel. This ϕ configuration provides better pixel uniformity but leads to larger central pixels, by an additional factor of 1/6.

Table 3.2: Timing delay from external trigger to digitisation.

	time delay [ns]
External trigger propagation from the sequencer to CAMEX	∼25
Shift of one pixel by the ϕ registers	250
Sum of the CAMEX register clocks for one pixel	7200
Multiplexing of the pixels	0 - 528
Cable propagation of analog signal to ADC	25
ADC internal electronic delay[9]	515 (505)[10]
Delay to full shift of the image area to the framestore area	∼33μs
Delay to the end of the CAMEX sequence	∼ 984μs
Delay to the end of the digitisation	∼ 984.5μs

Power Supply

A dedicated power supply development, tests, and assembly has been conducted at MPE. The final unit is a 6 units rack mounted power supply, optimized for the PNCCD. The device is fully remotely controlled through an Ethernet interface and powered by a single 24DC voltage. Particular care has been taken for the stability, the ease to use and to electromagnetic immunity. Its characteristics and development is reported in Ziegleder (2013).

The motivations of this development were both a question of compactness to meet the space requirements at the telescope, and the PNCCD performance, in particular to address the "common-mode" noise. Related to this issue, the staged analysis, the test campaign and the solution given are described in section 3.4.

The PSU is made of three boards, sharing the 23 specific voltages needed which vary both in required voltage and current outputs. The first board includes a microcontroller that takes care of internal control processes and communication to the user. In the framework of this thesis, we develop the communication tools on the PNCCD side and support the testing of the PSU by many test activities with the PNCCD at different stage of the development. In the appendix, we list in Tab. B.1 the various voltages required to operate the PNCCD. We will refer to those when discussing the PNCCD voltage optimization and the test campaign

lead to address the "common-mode" issue, see section 3.4.4.

Voltage optimization. The 23 optimum voltages may vary a little from one chip to the other. Initial voltage settings were provided by PNSENSOR and we latter optimize a few of them, still in collaboration with PNSENSOR.

The qualitative parameters considered where two-folds:

- noise level and uniformity between first and last lines, and from channel to channel,
- image sharpness (or PSF).

In parallel, we take care to preserve the correct PNCCD behaviour, *i.e.* correct reset and linearity.

The degree of freedom are essentially the reset, the depletion, and the digital CAMEX voltages. The reset voltages have a strong influence on the noise uniformity and level as they dictate the reset-FET behavior. This is discussed in details in section 3.3.3. The depletion voltage has an impact on the PSF, it should always be higher than the minimum voltage needed for full depletion. Higher values can improve marginally the sharpness. On the other hand, a too high voltage may not be allowed by the power supply. The CAMEX voltages have also some small influence on the noise map, and lower values are typically better for the life "duration" of the CAMEX units.

Based on those qualitative behaviour, the optimization was done empirically while estimating the noise uniformity, and the PSF (see section 3.3.3 and section 3.3.5). This processes lead to a better noise uniformity. Hence subapertures close to the first line readout will be less affected by the rising noise, see also section 3.3.3.

3.2.3 Camera housing

The camera housing has been subject to a dedicated development by PNSENSOR with the following objectives : compactness, minimum need for maintenance, and efficient compact cooling. Fig. 3.12 shows the three camera versions: 1) the initial "X-ray" version housing requiring constant pumping and cryogenic cooling. This involves a bulky cooling and pumping system, introducing vibrations directly measurable on Shack-Hartmann spot motions (see also section 3.4.2); 2) the first "Engineering" model for evaluation; 3) the final housing improved after our testing.

The internal main parts of the housing are as followed, see also Fig. 3.13 :

- the base plate of the housing features the different interfaces: cooling connectors, vacuum valve, housekeeping connectors and electronic feedthrough to control the PNCCD. All the following mechanical pieces are then fixed to this base plate, essentially by two vertical "posts".
- the water heat exchanger removing the dissipated heat,
- two Peltier modules, the warm sides being glued to the heat exchanger and the cold sides being glued to a first lower titanium cooling mask,
- A second cooling mask in contact with the PNCCD ceramic is screwed to the first. The substrate ceramic is glued to this upper cooling mask and allows a efficient cooling of the entire ceramic.
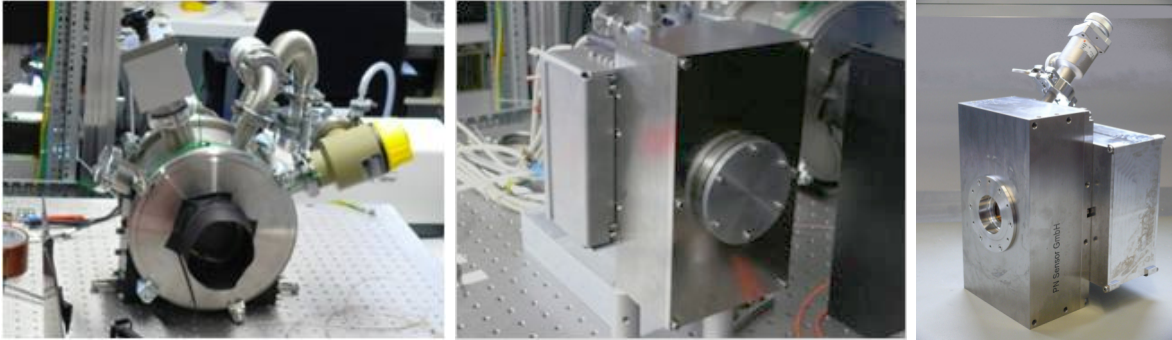
Figure 3.12: (Left) Initial camera housing inheritated from X-ray application. It required constant pumping and cryogenic cooling. (Middle) First "Engineering" housing model developed by PNSENSOR with a front side housing opening. (Right) Final housing model including its backside electronics and vacuum valve.

An external flange provides mechanical interfaces and includes the entrance glass window. The window is a $1''$ diameter, 3mm thick fused silica with both side coated with a 532nm anti-reflective coating. The chip itself is only 10.88mm away from the external surface of the window.

The entire housing is $212 \times 120 \times 82$ mm. The cooling is performed by thermoelectric (Peltier) modules, while the heat load is dissipated by cooling water (around 6°C). This allows an operation temperature as low as -35°C and hence negligible dark current at 1kHz frame rate. The camera housing is evacuated to about 1mbar and can be operated up to at least 50mbar allowing for low maintenance. The housing also includes three different temperatures, one pressure, and one humidity sensors. This allows us to monitor the cooling water, the housing, and the CCD temperature, but as well the pressure and to have a qualitative humidity measurement.

During the development phase by PNSENSOR, we performed several tests concerning the cooling capabilities, the vacuum tightness and the mechanical stability.

Good cooling capabilities are required to have good noise properties. We study the noise behavior with temperature in section 3.3.6. Following the chip characteristics, an operation temperature between -25° and -35°C is considered sufficient, ensuring in parallel a good lifetime of the cooling modules.

Vacuum operation ensure good cooling capabilities and avoid any hazardous condensation. The camera was required to be vacuum tight to prevent any constant pumping, and minimize the maintenance need. From a few long term measurements (over a few months), we measure a pressure rise rate of $\sim$0.12mbar/day. PNSENSOR measurements repeated over several days gives $\sim$0.2mbar/day. In both case, the camera could be operated for >6months to 1 year without maintenance, satisfying the ARGOS need.

Finally, mechanical stability ensures reliable slope measurements. The PNCCD was required to move by less than 1/10 of a pixel under gravity gradient. To evaluate internal flexures, we setup a tip-tilt camera test bench to be able to measure movement of $\lesssim 1\mu$m. We create a sharp spot on the PNCCD and tilt the camera, plus the small setup optics, from -90° to 90°. The measurements were repeated several times to ensure their reproducibility and compared to similar tests done with a commercial camera. The results were as follows.
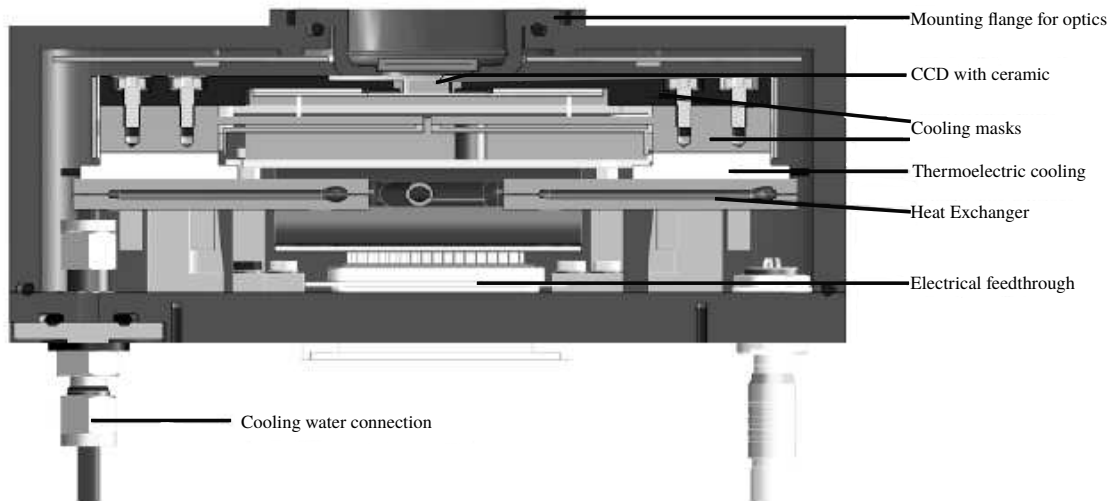
Figure 3.13: Cross-section of the final camera model. The main elements are annotated Light come from top through the entrance window and a few mm below the PNCCD chip. The backplane electronics are here not represented. Credit: Ordavo et al. (2011).

The "Engineering" model was not complying to our requirements but displayed internal flexure ~ 3 times higher. The revised mechanical model has now been implemented and follows our specifications. Its test results are presented in Fig. 3.14.

3.2.4 Software

Based on the drivers and distributed software tools provided by PNSENSOR, we develop a complete standalone software to control the camera. In its final definition, the software tasks should :

- provide individual control of the sequencer, the ADCs, the Peltier cooling, and the ARGOS power supplies,

- monitor the temperatures, pressure, and humidity, and other diagnostics,

- provide a well defined interface for remote operation,

- ensure the safety of the camera, and an easy-to-use normal operation procedure.

Based on a communication agreement with the ARGOS software (an ICE[11] interface), all functionalities have been implemented to allow engineering operation. On top of this code, a PNCCD state machine has been incorporated.

This state machine is intended to support the standard use, *i.e.* start/stop, of the PNCCD camera in a fully consistent way. The diagram of the state machine that we have developed is represented below in Fig. 3.15.

The PNCCD state machine can be in one of the following states :

---

[11]Internet Communication Engine, see `http://www.zeroc.com`, interface suggested by our MPIA ARGOS software colleagues.
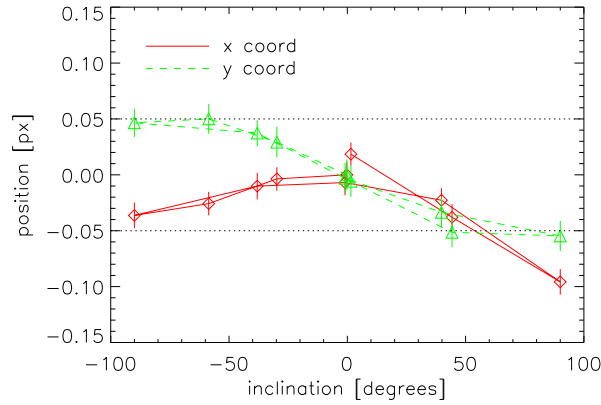
Figure 3.14: Result of a tip-tilt test with the final camera model. This is obtained from a centroid measurement on the chip. The total flexure tip-tilt amounts to ~0.1pixel=4.8μm and is therefore within our specifications. See text for more details.
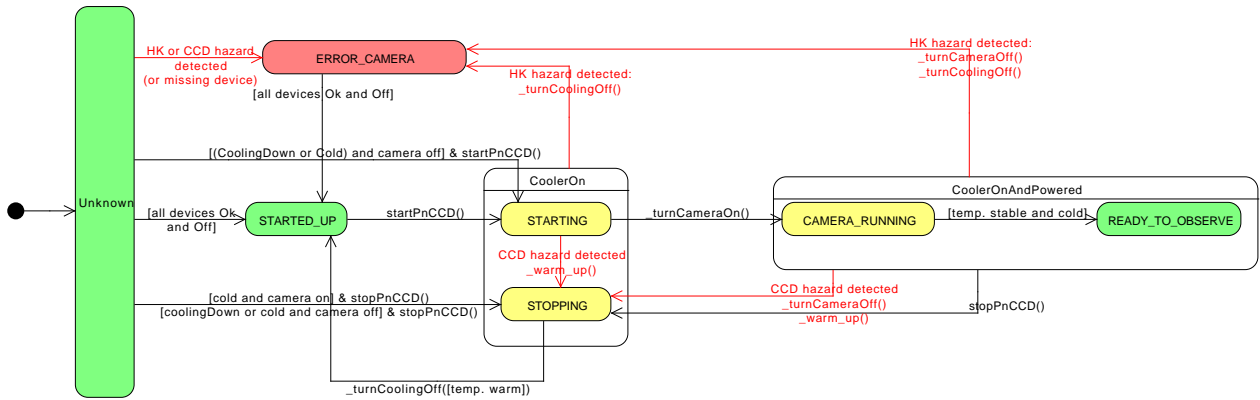
Figure 3.15: PNCCD state machine diagram displaying the possible transitions from states upon "event" being generated by a user (*i.e.* start/stop) or internal (e.g. ready to turn the camera on, hazard detected, etc.). The aim of this state machine is to ensure easy and safe operation. See text for more details.

- *Started Up* : the idle mode. The sequencer is programmed, the camera is monitored and ready to be started.

- *Starting* : a transitory mode where the camera is being automatically turned on. In this state, the camera is being cooled but the CCD is off.

- *Stopping* : a transitory mode where the camera is being automatically turned off. In this state, the camera is being warmed up (the cooling decreases progressively) and the CCD is already turned off.

- *Camera Running* : a transitory operational status. In that state, the cooling set point is not reached yet but the camera is already turned on and acquiring frames.

- *Ready to observe* : a steady operational status. In that state, the cooling set point is reached and considered stable and the camera is already turned on and acquiring frames. In that state, the temperature being stable, the offset/bias map can be acquired from dark frames, and normal operation can proceed.

- *Error* : the error state preventing any operation that could harm the PNCCD.

- *Unknown* : the unknown state is implemented to allow engineering operation, *i.e.* device oriented operations rather that using the fully automatized sequence.

In addition to react to 'start' or 'stop' commands from the user, the software reacts upon hazardous events, that can be linked either to "housekeeping" bad conditions (including the Peltier controller behavior) or "camera" (wrong voltages or currents, uncorrect sequencer behaviour, etc.). A more detailed description of the software functionalities and the state machine is given in Orban de Xivry (2013).

3.3   PnCCD detector performance

In the following, we characterize quantitatively the PNCCD performance. Repeated tests and their analyses have been performed during the development time of the three cameras, as they were assembled and optimized.

In the following sections, we present the key characteristics of the detector, most of which have been tested at MPE in the framework of this thesis. In particular we discuss in details the following parameters

- the readout noise – more particularly the "effective readout noise" – and its distribution (section 3.3.2 and 3.3.3)

- saturation and nonlinearity using the photon transfer curve technique (section 3.3.2)

- the gain factor and its distribution (section 3.3.3)

- bias stability over time (section 3.3.4)

- point-spread function and quantum efficiency[12] as characterized by PNSensor (section 3.3.5 and 3.3.1)

- the noise dependence with operating temperature (section 3.3.6).

---

[12]percentage of incident photon effectively detected and producing charge carriers, *i.e.* commonly photo-electrons.
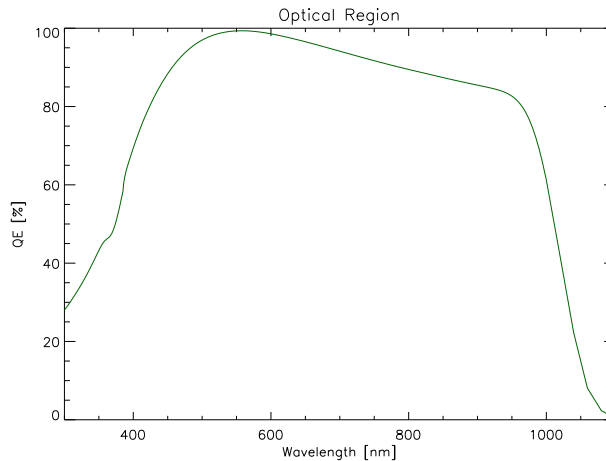
Figure 3.16: Quantum efficiency as optimized for Argos obtained by adjustment of anti-reflective coating. Credit: pnSensor.

While CCD characterization methods are not new, the pnCCD by, e.g. its fast framerate and column parallel readout, has requested refinement in the techniques used and specific considerations to understand fully its behavior. We summarize the pnCCD performance in section 3.3.7.

The standard test setup consists in an uniform illumination by means of an integrating sphere or collimated source with a diode light source filtered around 532nm. A shutter is used to record dark images. The acquisition is performed with the optical ADCs and using an optical receiving board integrated to a computer in collaboration with pnSensor and Jülich Forschungszentrum. The data discussed in the following sections uses the pnCCD in its "low gain" mode, at −25°C, and at a 1kHz frame rate, *i.e.* the baseline settings for Argos. Our tests are represented here for one of the final Argos camera, *i.e.* LBT#2. The other two final cameras display similar characteristics.

3.3.1 Optical properties

One of the key characteristics of the pnCCD is its very high quantum efficiency over a large wavelength range. Indeed, the internal quantum efficiency[13] is close to 100% between 300 and 950nm (Hartmann, 1999)[14].

The external, or final, quantum efficiency will depend on the anti-reflective coating and how it has been tailored to the desired application. The coating is based on two dielectric layers of SiO_2 and Si_3N_4 of tailored thicknesses to achieve the maximum QE in the desired wavelength range, *i.e.* for Argos at 532nm and 589nm[15]. The calculated efficiency is represented in Fig. 3.16 and was provided to us by pnSensor.

We should emphasize here that the near-IR or "red" responsivity of the pnCCD is particularly good compared to other CCD, and this thanks to its large depleted thickness.

---

[13]*i.e.* once an incident photon has passed the covering layers of the detector.

[14]$\lesssim$ 300nm, secondary processes kick in; $\gtrsim$ 950nm, radiation starts to get through the 300-450μm silicon material.

[15]in the perspective of a Sodium laser upgrade path.

3.3.2 Photon-transfer curves

A convenient and widespread tool to characterize CCD is the photon transfer curve technique. It allows one to derive useful quantities such as the readout noise, the conversion factor from ADU to e$^-$, the linearity and the dynamic range of the detector. Its fundamental principle is as follows. The camera processes the input light in an output digital signal. Knowing the input noise properties, *i.e.* photon noise[16], the output noise must include this theoretical expectation plus any other contribution from the camera electronics. This can be expressed by the following equation

$$\begin{aligned} \sigma_s^2 \quad &= \sigma_{RON}^2 + \sigma_{ph}^2 \quad [\text{ADU}] \\ &= \sigma_{RON}^2 + \frac{S}{g} \quad [\text{ADU}], \end{aligned} \tag{3.2}$$

with the total noise σ_s, the electrical noise σ_{RON} and the light counts S in [ADU] (σ_{ph}^2 [ADU] $= I[\text{e-}]/g^2$), g the gain in [e$^-$/ADU]. Our main question here is how the detector reacts under different level of illumination and how does the CCD noise contributions vary with it.

Based on those considerations, we acquire sets of 200 frames at different level of illumination. At each illumination, we perform the necessary correction : dark/bias subtraction, and common-mode correction. We compute the variance for each pixels and fit its dependence with illumination using equation 3.2. The results is represented in log-log scale in Fig. 3.17. Four regimes – in principle – can be distinguished : a slope of 0 in the low flux part readout noise dominated, a slope of 1/2 (in e^- units) photon-noise dominated, a slope of one dominated by detector characteristics, and then saturation. The higher flux region can be dominated by pixel response non-uniformity (PRNU), or fixed pattern, for which the noise become $\sigma_{\text{fp}} \propto S \times \text{PRNU}$. We do not observe it here and will discuss it in the "dynamical range" paragraph.

From this curve, we discuss in the following paragraphs the gain, the noise, and the linearity properties including the inferred dynamical range, *i.e.* the photon-noise dominated regime.

Gain variation. Before studying the gain factors, we infer the expected uncertainties and the required number of frame acquisitions.

Assuming that the readout noise is negligible, the gain is expressed by $g = S/\sigma_s^2$ and from error propagation we get,

$$\sigma_g^2 = \frac{1}{\sigma_s^4}\sigma_{\bar{s}}^2 + \frac{4S^2}{\sigma_s^6}\sigma_{\sigma_s}^2, \tag{3.3}$$

where $\sigma_{\bar{s}}^2 = S/(gN_{pixel})$ is the uncertainty on the average flux measurement, and $\sigma_{\sigma_s}^2 = \sigma_s^2/N_{pixel}$ is the uncertainty on the average total variance. Assuming $1/S \ll g$, the first term becomes negligible and we get the simple expression[17]

$$\sigma_g = \left(\frac{1}{N_{pixel}}\right)^{1/2} 2g. \tag{3.4}$$

---

[16]also referred as shot noise.

[17]the expression differ by a factor 2 with the one provided by Janesick (2001), p111. But he assumes that the variance is computed from the difference of two frames, which give $\sigma_s^2 = \dfrac{\sigma_s^2}{2N_{pixel}}$ and therefore $\sigma_g = \sqrt{\dfrac{2}{N_{pixel}}}g$. Our method is slightly different - the signification of N_{pixel} will also be detailed.
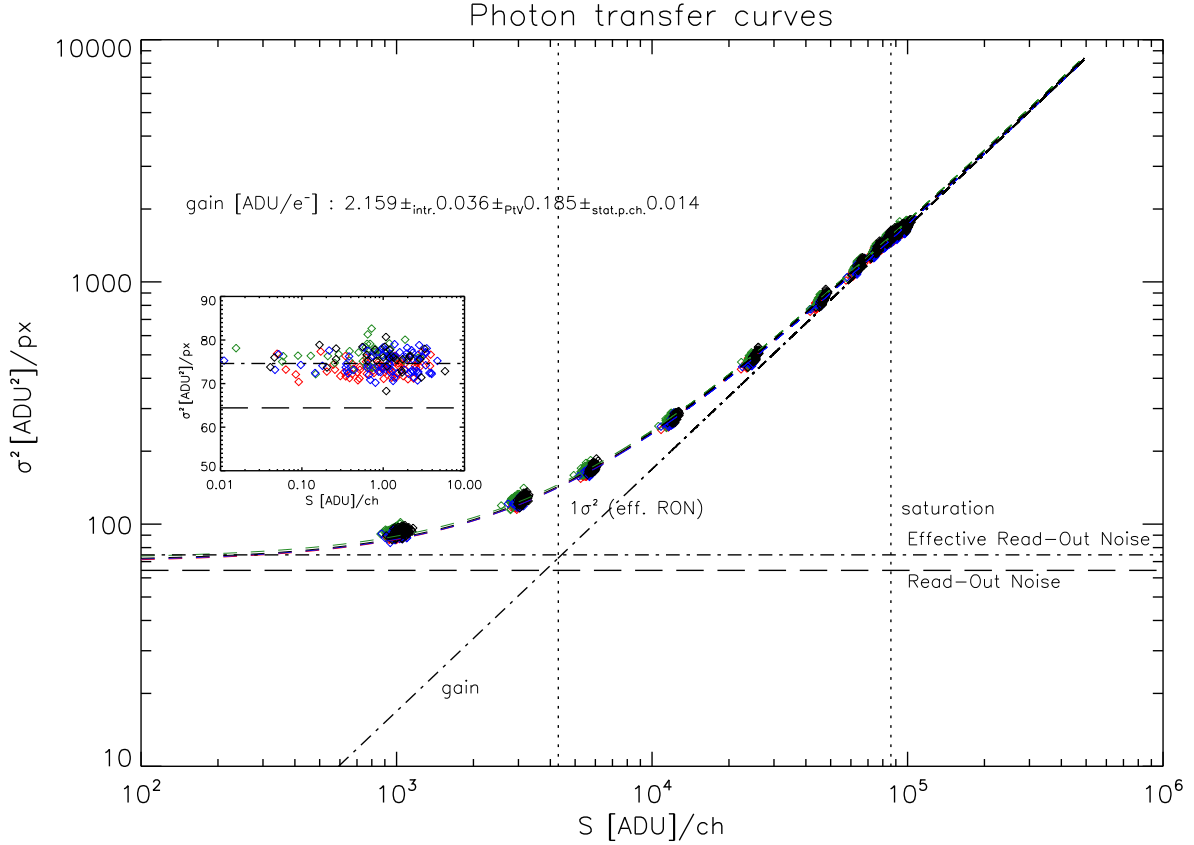
Figure 3.17: Photon-transfer curves in log-log scale. The total variance is expressed in [ADU^2]/pixel and the flux in [ADU]/channel. Three regimes can be distinguished : a read-out noise dominated regime at low flux of null slope, a photon-noise dominated region at higher flux, and finally saturation above $\sim 8 \times 10^4$ADU/ch.. Fixed pattern noise is not observed here. The total variance is computed independently for each channel/column and the fit is done considering all points. The "effective read-out noise", represented by the dashed-dotted horizontal line, is calculated based on readout noise measurements using full common-mode corrected dark images and adding the common-mode noise contribution. It matches correctly the dark measurement, see the zoom window. The oblique dashed-dotted curved gives the average computed gain. The two vertical dotted lines delimitate the "linear" range defined by one σ_{eRON} and the saturation level. We refer to the text for more details and discussion.

Therefore the relative error is σ_g/g and the number of pixel needed to achieve this precision is

$$N_{pixels} = \frac{4}{(\sigma_g/g)^2}. \tag{3.5}$$

The PNCCD frame are read in parallel, thus each channel/column has its own amplifier. As the gain may vary from amplifier to amplifier, it is more suited to compute the gain independently for each channels than for the overall image. In Fig. 3.17, we acquire 200 frames at 10 different illuminations from dark to saturated images. We fit the data excluding saturated frames[18]. As we performed the gain determination independently for each channel/column, the number of pixels relevant for the gain accuracy becomes $N_{pixels} = N_{illumination} \times N_{frames} \times N_{ill.\ pixel\ per\ ch.}$, or in our case $10 \times 200 \times 128$. This results in a $\sim 0.4\%$ relative statistical accuracy for the gain determination per channel. From our photon transfer curve linear fit, we obtain a statistical error amounting to $\sim 0.7\%$. The difference is interpreted as the contribution of the non-linearity, not taken into account in equation 3.5. In both cases, the error is negligible.

Apart from statistical variation, the gain may be intrinsically different from channel to channel. This is discussed later in section 3.3.3. The RMS of this intrinsic variation (from which the statistical error has been quadratically subtracted) is 0.033 [ADU/e$^-$] or $\sim 1.5\%$, and the PtV is 0.185 [ADU/e$^-$] or $\sim 8.5\%$.

In conclusion, the gain factor amounts to 2.159 [ADU/e$^-$][19], with an intrinsic variation of 0.033, a PtV of 0.185, and a statistical error per channel of 0.014.

Effective Read-out Noise. From the photon transfer curve fit, we obtain also the readout noise dominating in the low flux regime. From our computed gain, we can convert this readout noise in physical units. The average value obtained is 3.89e$^-$. We discuss in more details its distribution in section 3.3.3. This noise is essentially attributed to the readout electronics. There is however a contribution from the common-mode correction. This correction uses the eight covered pixels per CAMEX which is subtracted to the entire CAMEX line. From this considerations, we coined the term "effective read-out noise" as the sum of the readout noise and the common-mode correction uncertainties. This can be expressed as follows

$$\sigma_{eRON}^2 = \left(1 + \frac{1}{N}\right)\sigma_{RON}^2 + \frac{\sigma_{CM}^2}{N}, \tag{3.6}$$

where N is the number of pixels used for the common-mode correction. The effective read-out noise is therefore the readout noise incremented by the uncertainties on the read-out noise and on the common-mode noise for a constant level.

In Fig. 3.17, we represent two horizontal lines, *i.e.* the RON and the eRON levels. The "read-out noise" level is computed from a set of 1000 dark frames with common-mode correction using 132 pixels for which the common-mode contributors become negligible. The "effective read-out noise" is obtained applying equation 3.6, assuming a shot noise-type common-mode uncertainty, *i.e.* $\sigma_{CM}^2 = RMS_{CM}$. This matches well the data and the photon-transfer curve fit[20].

---

[18]those are determinated based on the photon transfer curves of only the last 8 lines which saturate first. This is also done individually for each channels. See later discussion.

[19]the mean gain per CAMEX unit is [2.149,2.192,2.127,2.166].

[20]As we will detail in the "common-mode" section, the RMS_{CM} value is ~ 6.5 ADU, and N is 7 pixels (the last covered pixel is neglected as its flux level is non-negligible due to PSF effect).
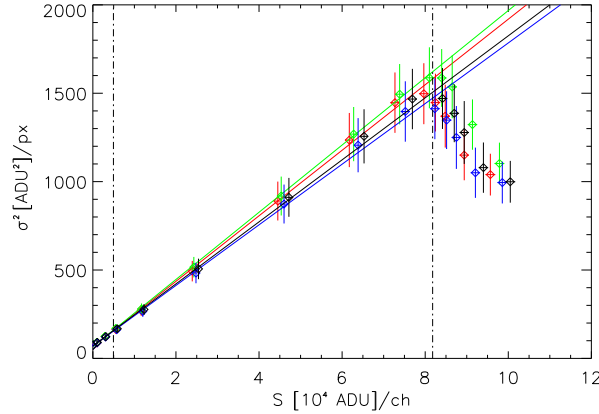
Figure 3.18: Photon transfer curve in linear scale computed for the eight last lines to be read. This procedure emphasizes better the PNCCD saturation depending on the first amplifier range. The saturation happens at ~8000ADU per channel or ~40000e$^-$ per channel. The dashed-dot vertical lines indicate the photon-noise dominated regime from one σ_{eRON} to saturation.

Saturation, non-linearity and dynamical range. As already mentioned, the dynamic range is driven by the amplifier saturation rather than the full well saturation. Computing the photon transfer curves using all the pixels, as we have done in Fig. 3.17, is therefore not appropriate. Instead we should consider the last pixels to be read, presenting the highest voltages at the amplifier input.

From this consideration, we compute the photon transfer curves for the last eight lines, see Fig. 3.18. As we can see, the saturation happens at ~8000 ADU per channel, or ~40000e$^-$/ch..

We then infer the deviation from linearity by taking the difference between the data and the fit, represented in Fig. 3.19. We use here the entire image area to minimize the statistical error. Considering the linear range from one σ_{eRON} to saturation, we find that the non-linearities amounts to $\lesssim \pm 1\%$. The linear range is indicated by dotted or dashed-dotted vertical lines in the various plots. The same operation is done for the gain which shows an overall very good linearity, see also Fig. 3.19.

From the photon transfer curves and the linear deviation plot, we do not see any third regime dominated by fixed pattern rather than photon-noise. PNSENSOR has performed PRNU measurements and obtain a PRNU<2% at 532nm. This low effect and being amplifier saturation limited rather than full well depth limited explains the absence of this "third" regime.

Finally, we can compute the dynamic range. It is usually expressed in dB by
Dynamic Range [dB] $= 20 \log N_{sat}/N_{noise}$, with N_{sat} the full well capacity or the output amplifier dynamic range and N_{noise} the total noise. Using this expression, the ARGOS PNCCD dynamic range is ~81 dB. However, effectively N_{sat} should be divided by the number of illuminated pixed readout by the output amplifier. Doing so, we obtain an "effective dynamic range" of ~38dB. This is a low dynamic range by CCD standards. This is the compromise to pay to obtain such high framerate of 1kHz.
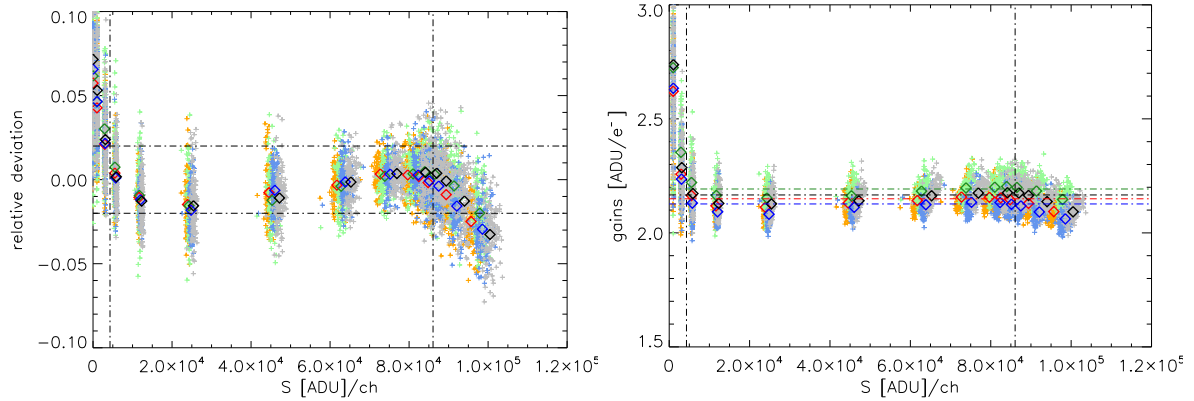
Figure 3.19: (Left) Relative deviation from linearity obtained by taking the difference between the data and the photon-transfer curve fit. The horizontal dashed-dotted lines indicate $\pm 2\%$. (Right) Gain non-linearity. The horizontal lines indicate the average gain values. The vertical lines indicate the photon-noise dominated regime from one σ_{eRON} to saturation.

3.3.3 Noise and gain distribution

In the last section, we have derived the mean gain and RON values. We study here in more details their distributions in the CCD image.

To perform this analysis, we use a set of 1000 dark frames and 1000 light frames and we solve equation 3.2 for the two fluxes. This is an efficient technique requiring little data acquisition and no fitting. The derived gain and RON values may however be bias by $<5\%$ due to non-linearity[21]. So the photon transfer curve technique will be preferred for the absolute values but the technique presented here remains efficient to study their distributions.

In Fig. 3.20, we present the pixel histograms of the noise and gain for one CAMEX and their respective Gaussian fits. We typically obtain 2.15 ± 0.13 [ADU/e$^-$] and 3.7 ± 0.11 e$^-$. The RON distribution displays an enhanced tail on the high end. This is explained in term of a non-uniform reset noise and is discussed in more details below.

In the two next paragraphs we study the gain and noise spatial distributions.

Gain channel to channel variation

The four CAMEX units read the 528 channels/columns in parallel, which means as many different amplification chains. This naturally results with some small gain discrepancies. To quantify this we measure the average gain per channel and compare it channel to channel. We represent it in Fig. 3.21. As already given, from this analysis, the gain RMS variation is $< 2\%$ and the peak-to-valley is $\sim 10\%$.

Noise along channels

Like the gain, the noise can vary from channel to channel as the amplification may slightly vary from one to another. A stronger gradient is however seen in the other direction, the readout direction, as shown in Fig. 3.22. This noise gradient vary from row to row, higher

---

[21]the gain is typically bias by non-linearity in the low flux regime. It typically underestimates the gain factors.
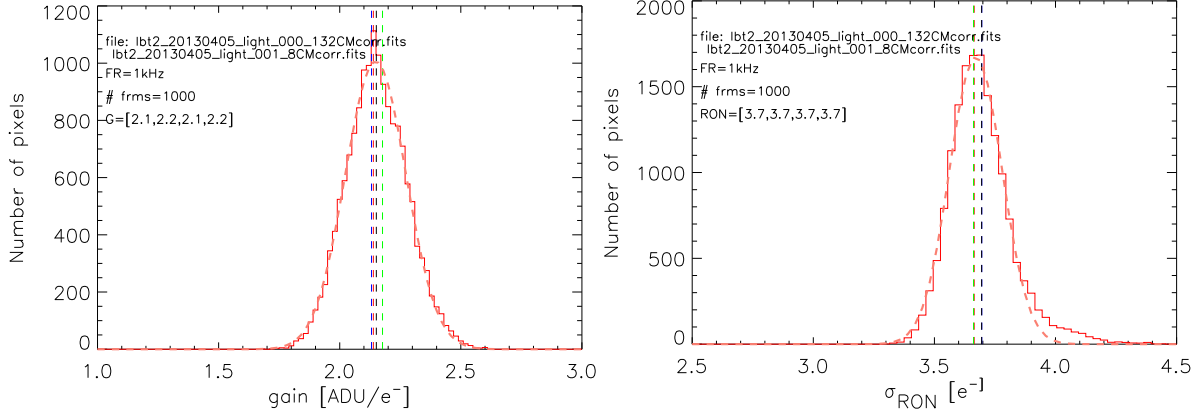
Figure 3.20: Gain and noise pixel histograms obtained from two (dark and light exposed) sets of 1000 frames with their fitted Gaussian distributions. The dark frames are full common-mode corrected by subtracting the average level over 132 pixels. The red curve is the distribution for the first CAMEX, the vertical lines indicate the mean values for each CAMEX unit. We can observe a "non-gaussianity" of the RON distribution at the high end. This is further discussed below.
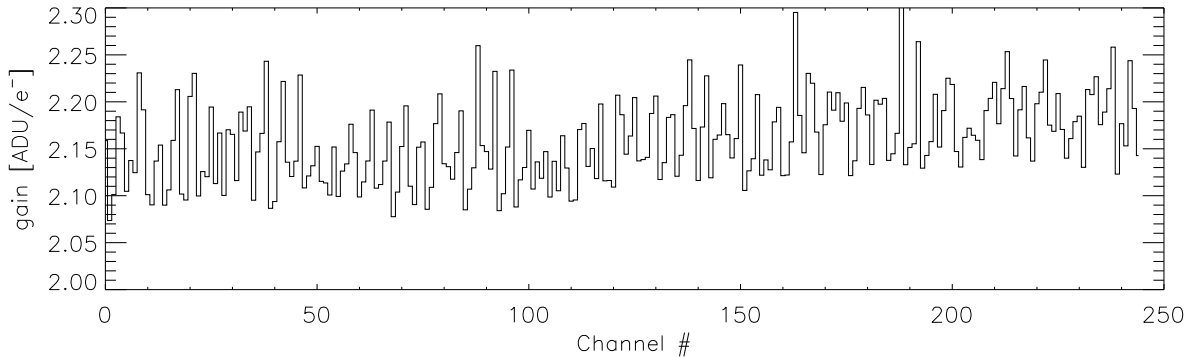
Figure 3.21: Mean gain from channel to channel for one half of the PNCCD. This is obtained with 1000 light and dark frames. Each CAMEX amplifiers behaves slightly differently, whence the small gain variations. The RMS gain variation is $< 2\%$ an the PtV is $\sim 10\%$.

in the first line and is quickly decreasing. In what follows, we explain it as a result of the ARGOS specific readout scheme and of possible "reset noise" origin.

In a standard CCD, each pixel is measured by difference of a "reference" voltage and the voltage created by the pixel charge packet. At each pixel, the output capacitor is reset to a nominal, reference, voltage by briefly pulsing the reset gate. When the reset pulse is turned off the gate resistivity increases by several order of magnitude, and the capacitor value becomes almost frozen. The CDS sampling system takes the difference between the signal value and the baseline, therefore cancelling out the reset noise.

The situation for the ARGOS PNCCD is however slightly different. As previously mentioned, the first amplifier is reset only once per frame and the multi-CDS uses the previous pixel voltage level as a baseline rather than a "reference" capacitor level. In that scheme, fluctuations, e.g. of the reset capacitance, will be averaged out as the successive lines are read. Hence the measured noise can be approximated by

$$\sigma_{meas} = \sqrt{\sigma_{kTC}^2/N_{px} + \sigma_{eRON}^2},$$ (3.7)

with σ_{kTC} the root mean square fluctuation. This non-uniformity of the noise is not seen with the normal PNCCD readout scheme as the pixel measurements are done with respect to a reset baseline rather than the previous pixel voltage level, hence any fluctuation is not averaged out.

In Fig. 3.22, we represent the derived noise map and the mean change over the lines. We fit these curves by equation 3.7 and obtain a $\sigma_{kTC} \sim 4.4\text{e}^-$ possibly originating from the reset capacitance[22].

The fast decrease and the noise homogeneity from channel to channel were taken into account during the voltage optimization, see section 3.2.2.

3.3.4 Bias stability

The bias stability is the variation of the bias with time. The bias[23] is computed by taking the median of a set of dark images at the operation temperature. The bias is a calibration measurement that needs to be acquired once in a while to allow its correct subtraction. The frequency of this calibration is thus function of the bias stability.

A reasonable stability is required to avoid to repeat this calibration too often. The bias stability has been verified at different stages of the project by us and PNSENSOR. We present here a few more recent results on one of the final camera based on sets of 1000 and 2000 dark frames for each time intervals considered : 1) we look at the evolution of the bias level over 90 minutes, 2) we compare the bias with a four days interval.

---

[22]If originating from the reset capacitance, the "reset noise" contribution in e^- can be written by (e.g. McLean, 2008)

$$\sigma_{kTC} = \frac{\sqrt{kTC}}{q}\sqrt{(1 - e^{-2t/RC})},$$ (3.8)

with k the Boltzmann's constant, T the temperature at the capacitor, C the capacitance, R the resistance of the reset transistor, q the electron charge. The time delay t is here of order of the pixel readout time $\sim 7.2\mu s$. Considering $T = -25$°C, $C \sim 25$fF and $R \sim 10^{11}\Omega$ as possible values (Hartmann et al., 2008, McLean, 2008), this noise contribution could amount to $\sigma_{kTC} \sim 4.4\text{e}^-$ as measured in our case. (Note that this is little dependent on the capacitance, but rather on the time delay and the resistance in the "off" state of the transistor.)

[23]we also refer to it as the "offset", or "dark" by reference to the acquisition procedure.
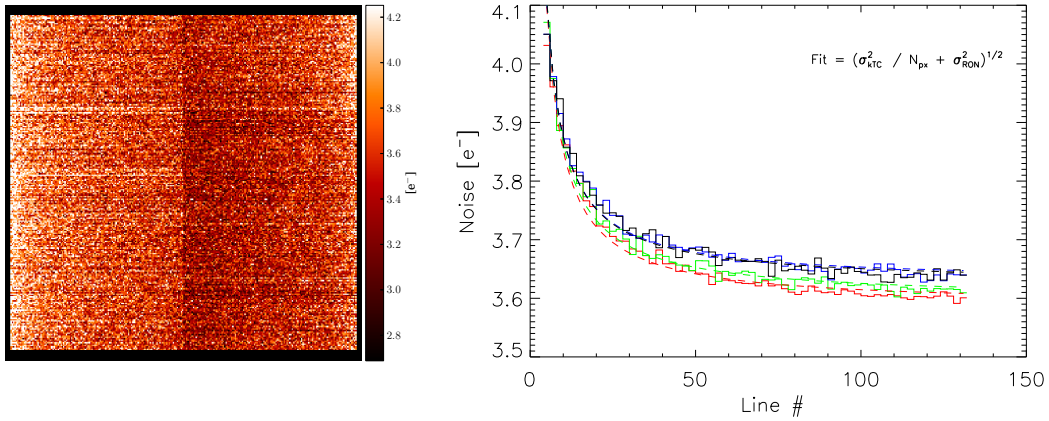
Figure 3.22: Noise distribution obtained from 1000 dark and light frames. (Left) Noise map obtained and converted to electrons using the gain map (hence the dark area where the detector is shielded). We can observe the higher value on the left and right side, the first lines to be read. (Right) average noise along a channel/column per CAMEX representing the spatial gradient. This is explained in term of reset noise. We fit these distribution by equation 3.7 and obtain $\sigma_{kTC} \sim 4.4\mathrm{e}^-$. See text for further discussion.

In Fig. 3.23 (right), we plot the evolution of the mean absolute difference of the bias with time. We see that the difference increases up to ~ 0.6 ADU or $< 0.3\mathrm{e}^-$ and although it increases, it also converges with time suggesting that part of this variation may be link to a full thermalization of the camera. The good behavior of the bias is confirmed by comparing the bias acquired with a four day intervals. Indeed, the mean difference in that case amounts to ~ 1.7 ADU or $\sim 0.8\mathrm{e}^-$.

As the bias change with time, structure may appear in the dark subtracted images. In Fig. 3.23 (left), we plot the average over the lines and over the channels. The variation over the channels does not seem to display any strong features, while the line variation displays a "S" feature. This feature appears in the readout direction and is an effect of the new power supplies on the readout. This was indeed not observed with previous PSUs. The evolution of this feature remains to be studied in more details.

As the system is being integrated and automatize, more systematic characterizations will be undergone. Those results suggest however that a single bias acquisition per night should be sufficient. A more systematic characterization could make use of the Allan variance over a long term well defined time sequence. We discuss it shortly in appendix B.2.2.

Another aspect of the bias is its stability with temperature. We have not performed any systematic characterization of that dependence. However, from experience, we can rely on the good control provided by the Peltier controller unit to ensure a constant temperature of $< \pm 0.5°$C.

3.3.5 Point spread function

The PSF response, in particular its FWHM, of the chip is of course of importance as we aim to accurately determine where any photon arrives.

This measurement was provided by PNSENSOR. For this purpose, the PSF is measured
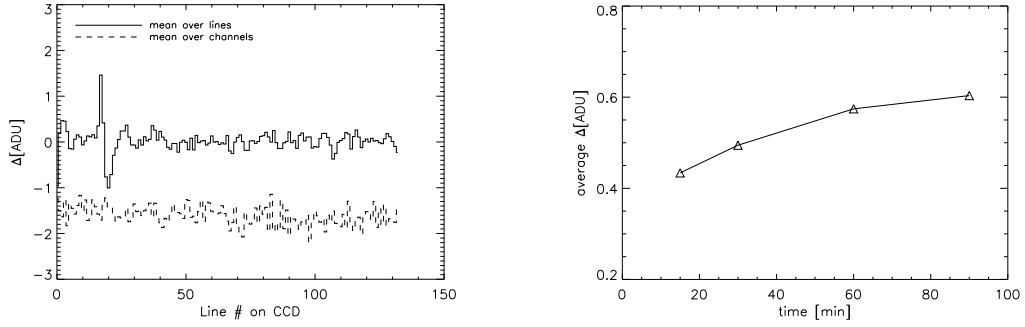
Figure 3.23: (Left) Average over lines (dashed) and channels/columns (solid) of the bias difference taken at a 30 minute interval. Each bias is computed by taking the median of 1000 frames. The dashed curve is shifted by -1.5ADU for representation reason. The solid curve, in the readout direction, shows a "S" feature which is very likely an influence of the new Argos power supplies. (Right) Evolution of the average absolute difference of the bias with time over 90 minutes. We see a convergence with time reaching $\sim$0.8 ADU or $<$0.3 e$^-$.

using a so-called virtual knife-edge method where a point like spot is projected onto the detector and is moved by small steps. A virtual region of pixels is used for the analysis for which the signal inside is compared to the total signal of spot. The resulting PSF is a Gaussian of FWHM as low as 20μm at 700nm or <0.5pixel (see also Ihle et al., 2008).

As a quick check and to avoid an unecessary complex setup, we try and retrieve the PSF width from a flat image. Indeed, one can try and constrain the PSF distribution at the edge of the illuminated area using covered pixels and light exposed ones. We can compute a response function from a flat illumination, convolution of a Gaussian with a square pixel (assuming a symmetric response),

$$R(x,y) = \frac{1}{2}\pi\sigma^2 \left[\text{erf}\,\frac{x+1/2}{\sqrt{2}\sigma} - \text{erf}\,\frac{x-1/2}{\sqrt{2}\sigma} \right] \left[\text{erf}\,\frac{y+1/2}{\sqrt{2}\sigma} - \text{erf}\,\frac{y-1/2}{\sqrt{2}\sigma} \right], \qquad (3.9)$$

with x and y the coordinates, σ the Gaussian width (symmetric). Comparing this function with our retrieved PSF from the flat image corners, we obtain a PSF width of $\sim$1px. Considering the naive approach (few measurement points, limitation of the covering accuracy and of the collimation of the flat light), this is in fair agreement with the pnSensor measurement.

3.3.6   Noise behavior with temperature

Thermal noise is an important contributor to the CCD noise. Two commonly distinguished noises depend on the temperature, the dark current shot noise and thermal noise generated in resistances[24].

Dark current can result from imperfections in the bulk depleted silicon by introducing electronic states between the valence and conduction bands. These intermediate states facilitate the electrons to thermally "hop" to the conduction band. Generated charges are then collected by the ϕ registers at each pixel and undistinguishable from photo-electrons. This

---

[24]also designated by Johnson noise.

dark current is corrected by dark map subtraction. However, as for photo-electrons, the dark current presents shot noise, hence the term "dark current shot noise".

PNSENSOR has performed dark current measurements at different frame rates. The reported value is typically $\sim 0.2 \mathrm{e}^-$/pixel/second measured at 100Hz and $-50°$C. Based on this value, we can estimate the dark current evolution with temperature by using the relation between the dark current generated in bulk silicon with the temperature (see equation B.1). For a temperature of $-35°$C to $-25°$C, the dark current amounts from ~ 1.5 to $5.2 e^-$/px/s. Extrapolating to our frame rate of 1kHz, the dark current noise is respectively of $\sim 0.04 \mathrm{e}^-$ and $\sim 0.07 \mathrm{e}^-$, *i.e.* the bulk dark current noise is negligible. See appendix B.2.1 for more details.

The other possible contributor is thermal noise generated by the random motion of electrons in an electrical conductor. It is a broadband white noise and varies $\propto \sqrt{T}$.

To characterize the noise behavior with temperature, we derive noise measurements at different operating temperatures. This is done in order to verify the reasonable dependence of the noise with temperature, and to determine an acceptable operating temperature range in the limit of the housing cooling capabilities. We performed these measurements at various stage of the project as it can depend on the chip, its electronics, and the voltage and clocking optimizations. We give in Fig. 3.24, the results converted to electrons for one of the final cameras. We observe a typical noise difference of 0.05-$0.1 e^-$ between $-30°$C and $-20°$C.

Motivated by the considerations described above, we fit a function $\sqrt{aT + b}$. Assuming this provides a reasonable fit, we can compare the predicted values with measurements of PNSENSOR at lower temperatures ($-50°$C or $-90°$C), and predict the noise increase with higher temperature. If we consider the temperatures $[-90, -50, -25, -10]°$C, the average noises become $[2.98, 3.41, 3.65, 3.79]e^-$. These values present a relatively large increase with decreasing temperature. Of course these predictions should be taken with caution considering the simplicity of the fitted function, the use of a single conversion factor at all temperatures, and the limited number of measurements.

The cooling of the camera allows temperatures down to $-35°$C. The Peltier units however age faster when operated at high load, hence one may prefer to relax the operating temperature. From these considerations, a temperature of $\sim -25°$C appear still reasonable. This is the current baseline for ARGOS (it also allows a low Peltier load of $\sim 50\%$ of their full range).

3.3.7 Summary of the pnCCD performance

We report the general characteristics of the PNCCD as provided by PNSENSOR in Tab. 3.3. In Tab. 3.4, we summarize the main characteristics derived in our analysis for one of the three final cameras.

We distinguish "low gain" and "high gain" for the two operating modes for ARGOS. The typical gain will be the "low gain" which provides the more suited dynamical range (see also the "photon-dominated range") but leads to a slightly higher read-out noise. The switch to the "high gain" mode may be considered in lower flux cases. The dynamical range is different for this two gains because it is not limited by the full well depth but by saturation of the first amplifiers of the CAMEX units.

It is interesting to note that the decrease between the two gains in the effective read-out noise is not as high as for the "standard" noise. Indeed, the common-mode RMS is essentially independent of the gain and its contribution is therefore larger for the high gain mode.
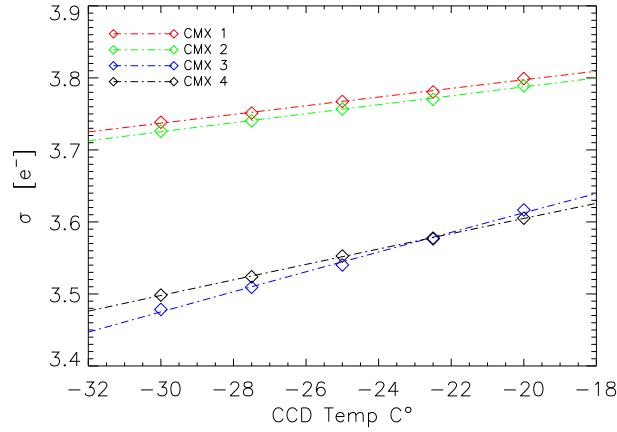
Figure 3.24: Noise versus CCD temperature. Each temperature measurement is done on 1000 frames, median dark subtracted, and full line common-mode corrected. Hence the noise here is the readout noise without the common-mode contribution. A fit by $\sqrt{aT + b}$ allows us to predict its evolution with temperature. Argos will typically operate the pnCCD at $-25°C$.

Table 3.3: General characteristics of the pnCCD as provided by HLL/pnSensor.

Parameter	Value
Type of CCD	Column-parallel, split frame transfer
Total number of pixels	69696
Pixel size	48 μm x 48 μm
Pixel in image area	248 x 256 pixels
Reference pixels	8 columns and 4 lines per CAMEX
Image area	11.9 x 12.2 mm^2
Quantum efficiency at 532nm	>98%
At [500nm,800nm]	>90%
Charge Transfer Efficiency	>0.99999
Full well capacitance	>50 000 e-
Dark current @-50°C, 100fps	0.196e-/pixel/s
"Hot" pixels	No hot pixels at 20fps
"Dark" pixels	No dark pixels at 900fps
Operating frame rate	10Hz-1000Hz

Table 3.4: Performance measured at MPE. Those are essentially the results of the photon-transfer curve technique. The "effective RON" is obtained from a fit to the PTC and include the contribution of the common-mode correction, see equation 3.6. The readout noise is obtained by using the PTC gains and a noise map derived from dark frames acquisition using all the pixel in one line to perform the common-mode correction, hence rendering the common-mode contribution negligible.

	"low" gain (Argos "standard")	"high" gain
Effective Read-out noise [e-]	3.89	3.50
Read-out Noise [e-]	3.72	3.26
Common-mode RMS [e-]	3.21	3.14
Mean variation along channels	<0.1	<0.1
Gain [ADU/e-]	2.16	8.33
Intrinsic gain variation	0.03 (1.5%)	0.14 (1.7%)
PtV gain variation	0.18 (8.5%)	0.79 (9.5%)
Amplifier Dynamic Range	$\sim$81dB	$\sim$ 69dB
Effective pixel Dyn. Range	$\sim$38dB	$\sim$27dB
Photon noise dominated range [e$^-$/ch.]	$\sim$ 2000 to 40000	$\sim$ 1500 to 8900

Finally, to be complete, we should mention that the readout noises (for "low" and "high" gains) we report are substantially higher than those reported by pnSensor, *i.e.* 2.5-3e$^-$. A number of reasons may explain this difference. First, as already mentioned our typical operation temperature is -25°C, where pnSensor operates at < -50°C. Second, the algorithms used for the noise computation differ. pnSensor uses a specific approach X-ray event oriented, as reported in Andritschke et al. (2008), where we use more standard techniques, e.g. sigma clipped average. We analyze this difference further in appendix B.2.3. We argue that this difference in the computation could amount up to 0.3e$^-$ in the reported readout noises. Finally, the readout timing may differ, such as different CDS operation and shaping times, resulting in different filtering performance, and lead to different noise properties.

3.4   Focus on the common-mode noise

As already mentioned multiple times, the pnCCD suffers from a correlated noise, the "common-mode" noise, critical for the good AO operations.

This noise is a fast offset variation (time variant), that results in a line-by-line variation. An illustration is given in Fig. 3.25. It affects the pnCCD in a correlated way. Being correlated, this noise has potentially a much stronger impact on the AO performance. Not only does it degrades the wavefront measurements – as a random noise does – but it can also inject frequency signals in the slope measurements, falsifying the reconstructed wavefront. Whence our dedicated effort to analyze it and decrease its effects. Its exact origin is not fully established, but from our test campaigns (see also section 3.4.4), the likely cause is electrical noise being injected by the DC power supplies and an improper grounding, especially between the CCD chip and the CAMEX units, leading to some differential coupling (rendering the noise subtraction problematic).

In the following sections, we examine this particular noise in a staged approach : we first
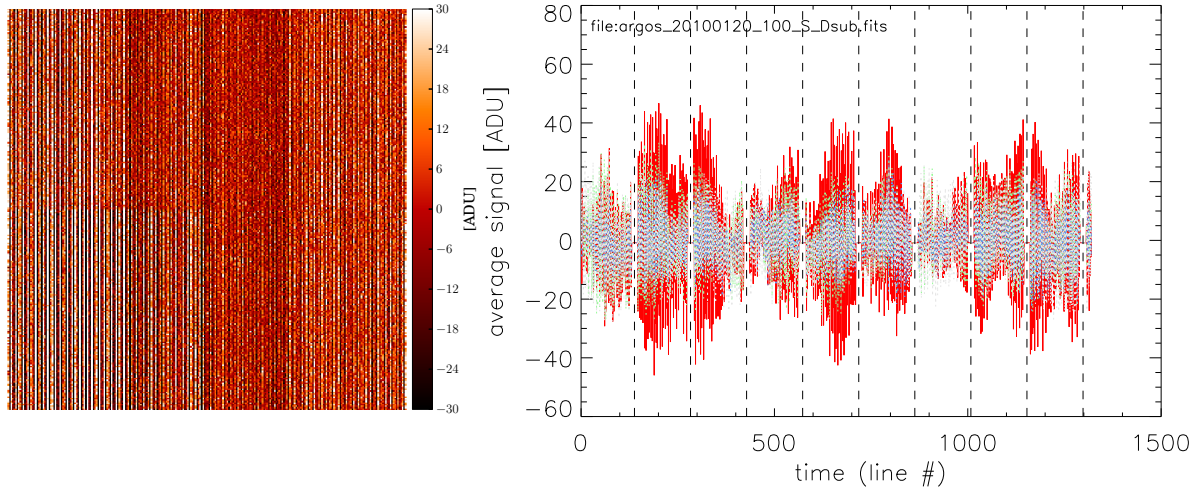
Figure 3.25: Illustration of the common-mode noise at the time of ARGOS FDR. (Left) PNCCD dark frame (N.B. the left halve of the CCD is read to the left, and vice versa, see Fig. 3.2). (Right) the average of each line per CAMEX (different colors) seemingly correlated to each other, the vertical dashed lines separate different frame. This illustrates the temporal aspect of the common-mode noise.

analyze in section 3.4.1 the frequencies in the signal and how it behaves for the different camera versions and correcting schemes. We then orient our analysis toward AO application by first studying the impact on the slope measurements in section 3.4.2, and then by performing closed-loop AO simulations, see section 3.4.3. We will then discuss the tests performed to try and understand the influence of the PNCCD power supplies on this noise, and finally the solutions found to minimize the common-mode noise impact (section 3.4.4). As shown in the following sections, our various efforts have lead to a large reduction in the common-mode RMS noise and to a negligible impact with respect to the expected AO performance.

3.4.1   Frequency analysis

As the common-mode is an offset time variant noise, Fourier techniques are the obvious choice for our analysis. As intuitively any frequency signal injected in the wavefront measurement may hamper strongly the AO performances, we aim to a background having a white noise spectrum of low intensity. The last criterion is to minimize the statistical noise introduced by our correction scheme, see equation 3.6.

We are interested both by the common-mode before and after correction. We consider the following cases when analysing the common-mode :

- Dark subtracted frame, also `Dsub`, designates dark or light frames that have been subtracted by a reference offset map. The latter is taken as the average of several hundreds of dark frames. Those will exhibit the raw common-mode noise.

- Common-mode corrected frame, also `8CMcorr`, for which we additionally use eight covered channels for correction. Typically the mean or the median of those covered pixels is

taken and subtracted over the full CAMEX line[25]. This is the default correction mode for Argos.

- Full common-mode correction where the average of all pixels in each line is used for the correction. This will represent the best correction.

While we always correct by a constant, we could in principle subtract by a polynom along the line, however, the few pixels on the side do not allow to robustly fit anything else than a constant. As a result, the common-mode should be as constant as possible to allow for a proper subtraction and no specific frequency peak residual.

It is clear from Fig. 3.25 that the frequency content is a mixture of various frequencies of different amplitudes, that we analyze further here.

Throughout the project, we have taken systematically the power spectrum of the various cases described above. We compute it as follows : we average each line of each CAMEX and we take the discrete Fourier transform of those vectors[26]. The Fourier variable is transformed in temporal frequency knowing the time delay between two pixels of a channel, *i.e.* $7.2\mu s - 7.6\mu s$ depending on the readout timing. Those spectra are taken for each frame of a data cube and then averaged[27]. This gives us low resolution ($\Delta f \sim 1kHz$), high signal-to-noise power spectra with the maximum frequency range we can probe by analysis of the detector images ($\sim 69kHz$).

In Fig. 3.26 and Fig. 3.27, we give a few selected measurements of the common-mode before and after our standard correction (using the covered pixels), including one typical frame, the related power spectrum and the pixel histograms, also illustrative of the residual additional noise compared to an expected Gaussian readout noise distribution. These selected measurements are based on four milestones of the pnCCD development that we designate by : *FDR*, the initial test camera (see Fig. 3.12), the *first LBT engineer camera* (see Fig. 3.12 middle), the *manual "PSU tower"*, the camera used with a full rack of high quality power supplies during our test campaign, and the Argos *PSU*, the final camera with its new PSU (see Fig. 3.12 right). Based on the presented figures, the following observations can be made :

FDR. While the uncorrected frame shows a pronounced frequency peak, the corrected frame shows little residuals with the exception of a small frequency peak. Quantitatively, the common-mode RMS level before correction is $\sim 6.5e^-/\sim 15$ ADU, and after correction $\sim 1.5e^-/\sim 3.3$ ADU. This was basically the status of the common-mode with the "test camera" which, although recognize as a possible issue, was not deemed critical.

1st LBT engineer. It reveals very problematic common-mode noise behavior[28]. Indeed, the common-mode RMS level before correction amounts to $\sim 15e^-/\sim 35$ ADU, and

---

[25]eight channels are covered but in practice only seven are used, the last one could be affected by PSF effect from adjacent pixels or only partial covering in the case of light frame.

[26]we use typically the Fast Fourier Transform provided by IDL, which implement the discrete Fourier transform

$$F_n = \frac{1}{N} \sum_{n=0}^{N-1} f_k \exp\left(-2\pi jnk/N\right),$$

which generates a symmetrical periodic function (the periods of the signal are split in their "positive" and "negative" complex components). A sinusoidal wave gives typically two frequency peaks, symmetric with respect to the middle, Nyquist, frequency. For clarity we only represent the first half part.

[27]an alternative would be to append the time vector of each frame in a long time series and take the Fourier transform of it. However the time lapse between two frames is not a multiple of the inter-pixel delay. The FFT of such long time series therefore creates unwanted aliasing.

[28] no satisfying explanation has been provided so far. Factors that may have played are : different integration
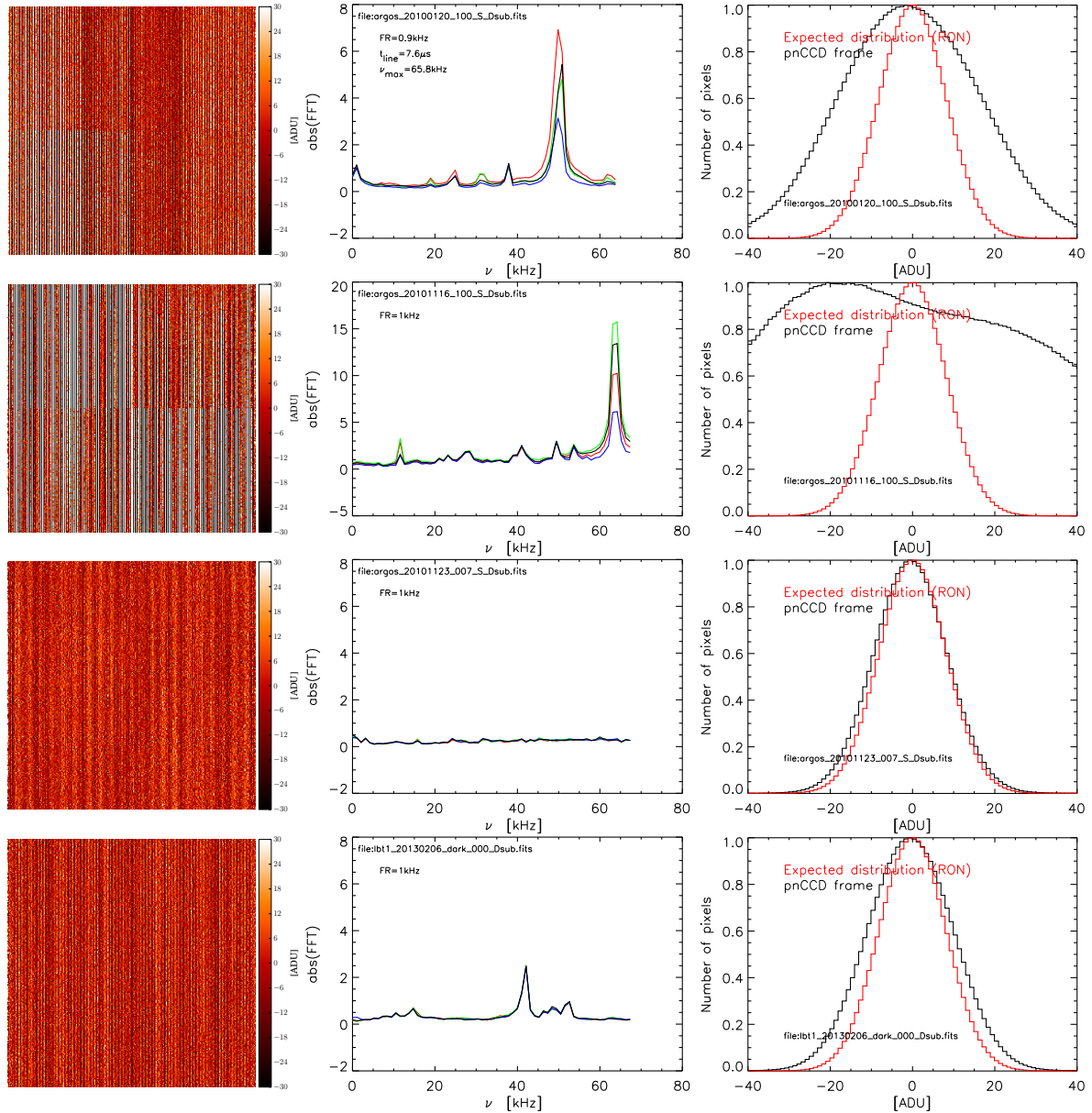
Figure 3.26: Selected key measurements of the common-mode noise characterization. Based on dark frames. From left to right: a) Dark frame offset map corrected without common-mode correction, the detector is read sidewise (left half to the left side, right half to the right side), b) Power spectrum for frames without common-mode correction, c) histogram comparing the uncorrected frame pixel histogram with an ideal Gaussian of $3.4e^-$ RON equivalent distribution (assuming a single $2.4ADU/e^-$ gain). From top to bottom, the different milestones measurements are : 1) FDR, 2) the 1st version of the LBT Engineer camera - note the difference of scales for the power spectra -, 3) using a manual (linear) PSU tower, considered as our "best"/smallest common-mode, 4) the ARGOS final common-mode characterization for the camera LBT#1.

---

in chip ceramic and backplane electronics, as well as different PNCCD manufacturing - with possible small modification of the chips themselves-, details of which are not known to us.
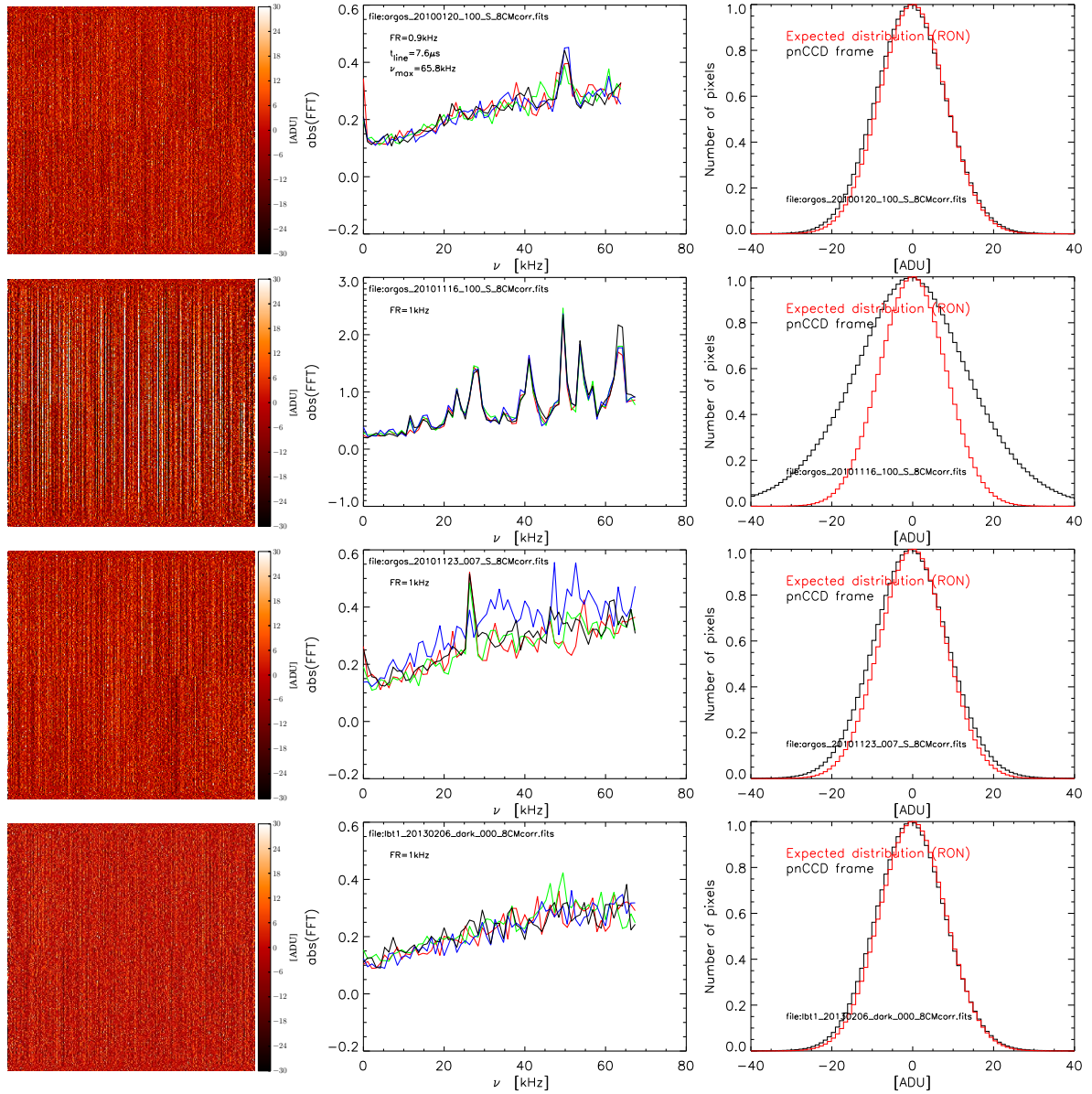
Figure 3.27: *con't.* Based on dark frames offset map corrected and with common-mode correction using the eight covered channels individually for each CAMEX. From top to bottom, the different milestones measurements are : 1) FDR, 2) the 1st version of the LBT Engineer camera - note the difference of scale for the power spectra -, 3) using a manual PSU tower, considered as our "best"/smallest common-mode, 4) the ARGOS final common-mode characterization for the camera LBT#1.

after correction to $\sim 5.5e^-/\sim 11.5$ ADU, with very pronounced frequency peaks in both case. It is clear that in this case, the common-mode is not constant over a CCD quadrant, processed by one CAMEX.

This result also highlights how critical the "common-mode" can be and lead to a dedicated effort to characterize its impact on ARGOS and to get it under control.

Manual PSU tower. While investigating the impact of the PSU on the common-mode, we have used a high quality power supply tower (see section 3.4.4). The common-mode performances obtained using those power supplies are much better than obtained previously, both before and after correction. Quantitatively, the common-mode RMS level before and after correction is $\sim 1.6 e^-/\sim 3.5$ ADU.

Argos PSU. The final camera – including filtering and new power supplies – displays much lower common-mode before correction and no distinct residual frequency peak. Quantitatively, the common-mode RMS level before correction is $\sim 3.1 e^-/\sim 6.5$ ADU, and after correction $\sim 1.4 e^-/\sim 3.15$ ADU.

The remaining common-mode RMS level of ~ 3.15 ADU is a consequence of the averaging using a small number of pixels, namely $\sigma_{cm;rms} = \sigma_{RON}/\sqrt{N_{px}} \sim 8.5/\sqrt{7} = 3.2$ ADU, in perfect agreement with the measured RMS level.

The summary presented above illustrates the evolution of the problem and our handling of it. Part of this process was also to identify the direct impact of this noise on ARGOS. In the next two sections we thus present the actual impact of the common-mode noise in the context of adaptive optics based on a Shack-Hartmann wavefront sensor : we first examine the impact on the centroiding by putting together an optical setup projecting a realistic SH pattern on the detector and measuring how accurate the spot positions can be measured. We then automatize the process by combining SH simulated spot patterns and detector backgrounds to study the improvement in centroiding accuracy. In a second stage, we perform GLAO closed-loop AO simulations incorporating measured CCD backgrounds. This procedure allows us to grasp fully the effects of the common-mode on the performances.

3.4.2   Centroiding accuracy

As discussed in section 3.1, the maximum measurement tilt error allowed is $\sim$53mas or ~ 0.1 pixel on the ARGOS pnCCD. In this section we analyze how the common-mode degrades this centroiding measurement, and this at various stages of the project. Our approach is here two folds. First, we built up a small SH optical test setup with the appropriate number of spots on the pupil diameter and of pixels per subaperture. We typically acquired sequences of images for different illumination and then evaluate the accuracy by taking the standard deviation of the spot position for a given illumination. Second, as the project evolved a more efficient way to perform this evaluation consists in simulating SH pattern and combining them with measured CCD images, and to reconstruct a sequence of images by including photon noise. The evaluation is then performed in a similar way.

A Shack-Hartmann optical setup.   Using this optical setup, we vary the light level and compute the average accuracy of the centroiding along the x coordinate (row, perpendicular to the readout direction), and y coordinate (column/channel, along the readout).

In Fig. 3.28, we show the results for the initial camera (*FDR* version). The following observations can be made :

- any vibration will obviously hamper the measurements. Indeed, the initial camera was requested to be pumped constantly, which introduced vibrations. This is one of the
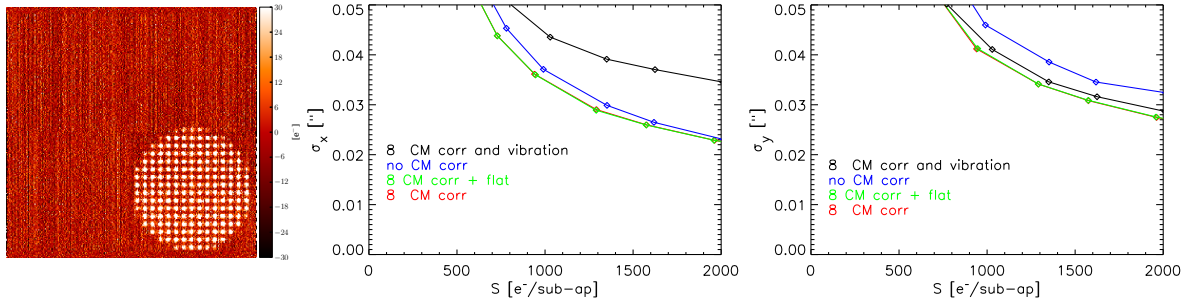
Figure 3.28: Centroiding accuracy measurement of SH spots from our optical setup (x axis is here in the horizontal direction, perpendicular to the readout axis; y is along the readout), (Left) Shack-Hartmann image created with our optical setup. (Middle) Centroiding accuracy as calculated from the x and (Right) y using a pixel scale of $0.56''$/pixel and a gain of 2.4 ADU/e$^-$. Four cases are considered : 1) reference common-mode subtracted (red), additionally flat fielded (green), not common-mode corrected (blue), and another set of measurements with vibrations (black).

main motivation for a vacuum tight housing. In this test, the chip being clamped horizontally, the vibration effect is perpendicular to the common-mode degradation.

- the common-mode introduces additional errors in the column/channel direction (y axis), as expected,

- after common-mode correction the y accuracy is not as good as the x accuracy. This can be attributed mainly to charge smearing in the y direction (the readout direction) and possible common-mode residuals.

 Indeed, in our setup, light is shining continuously on the detector. When the detector is column-parallel read-out, charges are detected at wrong location causing this smearing in the y direction.

 These tests teach us, first, that the common-mode indeed can degrade significantly the centroiding accuracy, second, vibrations should be absolutely avoided, third, the light exposure during readout can also degrade the measurement by smearing the charges and should be avoided.

Artificial Shack-Hartmann patterns. In a second step, and to monitor our progress in tackling the common-mode, we combine dark common-mode corrected PNCCD frames with three simulated SH patterns, see Fig. 3.29. This allow us to do a post analysis based on dark frame measurements only and to decouple the analysis from charge smearing caused by the non-gating of the light in our test setup. We perform several simulations by combining different backgrounds from :

- the 1st LBT engineer camera displaying strong common-mode residuals,

- the same camera with filtering of the reset voltage. This is also discussed in section 3.4.4,

- the final ARGOS PNCCD camera,
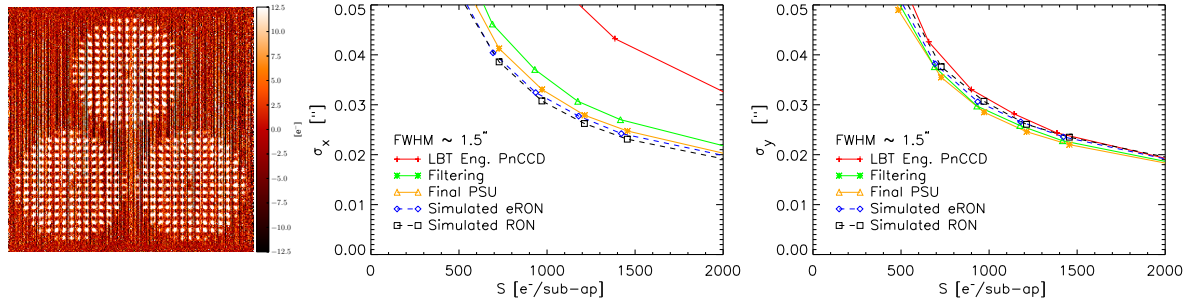
Figure 3.29: Combination of SH pattern simulations with PNCCD dark frames at different stages of the camera development. We compare here the average centroiding accuracy in function of illumination for different PNCCD backgrounds. We simulate the following cases : 1st LBT engineer camera, with reset voltage filtering, the final ARGOS PNCCD, a simulated $3.5e^-$ readout noise with (eRON) and without (eRON) common-mode correction. This comparison illustrates the improvements at each stage. (Left) illustration of a constructed frame with the first LBT engineering model background after common-mode correction displaying strong residuals. (Middle) centroiding accuracy along the readout direction. (Right) centroiding accuracy along the line direction. See text for further discussion.

- two simulated backgrounds with a $3.5e^-$ readout noise (RON), one of which is common-mode corrected to introduce the statistical error caused by the common-mode correction (eRON; see equation 3.6).

Based on those backgrounds, we create sets of cubes at different illuminations by scaling the SH pattern fluxes and introducing photon noise. We then compute the centroids and the centroiding accuracies. In Fig. 3.29, we plot the resulting average centroiding accuracy in function of the illumination.

We can observe a large improvement with, first, the filtering of the reset voltages and then with the final camera featuring the new PSU. This is particularly clear with the accuracy along the readout, for which the common-mode can have a maximal effect.

We see that with those two improvements we reach the same accuracy expected from full simulation. A small degradation in the readout direction is unavoidable due to the common-mode correction which is still necessary. This is also made clear with the *eRON* simulation.

Such analysis allows us to confront the PNCCD to an idealized chip of similar readout noise, and to study the impact of the common-mode in the degradation of the centroiding. However, in such analysis, the centroiding errors are computed with the usual standard deviation and do not translate the "non-Gaussian" errors, *i.e.* the common-mode noise is here treated as a Gaussian variation, and it gives an uncomplete description of the problem. More detailed effects can only be analyzed by performing closed-loop AO simulations.

3.4.3   Adaptive optics performance effects

In our continuous effort to understand the common-mode, we aim ultimately to understand its impact on the ARGOS AO performances. In this perspective, we perform closed-loop AO simulations that include the common-mode noise.

Table 3.5: Parameters of the GLAO simulation performed with the code YAO

Parameters	Value
Telescope	8.22m diameter with 0.9m central obscuration
Simulated	256 pixels along the pupil diameter
Number of iterations	1000 for a total of 1 seconds of simulation
Atmosphere	
Layer altitudes	[0,0.4,6,9] km
Layer fractions	[0.4,0.2,0.3,0.1]
Speed of layers	[11,20,29,35] km/h
Seeing θ	$[0.25,0.35,0.65,0.85]''$ at 2.2μm
r_0 at 500nm	$(\lambda/\theta)(500/\lambda)^{6/5} = [31, 22, 12, 9]$cm
LGS WFS	
Geometry	12km height, 300m depth
Beam	1 LGS, on axis, with $0.8''$ kernel, corrected for tip-tilt
SH specs	16 subap $0.56''$, 8 pixel wide
SH final	16 subap $0.534''$, 6 pixel wide, subap size $3.2''$
Centroiding	Noise depend on simulated background, threshold= 0
Flux per subapertures	[76, 114, 190, 380] e-
# of frames of PNCCD backgrounds	200 frames
PNCCD gain conversion	2.5 [ADU/e$^-$]
Frame delay	1ms

Based on the YAO simulation tool[29], we compare the ground-layer adaptive optics performances for different WFS detector backgrounds in various conditions of seeing and photon fluxes per sub-aperture.

To do so, we modify the YAO code in order to be able to introduce our own CCD background. To save computational power, we simulate only a single LGS at an altitude of 12km, and vary the WFS CCD background for different seeing and photon flux conditions. We have not optimized the wavefront computation and reconstruction but we adopt default typical settings. We list below the main simulation parameters, in Tab. 3.5.

The tip-tilt is virtually perfectly corrected, and the DM correction is based on the first 150 Karhunen-Loève modes. In summary, we intend to measure the evolution of the impact of centroiding error on the AO loop. In addition to the measurement errors, these simulations include a cone error, a modal fitting error and a temporal error. The cone error is the main contributor and is similar to the unsampled turbulence error in the case of a multiple LGS GLAO, see section 2.2.

The following CCD backgrounds are considered:

1. no photon and readout noise,

2. photon noise and 4e$^-$ RON,

---

[29]A Monte-Carlo AO simulation tool based on the YORICK language. See also http://frigaut.github.com/yao.

3. "First LBT Engineer" PNCCD camera background, uncorrected for common-mode. It displays the strongest correlated noise under consideration here.

4. ARGOS PNCCD uncorrected background. The final current camera version without common-mode correction.

5. "First LBT Engineer" PNCCD camera version background, with common-mode correction. We use the covered channels for the common-mode corrections.

6. "FDR" PNCCD camera background, with common-mode correction.

7. ARGOS PNCCD background corrected for common-mode. The final current camera version with the typical correction.

The simulations are analyzed based on the 50% encircled energy diameter (E50d) used as a proxy of the PSF FWHM. This approach proved to be more reliable than a correct PSF estimation and this due to the time limit of our simulation of only one second. We compare the gain in PSF size for four different flux ranges and four seeing conditions. The ranges in flux given are the PtV of the subapertures fluxes, and the seeing conditions are directly evaluated from the E50d by running open-loop simulations (instead of using our input seeing, see Tab. 3.5). The gain in FWHM is represented in Fig. 3.30.

It is worth noting first that the nominal case, *i.e.* RON=4e$^-$ at high flux, gives performances very similar to other ARGOS simulations presented in Fig. 2.1. Hence this validates the simulations done here and the different error contributions involved.

The simulation setup validated, we can examine our results and make the following observations :

- the simulation featuring no noise gives always the same performances as expected (no detection limit),

- in the realistic cases, the AO correction degrades towards lower fluxes, mostly when getting closer to the detection limit imposed by the noise (essentially the read-out noise),

- good seeing are more impacted by poor correction (poor centroiding) where the noise of the system becomes more quickly comparable to the atmospheric noise, *i.e.* the centroiding measurement contribution is higher in the total error budget,

- uncorrected common-mode completely jeopardizes the correction as it is essentially doing worst than no correction,

- corrected common-mode from frames *before* our common-mode campaign have a strong impact, although the PSF is still improved at high fluxes,

- the final PNCCD background (following our common-mode improvement in term of filtering and power supplies) behaves in the same way as a simulated RON=4e$^-$ ideal detector.

While already illustrative of the degradation introduced by the common-mode, it does not give us any information on the PSF shape and possible deformation by the common-mode. Hence, we can directly examine the simulated long-exposure (1 second) PSF, in particular in the low flux regime and for different seeing conditions. In Fig. 3.31, we represent three cases with PSF cuts along the x and y axis.
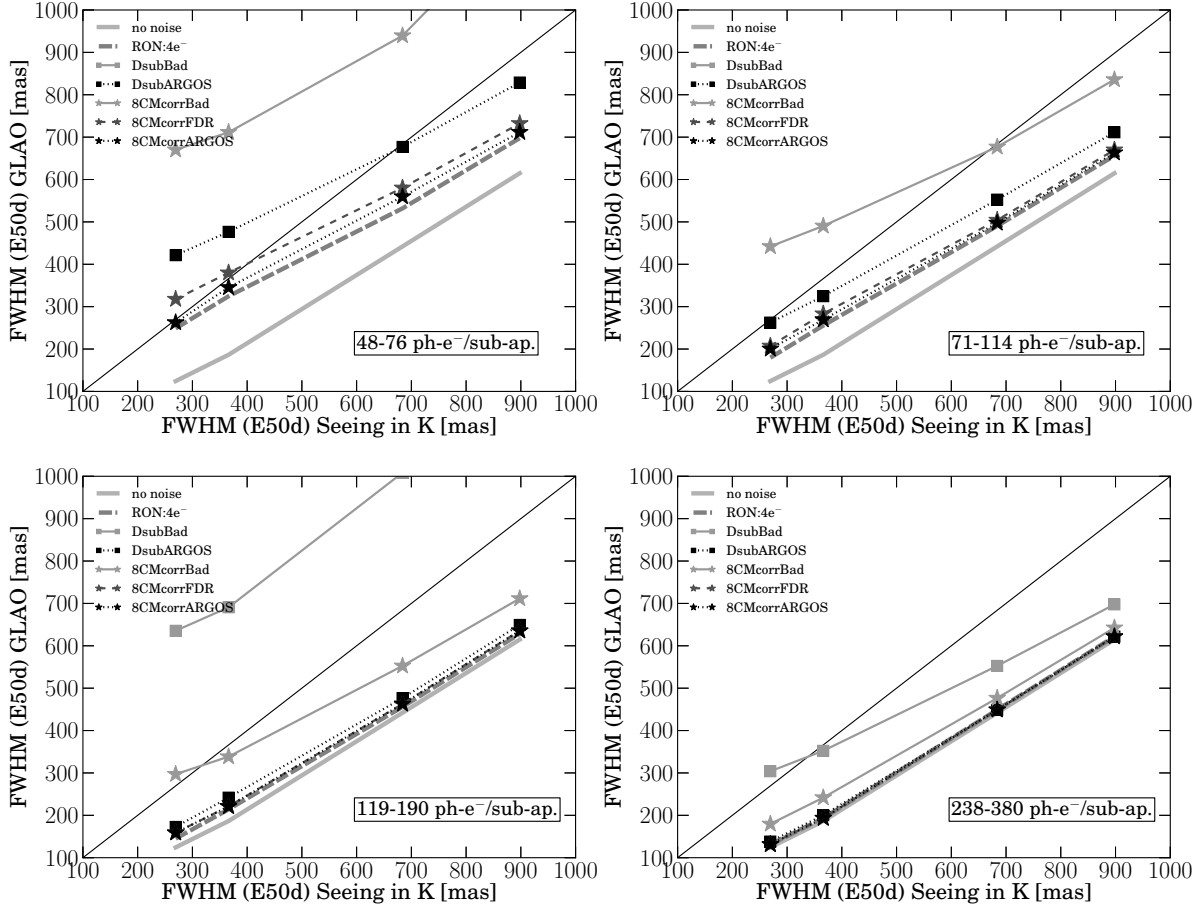
Figure 3.30: Comparison of GLAO FWHM versus seeing-limited FWHM for different detector backgrounds in different flux conditions (as given in the frame of each plots). Considering the short simulation time, we use in fact the 50% encircled energy diameter as a proxy for the FWHM. Apart from to reference ideal cases ('no noise' and '4e$^-$') which are similar to the ARGOS predicted performances Fig. 2.1, we compare dark only corrected cases for the "1st LBT engineer" camera (`DsubBad`) and for the "ARGOS" final version (`DsubARGOS`). Finally, we compare dark corrected and common-mode subtracted backgrounds for the same two camera versions (`8CMBad` and `8CMArgos`) plus the background at the time of FDR (`8CMcorrFDR`). The comparison is done for different flux and seeing regimes. We see that up to the lowest flux regime, the ARGOS results are very similar to an idealized 4e$^-$ RON detector. See also the text for further discussion.
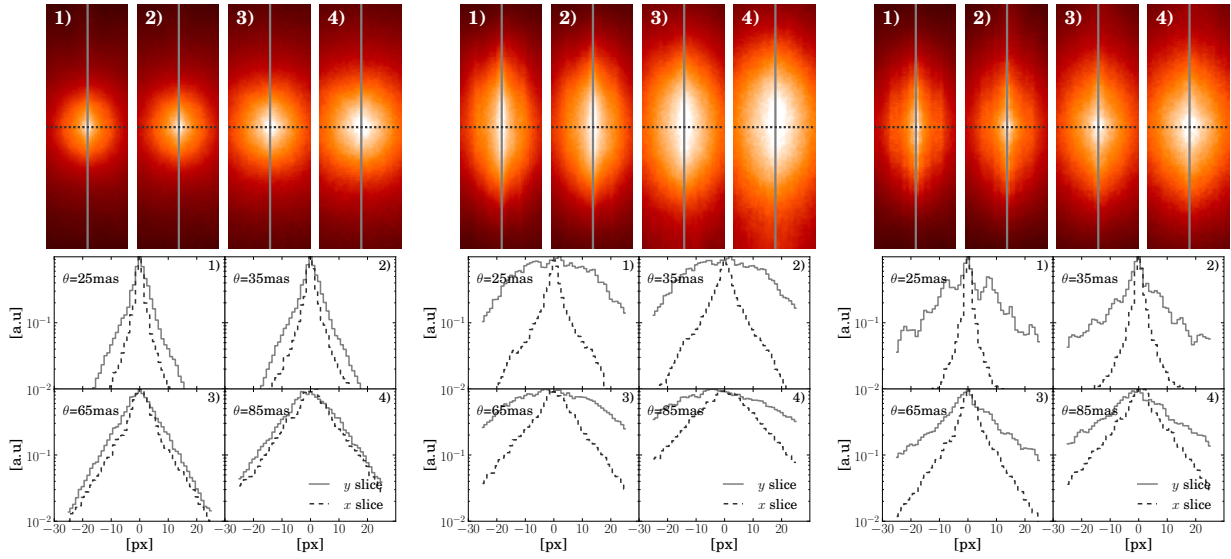
Figure 3.31: Example of PSF after GLAO correction for seeing of $\theta = [25, 35, 65, 85]$mas in the lowest flux regime [48-76]ph-e$^-$/sub-ap., for different backgrounds. (Left) the ARGOS background common-mode corrected (8CMcorrARGOS). (Middle) with the "1st LBT engineer" common-mode corrected (8CMcorrBad) in the lowest flux regime. (Right) PNCCD background with strong and well defined common-mode frequency (not considered for the FWHM gain analysis), in the large flux bin of [238-380] ph-e$^-$/sub-ap.. The frequency in PNCCD background translates in replica of the PSF peak along the y axis.

From this analysis, it is clear that the common-mode affects the AO operation in its specific direction (here y axis). It tends to enlarge the PSF along the y axis perpendicular to the readout direction and along the common-mode variation. It is also clear that the "1st LBT Engineer" camera would have strongly degraded the PSF even after common-mode subtraction.

In this analysis, we also see that the centroiding accuracy becomes relevant for photons fluxes < 150 per subaperture. We should note here that the subaperture size used in the simulation was 6×6 pixel wide instead of the ARGOS 8×8 size. This difference has an impact at low flux. In fact a smaller subaperture is more likely to behave well at low flux, as the total SNR is higher than for larger subarpertures (due to smaller RON and background contributions). Hence the centroiding accuracy for ARGOS cannot be expected to perform in an optimum way at photon flux around 150 per subaperture per frame.

Finally, for simplicity, we do not simulate 3 LGS but only one. As the common-mode variation is in phase between the four quadrants (see e.g. Fig. 3.25), it would affect similarly the three SH patterns. The conclusions should therefore be unchanged and this simplification is not expected to have any impact on our analyses.

3.4.4   Tackling the common-mode issue

We attempt to summarize here the lessons learned from the various test campaigns undertaken, *i.e.* which PNCCD voltages appear to be sensitive, which tentative explanations to the

origin of the common-mode can be reached, and how the problem is resolved for Argos. We emphasize however that a rigorous understanding of the common-mode is beyond the scope of this work, and can only be undertaken by HLL/pnSensor in the knowledge of the pnCCD and CAMEX designs.

Most of the tests have been performed on the "1st LBT engineer" camera. The first step in these campaigns has been to demonstrate the effect of external power supplies on the common-mode. This has been allowed by using a full rack of manual linear power supplies (assembled by pnSensor), implying manual operation and the complicated overhead to power the camera. The first assessment has been the possibility of an almost common-mode noise free, and certainly of a uniform correction with no particular frequency residuals. The power supply "tower" provided our reference measurement. It has been used in combination with the initial power supplies provided by pnSensor, and with the newly developed PSU. These combinations have allowed to pin-out sensitive voltages, and to support the new PSU development. The test campaigns combining this PSU "tower" with other PSU totalize >20 days of dedicated measurements with the camera, performed alone, in collaboration with pnSensor, and with the MPE electronics workshop[30]. In addition to the PSU tests, *RC* filters were also tested at strategic voltages.

We distinguish two types of problems, having different consequences and possibly different causes:

1. the amplitude of frequency peaks in the Fourier transform taken from the uncorrected frame,

2. the presence or not – and if yes the amplitude – of residuals after common-mode correction[31].

The second point is the most critical one as we cannot allowed any specific frequency components to remain in the corrected background as illustrated in the previous sections. The amplitude in the uncorrected frame is less critical, but should be minimized in order to not increase the effective read-out noise; in addition possible remaining residuals are likely to be smaller if the original amplitude is lower.

From the large amount of data, the multiple aspects of the problem and the various test conditions, it is not straightforward to extract and summarize useful information. To do so, we condense our results in Tab. 3.6 with qualitative appreciation of the impact of the voltages/tests on the common-mode (more information on the voltage significations can be found in Tab. B.1). The conclusions that one can draw are that

- in term of amplitude of the common-mode, most of it is generated at the CAMEX level,

- the on-chip amplifier and current source do play a role here but minor in term of amplitude contribution,

- pnCCD specific voltages do not seem to play any relevant role[32],

---

[30]This do not totalize previous effort of characterizing the common-mode, the time to perform the analysis, neither the development time required by the MPE electronics workshop, or the work of integration of the new PSU to a fully operational usage with the pnCCD.

[31]using our standard procedure, *i.e.* subtracting the median of 7 covered pixels

[32]although some frequency peaks can propagate but at a low level and with no residual after correction.

- there is a differential (or column-varying), likely capacitive, coupling between the on-chip amplifier plus current source and the CAMEX unit when the CCD is on. This is likely to be the cause of the non-uniformity of the common-mode.

Table 3.6: Qualitative representation of the major learnings from our test campaigns:
✓: major peak present, additional '*' express the strength;
×: no specific frequency peak,
∼×: very low contribution/different peak than the main one observed during those tests
We refer to Tab. B.1 for the description of the individual voltage role.

Tests description/voltage influences	1. main peak in uncorrected frms	2. residual in corrected frms
CCD powered with ISEG	**✓	*✓
CAMEX powered only [33]	**✓	×
CCD powered with R&S	∼×	×
reset (RFGA) without C-filter	✓	✓
reset (RFGA) with C-filter	✓	∼×
FFDR	✓	×
VBST	∼×	×
RSTA	∼×	×
VSS/VDD	*✓	✓
VSST/VDDT	**✓	*✓
VCC	✓	×
RSTA, GRA, phi's, RK,	(∼)×	×

Two elements of explanation could be:

- the power supplies by their own design "inject" electrical noise in the supplied DC voltages,

- the improper grounding leads this noise to be picked up by the on-chip amplifier and the CAMEX chip[34]. A "ground-loop"[35] could form and a current could flow between the different on-chip amplifiers along the CCD boarder. This would create a varying perturbation along a line rendering the correction problematic.

The ARGOS solutions are:

- the filtering of the reset amplitude and offset voltages, as proposed by PNSENSOR. This is done by introducing two capacities just before the reset pulse generation[36].

- the development of new power supplies with particular care on on-chip amplifier voltages and CAMEX voltages,

---

[33]it does not include the current source VSSS.

[34] a possibility could be when the CDS integrator is connected to ground to allow the signal charge packet to be transferred to the CCD anode; improper ground would not properly isolate the previously measured pixel value serving as the baseline for the incoming pixel.

[35] "a ground-loop forms when two interconnecting parts of an electronic system are separately connected to ground via small – but – different – impedance paths." (McLean, 2008).

[36] The filter ($C = 100\mu F$, $R = 0.024\Omega$) is low-pass filter rejecting well frequencies at around 60kHz, the main frequency peak in our common-mode.

- the additional possibility to filter the CAMEX voltages.

The first two solutions have proven sufficient for the ARGOS camera at MPE and INAF laboratories. As already mentioned, a more details and rigorous analysis can only be tackled by HLL/PNSENSOR, and is beyond the scope of this manuscript.

In summary, our various efforts have lead to a reduction of a factor $\sim$10 in the common-mode RMS and to a negligible impact with respect to the expected AO performance.

3.5 A short comparison

Before concluding we attempt a short comparison of the ARGOS PNCCD camera with two current state-of-the art alternatives : the OCAM2, an AO development based on an EMCCD, and the "steadily-improving" sCMOS technology. We describe shortly these two alternatives. We then attempt to compare these solutions by reporting their key characteristics in Tab. B.3 and by performing a simple SNR comparison. Information on those technologies are essentially gathered from manufacturer websites.

OCAM2, featuring an EMCCD

EMCCD are normal CCD with additional multiplication registers. Those registers lie typically between the storage area and the on-chip amplifier that performs the conversion from charge to voltage, and feature much higher than normal clock voltages. As the charges are tranferred, impact ionization can produce secondary electrons. Repeating the process over 100-1000 stages (or clocks), the signal can be amplified by a gain typically up to 1000, before any introduction of readout noise (at the on-chip amplifier). Therefore, EMCCD are virtually readout noise free and particularly well suited for low light level applications. The probabilistic nature of the electron multiplying process comes with an increased shot noise, typically (as measured and theorized) by a factor $f = \sqrt{2}$. High amplification gains will also limit the dynamic range limited by the amplifiers.

The OCAM2 is a recent AO camera featuring a CCD220, and has benefited of dedicated controller design. This control electronics – including ADCs – and the chip are embedded in a new compact housing (e.g. Feautrier et al., 2011). It is the new leading AO camera, and will for example be used by SPHERE, the planet imager, and likely by ERIS, the foreseen successor of SINFONI. At the time of writing, an improved version has been released reaching >2kHz frame rate.

Scientific CMOS camera

CMOS, complementary metal oxide semiconductor, differs from CCD in that each pixel possesses its own on-chip amplifier converting the pixel charge to a voltage. CMOS detectors are usually recognized to have less uniformity[37] but as well to have very high pixel bandwidth due to the readout parallelization, and since more recently, low read noise. The architecture of CMOS detector also usually provides amplifiers and ADCs on the chip.

---

[37]in term of gain and noise. This lower uniformity is due to unique on-chip amplifier for each pixel.

CMOS technology is wide spreaded in circuitry design and is used in a wide range of application. This thus make CMOS detector also relatively cheap.

Due to their high multiplexing capabilities, there are also investigated as a potential technology for the future large AO detectors for ELTs (Downing et al., 2008, 2010).

Comparison

We present in Tab. B.3 the characteristics of the ARGOS PNCCD camera, the OCAM2 and a sCMOS camera from the company PCO.EDGE.

As discussed in section 3.1, there are a number of ways to compare AO camera. One of them is the signal-to-noise ratio than can be reached. A simplified estimation of it can be written by

$$SNR = \frac{QE \ N_{ph}}{\sqrt{QE \ N_{ph} \ f^2 + n_{px}(\sigma_r^2 + N_d \ f^2)}}, \tag{3.10}$$

with QE in %, N_{ph} the number of photons per sub-aperture, f the excess noise factor which is the parametrization of a statistical variation in gain in the case of electron multiplication, n_{px} the number of pixels in the subaperture, σ_r the readout-noise, N_d the average dark counts in e$^-$ also subject to the multiplication process.

In Fig. 3.32, we plot three SNR curves in function of the number of photons for our three cameras under consideration in Tab. B.3. We represent in the shaded area the typical flux regime (with some margin) expected for ARGOS. We see that the ARGOS PNCCD is superior to the sCMOS due to its higher QE and similar RON, and stays competitive to the OCAM2 which at high flux loose its multiplication benefit that artificially reduce the QE by a factor f. This is however only a conceptual comparison, in particular we do not take the EMCCD dynamic range into account.

Finally, ARGOS requires a large number of pixels per subaperture due to its GLAO concept. A larger number of pixels per subaperture also means an increased noise. Hence by design, ARGOS requires a large amount of photons per subaperture. Within that frame the PNCCD appears to be a competitive solution and to be well suited.
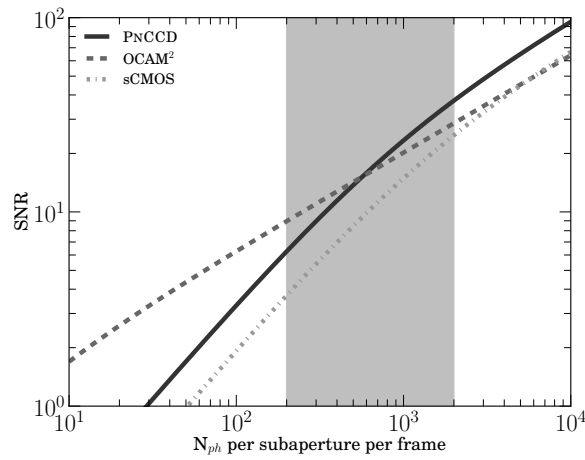
Figure 3.32: Signal-to-noise comparison, based on equation 3.10 and the values reported in Tab. B.3, for a subaperture containing 64 pixels. We ignore here the dynamic range limitation of the different detectors. The shaded area correspond to approximately the photon flux expected for ARGOS from 200 to 2000 photons per subaperture per frame. The parameters of the curves are $[QE, f, RON, n_{px}, N_d]_{\text{pnCCD}} = [0.98, 1, 3.5, 64, 0.0002]$, $[QE, f, RON, n_{px}, N_d]_{\text{OCAM2}} = [0.82, \sqrt{2}, 0.3, 64, 0.01]$, and $[QE, f, RON, n_{px}, N_d]_{\text{sCMOS}} = [0.5, 1, 2.4, 64, 4]$. The OCAM2 is the best below $\sim$500photons/subaperture where its multiplication gain comes to a great advantage. Above the PNCCD performs better due to its higher QE and no excess noise factor. The PNCCD is better than the sCMOS by a factor > 1.5 in the photon flux range of interest.

3.6   Conclusions

In this chapter we have presented the development, testing, characterization and optimization of the ARGOS pnCCD wavefront sensor detector. In that framework, I have played a major role in bringing the early "X-ray" camera into a state-of-the-art AO camera, covering all aspects of its foreseen operations. In that context, a large emphasis has been given to the study of the common-mode impact and its resolution.

This correlated noise is now considered to have a negligible impact on the ARGOS operation. The overall pnCCD camera presents excellent performances with 1) its 1kHz frame rate and $3.5e^-$ RON, 2) its compact, stable, and low-maintenance housing, and 3) its well integrated system and standalone software constantly monitoring the camera.

The GLAO design of ARGOS requires large subapertures, and thus a large photon flux in order to keep the centroiding measurement error at a low level. In this flux range, the pnCCD is fully competitive with the OCAM2 the new leader in term of low-flux fast AO camera and superior to current sCMOS technologies.

The three cameras have been entirely completed and validated. Two of them have been successfully integrated to their respective wavefront sensor system, and are now in intensive use for the WFS testing, development, and validation before being brought to LBT.

As the key elements of the wavefront sensing, the pnCCD camera successfull integration is closely related to the ARGOS wavefront sensing computer subject of the next chapter.

WAVEFRONT SENSING COMPUTATION OF ARGOS:
THE SLOPE BASIC COMPUTATIONAL UNIT

ARGOS implements a Shack-Hartmann sensor that measures the wavefronts from three Rayleigh laser guide stars. Its principles are simple and intuitive: the primary mirror is re-imaged onto a dense array of micro-lenses. At the focus of the lenslet array a CCD detects an image array of the guide star. This is illustrated in Fig. 1.6. The displacement of a sub-image being proportional to the local wavefront gradient, the basic equation of a Shack-Hartmann for one subaperture is

$$\vec{\delta} = m f_l \vec{\nabla} z,$$

where $\vec{\delta}$ is the displacement of the guide star sub-image, $m = f_{telescope}/f_{collimator}$ is the demagnification of the optical system, f_l is the lenslet focal length, and $z(x, y)$ is the aberration we aim to measure. The aberration expressed as a phase is $\phi = kz$, with $k = 2\pi/\lambda$.

The wavefront reconstruction convert the local wavefront gradient measurements in either aberration discrete measurements or modal coefficients (resp. *zonal* or *modal* approach), and corresponds to the inversion of this problem.

In this chapter we discuss the wavefront sensor computer that processes the PNCCD images and returns the local wavefront gradients. We do not explicitly discuss the wavefront reconstructor here, which was designed and put into operation before the advent of ARGOS (see Xompero et al., 2008, for a description of the performed tasks).

We first describe in section 4.1 the design requirements we have derived in terms of computational needs, necessary interfaces, and requested operations. In section 4.2, we present the hardware chosen to fullfill our requirements and its key features as designed and assembled by MICROGATE. From the newly developed ARGOS wavefront computer, we describe in section 4.3 the various steps performed to bring it to the level of a functional device, including its configuration, its interface and computation validations. In section 4.4 and section 4.5, we discuss the performance of the system in terms of measurement accuracy and temporal behavior, of interest in our AO context. Finally, in section 4.6, we present an optical test bench realised to demonstrate the operability and to incorporate three key components of the wavefront sensor system : the PNCCD wavefront sensor, the BCU wavefront computer, and the optical gating.

In the framework of this thesis, I first derive the design requirements. I then setup the BCU so that it can interface properly, test it and ensure it performs according to the

specifications, and develop in that context the necessary configuration tools. Finally, I analyze its performances and validate it in an integrated test bench.

4.1   Argos slope computation requirements

Argos aims at measuring and correcting for the ground layer in order to provide a wide field partial correction. This definition drives the system design as detailed in Chap.2. The general requirements translated to the wavefront sensor computer can be described as follows :

- In nominal conditions, it must compute the x and y local wavefront gradients for three SH pupils, each containing 176 subapertures, hence 1056 displacements.

- It should do so at 1kHz based on pnCCD images of 264×264 pixels. This includes a custom data protocol and data calibration.

- Minimum time delays in term of latency and jitter should be ensured (see our further discussion in section 4.5).

- As the nerve center of the Argos wavefront sensing, it must provide the interfaces to the other wavefront measurements, in particular the NGS tip-tilt mandatory for the AO operation, and the measurements of a third WFS (from the natural guide star wavefront sensing unit or from a future possible Sodium laser guide star wavefront sensor). In addition it shall compute the LGS tip-tilt signals, to be corrected by piezo mirrors in the WFS optics.

- Finally, the computer must transmit the wavefront measurements to the LBT real time reconstructor and deformable mirror controller (equivalently designated by LBT RTC or RTR).

In the two next sections, we further detail the hardware interfaces and requested operations.

4.1.1   Hardware interfaces

The Argos computer should centralize all Argos related wavefront measurements. Hence part of the unit complexity is due to its several interfaces.

We show in Fig. 4.1 the necessary foreseen interfaces in schematic form, and the data flow directions. The Argos computer is here labeled by "LGS BCU". The "inputs" to the computer are :

- The pnCCD frames either as digital signals sent by the data acquisition boards of the detector system through two fiber channels or as analog signals digitized internally (see section 3.2.2 for a discussion). This interface is by far the most demanding by its data rate – ~ 140MByte/sec – and by its spread over time. Indeed the data flow spread of the readout time is only marginally shorter than the framerate. Note that the diagram illustrates only the initial interfaces using two optical fibers. The second option consists of 8 analog cables providing the pixel measurements directly from the pnCCD backplane electronics.

- The NGS tip-tilt slopes and APD counts provided by the Bonn tip-tilt unit (*i.e.* the NGS tip-tilt computer, see also Elberich & Connot 2012).
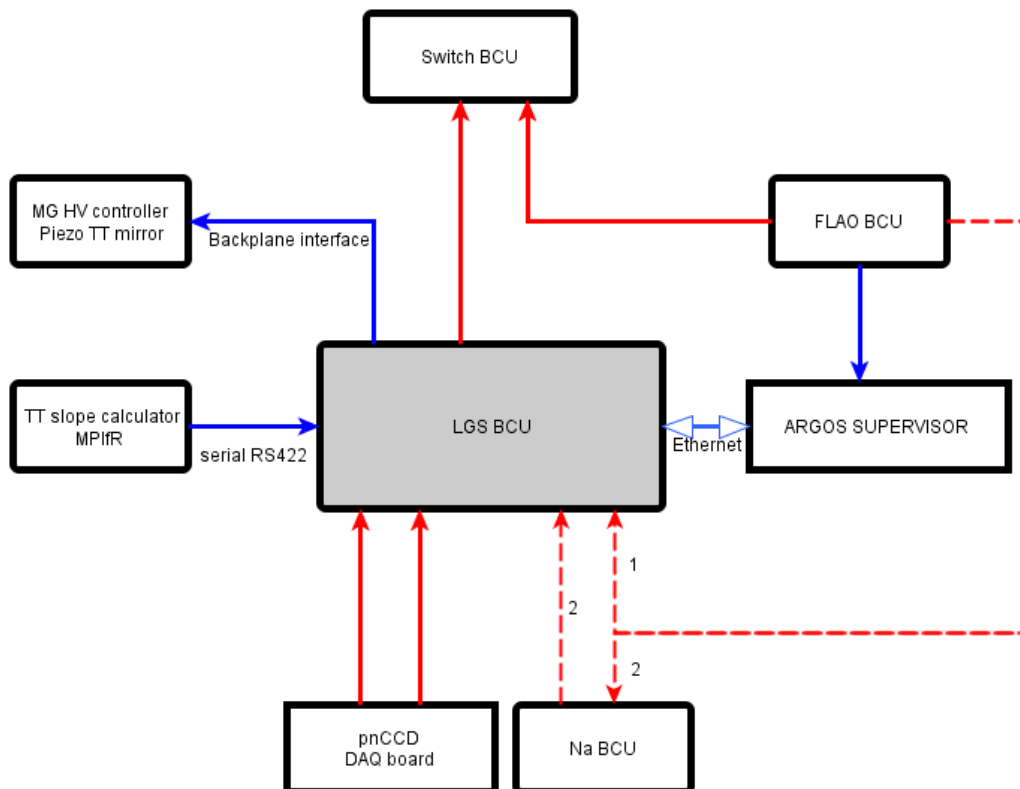
Figure 4.1: Sketch of the ARGOS WFS computer interfaces (LGS BCU). The red lines designate fast optical links. The dashed red lines represent two variants. The nominal possibility (1) featuring an interface with the FLAO BCU, *i.e.* the pyramid NGS WFS. The second possibility (2) is foreseen for the "upgrade path", featuring a Sodium laser guide star, in which case the FLAO is pipelined through the Na BCU. We refer to the text for further details on the interfaces.

- The third WFS measurements either from the NGS pyramid WFS (so-called "FLAO BCU") or from a Sodium LGS (a possible upgrade of Argos).

From its internal computation, the Argos computer should provide :

- The total slope vector sent to the LBT RTC for computation of new modal coefficients and control commands of the deformable mirror. This is designated in Fig. 4.1 by "switch BCU", the unit selecting the WFS input to the LBT RTC.

- Three individual LGS tip-tilt measurements for field pointing of the LGS onto the pnCCD chip.

Diagnostics download and control of the device are done through a standard Ethernet interface, and designated here by the "Argos Supervisor".

4.1.2   Requested operations

At reception of the pnCCD pixels, the wavefront computer has to perform a sequence of tasks before delivering the local wavefront gradients, *i.e.* the slopes, to the wavefront reconstructor.

Those tasks are the consequence of the pnCCD characteristics, and of a set of requested operations. They are originally described in Orban de Xivry (2010).

We review here the main operations and, when necessary, justify their implementation. First, a pnCCD image needs to be reduced:

1. Subtraction of the offset map. The offset map is measured beforehand from a set of dark frames and is uploaded to the computer before operations.

2. As discussed in Chap.3, we need to correct for a line to line, time and CAMEX dependent offset variation, *i.e.* the common-mode noise. For this purpose, pixels outside the Shack-Hartmann pupils can be used, averaged line-wise and used for subtraction line-by-line.

3. We require also an optional gain correction. With its parallel readout, the pnCCD displays small variation in the amplification gain from channel to channel, as discussed in Chap.3. This variation can affect the slope measurements in a systematic way. We compare in Fig. 4.2 the x and y spot position measurements for gain corrected and uncorrected images in function of the sub-aperture flux. Although small, the channel-to-channel x direction shows a systematic difference. As the gain variation can vary from one chip to another, we have allowed for such possible correction.

Once the data have been calibrated, the centroids are calculated following a center of gravity algorithm, the slopes are then calculated by subtraction of the reference positions (acquired during calibration of the WFS). We propose a general formulation of the center of gravity, *i.e.* for each subaperture a,
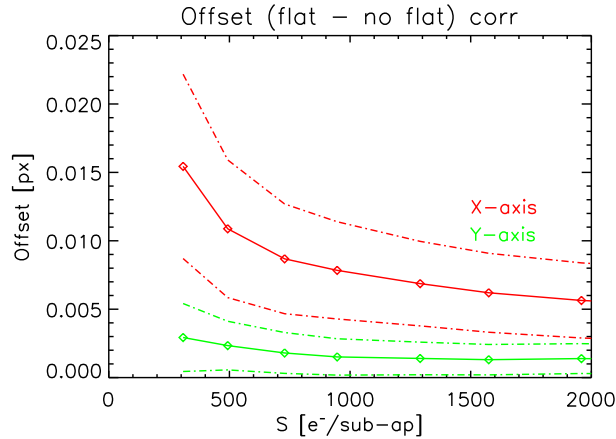
Figure 4.2: Comparison of x and y spot positions between gain corrected and uncorrected PNCCD frame. The x coordinate corresponds to the direction of the channel gain variation. We can observe a small systematic difference between gain corrected and uncorrected (red curve). The dashed-dot curves represent the 1σ dispersion between all the sub-apertures of one SH pupil. We have used here a SH optical test setup, see also section 3.4.2. This systematic difference is due to the chip channel-to-channel gain variation.

$$x_a = \gamma K^{-1} \sum_{i;I_{i,a}>I_{a;T}}^{N} x_i W_{i,a} (I_{i,a} - I_{a;T})^n$$

$$y_a = \gamma K^{-1} \sum_{i;I_{i,a}>I_{a;T}}^{N} y_i W_{i,a} (I_{i,a} - I_{a;T})^n \tag{4.1}$$

with K defined as :

$$K = \sum_{i}^{N} W_{i,a} (I_{i,a} - I_{a;T})^n$$

where the index i designates pixels and a subapertures. $I_{i,a}$ is the flux for the pixel i of the subaperture a, and x_i and y_i are the coordinates of the pixel i, identical for each subaperture. $W_{i,a}$ is a predefined weighting function sub-aperture dependent. In conjunction with the weighting function, a coefficient γ can be used to ensure linear response between estimated and real position. The factor n is either 1 or 1.5. The latter case is equivalent to weighting by the signal-to-noise assuming a photon noise dominated regime. The threshold $I_{a;T}$ is either a constant value per sub-aperture, or determined dynamically $I_{a;T} = \alpha I_{a;max}$, with $I_{a;max}$ the maximum pixel flux of the subaperture of the current frame.

We describe the possibilities of this general formulation in section 4.4.

At this point, the LGS slopes have been calculated and are ready to be sent to the wavefront reconstructor.
The remaining task concerns essentially the handling of the interfaces with other devices :

1. The average LGS tip and tilt slopes are calculated to correct for field pointing error. This is an independent closed-loop that leads to the control of three piezo-mirrors in

each WFS, and aims to remove the tip-tilt from the LGS slopes. The LGS tip-tilt is not used for the wavefront correction.

2. The reception of the NGS tip-tilt from a serial interface, and of the measurement of a third WFS from an optical interface.

After those last operations, a final slope vector is created and sent to the wavefront reconstructor. Diagnostics are also available for download to the "Argos supervisor".

4.2   Hardware choice and description

The wavefront computer design is based on the Basic Computational Unit architecture proposed by the company Microgate. This choice has been driven by 1) the expected easy integration to a similar hardware used for the adaptive secondary at LBT, including its reconstructor computer, 2) the proved reliability of the unit, 3) the deterministic nature of a DSP-based computer. The later point is further discussed in section 4.5.

Based on this architecture and our requirements, Microgate has designed a custom LGS BCU for Argos. Its design is documented in the Argos BCU minicrate system design document (Andrighettoni & Biasi, 2011). This integrated Argos BCU mini-crate is shown in Fig. 4.3.

Figure 4.3: Picture of the Argos BCU featuring from top to bottom, the BCU board providing the interfaces and controlling the data flow, the DSP board performing most of the computation and including the BCU built-in ADCs (fed by the eight analog input channels), and the two high voltage controller boards controlling the three LGS tip-tilt mirrors in the WFS system. Also connected are the ethernet cable for configuration and diagnostics download, and the sequencer cable to clock the BCU built-in ADCs.

The main elements of the system and the data flux, also presented in Fig. 4.1, are :

- The "BCU" board which is the arbitrator of the entire real time system and provides all the interfaces shown in Fig. 4.1.

- One Microgate 2nd generation DSP board, named DSP-16do used to satisfy the high computational performances requested by Argos, driven by the large pnCCD frame and leading to data rate of $\sim$140MBytes/sec.

- Two high-voltage controller boards used to drive the three piezo tip-tilt mirrors for the field pointing of the three Shack-Hartmann. Each board has 6 strain gauge inputs and 6 high voltage outputs, so the first board drives two mirrors and the second the third mirror, three inputs and three outputs are not used.

- The ARGOS supervisor is connected to the BCU mini-crate using a standard 1Gbit Ethernet link, this link is used for system initialization, including firmware download, parameter configuration, and computation enabling. In operation, the same link is used to acquire and monitor the diagnostic data, e.g. PNCCD frames and calculated slopes.

- The APD counts and the tip-tilt slopes acquired and computed by the Bonn unit are sent to the BCU using a serial link. This link is asynchronous, which means that the serial data are stored in a local buffer and then passed to the BCU-DSP to be included to the slope vector.

- The optional third WFS is connected to the BCU mini-crate using the third fiber link. If a new set of slopes arrives at the ARGOS system it is copied to the BCU-DSP memory with a dedicated mechanism. The new data set is then included in the slope vector and passed to the deformable mirror together with the next PNCCD slope vector.

- The PNCCD interface is a dedicated module directly linked to the PNCCD optical ADCs. The received frame is copied to the DSP-16do board and the slope computation is executed, the computation is done in parallel to the pixel download in order to minimize the slope computational time lag.

- The alternative PNCCD interface (after upgrade of the BCU) connects the 8 analog signal cables directly to the DSP board which now contains 4 ADC units to digitize the PNCCD signal. After digitisation, the data are directly transferred to the computing part of the board without passing through the BCU board.

- Once the computation is completed, the BCU-DSP reads back the new slope vector and collects the new asynchronous data (NGS tip-tilt and third WFS measurements). The entire vector is prepared according to the deformable mirror switch BCU standard input and sent to the switch BCU using the fourth fiber link to start a deformable mirror command update mechanism.

- After completion of the deformable mirror command update, the system creates and saves the diagnostic records. The data is stored in the BCU SDRAM bulk memory and, if enabled, downloaded to the ARGOS supervisor using an automatic and efficient mechanism. The PNCCD pixel frames are stored in the DSP-16do SDRAM bulk memory. The diagnostics mechanism allows two modes: a "burst" and a "decimated"[1] real-time diagnostic savings. The "burst" mode allows one to save ~ 1000 continuous PNCCD frames at 1kHz, downloadable off-line by the user. The "real-time" mode allows one to download the PNCCD frames at $\sim 25 - 50$Hz while in full operation. The main limitation is actually more the Ethernet interface rather than the internal BCU mechanism. The other diagnostics, including slopes, can be downloaded in real time at 1kHz.

---

[1]in the so-called "decimated" mode, a fixed number of diagnostics (given by the decimation factor) are disregarded before one is saved, leading to a smaller bandwidth and allowing a "real time" continuous saving mechanism.

From this newly developed ARGOS wavefront computer, we describe in the next section the operations and tests performed to bring it to a fully functional level.

4.3   Hardware interfaces and slope computation implementation validation

All the DSP devices of the ARGOS BCU mini-crate at the start-up and after a reset are in idle condition. The first step of the system initialization is the DSP firmware upload, then the control variable initializations and finally the start of the code.

The low-level configuration software has been developed by ARGOS colleagues at Heidelberg. Based on those tools, we have developed in the framework of this thesis several configuration scripts following the memory mapping of the BCU (Andrighettoni & Biasi, 2011). We have tested and debugged the hardware interfaces, verified and debugged the various computational steps. This debugging has been done in collaboration with MICROGATE.

The developed configuration tools consist of creating the correct vectors and matrices according to the DSP memory pointers. They include for example, the subaperture definitions, the common-mode pixel definitions, the weighting function in the centroiding calculations, and several other mapping and parameter initializations.

We describe in the following sections the work done on hardware interfaces and slope computation validation, including the tools developed in that framework.

4.3.1   Hardware interfaces: pnCCD and NGS tip-tilt

The pnCCD interface

As discusses CHAP.3, two configurations are envisaged :

- Two fiber channels linking the two optical ADCs to the BCU board. Internally, this is a dedicated module that copy the frames to the DSP16-do board using the internal 32 bits bus. The computation by the DSP16-do is done in parallel to the pixel download.

- Eight analog cables linking the backplane PNCCD electronics directly to the DSP16-do board which includes the integrated ADCs (*i.e.* the so-called BCU built-in ADCs). In this case, the data are directly copied to the DSP unit by an integrated bus, *i.e.* the data do not use the 32 bits bus between the BCU and the DSP boards. This means less traffic between the two boards of the BCU minicrate.

Those two configurations involved different internal mechanisms and have required dedicated debugging.

The optical dedicated module has been initially developed with the help of a framegenerator. This cPCI board was intended to simulate the data protocol and data flux of the PNCCD and to ease the optical module development. It has been provided to us by PNSENSOR and was developed by STRÜCK INNOVATIVE. Obtaining a functional interface has however proved more difficult. First, for protocol reasons[2], the ADCs and BCU boards were initially not

---

[2]the optical ADCs using a different synchronizing mechanisms than the framegenerator.

communicating with each other. Second, the real data flux is spread over almost the entire ∼1ms as the PNCCD frame is being read, in contrast to the framegenerator. This proved to be challenging in term of traffic handling, especially at the 32 bits bus level. This was debugged in collaboration with MICROGATE.

The second, later, configuration was more easily made functional. Indeed, protocol and data flux were fully integrated into the DSP-16do board and developed by MICROGATE. The challenges were here in terms of ADC capabilities and differences with the optical ADCs, see CHAP.3 for discussion.

NGS tip-tilt

The link to the NGS unit is a serial link with its own communication protocol defined in Elberich & Connot (2012). At reception, the data are stored in a buffer and passed to the BCU-DSP to be appended to the slope vector. When no new data is available, null slopes are written to the final slope vector. If the LGS slope computation is not triggered, the tip-tilt data are ignored.

The tip-tilt unit has been preliminary integrated and tested in conjunction with the framegenerator. In Fig. 4.4, we illustrate the result of one test. The figure shows the difference in framecount between the "PNCCD" and the NGS tip-tilt data for a total duration of 50 seconds. A constant difference means that the two are in phase. The regular steps reveal a slight difference Δt between the framegenerator and the NGS framerate[3]. Finally, the plot shows a few positive glitches (one or two counts), suggesting that the "PNCCD" framecount is incremented while the NGS tip-tilt count not. This can happen if a NGS tip-tilt data packet error is detected by the BCU validity check, and is not passed to the BCU-DSP.

The regular steps are the direct consequence of an asynchronous link. The glitches are seldom and expected to have a negligible impact on the AO performances. While this is a preliminary validation of the interface, more tests with the final BCU firmware and the PNCCD interfaces will have to be performed.

Remaining interfaces

The high voltage controller interfaces to the piezo mirrors are tested at INAF. The two remaining fiber channel links should be tested at the LBT.

4.3.2   Data reduction and slope computation validation

Another important aspect of the BCU validation is the verification of the computation sequence. In that respect, the BCU offers a debugging mechanism allowing one to check the slope computation and the data flux.

Our approach is as follows. We develop Python classes for 1) the configuration of the subapertures and various remapping allowing to shift the entire SH pupils, 2) the weighting function $W_{i,a}$, see equation 4.1, allowing the windowing and deletion of subapertures, 3) the common-mode pixel definition.

Using those configuration tools together with the software framework (provided by our ARGOS

---

[3]*i.e.* $N_{cst}\Delta t = 1$ms, with N_{cst} the number of records between two steps, here 662. Hence if we take the framegenerator as the 1kHz reference, the NGS framerate is ~ 1001.5kHz.
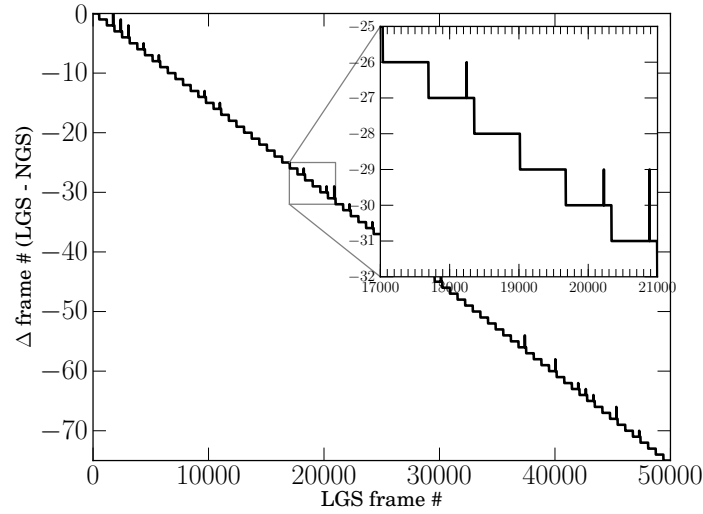
Figure 4.4: Difference of the frame numbers between the PNCCD frame (here simulated by the framegenerator) and the NGS tip-tilt frame for 50 seconds. Regular steps are ~ 660 counts appart, and glitches of 1 to 2 counts can be seen. See text for discussion.

software colleagues), we configure appropriately the BCU, upload a known frame to the DSP memory, and finally trigger the computation. We then retrieve the slope diagnostics. In parallel, we develop another Python code that implements the same slope computation and uses the same configuration, *i.e.* the same Python objects, as used by the BCU configuration. Finally, we compare the slope calculation performed by our code with the one retrieved from the BCU diagnostics. A test is validated if the differences of the slopes is null everywhere.

The test is repeated for different data calibration and slope computation configurations to cover at best the user cases.

This allows us to debug the configuration, in particular the appropriate various necessary remapping, and to identify a few computational errors. More realistic tests have also been performed, as presented in the next paragraph and in section 4.6.

Further validation by wavefront reconstruction

As a demonstration of the configuration and calculation validity, we perform the following experiment. First, we simulate ARGOS Shack-Hartmann measurements of several Karhunen-Loève modes[4]. Second, after appropriate configuration, we upload those frames to the BCU memory and trigger the slope computation. We then retrieve the slopes through the diagnostics mechanism. Finally, we use those slopes to compute the wavefront by iterative integration and verify that we obtain the correct injected modal basis. A sketch of our procedure and its results is given in Fig. 4.5. Our wavefront reconstruction algorithm is presented here below.

The wavefront is obtained by iterative integration of the slopes, it does not require any calibration and is intended only for qualitative representation. This algorithm can also be used for online wavefront visualization as the computation is minimal and requires only a few

---

[4]we use here the modal basis generated by the simulation tools YAO (see also section 3.4.3) to create its interaction matrix.

K-L SH simulation   ARGOS BCU x and y computed slopes   Derived K-L modes

upload & BCU configuration   Diagnostics download   iterative WF reconstruction
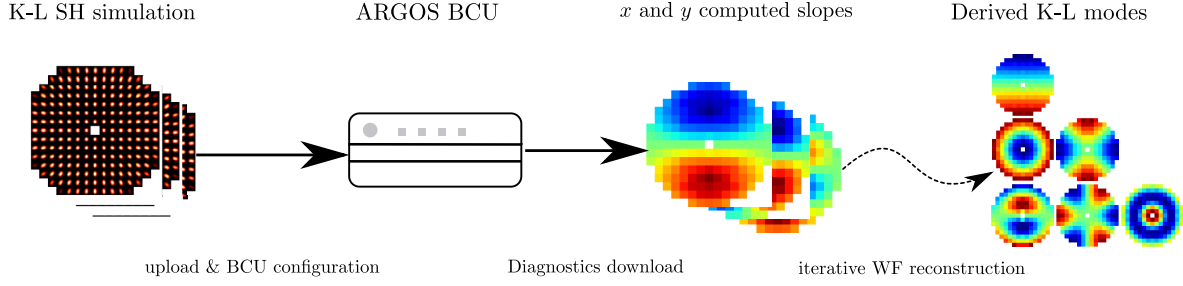
Figure 4.5: Sketch of the configurability and computation demonstration of the BCU. A set of appropriately simulated Karhunen-Loève (K-L) modes is first uploaded to the BCU, the BCU is then configured and the computation triggered. From the downloaded diagnostics, we retrieve the slopes and compute the wavefront by a simple iterative algorithm, as presented in the text. As expected we recover correctly the simulated modes.

tens of iterations.

The algorithm is as follows. Considering that the slopes are simply the derivative of the local wavefront, we want to minimize the reconstruction error $e_{i,j}$ between the calculated wavefront derivatives w' and the measured slopes s and t. Using a centered derivative, *i.e.* $y' = \frac{y_1 - y_{-1}}{h}$, the reconstruction error for each local measurement i, j can be written as

$$e_{i,j} = \frac{1}{4} \left[((w_{i+1,j} - w_{i-1,j}) - s_{i,j})^2 + ((w_{i,j+1} - w_{i,j-1}) - t_{i,j})^2 \right], \tag{4.2}$$

with $s_{i,j}, t_{i,j}$ are the x, y gradient measurements, $w_{i,j}$ is the wavefront we want to reconstruct. The total error is $\epsilon = \sum_{i,j} e_{i,j}$. For a minimum error, we want $\dfrac{\partial \epsilon}{\partial w_{i,j}} = 0$. By developing the derivative and performing an iterative computation, one obtains the following algorithm,

$$\begin{cases} w_{i,j}^0 & = 0 \\ w_{i,j}^{n+1} & = \dfrac{1}{N} \left[m_{i+2,j}(w_{i+2,j}^n - 2s_{i+1,j}) + m_{i-2,j}(w_{i-2,j}^n + 2p_{i-1,j}) \right. \\ & \quad \left. + m_{i,j+2}(w_{i,j+2}^n - 2t_{i,j+2}) + m_{i,j-2}(w_{i,j-2}^n + 2t_{i,j-2}) \right] \\ \text{with} \\ N & = m_{i+2,j} + m_{i-2,j} + m_{i,j+2} + m_{i,j-2} \end{cases} \tag{4.3}$$

where $m_{i,j}$ is a "pixel" mask, equal to 1 if the local gradient i, j is part of the pupil, 0 if not. Empirically, we find that the algorithm typically converges after 10 to 50 iterations. Considering the small map we are interested in, *i.e.* $3 \times 15 \times 15$ elements, the overall computation is fast and allows online viewing at a minimum of a few Hz.

Fig. 4.5 represents this qualitive tests and its results, where the Karhunen-Loève simulated modes are correctly reconstructed on the far right using our iterative algorithm described above. This, together with a direct quantitative verification of the slope computation (see the beginning of this section), validate first the accurate computation of the slope, and the good re-organization and ordering of the slopes as attested by our valid reconstruction.
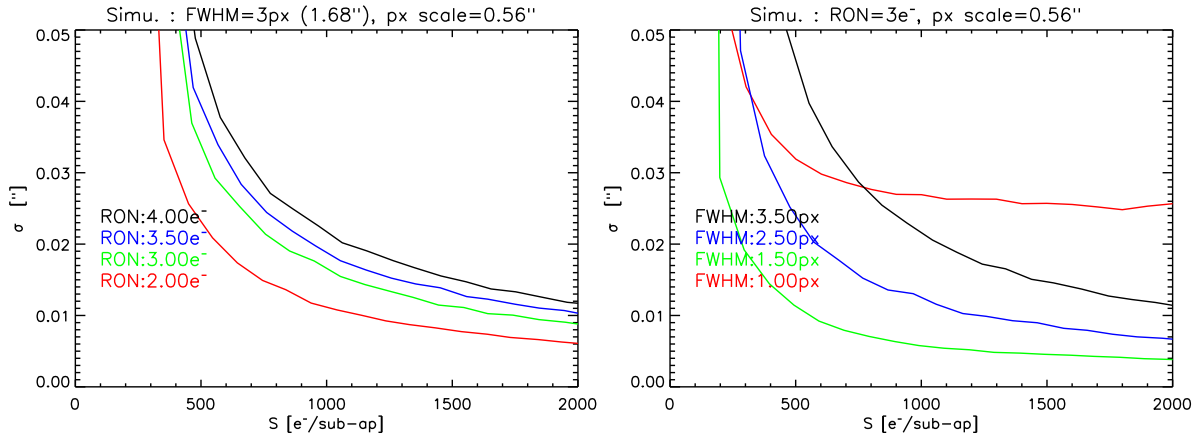
Figure 4.6: Detector readout noise (left) and finite spot sampling (right) effects on the centroiding accuracy in function of the flux per subapertures. We observe that the accuracy smoothly degrades as the RON increases. As the sampling decreases, it reaches an optimum and then quickly degrades (for a FWHM between 1.5 pixel and 1.0 pixel). The initial improvement is the decreased effect of the RON as the spot gets more concentrated. The fast degradation translates the undersampling. As demonstrated by Winick (1986), the optimum sampling correspond to a spot FWHM equals to 1-2 pixels.

4.4   Centroid algorithms

A Shack-Hartmann wavefront sensor samples the wavefront producing an array of spots on a detector. The local wavefront gradients are given by the spot displacements. Hence a good estimation of the wavefront distortion requires good measurements of the spot positions.

The methods of measurement use classically a center of gravity approach for its efficiency and low need of computation time. The causes of errors in the centroiding measurements are multiple, such as photon noise and readout noise, but also CCD sampling and finite FoV leading to non-linear response. If the wavefront is also coarsely sampled, *i.e.* $d/r_0 \geq 1$ with d the subaperture size and r_0 the Fried parameter, the spots are not diffraction limited and atmospheric effects perturb the measurements. This is usually referred to as speckle noise.

We illustrate the detector readout noise and the finite sampling effects on the centroiding accuracy as a function of the subaperture flux in Fig. 4.6. To do so, we simulate a Gaussian spot with readout and photon noise in a 8×8 pixels subaperture. We typically generate 100 spots with random spot positions uniformly distributed between ±0.5 pixel from the center of the subaperture. The accuracy is computed as the standard deviation of the estimated positions from the reference positions, using the ARGOS pixel scale of 0.56″.

As observed in Fig. 4.6, the coarse sampling of FWHM∼1px strongly increases the error. Winick (1986) has shown that in most flux conditions the optimum sampling corresponds to a spot FWHM of 1-2 pixels. In fact oversampling does not *per se* increase the sampling error but does increase the effect of detector noise and thus the final centroid error (Thomas et al., 2006).

The selection criteria of the best centroiding algorithm are typically based on the detection limits, the flux range with optimal behavior, and the linearity. Although in closed-loop operation, the spots are usually well centered, in practice the spot position can be offset to

compensate for non-common path aberrations. In addition, ARGOS is a GLAO system that in normal conditions will not operate at diffraction limit and the spots are expected to wander around their reference positions (see also equation 1.15). Finally, spot elongation will also contribute to non-linear effects.

The detection limit is on the other hand less of a concern for ARGOS. Indeed, the expected photon flux return is high, and we expect typically >700 photons/subaperture/frame. Nevertheless, an improved sensitivity could extend the operational range of ARGOS.

We have proposed a general algorithm, see equation 4.1, that condenses several algorithms proposed in the literature (see in particular Thomas et al., 2006, Kasper, 2000). We discuss here three algorithms that are possible with our general formulation and the benefits of each for future optimization with ARGOS.

Threshold Center of Gravity (TCoG)

To overcome the loss of precision at low flux when the size of the subaperture increases, one commonly uses a thresholding method. Depending on the threshold level, it can also improve the linearity. There are several methods to determine a threshold. We consider two possibilities, a fixed threshold typically of order of a few σ_{RON}, and a dynamic threshold where the maximum value $I_{\max}$ is first determined and the threshold is then set to $I_T = \alpha I_{\max}$. The implications of this dynamic threshold are described by Lardière et al. (2009) who show that most of the errors induced by the LGS spot elongation are cancelled out without altering the centroid accuracy in the presence of noise. The theshold is subtracted from the spot image and only non-negative values are used for the centroid computation, *i.e.*

$$\hat{x}_{\text{TCoG}} = \frac{\sum_{I>I_T} x(I - I_T)}{\sum_{I>I_T} (I - I_T)}. \tag{4.4}$$

As mentioned by Thomas et al. (2006), it is important to subtract the threshold before the calculation in order for the estimator to be linear.

Compared to the simple CoG, the form proposed here improves the linearity, *i.e.* it mitigates the spot elongation and truncation effects, and can improve the noise behavior if the threshold is properly optimized, *i.e.* the parameter α should be optimized as a function of the number of photons to minimize the readout noise contribution as the photon count decreases[5].

It is important to note that the spot has to be detected. Indeed if the light level is too low (e.g. $I_{\max} < I_T$), the centroid measurements become unreliable.

Weighted Center of Gravity (WCoG)

As proposed by Nicolle et al. (2004) and Thomas et al. (2006), the weighted centroiding method is a further improvement.

---

[5] Rousset (1999) shows for a Gaussian spot that the RON contribution to the phase variance is

$$\sigma_{\phi,N_r}^2 = \frac{\pi^2}{3} \frac{N_r^2}{N_{\text{ph}}^2} \frac{N_s^4}{N_{\text{samp}}^2},$$

where N_r is the readout noise, N_s the total number of pixels used for the centroiding calculation, N_{ph} the total spot photon flux, and N_{samp} the number of sampling pixels under the FWHM of the spot. If appropriately chosen, the threshold can minimize the readout noise contribution by decreasing N_s.

This algorithm consists in weighting the pixels of the spot image by a fixed[6] function W. This can be use for windowing purpose (if the spot size and motion allow it), *i.e.* to reduce the effective aperture size and thus the readout noise contribution. The weighting function can also be set, e.g., to a Gaussian centered at the reference spot position. The WCoG implemented here is computed as

$$\hat{x}_{\mathrm{WCoG}} = \gamma \frac{\sum_{I>I_T} x W (I - I_T)}{\sum_{I>I_T} W (I - I_T)}, \tag{4.5}$$

where the coefficient γ is needed to ensure the linear response between estimated centroid and real position. Thomas et al. (2006) derive an analytical value in the case of a Gaussian spot and a Gaussian weight,

$$\gamma = \frac{N_T^2 + N_w^2}{N_w^2},$$

where N_T, N_w are respectively the FWHM of the spot and of the weighting function in pixels. For Nyquist sampling, Thomas et al. (2006) also find an optimal width of the Gaussian weighting function $N_{w,\mathrm{opt}} \simeq 4.5$ pixels in the photon noise only case. The gain brought by the WCoG can be large over the simple CoG, but it requires to adapt the Gaussian weight function width N_w depending on the flux per subaperture and its spot size (e.g. Fusco et al., 2004, Thomas et al., 2006).

Weighted Weighted Average Pixels (WWAP)

A variant of the WCoG was proposed by Kasper et al. (1999), Kasper (2000). The motivation for this algorithm is to weight each pixel by its signal-to-noise ratio, proportional to the square-root of its intensity in the photon limited case,

$$\hat{x}_{\mathrm{WWAP}} = \frac{\sum_{I>I_T} x (I - I_T)^{1.5}}{\sum_{I>I_T} (I - I_T)^{1.5}}. \tag{4.6}$$

Kasper et al. (1999), Kasper (2000) show that this algorithm is superior to the threshold algorithm at all flux levels. Being a "following weight", *i.e.* the weight is not fixed as for the WCoG, it does not require the additional coefficient γ.

We have discussed here the parameters driving the performances of the local wavefront gradient measurements. While the phase variance error for ARGOS will be in principle driven by unsampled turbulence, providing a general algorithm that allows operation under various conditions renders the system more robust. We have presented here different algorithms that can be considered in practice and we have detailed a few guidelines and caveats for their usage. While these algorithms have been shown to significantly improve the accuracy of the measurements, a detailed study including the ARGOS expected spot profile, motion and elongation, the atmospheric effects, and truncation aspects would be required to optimize the centroid measurements specifically for ARGOS.

---

[6]a variant is a "following" weight where the function is centered on the current spot position (e.g. on the pixel with maximum flux).

4.5 Temporal Considerations

Apart from centroiding errors, the wavefront computer participates to the temporal error budget. As discussed in CHAP.1, the temporal error translate into the inability to respond instantly to a wavefront distortion. This error is caused by a finite correction bandwidth driven primarily by the wavefront measurement frame rate, and caused by the time delay between the wavefront sampling and its correction. Time delays come in two forms, pure time delays or "latencies", and random delays or "jitter".

Temporal errors are not expected to drive the total ARGOS AO budget, which is limited by spatial sampling. However, low latencies and deterministic computation help to make the system robust. Those considerations, although secondary, have also driven the choice to a DSP-based wavefront computer, the ARGOS BCU.

We will first gain some insights into latency and jitter effects on the closed-loop bandwith and its stability. We present then the actual data flow related to the ARGOS BCU showing how this leads to its good performance.

A Toy Model

Control theory provides the obvious framework to understand closed-loop systems and their temporal behavior.

We use a general formulation of an AO system as presented by Demerlé et al. (1994). The model is represented in Fig. 4.7 and considers the following elements: a wavefront sensor, a wavefront computer, a controller and a deformable mirror. The system being described by its several transfer functions (where $s = j\omega$ is the Laplace variable), respectively $WFS(s)$, $WFC(s)$, $C(s)$ and $DM(s)$ which we develop following the approach of Demerlé et al. (1994).
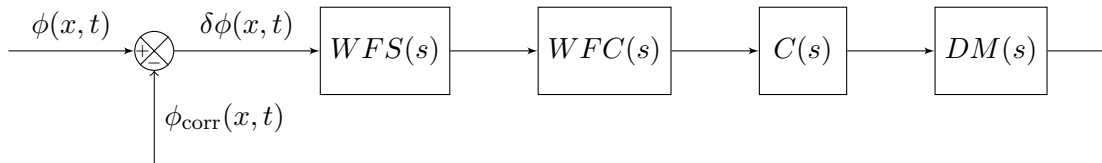
Figure 4.7: Block diagram of an adaptive optics system. With ϕ the input aberration, $\delta\phi$ the residual, $WFS(s)$, $WFC(s)$, $C(s)$, $DM(s)$, the wavefront sensor, the wavefront computer, the controller and the deformable mirror transfer functions.

The wavefront sensor temporal behavior is characterized by its integration time t_i during which the wavefront is averaged. This leads to an integrator subtracted by its delayed version[7], hence the transfer function

$$WFS(s) = \frac{1 - e^{-t_i s}}{t_i s}.$$

The wavefront computer is itself simply modelled by a time delay τ_c. This delay is needed to readout the CCD and to perform the slope computation. Thus the transfer function

$$WFC(s) = e^{-\tau_c s}.$$

---

[7]we recall here that the Laplace transform of a time lag is $e^{-t_i s}$ and of an integral is $1/s$.

The controller converts the wavefront measurements into deformable mirror commands, and implements the optimization of the AO closed-loop response. A classical[8] temporal compensator is a simple integrator of gain K to which an additional computational delay τ_r is added, hence the transfer function

$$C(s) = \frac{K}{s} e^{-\tau_r s}.$$

In an optimized and parallelized system τ_r is small compared to τ_c and can be neglected. We shall discuss it within the ARGOS computation architecture.

The deformable mirror behavior includes here the holding control voltages, the high voltage converter used to drive the actuators, and the deformable mirror response. To a first order, they can also be described by a pure delay τ_d, *i.e.*

$$DM(s) = e^{-\tau_d s}.$$

From the above considerations, we obtain the closed-loop transfer function

$$H(s) = \frac{K(1 - e^{-t_i s})e^{-\tau s}}{t_i s^2 + K(1 - e^{-t_i s})e^{-\tau s}}, \tag{4.7}$$

where $\tau = \tau_c + \tau_r + \tau_d$ represents the total delay not due to the wavefront integration. The gain parameter K should then be chosen to maximize the bandwidth and ensure the stability of the loop.

Based on this description of the AO system, we can comprehend the impact of latency and jitter in terms of closed-loop bandwidth and stability. ARGOS typical integration time is $t_i = 1$ms. The total delay τ can be parametrized by $\tau = \tau_0 + \tau_1$ where τ_0 is the fixed delay introduced by the PNCCD readout $\lesssim 1$ms, and the controller computation, the data transmission delays and the deformable mirror settling time. Hence we assume a conservative delay $\tau_0 = 2$ms. The delay τ_1 is then the additional delay introduced by the wavefront computer, *i.e.* the BCU, of interest here.

Latency. We consider computational delays of $\tau_1 = [0, 200, 500, 1000]\mu s$ with $t_i = 1$ms, and $\tau_1 = 0$ with $t_i = 2$ms. For each of those delays, we adjust the gain in order to have a maximum peak of ~ 1dB, ensuring similar loop stability whatever the delay[9]. The Bode diagrams of the closed-loop transfer functions, equation 4.7, are shown in Fig. 4.8 (left). Reading out from the closed-loop Bode diagrams the bandwith at -3dB, we can compare the obtained bandwith for different delays τ_1.

For τ_1 and $t_i = 1$ms, we get back the rule-of-thumb of a factor ~ 10 between the sampling frequency (1kHz) and the closed-loop bandwith (~ 100Hz) used to calculate the temporal error, see equation 2.4. As the delay $\tau_1 = [200, 500, 1000]\mu s$ increases, the gain needs to be lowered to ensure the same degree of stability and the closed-loop bandwith decreases from 100Hz to $\sim[90,80,70]$Hz. It is also worth noting that a longer integration time is better than a longer time delay, as observed by considering the $t_i = 2$ms case. Hence long latencies should be avoided in agreement with the targeted temporal error.

---

[8]The optimization of the controller is a topic of active research, in particular for extreme AO systems where a prediction algorithm can significantly improved the correction performance. Regardless of those considerations, a simple integrator is common-use and will – at least at the beginning – be the ARGOS case.

[9]this is obtained by considering the Nichols chart and ensuring for the open-loop a phase margin $>45°$and a gain margin >6dB.
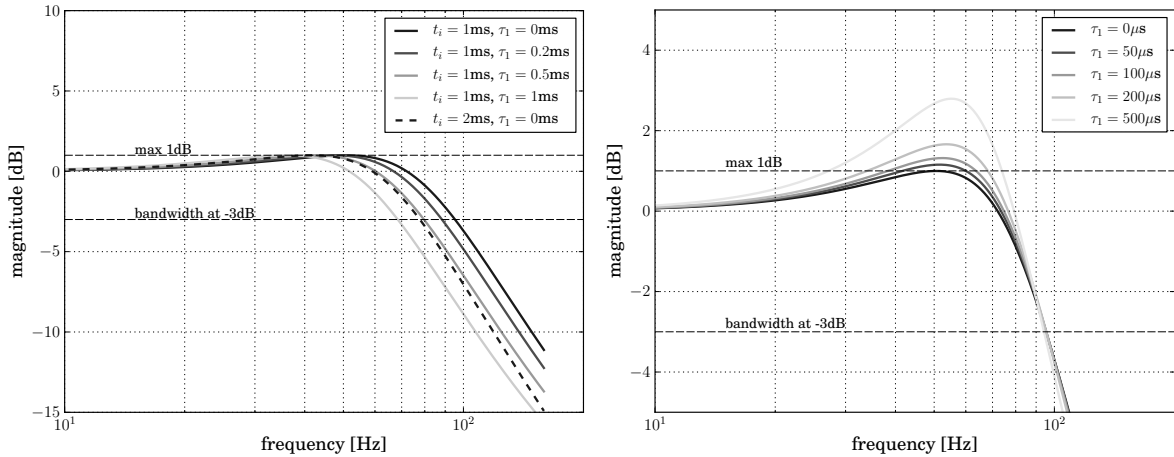
Figure 4.8: Bode diagrams of the closed-loop transfer equation 4.7 illustrating latency and jitter effects. (Left) Decrease of closed-loop bandwidth due to latency. The integration time t_i is 1 or 2 ms. The parametrized delay τ_0 is fixed to 2ms and the τ_1 varies from $\tau_1 = [0, 200, 500, 1000]\mu s$ and denotes here the additional delay introduced by the wavefront computer. The controller $C(s)$ gain has been adjusted for each case to ensure similar loop stability (a maximum of 1dB), see also the text for a short discussion on the caveat of such approach. (Right) Simple jitter illustration, see also text for caveat. We consider here t_i=1ms with additional delays $\tau_1 = [0, 50, 100, 200, 500]\mu s$. The controller gain was optimized for $\tau_1 = 0\mu s$ and kept fixed for the other cases in order to qualitatively understand the impact of the jitter. As expected, when the jitter increases, the loop gets less stable.

Jitter. A jitter is a difference between the nominal and actual time delay. It is a random variable described by a probabilistic distribution function that depends on the RTC architecture. The jitter is normally studied through closed-loop simulation by injecting a jitter probability distribution. It is beyond our scope to perform such simulation. Instead as an illustrative but biased example, we consider the jitter as a latency not accounted for, *i.e.* for which the gain has not been adjusted.

Using the gain adjusted for $t_i = 1$ms and $\tau_1 = 0$ms, we represent in Fig. 4.8 (Right), the Bode diagrams for additional delays of $\tau_1 = [50, 100, 200, 500]\mu s$. We can observe that the overshoot increases, hence the stability worsens. Such overshoot would degrade the correction and, if extreme, can render the AO system unstable. From jitter effect simulation, Pettazzi et al. (2012) shows that below $1 - 10\%$ of the sampling time, the jitter is fully negligible. Above 10%, it quickly degrades the AO performances.

4.5.1   Argos BCU data flow

The ARGOS BCU operations are almost fully pipelined performing the data reduction and slope computation as soon as the pixels are available. A conceptual flow diagram is given in Fig. 4.9.

These parallelized operations ensure a minimum latency. Nevertheless, at the last pixel download, the BCU still needs to perform a number of operations, in particular

- the last line common-mode and gain corrections,
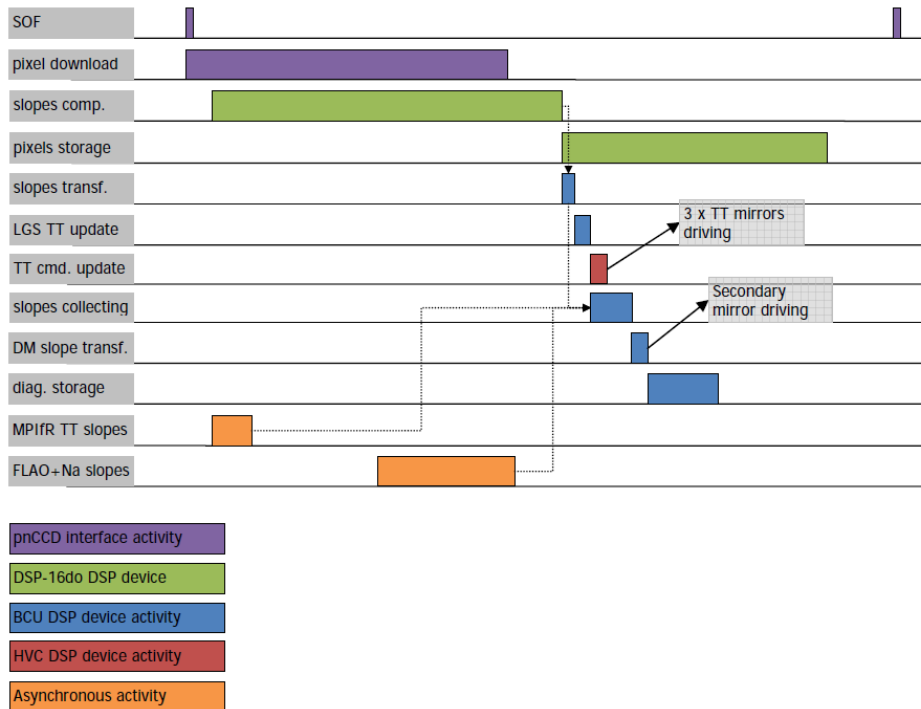
Figure 4.9: Conceptual data flow diagram of the ARGOS BCU from first pixel download to slope finalization and diagnostics savings. The latency is calculated from the final pixel download to the final slope construction. The synchronization is done through real time communication, *i.e.* the start-of-frame (SOF) is given by the start of a PNCCD frame. This representation is only indicative and we refer to the text for proper timing estimations. Credit : Andrighettoni & Biasi (2011).

- the slope computations of sub-apertures that include pixels in the two middle lines of the PNCCD, the two last lines to be readout,

- the transfer of the LGS slopes to the BCU board, and the computation of the LGS tip-tilt for correction,

- the collection of the NGS tip-tilt, the third WFS, and the LGS slopes to form the final slope vector,

- finally sending the slopes to the deformable mirror.

The delay from the last pixel download to the end of slope computation depends on the number of subapertures that contain pixels of the two middle lines of the PNCCD. The baseline for ARGOS is 29 subapertures. From measurements performed by MICROGATE directly on the boards[10], one slope computation is $\sim 2\mu$s, hence a total of $\sim$60μs. From the last slope computation to the final slope vector reordering, a delay of $\sim$30μs has been measured on

---

[10]The measurements quoted here are directly read off from the oscilloscope traces in Andrighettoni & Biasi (2011). Those measurements have been performed using the frame generator to simulate the PNCCD optical interface, and with the first firmware versions. The values might slightly differ from the up-to-date firmwares (result of the debugging operations), and with the built-in ADCs.

the BCU board (Andrighettoni & Biasi, 2011). The total delay therefore is estimated to be $< 100\mu s$.

The BCU has a deterministic timing with extremely low jitter $< 1\mu s$ (Biasi, 2012) which is completely negligible here. As a comparison, a GPU based architecture for the NFIRAOS for the TMT currently provides PtV jitter $< 50\mu s$, with a RMS of $2.2\mu s$ and some rare events of $\sim 150\mu s$, see Wang (2012).

Comparing those values with our toy model, we can conclude that the ARGOS BCU latency and jitter estimations are very good and should have a negligible impact on the ARGOS error budget.

The LBT reconstructor that includes the wavefront reconstruction and the deformable mirror control has a latency of $\sim 260\mu s$ (Biasi, 2012). The exact value may however slightly vary depending on the exact modal computation. Hence the total delay, excluding the readout, is $\lesssim 400\mu s$. Those delays are reported in the ARGOS timing diagram represented in Fig. 2.8.

4.6   A demonstration test bench : preliminary validation of the wavefront sensing

In the last sections, we have presented the design and the validation of the wavefront sensor computer as a sub-system unit. Ultimately however this unit has to work as an integrated part of the ARGOS Wavefront Sensor system. Prior to the integration with the WFS optics at INAF, we have developed a test bench that integrates three key components of the WFS system: the WFS camera, its computer, and the optical gating unit. The objectives are essentially two folds: integration and validation of the system. This has also been presented in Orban de Xivry & Rabien (2012). We discuss first the bench setup and then its results.

Modus operandi

The setup intends to integrate in realistic conditions the PNCCD camera, the BCU, and the ARGOS Pockels cell. We present in Fig. 4.10 the schematics of our test bench.
It consists of

- a source at wavelength of 532nm,

- collimating optics, pupil stop, and re-collimating optics. This allows us to obtain a 5mm diameter collimated beam that can be injected into the Pockel cell.

- the aligned Pockel cell, described in CHAP.2, consists of a first linear polarizer, a first active BBO crystal, a birefringent quartz crystal to rotate by 90° the polarization, a second BBO crystal, and a last polarizer.

- After the optical gating, we place a lenslet array (with a pitch of 300μm), and re-imaged the spots on the PNCCD detector with the appropriate magnification in order to match the desired spacing between the spots.

A common pulse generator controls the high voltage driver of the Pockels cell and triggers the frame transfer of the PNCCD after an appropriate delay at 1kHz. Similarly to the final operation mode, the Pockels cell is typically "opened" ten times (corresponding to the 10 laser pulses operated at a 10kHz repetition rate), before reading out the detector. Moreover,

the switching time is appropriately delayed to not fall within the PNCCD image to framestore charge transfer duration, *i.e.* ∼40μs (see section 3.2.2).

While the timing is fully realistic, the injection into the Pockel cell differs from the foreseen system. Here we inject a 5mm collimated beam where for ARGOS the beam convergence will vary as a function of the altitude as the laser pulse propagates in the atmosphere. Morevover low altitude contribution will be diluted due to the spatial extension of the source not in focus. We have here a continuous light source providing a wealth of photons at any given time.

At the time of realisation, the PNCCD ADCs and the BCU could not be interfaced in real time. Therefore, we acquired a data cube from the PNCCD frame grabber and uploaded frame by frame the data to the BCU. Once the BCU is correctly configured (see section 4.3), the computation is triggered and the resulting slopes are acquired through the BCU diagnostics mechanism. The obtained slopes are used for further off-line analysis.
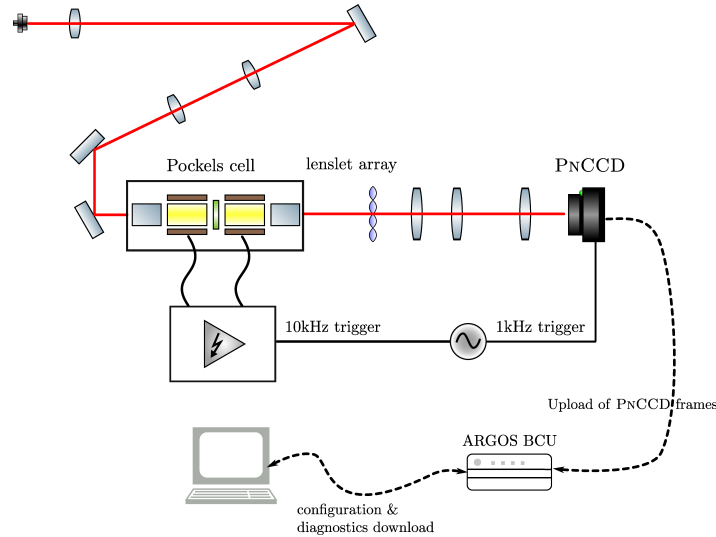
Figure 4.10: Demonstration test bench setup. The red curve is the optical path. Solid black curve are electric signal. Dashed black curves are data signal. See text for a full description.

Analysis and Results

Based on our measurements, we illustrate here the configurability and the advantages of the general formulation of the centroiding computation. The Shack-Hartmann pattern produced on the PNCCD has a similar pupil and subaperture size as for ARGOS, *i.e.* 15 subapertures along the pupil diameter each 8×8 pixels wide. The FWHM is approximately 2.5 pixels (equivalent to 1.4″) and the spots are slightly elongated. A data cube of 200 frames is acquired, and the slopes are then computed for each frame by the BCU. From the resulting slopes, the centroiding accuracies are computed as the standard deviation over the 200 frames. The flux for each subaperture is computed off-line by taking the sum of the pixel fluxes minus the flux threshold, see also equation 4.1. The flux computation is the same for the three algorithms.

We illustrate here three different variants allowed by the algorithm implemented in the ARGOS BCU:
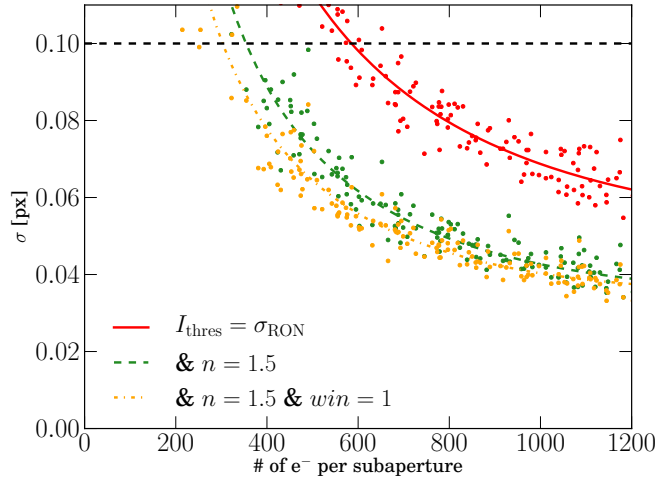
Figure 4.11: Centroiding accuracy in function of flux per subaperture per millisecond for three different algorithms. Each point is a subaperture, the solid curves represent the second order polynomial fits, and the dashed-line is the minimum accuracy requirement, see Chap.2 and section 3.1. This illustrates the operability of three components of the WFS: the pNCCD, the BCU, and the Pockels cell. It also illustrates the possible gains in term of centroiding precision by adapting the implemented algorithm. See text for a discussion.

- The TCoG algorithm with a fix threshold, $I_T \sim \sigma_{\mathrm{RON}}$. This threshold is kept for the other two algorithms.

- The WWPA using a "signal-to-noise" ratio weighting by setting $n = 1.5$ in equation 4.1,

- The WWPA combined with a windowing of the subaperture: using 6×6 subapertures instead of 8×8. Note that the flux is still computed on the 8×8 subaperture.

As the spot light flux varies within the pupil, we do not need to repeat the measurement for different illuminations. In Fig. 4.11 we represent the centroiding accuracy as a function of the subaperture photo-electron flux. Each point represents a subaperture and the curves are the respective fits. In our particular case, we clearly see the improvement brought by each algorithm, in particular the weighting by the signal-to-noise ratio.

It is as well important to note that in the simple case of the $1 \times \sigma_{\mathrm{RON}}$ fix threshold, the centroiding accuracy is identical in both the x and y axis of the CCD frame, which further confirm that the common-mode noise residuals do not impact the measurements (see also section 3.4). This is still true for an additional windowing, reducing the subaperture size to 6×6 pixels. The weighting by the SNR (assuming photon limited regime as given in equation 4.6) however does not improve the accuracy uniformly for x and y. In fact, the improvement is not as good in the y direction, the direction of the elongation. This illustrates well the advantages and disavantages of the WWAP algorithm, particularly good for round symmetric spot but less for elongated ones.

The expected backscattered flux from the Argos lasers should result in more than 700 photons per subaperture per milli-second. Considering the high QE of the pNCCD, this translates to a similar number of photo-electrons. As also illustrated in Fig. 4.11, this should

always be enough to perform accurate slope measurements. The general algorithm provides also a large margin for improvement from the simple CoG and allow it to cover a wide range of fluxes.

This test bench has demonstrated the joint operability of the pnCCD, the BCU and a Pockels cell. Readout-noise and common-mode have also been analyzed in this context showing no discrepancies with our reference measurements. This verifies in practice that the fast high-voltage driver of the Pockels cell is not directly perturbing the pnCCD readout.

We have also illustrated the gain that an optimized algorithm brings in term of precision and sensitivity. However we have not studied the non-linearity effects from spot elongation or window truncation for which the WWPA algorithm may be less efficient.

4.7   Conclusions

We have presented in this chapter the Argos wavefront sensor computer from its theoretical design to its final functionality. The performance and flexibility have been discussed in term of possible algorithms and computation time – both providing Argos with large margins from its nominal operation point in term of photon flux and speed. Indeed, the estimated latency of $< 100\mu s$ is negliglible in the temporal error budget and the jitter in such DSP-based architecture is minimum. Moreover, while the nominal photon flux per sub-aperture per frame is estimated to be ~ 1800, the flexible algorithm could allow fluxes below $< 400 photons/subaperture/frame$ while preserving a good centroiding measurement.

This lead us to demonstrate the operability of three key components of the WFS (pnCCD, BCU, and Pockels cell) in an optical test bench. Following these preliminary tests, these hardware components have been integrated successfully to the WFS system at INAF before a later installation at LBT.

THE ROLE OF SECULAR EVOLUTION IN THE BLACK HOLE GROWTH OF NARROW-LINE SEYFERT 1 GALAXIES

This chapter is to a large extent a re-print of the publication Orban de Xivry et al. (2011), MNRAS, 417. From the initial paper, we extend here the introduction (section 5.1) and the discussion on the suggestive link between NLS1 and high black hole spin (section 5.5.2) in the light of more recent development in that field. We add a small discussion on the possible selection bias possibly explaining part of the differences between NLS1s and BLS1s (section 5.5.1). Finally, we also provide more details on the performed photometric fittings in this chapter (with part of the paper's appendix included here) and in appendix C.

Abstract

Narrow-Line Seyfert 1 (NLS1) galaxies show extreme properties with respect to the other Seyfert galaxies. Indeed, they are thought to be accreting at Eddington rates and to possess low mass black holes. Therefore, they may represent a key class of objects for understanding the co-evolution of black holes and their host galaxies. We propose that NLS1s represent a class of AGN in which the black hole growth is, and has always been, dominated by secular evolution. Firstly, by looking at the NLS1 host galaxy properties in the literature, we show that the evolution of NLS1s is presently driven by secular processes, much more so than for Broad-Line Seyfert 1s (BLS1s). Secondly, we study the bulges of NLS1 and BLS1 galaxies. Our results demonstrate that NLS1 host bulges are pseudo-bulges and are statistically different from BLS1 bulges. This difference points to the particular importance of secular processes in the past evolution of their hosts. We build on this result to understand the implications on their evolution and the duration of their duty cycle. We show that NLS1s are not necessarily in a special phase of black hole growth and that several Gyr are required for their black hole masses to become similar to BLS1s. Finally, in the light of our results, we discuss the location of NLS1 galaxies on the M_{BH}-σ plane and speculate about the connection between the NLS1 galaxy properties and their black hole spin.

5.1 Introduction

Since their discovery, Narrow-Line Seyfert 1 (NLS1) galaxies have always been recognized as particular objects holding important clues on the driving mechanisms of nuclear activity.

First identified as objects similar to Seyfert 1s with narrower Balmer lines, they were soon recognized as having exceptional spectral properties, both in their emission lines and in their continuum (see Komossa, 2008, for a review).

To mention the most important ones, in addition to the formal classification[1], NLS1s are also recognized to often display strong FeII emission formed in a dense medium comparable to the BLR and unseen in Seyfert 2s. NLS1s have also remarkable soft X-ray properties with a large dispersion in the soft (0.1-2.4keV) photon indices ($\Gamma \sim 1 - 5$), and rapid X-ray varibility. Hence strong soft X-ray excess is a common characteristic but not universal among NLS1s where some have lower photon indices more typical of BLS1s ($\Gamma \sim 2$). Finally, NLS1s show the strongest and fastest X-ray variabilities in AGNs. In conclusion and to quote Pogge (2011), "while NLS1s are a fairly well-defined and distinctive subclass of AGN, they are also a diverse subclass".

Despite this "mixed bag", principal components analyses (e.g. Boroson, 2002) have shown that NLS1 galaxies are clustered at one extreme end of the AGN parameter space which is now usually interpreted as the high-Eddington (L/L_{Edd})/low-accretion mass ($\dot{M}$) corner[2]. Likewise, they are thought to possess small mass black holes and to have high Eddington accretion rates (e.g., as suggested by reverberation mapping BH mass measurements, and comparison to the AGN luminosities Peterson et al., 2004). In this sense, NLS1s could represent key objects in understanding the AGN phenomena and the co-evolution of massive black holes and their host galaxies.

While the main defining criteria of NLS1s with respect to BLS1s is the empirical threshold at $\mathrm{FWHM}(\mathrm{H}_\beta) \sim 2000$ km s^{-1}, the properties of NLS1s have been extensively studied across many wavelength ranges. Trends and correlations have been identified using first small samples and later corroborated by larger surveys (e.g. Véron-Cetty & Véron, 2001, Williams et al., 2002, Zhou et al., 2006). Many scenarios have been considered to explain these properties, in particular their high accretion rates ($L/L_{\mathrm{Edd}} \simeq 1$, e.g. Boroson, 2002, Grupe, 2004, and reference therein) and low black hole masses (typically of order $10^6 M_\odot$, e.g. Boller et al., 1996, Zhou et al., 2006, Ryan et al., 2007), but also, e.g., outflows, winds and density effects, high metallicity, particular broad line region thicknesses and densities, etc. (see Komossa, 2008, and references therein). While these scenarios can elucidate the nuclear properties of NLS1s, they hardly explain the origin of the fundamental differences between NLS1s and BLS1s and, in particular, that NLS1s appear to be more than just Seyfert 1s with narrow lines. A few key questions could be formulated as follows: which particular mechanisms would lead to the Eddington accretion rates commonly seen in NLS1s but observed less often in BLS1s? What causes the difference in black hole growth of NLS1s and BLS1s that results in low mass black holes in the former case? Could differing host galaxy evolution explain the differences between NLS1 and BLS1 galaxies?

In this paper, rather than studying the active nuclei, we investigate the host galaxies of NLS1s and contrast their properties to those of BLS1s, pursuing the hypothesis that different host galaxy evolution could explain the differences between NLS1s and BLS1s. In particular, we explore the relative role of secular processes in the evolution of NLS1 and BLS1 galaxies. Reviewing the literature on the morphology and the star formation in NLS1 and BLS1 hosts, we emphasize, in section 5.2, the present-day differences in their respective host galaxies.

---

[1] 1) narrow permitted lines only slightly broader than the forbidden lines; 2) [OIII]/H$_\beta$ < 3 unlike what is seen in Seyfert 2s; 3) FWHM(H$_\beta$)<2000km s^{-1}.
[2] *i.e.* a high relative mass accretion rates but low M_{BH}.

Afterwards, in section 5.3, we turn to the past evolution of NLS1 and BLS1 hosts. We perform a bulge-disk decomposition of samples of NLS1 and BLS1 galaxies and look at their bulge properties. Using previously established criteria (Kormendy & Kennicutt, 2004, Fisher & Drory, 2008, Gadotti, 2009), we are able to distinguish pseudo- from classical bulges. This enables us to determine the main processes that have driven the evolution of the NLS1 and BLS1 hosts. We analyse the differences of NLS1 and BLS1 host bulge property distributions, concluding that NLS1 galaxies contain pseudo-bulges and, hence, have always been dominated by secular evolution. Finally, in section 5.4 and section 5.5, we investigate the cosmological context of the NLS1 host phenomenon driven by such an evolutionary mode. We shortly discuss the effect of selection bias. We then note the link between secular evolution and rapidly spinning black holes, and speculate on the location of NLS1 galaxies on the $M_{BH} - \sigma$ relation. We conclude by summarizing our picture of the NLS1 galaxy phenomenon and present ways to further test our proposition.

When calculating distances and look-back times, we assume a general relativistic Friedmann-Robertson-Walker (FRW) cosmology with matter-density parameter $\Omega_m = 0.3$, vacuum energy-density parameter $\Omega_\Lambda = 0.7$ and Hubble parameter $H_0 = 70$ km s^{-1} Mpc^{-1}.

5.2 Secular evolution in NLS1 host galaxies

In this section, we review the literature that has been published concerning the differences in the host galaxy properties of NLS1s and BLS1s. We focus in particular on the morphology and the star formation rate, and emphasize the role of present secular processes in distinguishing between these two classes of type 1 AGN.

5.2.1 Morphological properties

Large-scale bars

The morphology of NLS1 host galaxies has been studied in several papers (Crenshaw et al., 2003, Deo et al., 2006, Ohta et al., 2007, Ryan et al., 2007). The main results can be summarized as follows:

NLS1 host galaxies are likely to be strongly barred (much more than BLS1 ones) and their nuclear dust morphology is likely to be a grand-design spiral.

The bar frequency among NLS1 and BLS1 host galaxies has been studied by Crenshaw et al. (2003) and Ohta et al. (2007). The first paper reports a visual study based on an HST survey of 91 Seyfert galaxies (13 NLS1s and 78 BLS1s) at $z \leq 0.035$ (Malkan et al., 1998) and 6 additional NLS1s at $z \leq 0.084$ (HST archives in the Véron-Cetty et al., 2001 sample). The results are striking: 91% of the sample is classified as spiral galaxies among which 65% of NLS1s have bars, and 25% of BLS1s have bars. More particularly, the authors look at the fraction of barred spiral galaxies in their sample as a function of the full width at half maximum (FWHM) of the broad component of the H_β emission line. As presented in Fig. 5.1, they obtain a clear difference between the two regimes of NLS1s and BLS1s. We note that in this figure, since FWHM measurements are not available for every BLS1, we have made a single bin for the BLS1 class.

The results from Ohta et al. (2007) are more conservative. They use an heterogeneous set of data of NLS1 galaxies and look at the morphology and the possible trends with the NLS1
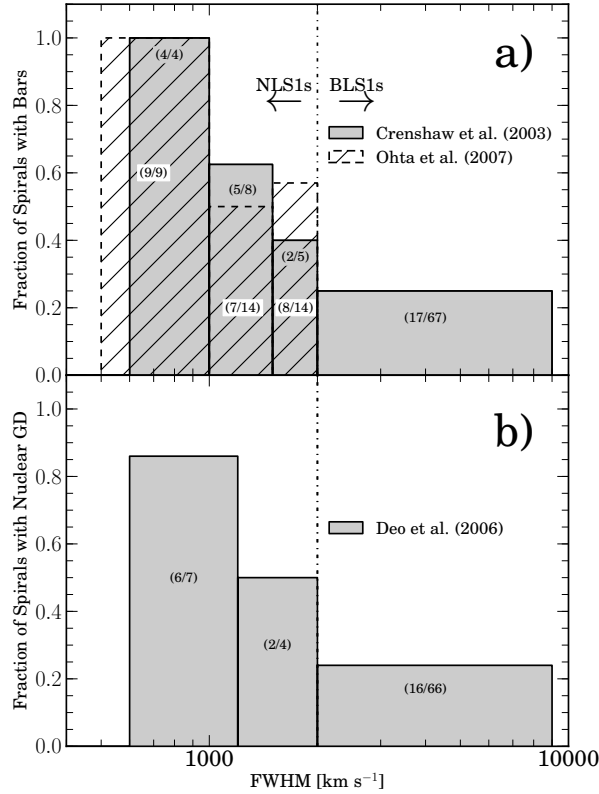
Figure 5.1: Histograms presenting the fraction of Seyfert 1 spirals a) with bars and b) with nuclear grand-design spirals as a function of the FWHM of their broad emission line, $H\beta$. Drawn from data reported in Crenshaw et al. (2003), Ohta et al. (2007) and Deo et al. (2006).

properties. They perform a visual and a quantitative classification based on ellipse fitting of isophotes. While they confirm the high bar fraction among (spiral) NLS1 hosts, they do not observe a clear trend with the FWHM. Nevertheless, if we consider only the fraction of spirals with strong bars (SB but not SAB), the trend does appear clearly using their visual classification (as represented in Fig. 5.1). Turning to their quantitative classification, we note that one of the criteria Ohta et al. use to identify the bars is an ellipticity $\epsilon_{bar} \geq 0.25$, where $\epsilon_{bar} = \max(\epsilon_{galaxy})$. However a common practice to identify *strong* bars is to use $\epsilon_{bar} \geq 0.45$ (e.g. Shlosman et al., 2000). Applying this latter criterion on their sample by examining the ellipse fit plots, we obtain, for the respective bins in Fig. 5.1 (*i.e.* 500–1000, 1000–1500, 1500–2000 km s^{-1}), bar fractions (*i.e.* 89%, 46% and 57%) similar to their visual classification (*i.e.* 100%, 50% and 57%, see Fig. 5.1).

Circumnuclear morphology

In a study of nuclear dust morphology in a matched-paired sample of active/inactive galaxies and barred/unbarred galaxies, Martini et al. (2003) show that grand-design nuclear dust spirals are only found in galaxies with a large-scale bar. However, while not finding any universal nuclear morphology in active galaxies, they do find similar features in the circumnuclear environments of both active and inactive galaxies. In another study, Deo et al. (2006) investigate

the nuclear dust morphology in NLS1 and BLS1 host galaxies based only on the HST survey conducted by Malkan et al. (1998). Their study also shows that the grand-design nuclear dust spirals are largely present in barred galaxies. They classify the nuclear structures and find that (1) the nuclear dust morphologies in NLS1/BLS1, Barred/Unbarred are mainly nuclear dust spirals, (2) in the "nuclear dust spiral" class, NLS1s are more likely to have grand-design spirals than BLS1s. Fig. 5.1 also shows that this fraction of grand-design spirals in NLS1s follows the same trend with the FWHM(H$_\beta$) as the bar fraction.

As we expect strong bars to drive a circumnuclear spiral structure (Maciejewski, 2004a,b) and to drive gas inwards (Sakamoto et al., 1999, Sheth et al., 2005), we expect the presence of such asymmetries in host galaxies to result in an enhanced star formation in the central kiloparsecs.

5.2.2   Star formation

In a recent paper, Sani et al. (2010) study the link between star formation in the central kpc vs. FWHM(H$_\beta$) in NLS1 and BLS1 host galaxies. After discussing carefully possible luminosity and distance effects, they conclude that NLS1s are associated with more intense star formation than BLS1s (with on average a star formation to AGN ratio > 2 times larger in NLS1s). More generally, they find that type 1 AGNs with narrower broad emission lines reside in hosts containing more intense star-forming regions.

Finally, they find a connection between high Eddington ratio and high star formation rates concluding that NLS1s are characterized by smaller black hole (BH) mass, larger Eddington ratio and stronger star formation activity compared to their broad-line counterparts.

5.2.3   Secular processes all the way to the SMBH

As discussed above, the current morphology of NLS1 host galaxies is distinguishable from other Seyfert galaxies. Indeed, in contrast to BLS1s, NLS1 galaxies are likely to be strongly barred and to show more intense central star formation. This is in line with the fact that bars are known to drive gas into the central kiloparsecs (Sakamoto et al., 1999, Sheth et al., 2005), and that nuclear star formation is enhanced in barred galaxies (Ho et al., 1997).

While no universal fueling mechanism for low-luminosity AGNs seems to operate in galactic nuclei (Martini et al., 2003), the NLS1 host morphology typically exhibits a circumnuclear grand-design spiral. This appears to be linked to the presence of strong bars (Martini et al., 2003, Deo et al., 2006), and indeed bars are able to drive circumnuclear spiral structures (Maciejewski, 2004a,b). Hence, NLS1 galaxies show uninterrupted asymmetries able to drive the gas inwards from a few kpc to a few tens of pc. The particular strength of secular processes in NLS1s could therefore account for the high central star formation and presumably to the large Eddington rates observed in NLS1s.

5.3   Bulges of NLS1 host galaxies

Since strong secular evolution is currently occurring in NLS1s, it is important to ask whether or not secular processes have shaped the NLS1 host galaxies by dominating their past evolution and hence influencing their black hole growth.

We address this issue by examining the bulges of NLS1 host galaxies and comparing them to those of BLS1s, since one can expect to observe evolutionary dependent bulge characteris-

tics. Specifically, an evolution driven mainly by galaxy mergers will result in different bulge properties than if the evolution is mainly driven by internal secular evolution.

In this section, we compare NLS1 and BLS1 galaxies by performing a photometric bulge-disk decomposition of homogeneous samples of NLS1s and BLS1s. This comparison is put in perspective with previous studies on the distinction between pseudo- and classical bulges in inactive galaxies (Kormendy & Kennicutt, 2004, Fisher & Drory, 2008, Gadotti, 2009), and also on the bulge-disk decomposition of two galaxy samples composed exclusively of NLS1s (Ryan et al., 2007, Mathur et al., 2012).

5.3.1   Pseudo-bulges and secular evolution in disk galaxies

Kormendy & Kennicutt (2004) review in detail the formation of pseudo-bulges by secular processes. As dense central components of galaxies, pseudo-bulges differ from classical bulges in that they were made slowly by disks out of disk material while classical bulges are "merger-built" bulges. Therefore, pseudo-bulges are formed by internal secular processes such as bar instabilities, spiral structures, etc. as opposed to galaxy mergers or external secular evolution (minor mergers, prolonged gas infall, etc.).

As pseudo-bulges retain memory of their disky origin, it is possible to disentangle them from classical bulges. Kormendy & Kennicutt (2004) pointed out the Sérsic index as one way to identify them. Indeed, since a pseudo-bulge forms from gas accreting from the disk, it has a surface brightness profile similar to that of the outer disk and therefore would have a low Sérsic index $n_b \sim 1 - 2$.

Fisher & Drory (2008) have studied in great detail the structure of classical bulges and pseudo-bulges using high-resolution data (77 inactive galaxies with data in the HST archive and $z \lesssim 0.01$). They use morphological signatures to first visually classify the bulges of nearby galaxies as pseudo or classical. They then perform a bulge-disk decomposition and study in particular the distribution of Sérsic indices. They find that, statistically, pseudo-bulges have Sérsic indices $n_b < 2$ while classical bulges have $n_b > 2$. This result shows that the Sérsic index is a good statistical tool to test if a class of objects has classical or pseudo-bulges.

Finally, Gadotti (2009) also study pseudo- and classical bulges using a large, low resolution, SDSS sample of galaxies ($\sim$1000 inactive galaxies with $0.02 \leq z \leq 0.07$). He uses the position in the $< \mu_e > -r_e$ plane, also called the Kormendy relation[3], to study the bulge properties and identifies pseudo-bulges as being fainter in surface brightness for a given half-light radius (much fainter than predicted by the correlation fit to elliptical galaxies). Where Gadotti (2009) clearly sees independent groups in his i-band density plot of the Kormendy relation ($< \mu_e > -r_e$ relation), Fisher & Drory (2008, 2010) only find that pseudo-bulges scatter around the photometric projections of the fundamental plane.

Nevertheless, all these authors (Fisher & Drory, 2008, Gadotti, 2009, Fisher & Drory, 2010) agree that most of the pseudo-bulges have a low Sérsic index $n_b < 2$ and that they tend to be less prominent than classical bulges (in particular, they tend to have a low bulge-to-total light ratio).

Based on these considerations for bulge classification in inactive galaxies, we will use the Sérsic index to identify the prevailing bulge type in the NLS1 and BLS1 populations as pseudo- or classical. We will then study the prominence of NLS1 and BLS1 bulges.

---

[3]relation between the mean effective surface brightness within the effective radius $< \mu_e >$ and the half-light radius r_e, which is a projection of the photometric fundamental plane.

5.3.2   Bulge/disk decomposition

Building on the work of Fisher & Drory (2008) for inactive galaxies, we select archive HST images of Seyfert galaxies to study the bulges of active galaxies, in order to assess whether the bulge characteristics of NLS1s and BLS1s might explain, by their evolutionary implications, the distinctions between these two classes of AGN. Crucially, by performing the bulge-disk decomposition for samples of both NLS1s and BLS1s, we minimize the impact of any systematic errors that our fitting procedure might generate.

We select NLS1 and BLS1 galaxies from the Malkan et al. (1998) HST imaging survey of nearby AGNs. This survey contains a uniform sample of 91 Seyfert 1 galaxies at $z \leq 0.035$ observed with the Wide Field Planetary Camera 2 (WFPC2) through the F606W filter. This sample, also used by Crenshaw et al. (2003) and Deo et al. (2006) in their morphological studies, contains 11 NLS1 galaxies and 80 BLS1 galaxies. The 11 NLS1 galaxies are genuine NLS1s as identified by Véron-Cetty et al. (2001) on the basis of their optical spectra (broad component of $H\beta < 2000$km s^{-1} and strong FeII emission) and are listed in the catalog of Véron-Cetty & Véron (2010). We therefore initially select all the 11 NLS1 galaxies available, as well as 21 of the 80 BLS1s. The BLS1 sample selection is made in a way to roughly match the $\sim$25% fraction of such hosts that are strongly barred (Crenshaw et al., 2003). Their individual Seyfert classifications are reported in Tab. 5.1. These are taken from Véron-Cetty & Véron (2010) with 2 exceptions. IC1816 is classified by Márquez et al. (2004) as a type 1. Because their spectrum shows clear evidence of broad emission, we have adopted this classification. For NGC5252, we have followed the classification as a type 1.9 given in Osterbrock & Martel (1993), because the presence of broad Hα, with a measured FWHM of $\sim$2500 km s^{-1}, is confirmed by Acosta-Pulido et al. (1996). We note that the broad Hα is very clear in polarized light (Tran, 2010), and shows dramatic variations over a period of several years. This may be why there is some uncertainty about its classification as a type 1 or 2. Following this initial selection, we refine our sample based on the limited field of view (FoV) of WFPC2 by rejecting objects with $z < 0.010$ or scales $\leq$0.23 kpc/$''$ in order to obtain a reasonable minimum FoV of $\gtrsim$8$\times$8kpc on each object. This criterion ensures that the disk of the host can be fitted properly, while the redshift limit of the original source catalogue ensures that the bulge is sufficiently well resolved. The two final samples for which we performed the bulge-disk decomposition are composed of 10 NLS1s and 19 BLS1s, and are given in Tab. 5.1. Finally, we check that the mean redshift is not strongly biased with respect to the NLS1 sample ($< z_{\mathrm{NLS1}} >= 0.024$, $< z_{\mathrm{BLS1}} >= 0.027$), and that no particular circumnuclear morphology has been selected.

To perform the bulge-disk decomposition of these 29 galaxies, we use the two-dimensional profile fitting algorithm GALFIT[4] (Peng et al., 2010). For each galaxy we iteratively fit three components: a Gaussian profile, a Sérsic profile and an exponential profile (see also Appendix C.1). These components are aimed at modelling respectively the nuclei, the bulges and the disks of our galaxies. While these HST data of nearby AGN have small pixel scales (see column 4 in Tab. 5.1) enabling us to better constrain the central regions of the galaxies, the FoV of WFPC2 ($\sim 35''\times35''$) is small relative to the full extent of the galaxies. This makes it hard to constrain the sky level. This issue has already been addressed to some extent by the refinement of our sample selection to objects with $z \geq 0.010$. We cover it further in a paragraph below when we discuss our treatment of the possible coupling between the background level and the exponential profile. Finally, we analyze the robustness of our

---

[4]http://users.obs.carnegiescience.edu/peng/work/galfit/galfit.html

Table 5.1: HST sample of NLS1s and BLS1s. Columns: (1) object name; (2)-(4) J2000 coordinates and redshift from Nasa/IPAC Extragalactic database (NED); (5) luminosity distance in Mpc for an $H_0 = 70$km s^{-1} Mpc^{-1}, $\Omega_m = 0.3$ and $\Omega_\Lambda = 0.7$ cosmology; (6) respective scale, the WFPC2 pixel scale is $0.0456''$; (7) morphological classification (from Malkan et al., 1998, MGT); (8) Seyfert classification according to the Véron-Cetty & Véron (2010) catalog except for IC1816 and NGC5252, see also the main text. S1 classification designates a type 1 AGN with unspecified sub-type; (9) FWHM of the broad component of $H\beta$ (or in a few cases, $H\alpha$), the NLS1 measurements are from Véron-Cetty et al. (2001), the BLS1 measurements are taken from Crenshaw et al. (2003), see also references therein.

Object Name	R.A. (J2000)	Dec. (J2000)	z	D (Mpc)	px sc. (kpc/$''$)	Morpho. (MGT)	AGN type	FWHM (km s^{-1})
NLS1 SAMPLE								
KUG1136	11 39 13.9	+33 55 51	0.032	131.84	0.64	SB0	S1n	1145
MRK0042	11 53 41.8	+46 12 43	0.024	99.83	0.48	SBa	S1n	865
MRK0335[a]	00 06 19.5	+20 12 11	0.025	109.12	0.50	?	S1n	1350
MRK0359	01 27 32.5	+19 10 44	0.017	71.31	0.35	SBb/c	S1n	900
MRK0382	07 55 25.3	+39 11 10	0.034	139.74	0.68	SBa	S1n	1280
MRK0493	15 59 09.6	+35 01 47	0.031	127.87	0.62	S(B)a	S1n	740
MRK0766	12 18 26.5	+29 48 47	0.012	50.65	0.25	SBc	S1n	1630
MRK0896	20 46 20.8	−02 48 45	0.027	111.91	0.54	Sc	S1n	1135
MRK1044	02 30 05.5	−08 59 53	0.016	67.20	0.33	Sa	S1n	1010
NGC4748	12 52 12.4	−13 24 53	0.014	58.94	0.29	Sa	S1n	1565
BLS1 SAMPLE								
ESO438G9[b]	11 10 48.0	−28 30 04	0.024	99.83	0.48	SBc/d	S1	5000
F1146	08 38 30.8	−35 59 33	0.032	131.84	0.64	Sb	S1	4300
IC1816	02 31 51.0	−36 40 19	0.017	71.31	0.35	SBa/b	S1	...
Mrk0279	13 53 03.4	+69 18 30	0.031	123.89	0.60	Sa	S1.0	6860
Mrk0290	15 35 52.3	+57 54 09	0.029	123.89	0.60	E	S1.5	2550
Mrk0352	00 59 53.3	+31 49 37	0.015	63.08	0.31	E	S1.0	3800
Mrk0423	11 26 48.5	+35 15 03	0.032	131.84	0.64	Sb	S1.8	9000
Mrk0530	23 18 56.6	+00 14 38	0.029	119.91	0.58	Sa	S1.5	6560
Mrk0595	02 41 34.9	+07 11 14	0.028	111.91	0.54	Sa	S1.5	2360
Mrk0609	03 25 25.3	−06 08 38	0.032	139.74	0.68	Sa/b	S1.8	...
Mrk0704	09 18 26.0	+16 18 19	0.029	119.91	0.58	SBa	S1.2	5500
Mrk0871	16 08 36.4	+12 19 51	0.034	139.74	0.68	Sb	S1.5	3690
Mrk0885	16 29 48.2	+67 22 42	0.026	103.87	0.50	SBb	S1.0	...
Mrk1126	23 00 47.8	−12 55 07	0.010	46.48	0.23	Sb	S1.5	...
Mrk1400	02 20 13.7	+08 12 20	0.029	119.91	0.58	Sa	S1.0	...
NGC5252	13 38 15.9	+04 32 33	0.022	95.79	0.46	S0	S1.9	2500
NGC5940	15 31 18.1	+07 27 28	0.033	139.74	0.68	SBc	S1.0	5240
NGC6212	16 43 23.1	+39 48 23	0.030	123.89	0.60	Sb	S1	6050
IISZ10	13 13 05.8	−11 07 42	0.034	139.74	0.68	?	S1.5	3760

[a]From the bulge disk decomposition, MRK335 seems better described by a unique high Sérsic profile. This object is therefore rejected from our bulge analysis.

[b]From the bulge disk decomposition, ESO438G9 seems a bulgeless galaxy. This object is therefore rejected from our bulge analysis.
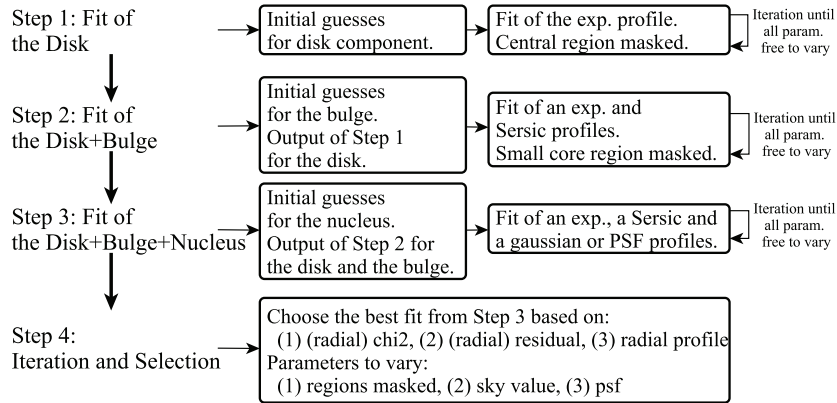
Figure 5.2: Our iterative fitting procedure.

fit by studying the effect of saturated regions in the images and the dependence of the fits to the PSF. We detail our iterative fit procedure in a paragraph below, our treatment of additional structures such as bars, rings and spirals, and the particular attention given to the background level. We present all our fits in Fig. C.1 to Fig. C.8 and our fit results and inferred values in Tab. C.1 to Tab. C.4.

The relevant results of our fits are given in Tab. 5.2. Among them, the reduced chi-square value χ_ν^2 from the fit, first indicator of its quality. Our mean χ_ν^2 values are 1.1 for NLS1s and 1.06 for BLS1s, reflecting the overall acceptability of the fits.

During this process, we have found two objects for which no acceptable bulge disk decomposition could be performed. Specifically, the morphology of MRK335 is mainly point-like and is better described by a single high Sérsic index profile, while ESO438G9 seems to be a bulgeless galaxy also consistent with its morphological type. We have therefore excluded these two objects from the bulge analysis discussed in Section 5.3.3, which is performed on 9 NLS1 and 18 BLS1 galaxies.

Fit procedure

To accomplish the bulge-disk decomposition, we use the two-dimensional profile fitting algorithm GALFIT (Peng et al., 2010), which allows, by minimizing the χ^2 value, to model the light profiles using e.g. Sérsic profiles.

Since we fit HST images, we generate the PSFs with the TINYTIM[5] code for the WFPC2 camera as well as the F606W filter. For each image, we create a PSF referenced to the galaxy center with an uniform weight along the wavelength range.

Initial parameters are estimated from visual inspection of the images (positions, P.A., ellipticities, radii, etc.). Nevertheless, our iterative fit procedure, as described hereafter, ensure that the choice of initial estimates do not influence the final results.

Our procedure can be divided in 4 steps as summarized in Fig. 5.2. For each step we create appropriated masks to remove regions from the fits.

1. We start by fitting only the disk of the galaxies using an exponential profile and masking the central region.

---

[5]http://www.stsci.edu/software/tinytim/

Table 5.2: Results of the bulge disk decomposition for the NLS1s and BLS1s. Columns: (1) object name; (2) fitted components. The different components p, g, s, d, b stand respectively for PSF, Gaussian, Sérsic, disk (exponential) and background (sky). Components are put in brackets if one or more of their parameters are kept fixed in the fit; (3) the $FWHM_g$ of the Gaussian component in kpc; (4) the bulge Sérsic index; (5) R_b, the effective radius of the bulge in kpc; (6) R_d, the scale radius of the disk in kpc; (7)-(8) axis ratio of the bulge and the disk components; (9)-(10) B/D and B/T, the bulge-to-disk and bulge-to-total luminosity ratios; (11) χ^2_ν, the reduced χ^2 of the obtained fit. See also Appendix C and Tab. C.1 to Tab. C.4.

Object Name	Comp.	$FWHM_g$ (kpc)	n_b	R_b (kpc)	R_d (kpc)	q_b	q_d	B/D	B/T	χ^2_ν
NLS1 SAMPLE										
KUG1136	g+s+d+b	0.07	1.21	0.95	3.15	0.76	0.62	0.20	0.17	1.16
MRK0042	g+s+d+b	0.07	1.27	0.44	3.12	0.82	0.58	0.21	0.18	0.95
MRK0335[a]	g+s+b	0.18	3.41	1.27	–	0.93	–	–	–	1.20
MRK0359	g+s+d+b	0.08	1.41	1.19	7.45	0.67	0.83	0.12	0.11	1.03
MRK0382	g+s+d+b	0.12	1.36	0.52	3.02	0.94	0.54	0.46	0.31	1.49
MRK0493	g+s+d+b	0.08	0.74	0.34	3.74	0.97	0.41	0.17	0.15	1.02
MRK0766	g+s+d+b	0.06	1.88	0.15	1.21	0.74	0.44	0.13	0.11	1.05
MRK0896	g+s+d+b	0.10	2.06	0.37	2.82	0.77	0.71	0.18	0.15	1.34
MRK1044	g+s+d+b	0.07	1.45	0.20	1.18	0.91	0.76	0.44	0.30	1.05
NGC4748	g+s+d+b	0.07	1.93	0.25	1.89	0.98	0.68	0.25	0.20	0.68
BLS1 SAMPLE										
ESO438G9[b]	g+d+b	0.06	–	–	1.76	–	0.52	–	–	1.39
F1146	g+s+d+b	0.07	3.74	0.90	2.09	0.47	0.65	1.22	0.55	1.54
IC1816	g+s+[d]+b	0.07	1.98	0.41	[4.47]	0.92	0.67	0.11	0.10	0.84
Mrk0279	p+s+d+[b]	–	2.18	2.48	11.11	0.58	0.56	0.57	0.36	0.97
Mrk0290	g+s+d+b	0.10	4.06	0.47	2.22	0.86	0.88	0.90	0.47	1.11
Mrk0352	g+s+d+b	0.05	4.49	0.90	1.59	0.98	0.76	0.79	0.44	0.84
Mrk0423	[s+d]+b	–	2.13	0.43	1.72	0.69	0.68	0.73	0.42	1.62
Mrk0530	[g]+s+d+b	0.17	2.4	1.04	4.04	0.85	0.65	0.60	0.38	0.75
Mrk0595	g+s+[d]+b	0.06	3.47	0.74	1.86	0.66	[0.75]	1.92	0.66	1.30
Mrk0609	g+s+[d]+[b]	0.15	2.28	1.48	[2.53]	0.79	[0.95]	1.60	0.62	2.52
Mrk0704	g+s+d+b	0.16	2.88	1.19	6.29	0.70	0.50	0.75	0.43	1.25
Mrk0871	g+s+d+b	0.12	1.28	0.61	3.78	0.52	0.38	0.13	0.11	0.91
Mrk0885	g+s+d+b	0.07	2.62	2.70	9.05	0.74	0.52	0.32	0.24	0.83
Mrk1126	g+s+d+b	0.04	1.86	0.27	1.78	0.86	0.66	0.17	0.15	0.47
Mrk1400	g+s+d+b	0.12	1.7	0.55	2.27	0.61	0.31	0.32	0.24	0.98
NGC5252	g+s+d+b	0.07	3.9	2.42	3.20	0.53	0.44	0.58	0.37	0.35
NGC5940	g+s+d+b	0.10	1.23	0.30	3.77	0.89	0.66	0.06	0.06	0.99
NGC6212	g+s+d+b	0.09	1.52	1.23	2.88	0.75	0.70	0.77	0.43	0.87
IISZ10	g+s+d+b	0.18	1.92	1.56	4.29	0.91	0.72	0.70	0.41	0.57

[a]From the bulge disk decomposition, MRK335 seems better described by a unique high Sérsic profile. This object is therefore rejected from our bulge analysis.

[b]From the bulge disk decomposition, ESO438G9 seems a bulgeless galaxy. This object is therefore rejected from our bulge analysis.

2. Once a reasonable model is obtained, we fit an additional Sérsic component to model the bulge. Our initial estimate of the Sérsic index is $n_b = 2$ (*i.e.* the index threshold between pseudo- and classical bulges), while the other parameter initial estimates are based upon visual inspection. When fitting, we first keep the outputs of our step 1 fixed in the fit and then free to vary (together with the Sérsic profile parameters). During this step we mask only the core of the galaxies (5 to 10 pixels radius) to avoid possible influence of the central nucleus or AGN source.

3. We then fit an additional Gaussian (with initial FWHM of 2.5 pixels) to model the AGN and iterate, if necessary, until all parameters are free to vary. As a non-negligible fraction of the images presents a saturated core with charges leakage along the columns (34% in total, 50% in the NLS1 and 26% in the BLS1 samples), we mask carefully these pixels. We also verify the resulting FWHM of the Gaussian and its axis ratio. An additional motivation to use a Gaussian instead of a PSF is to model any nuclear star cluster which, if not accounted for in the fit, will artificially increase the bulge Sérsic index.

During these three steps, we judge the quality of the fit based on the residual images, the χ^2 values, and the parameters values (ensuring that they are physically meaningful : the magnitude of the components have to be greater than the sky level, the Sérsic index value should be acceptable, in particular $n_b < 8$, and the physical radii R_b and R_d should be reasonable).

4. At the end of the third step, we additionally look at the radial profiles of the model, its components, and the original image. These plots, together with the radial residual and the radial χ^2_ν enable us to diagnostic possible problems and identify influences of non-fitted structures. Upon examination of these plots and the image residuals, we decide whether it is necessary to mask relevant structures such as rings or spirals. We refine the masks and the fits until the radial profile of the model does not appear to be influenced by these structures but do translate correctly the bulge and the disk components.

While the GALFIT outputs provide errors, those are purely statistical and are insignificant compared to systematic errors. In the following sections, we discuss the robustness of our fits to different parameters: the treatment of additional structures (deviation from idealized profiles), the unprecise knowledge of the background level, the core saturation and the PSF. Those parameters give indirect information on the systematic errors. Finally, we give in Fig. C.1 to Fig. C.8 (appendix C) all our fits where we indicate by open symbols the radial ranges entirely or partially masked. The radial residual and the radial χ^2_ν, given in the upper panels, also provide indirect information on the fit errors.

Choice of fitting range: treatment of additional structures   As already mentioned, any nuclei is accounted for in the fits by the use of a small Gaussian profile. The alternative consists of removing the nucleus from the fit by masking it. Nevertheless, with such a procedure, the bulge-disk decomposition is sensitive to the quality of the mask of the nucleus and can also be affected by the reduced number of constraints, *i.e.* the bulge can be under-constrained if the mask is too large. Despite these considerations, we try the alternative and mask systematically the central region of the images. We use a default circular mask with 10 pixels radius, adjusting it only in a few cases (4/28) to have a minimum radius of 5 times the standard deviation σ of the Gaussian component (2/4) or to keep a reasonable number of constraints for the bulges (2/4). The median Sérsic index difference between the fits with nucleus masked and the fits with the nucleus included is reasonably small: 0.22 and 0.29 for

the NLS1 and BLS1 sample respectively. This test shows that to mask the nucleus instead of fitting it by a Gaussian component biases slightly the Sérsic indices to higher values. Nevertheless, except for a few cases (3/28 with $\Delta n_b > 2$ and 2/28 with $2 > \Delta n_b > 1$), the increase remains small, acknowledging the robutness of the fits.

As our samples are made of high resolution HST data, they also present many structural details. The effect of deviations of surface brightness such as rings, bars or spirals are considered in the last step of our fitting procedure (step 4). Upon examination of the radial profiles and the residual image, we identify, if any, potential additional structures and manually create appropriate 2D masks. We then refit our model and iteratively adjust the mask according to the radial profile and residual image. We recognize that this practice is subjective but nonetheless we believe it to be necessary. Indeed, modelling structural details – such as inner rings – is a complex task, and the fit of any additional component requires more constraints, which cannot be provided by our single snapshot HST images (indeed the current bulge/disk models already give $\chi_\nu^2 \sim 1$ for most of the fits). The alternative practice of not masking these structures could lead to wrong results. For example, in the case of MRK 42, presented in Fig. C.1, we first do not mask the inner-ring and obtain a compact bulge with $n_b \sim 0.7$ (in our step 3), while after masking the stucture, we obtain a more reasonable Sérsic index $n_b \sim 1.27$ (in our step 4), which – according to the radial profile in Fig. C.1 – is a much more accurate model of the bulge. Finally, our iterative process ensures that the regions we mask are physical additional structures in the galaxies.

Background level Given that the background may be coupled to the disk profile, an important aspect of bulge-disk decomposition is to correctly fix the sky level. Since no precise sky measurements are available for our HST images and that the galaxies filled most of the field of view, we have to fit the background level together with the other components and minimize the coupling with the disk profile. Therefore, we take a particular care to any additional light profiles in the images such as stars, satellite galaxies or remaining large cosmic rays. These are carefully masked so to minimize their influence on the sky level. Despite this particular attention, we fix the sky level in 2 cases – MRK279 and MRK609, both part of the BLS1 sample – at the value obtained in our step 1 (*i.e.* fit of the disk and the background only). If the sky is not fixed, the resulting parameters are not physical: in the case of MRK 279 the background becomes negative and the radius of the disk excessively large; in the case of MRK 609 the sky becomes extremely large and the disk and the bulge shrink (with $n_b < 0.5$).

Reliability of the bulge/disk decomposition

We analyze here possible effects influencing our fit results : the core saturation in the images and the choice of PSF.

As already mentioned, a non-negligible fraction of the images presents saturated core with charges leakage: 50% in the NLS1 sample and 26% in the BLS1 sample. To minimize any effect on our fits, we mask carefully the saturated pixels and the pixels affected by charges leakage. Looking at the Sérsic indices, we find that galaxies with saturated core have a mean Sérsic index $< n_b > = 2.27$ and galaxies without saturated core have $< n_b > = 2.06$. Therefore, if the saturation still affect our images, it would tend to increase the Sérsic index. As our NLS1 sample is more affected by saturation than our BLS1 sample, it would tend to increase the mean Sérsic index of NLS1s. Consequently, any remaining effect of the saturation cannot

account for the difference between NLS1 and BLS1 host bulge Sérsic indices but would tend to decrease it.

We test the dependence of our fit to the PSF used for convolution by refitting our NLS1 sample with different PSFs. The PSFs for this test are also generated with TinyTim but, instead of using an uniform weight along the wavelength range, they are produced at the central mono-wavelength of the filter F606W. The difference in Sérsic index ranges from 0 to 0.01 except for one object where it is 0.06. Therefore, we conclude that the PSFs are not critical in our fits and that our choice of using an uniform weight along the wavelength range to create the PSFs with TinyTim is acceptable.

5.3.3 Structural properties of NLS1 and BLS1 host galaxies

The Sérsic index n_b in the bulges

In Fig. 5.3, we compare the results obtained for the 9 NLS1 galaxies to the distribution found by Fisher & Drory (2008) for pseudo- and classical bulges. According to their results, the mean Sérsic index of pseudo-bulges is 1.69 with only $\sim$10% of them having an index greater than 2. For our NLS1 sample, we find $< n_b > \sim 1.48$ (and a standard deviation for the distribution of $\sigma_n \sim 0.39$) with none of them significantly exceeding a Sérsic index of 2.

The bottom panel of Fig. 5.3 compares the distribution of NLS1 and BLS1 host bulge Sérsic indices from the analysis of our samples. While the two distributions are clearly different, BLS1 host bulges also tend to have lower Sérsic indices than the Fisher & Drory (2008) classical bulges. We find $< n_b > \sim 2.54$, $\sigma_n \sim 0.97$ for BLS1 host bulges, in contrast to $< n_b > \sim 3.49$ obtained by Fisher & Drory for classical bulges. Thus, our results suggest that BLS1s do not have "pure" classical bulges, but rather mixed bulges composed of pseudo- and classical components.

It is appropriate to mention here the work of Laurikainen et al. (2007). They found that, for inactive galaxies, the mean bulge Sérsic index is $\sim$2.5 or less across the Hubble sequence. These results can also be interpreted as the existence of a large range of composite bulges between the two extreme "pseudo-" and "classical" bulge types. Putting this result into perspective with our bulge/disk decomposition suggests that the bulges of NLS1 hosts are likely to be "pure" pseudo-bulges, while the bulges of BLS1 hosts appear to be composite bulges and hence have Sérsic indices distributed around $n_b \sim 2.5$.

In order to test the significance of the difference between the Sérsic index distributions of NLS1s and BLS1s, we use the Kolmogorov-Smirnov test. As such, the cumulative distributions of the Sérsic index are presented in Fig. 5.4. The slopes of these distributions reflect the difference in the dispersions given above ($\sigma_n \sim 0.39$ and 0.97 for the NLS1 and BLS1 samples respectively). They emphasize that the population of NLS1 bulges appears to be like the population of pseudo-bulges, while the properties of the BLS1 bulges are more widely distributed between pseudo- and classical bulges. While we cannot fully reject the null hypothesis of the Kolmogorov-Smirnov test, it yields a probability of $< 1.2\%$ that the NLS1s and the BLS1s are drawn from the same parent distribution. This is a remarkable result that again underlines the connection between black hole and bulge properties.

Since a result from Weinzirl et al. (2009) suggests a possible link between bars and bulges, we verify that the relative bar fractions in our samples have a minimum impact on our result of Fig. 5.3. Indeed, as described previously in section 5.3.2, our selection of NLS1s and BLS1s respects the relative bar fraction observed, *i.e.* $\sim 25\%$ in BLS1 and $\sim 75\%$ in NLS1 galaxies.
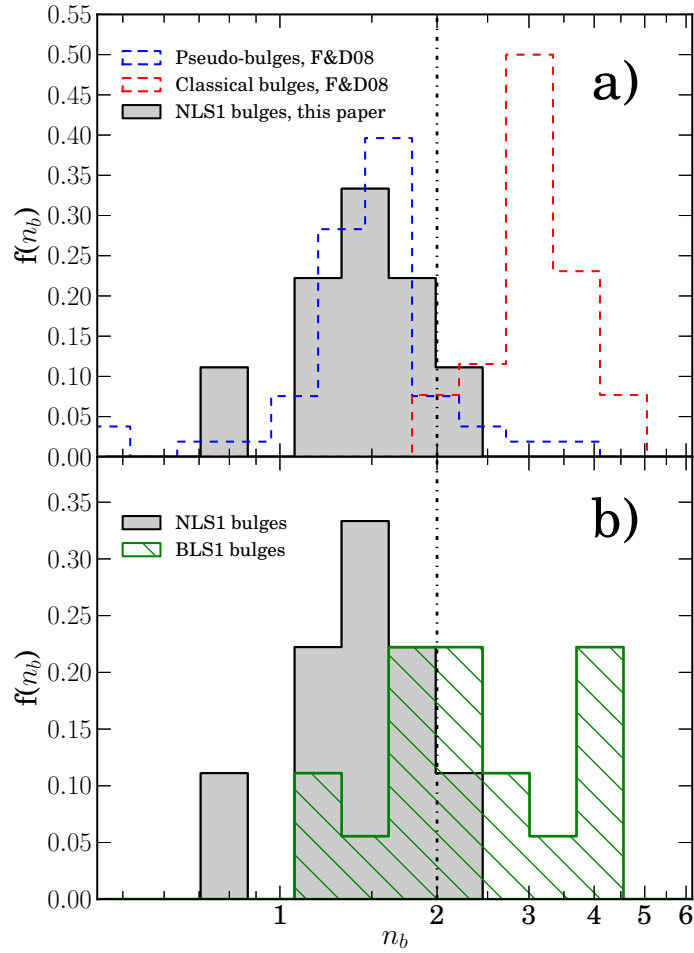
Figure 5.3: Histogram of bulge Sérsic indices, n_b. a) NLS1 host bulges (9 objects) from our sample compared to pseudo-bulges (53) and classical bulges (26, we do not include their sample of elliptical galaxies) from Fisher & Drory (2008). b) NLS1 host bulges compared to BLS1s host bulges (18 objects).
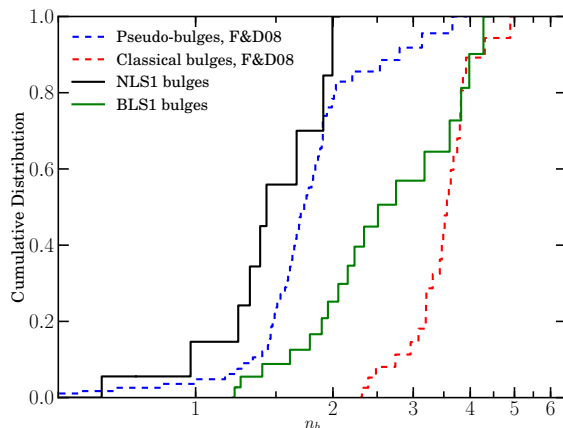
Figure 5.4: Cumulative distribution vs. the Sérsic index for pseudo- and classical bulges (Fisher & Drory, 2008), and NLS1 and BLS1 host bulges, this paper.

Therefore, we consider in Fig. 5.5 (*right*) the distribution of bulge Sérsic indices of NLS1 and BLS1 galaxies with bars only. While we observe a general small shift towards lower Sérsic indices (as expected from, e.g., Weinzirl et al., 2009), NLS1 and BLS1 are clearly distinct. Following this observation, we reasonably conclude that although the presence of a bar can be linked to the bulge Sérsic index, it does not imply that the bulge is a pseudo-bulge. Thus, our result that NLS1s tend to possess pure pseudo-bulges in contrast to BLS1s, is not a consequence of different bar fractions in the two populations.

Finally, we consider the influence of the Seyfert type of the BLS1s on our Sérsic measurements. Indeed, changes from type 1 to intermediate type Seyferts can be attributed to changes in the ionizing radiation of the AGN (e.g. Goodrich, 1990), or to variation in the absorbing material (Maiolino & Rieke, 1995, Forster, 1999), or as well to different inclination of the host galaxies (e.g. Maiolino & Rieke, 1995, Ramos Almeida et al., 2009). These effects can explain the large Balmer decrements in the optical spectra of intermediate type galaxies but can also indirectely bias our Sérsic index measurements. Indeed, in the case of intermediate type Seyferts, a fainter AGN would ease the fit, but an excess of dust in the host galaxy and projection effects (nearly edge-on host spirals) can make fitting the host harder. For these reasons, we check whether there is any systematic effect on our fits by looking at the Sérsic index versus the Seyfert type of the BLS1s (given in Tab. 5.1), the result is given Fig. 5.5 (*left*). Since no trend of the Sérsic index with the BLS1 sub-class can be observed, we can be confident that our fits are not biased by systematic effects related to the intermediate BLS1 classifications.

Similarly, NLS1s are a sub-class of type 1 AGN, for which the Seyfert sub-classification is based solely on the properties of the AGN itself. But our result also shows that the bulge properties of the NLS1 host galaxies do represent a distinct sub-class of the bulges of BLS1 hosts.

Bulge prominence and fundamental plane projections

Building on our fit results, we study the bulge prominence by looking at the size distribution of the bulges, as well as the bulge-to-disk (B/D) and bulge-to-total (B/T) light ratios. The
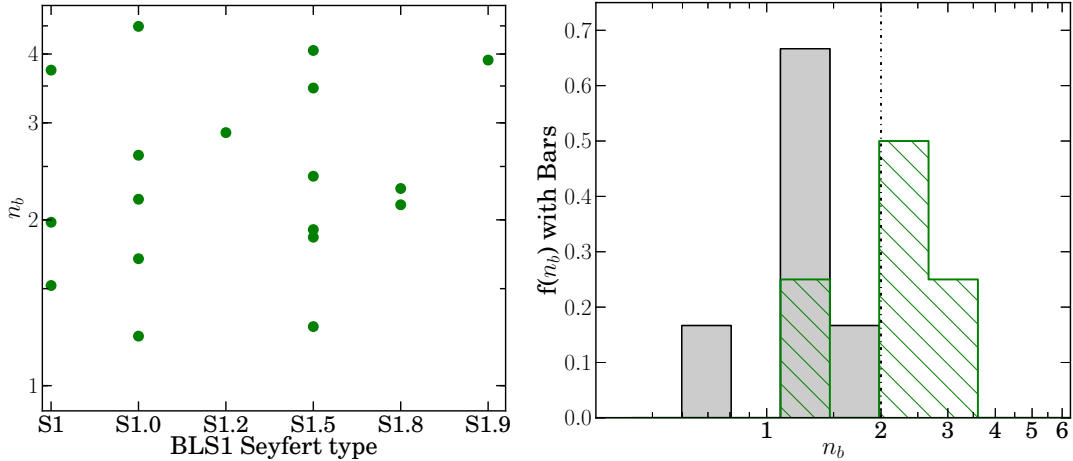
Figure 5.5: *(Left)* BLS1 Seyfert type versus their respective Sérsic index. Since there is no trend, the Sérsic index does not seem affected by the Seyfert classification of our BLS1s. *(Right)* Histogram of bulge Sérsic indices, n_b, of NLS1 (6 objects) and BLS1 (4 objects) barred galaxies, see also Tab. 5.1 for the classification and Tab. 5.2 for n_b.

first objective here is to further explore the differences between NLS1 and BLS1 host bulges. But doing so also enables us to confirm the validity of our bulge-disk decomposition.

We compute the B/D and B/T light ratios using our fit parameters (see Equation C.8 and Equation C.9) given in Tab. 5.2, and present their distribution in Fig. 5.6 *(left)*. The median B/T of 0.39 in BLS1s and 0.17 in NLS1s indicates that NLS1 galaxies have lower B/T light ratios than BLS1s. We compare these distributions to $<$B/T$>= 0.41$ for an average classical bulge and $<$B/T$>= 0.16$ for an average pseudo-bulge given by Fisher & Drory (2008). Gadotti (2009) also finds similar values. The B/T ratio therefore provides strong support for our conclusion that NLS1 bulges are pseudo-bulges, while BLS1 bulges are largely composite or classical.

In the same Fig. 5.6 *(right)*, we also plot the B/T light ratios versus the Hubble Type, the Sérsic index, and the effective radius of the bulges. As expected, the mean B/T ratio tends to decrease with the Hubble Type (e.g. Graham & Worley, 2008, Masters et al., 2010), and hence it appears that NLS1 galaxies tend to be of later type than BLS1 galaxies (Fig. 5.6 *(left)*). The two last plots illustrate again that NLS1 bulges have less prominent (i.e. smaller, fainter, less cuspy) bulges than BLS1 bulges.

While the Sérsic index is a convincing tool to distinguish pseudo-bulges from classical bulges (Fisher & Drory, 2008), Gadotti (2009) uses the Kormendy relation ($< \mu_e > -r_e$) to identify pseudo-bulges as fainter bulges than predicted by the fundamental plane of elliptical galaxies. In Fig. 5.7, we present the Kormendy relation, the surface brightness magnitude at the effective radius (see equation C.5 and equation C.7), and the Sérsic index versus the effective radius of the bulge. For Fig. 5.7 a) and b) we have overdrawn linear fits to the data for the BLS1 sample. While these do not reveal any marked offset between the two NLS1 and BLS1 classes, NLS1 bulges are systematically fainter than those of BLS1 (i.e. they tend to lie under the line). This result is consistent with the common structural properties we are finding for the NLS1 class. Finally, Fig. 5.7 c) shows NLS1 and BLS1 host bulges, together with pseudo- and classical bulges (from Fisher & Drory, 2008) in the $n_b - r_e$ plane. Again, it
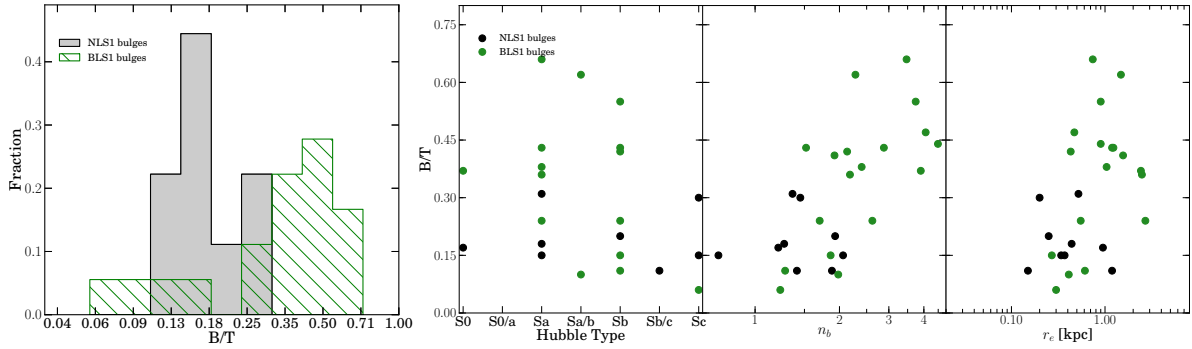
Figure 5.6: *(Left)* Distribution of bulge-to-total light ratio in NLS1 and BLS1s galaxies. According to (e.g. Masters et al., 2010), NLS1 galaxies would therefore be later type galaxies than BLS1. *(Right)* Verification of the mean B/T decrease with the Hubble Type, B/T against the bulge Sérsic index and against the bulge effective radius. The two last plots confirm the link between B/T light ratios and the prominence of the bulge.

shows clearly that NLS1s lie in the region occupied by pseudo-bulges, while BLS1 are spread over the whole range of pseudo- and classical bulge properties.

Finally, we also look at the distribution of Sérsic indices with the FWHM of the broad component of Hβ in Fig. 5.8. While the sample is not large enough to make conclusive remarks, we note the existence of a correlation of the FWHM with the Sérsic index, confirmed by a Spearman's rank correlation coefficient of ~ 0.49. This correlation indicates, at least in the low FWHM($H\beta$) range, a possible connection between the bulge concentration and the broad line region.

Complementary Studies

Three other studies support our conclusion about the bulges of NLS1s.

In studying the central engines of NLS1 galaxies, Ryan et al. (2007) perform a bulge disk decomposition of 11 NLS1s galaxies with $z \leq 0.05$ in the J-band and K_s-band using adaptive optics data from the 3.6m CFHT. Their mean Sérsic indices are $< n_J >= 1.52$ and $< n_K >= 1.38$, and standard deviations σ_n of ~ 0.44 and ~ 0.48 respectively. As the Sérsic index seems to be, at most, weakly correlated to the photometric band (see e.g. Fisher & Drory, 2008, who compare the Sérsic index in the V and in the H bands), the Ryan et al. decomposition supports our results.

In studying low black hole mass systems, Greene et al. (2008) argue that most of their disk galaxies have pseudo-bulges. Since these systems have small FWHM(H$_\beta$), they are also likely to be NLS1s although the relative FeII strengths they found are lower than in classical NLS1s (Greene & Ho, 2004).

In a more recent paper, Mathur et al. (2012) study 10 NLS1 galaxies (ACS/HRC using the F625W filter). They perform a similar bulge disk decomposition (*i.e.* they fit a Sérsic profile for the bulge and an exponential profile for the disk), and also conclude that they have pseudo-bulges. While our conclusions are based mainly on the Sérsic index, they use the Kormendy relation, as advised by Gadotti (2009), to conclude on the pseudo-bulge nature of NLS1 bulges. Indeed, they do not find systematically low Sérsic indices but obtain a mean Sérsic index of $< n >= 2.61$ and a large Sérsic index dispersion $\sigma_n = 1.82$. In fact only six
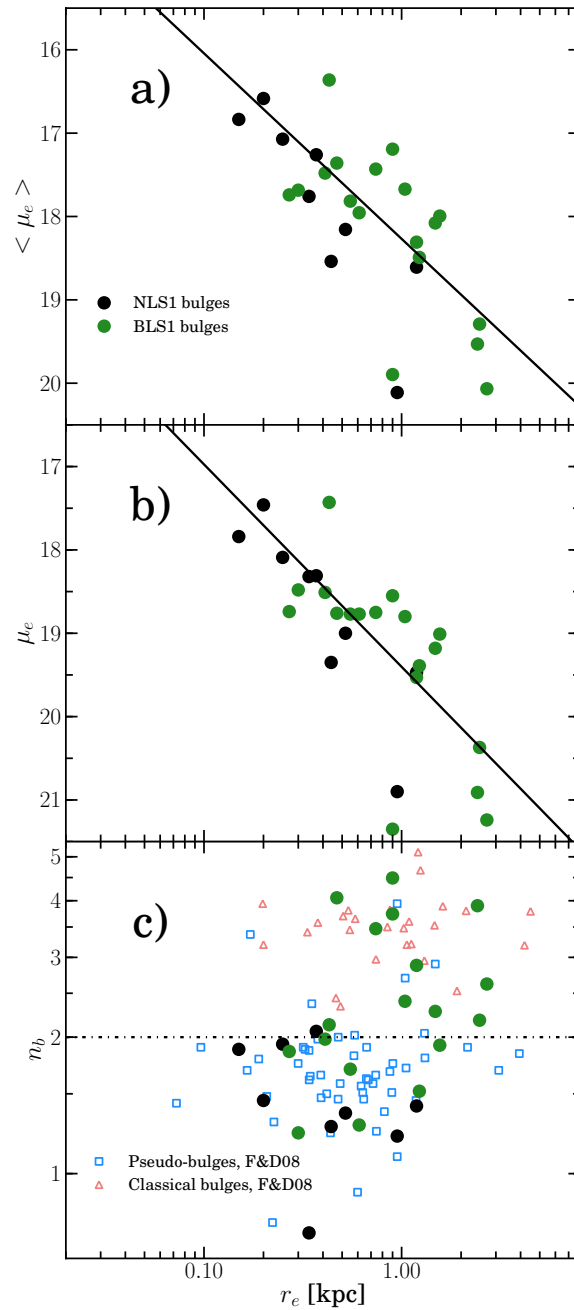
Figure 5.7: Relations of bulge parameters with the effective radius r_e of the bulges. a) Kormendy relation, *i.e.* the mean surface brightness magnitude within the effective radius versus r_e. b) Surface brightness magnitude at the effective radius versus r_e. The solid lines are the linear fit found for BLS1s from our sample. The magnitudes are given in the STMAG system. c) Effective radius vs. Sérsic index comparing classical and pseudo-bulges from Fisher & Drory (2008) with our samples of NLS1s and our BLS1s. The NLS1s seem to lie at the expected $r_e - n_b$ of typical pseudo-bulges.
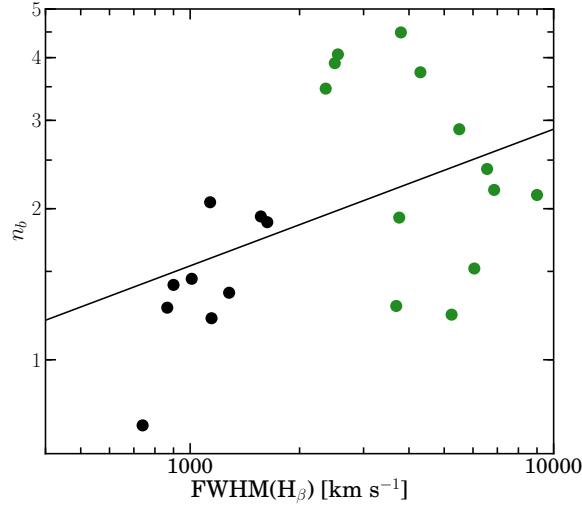
Figure 5.8: FWHM vs Sérsic index. NLS1s and BLS1s are represented by black and green dots respectively. The linear fit is based on the two samples. The Spearman's rank correlation coefficient is ~ 0.49.

out of the ten galaxies in their sample have Sérsic index values consistent with pseudobulge profiles. To try and understand this difference, we note that the Mathur et al. (2012) sample differs from that presented by us here. Specifically, their sample is found at larger redshift, $< z > \sim 0.24$, leading to a scale in kpc/$''$ on average ~ 4 times larger than in our sample. A large scale limits how well the fit is constrained by the central regions, and confusion in the light distributions between the nucleus and the bulge may arise, possibly leading to higher Sérsic indices.

One caveat to these works is the lack of a comparison sample of BLS1 hosts, which our results show is important. By including one, we show that one should consider the hosts of NLS1s to be a sub-set of all BLS1s, rather than being totally separate. The distinction between NLS1 and BLS1 hosts is thus that while NLS1 hosts specifically have pseudo-bulges, BLS1 hosts have a range of bulge types including pseudo-bulges, composite bulges, and classical bulges.

5.3.4 Secular evolution has always prevailed

The Sérsic index distribution and the prominence of the bulge both indicate that, statistically, NLS1 hosts have "pure" pseudo-bulges, in contrast to BLS1 galaxies. The consequence of this result (Kormendy & Kennicutt, 2004) is that internal secular processes must have dominated the past evolution of NLS1 hosts. And therefore it is from this perspective that one should attempt to explain the particular AGN properties observed in NLS1 galaxies (such as low black hole mass, high accretion rates, etc.).

5.4 NLS1 evolution and black hole growth

We explore here the implications of our conclusion that secular processes have dominated the evolution of NLS1 galaxies. We focus on the issue of the black hole growth of NLS1s, and in

understanding whether or not NLS1 galaxies are in a special phase of black hole growth.

5.4.1 Expected galaxy populations that have evolved through secular evolution

Over the last few years, the relative importance of major mergers versus minor mergers and secular processes in driving galaxy formation and evolution has become a key issue in simulations and semi-analytic models. Genel et al. (2008) and Parry et al. (2009) offer two different perspectives to understanding the growth processes of dark matter halos and galaxies. Both studies conclude that major mergers are not necessarily the main driver of galaxy mass evolution.

Genel et al. (2008) investigate, by analysing cosmological simulations, the growth of dark matter halos. They extract halo merger fractions and mass accretion rates from the Millenium simulation in order to study the possible role of major mergers in the evolution of halos from $z \sim 2$ to $z = 0$. Following the fate of halos in the mass range $11.5 \leq \log M_{z=2.2} \leq 12.8$, they find that $\sim 1/3$ of halos which reach z=0 have not undergone any major mergers since $z \sim 2.2$ and that such halos gain $\gtrsim 70\%$ of their new mass via mergers less intense than 1:10, demonstrating the importance of non-major merger processes. In a following paper, Genel et al. (2010) also show that, independently of halo mass, $\sim 40\%$ of the mass in halos have been assembled through smooth accretion.

Parry et al. (2009) study galaxy growth by analysing two different galaxy formation models, both also based on the Millenium simulation. Their statistical results are revealing. For both models, they find that only $\leq 49\%$ of ellipticals, $\leq 3\%$ of S0s and $\leq 2\%$ of spirals undergo a main branch major merger (mass ratio greater than 1:3) in their entire formation history. In other words, $\sim 98\%$ of spiral galaxies – which are the most common morphological type of NLS1s host galaxies – do not undergo any major merger. These results are largely independent of total stellar mass of the galaxy except for ellipticals. In a further step, they quantify the relative impact of disk instabilities, major mergers and minor mergers on galaxy morphology by determining the stellar mass fraction from each process as a function of the total stellar mass. For both models, they find that instabilities and minor mergers are the main mass contributor, with their relative contributions depending on the treatment of disk instabilities in the models (see Parry et al., 2009 and references therein).

While it is beyond the scope of this paper to discuss the treatment of the various physical processes in these galaxy formation models, one clear conclusion is that even hierarchical cosmological simulations give rise to large galaxy populations that have evolved through secular processes. Interestingly, observational studies also reach similar conclusions.

Weinzirl et al. (2009) study present day ($D < 60$Mpc) spiral galaxies. By performing two dimensional multi-component decompositions of 143 high mass ($M \geq 10^{10}\,M_\odot$) spirals, they analyze the bulge Sérsic index and B/T distributions. Their results highlight the large fraction of bright spirals having B/T$\leq$0.2 ($\sim 69\%$) and $n \leq 2$ ($\sim 76\%$) where many of them host bars ($\sim 66\%$). By comparing their result to theoretical predictions, they find that $\sim 66\%$ of present day high-mass spirals have not undergone a major merger since $z \leq 2$ and likely not even since $z \leq 4$. This conclusion conveys the importance of minor mergers (in the present case for a mass ratio $< 1:4$) and secular processes since $z \leq 4$.

Finally, Cisternas et al. (2011) recently analyzed the relevance of different triggering mechanisms for AGN activity. Based on visual analysis of 140 AGN and 1264 inactive galaxies with HST imaging, they measure the fraction of distorted morphologies which they take to

be a signature of recent mergers. They conclude that the bulk of black hole accretion has been triggered by secular processes and minor interactions since $z \sim 1$.

By assessing the role of secular processes, these various theoretical and observational lines of evidence offer a cosmological context to our conclusions concerning NLS1 hosts. They show that a significant fraction of galaxy mass and a large number of galaxies have evolved from early cosmic times without any mergers. It is reasonable to suggest that NLS1s, which our analysis shows must have evolved without mergers, may be tracers of this population of galaxies. Our attempt, in the rest of this section, to put this hypothesis on a more quantitative basis leads us to an estimate of the duty cycle of NLS1s.

5.4.2   How common are NLS1s?

In the last decade, various surveys of nearby galactic nuclei have found that the fraction of objects classified as AGNs is surprisingly large. They show that, of all local galaxies, approximately 10% are Seyferts and 40% can be considered active (see Ho, 2008 and references therein).

Looking at the NLS1s, several surveys using optical and X-ray selected samples (e.g Williams et al., 2002, Crenshaw et al., 2003, Zhou et al., 2006) find that they make up approximately 15% of Seyfert 1 galaxies. Based on the unified AGN scenario, one can expect that this fraction should apply also to type 2 Seyferts: that $\sim$15% of Seyfert 2 galaxies may have narrow broad emission lines that are hidden from sight by the obscuring torus. Such a possibilty has already been suggested by Zhang & Wang (2006), who argue that Seyfert 2s without a hidden BLR (i.e. one that cannot be observed in polarised light) are the counterparts of NLS1s. Taking this further, one could reasonably argue that the NLS1 definition might extend even to the lower luminosity AGN.

Combining these fractions together leads to the assessment that 2–6% of local galaxies could be "NLS1-like" galaxies, *i.e.* active galaxies with "narrow" broad lines whether obscured or not, the evolution of which has been dominated at all cosmic times by secular processes.

5.4.3   Duty cycle of NLS1 black holes

Our analysis in section 5.3 shows that NLS1 galaxies statistically have a bulge Sérsic index $n_b < 2$ and a bulge-to-total light ratio $B/T < 2$. The observational study of Weinzirl et al. (2009), corroborated by the theoretical study of Parry et al. (2009), argues that approximately 2/3 of local spiral galaxies[6] have similar properties to NLS1 hosts. Assuming that each galaxy among this population can potentially undergo nuclear activity and become "NLS1-like"[7], we can estimate the duty cycle of NLS1s. We argue above that "NLS1-like" objects may comprise as much as $\sim$6% of local galaxies (note that we use the upper end of the range above in order to be conservative later in our estimates of black hole growth). This implies that their duty cycle should be around $\sim$9%.

Since the Hubble sequence formed at z$\sim$1 (van den Bergh et al., 2000, Kajisawa & Yamada, 2001, Conselice et al., 2004, Oesch et al., 2010, Cassata et al., 2010) with bars becoming numerous at this redshift (Abraham et al., 1999, Elmegreen et al., 2004, Jogee et al., 2004,

---

[6]high mass ($M_\star \geq 1.0 \times 10^{10} M_\odot$) low-to-moderately inclined ($i < 70°$) spirals.

[7]clearly the 2/3 of the local galaxies are not necessarily potential true NLS1s; but, given that their hosts appear to have evolved over cosmic time in a similar way, they might be "NLS1-like", as defined in Section 5.4.2, during their accretion phase.

Marinova & Jogee, 2007, Sheth et al., 2003, 2008), accretion driven by large-scale bars can only have occurred in the last ~7.7Gyr. With a duty cycle of ~9%, this means that NLS1s have actively accreted onto their BHs for ~690Myr.

Assuming their black holes are accreting at the Eddington rate, the e-folding time of their BH build-up is given by the Eddington time-scale, $t_E \approx 4.4 \times 10^8$ yr. Therefore, the black hole mass increase is given by (e.g. Volonteri, 2010) :

$$M_{\mathrm{BH}}(t) = M_{\mathrm{BH}}^{\mathrm{seed}}(t_0) \exp \left(\frac{1 - \epsilon}{\epsilon} \frac{\tau}{t_E} \right), \tag{5.1}$$

where t is the current (observed) time, and $\tau = t - t_0$ is the total accretion duration since the initial time t_0. The radiative efficiency ϵ is a key parameter, and can have a major impact on the black hole growth rate because it is inside the exponential term. The standard value of ϵ is ~ 0.1. Adopting this then, and assuming a seed mass $M_{\mathrm{BH}}^{\mathrm{seed}}(t_0) = 10^3 - 10^4 M_{\odot}$, the current mass $M_{\mathrm{BH}}(t)$ could range from 10^9 to $10^{10} M_{\odot}$. On the other hand, accretion onto a fast rotating Kerr BH can lead to a radiative efficiency $\epsilon \sim 0.2$ or higher (Volonteri et al., 2005, Jogee, 2006). For the same $M_{\mathrm{BH}}^{\mathrm{seed}}(t_0)$, this higher radiative efficiency implies a much slower BH growth and leads to current BH masses between 5×10^5 and $5 \times 10^6 M_{\odot}$.

Based on these very simple estimates, we reach two conclusions. Firstly, NLS1s are not necessarily in a special phase of their black hole growth. Their black holes have required 7–8 Gyr to grow to their current size. To increase their black hole mass by another factor 10 requires – for a 9% duty cycle and $\epsilon = 0.2$ – another ~2.8 Gyr. Thus, despite their high Eddington ratios, NLS1s are not imminently evolving into BLS1s, although they may do this eventually. Secondly, the low BH masses of NLS1s (with respect to BLS1s) can easily be accounted for by a high radiative efficiency. The theoretical and observational evidence for rapidly spinning black holes in NLS1s is the topic of the section 5.5.2.

5.5   Discussion

5.5.1   Differences in NLS1 and BLS1, a selection bias

To the question[8] "are NLS1s a special class of AGN?" Valencia-S. et al. (2013) answer a clear "no". They argue that implicit selection effects (using FWHM(Hβ) <2000km s^{-1}) in NLS1 samples can in principle account, at least partially, for many of the observed properties analyzed in comparison to BLS1s. Their main point is that by selecting sources with FWHM(Hβ) <2000km s^{-1} and assuming a virialized BLR (this is however controversial, see e.g. Marconi et al., 2008), a maximum limit on the black hole mass is implicitly imposed and likewise a maximum bolometric luminosity. Hence, low black hole masses ($\sim$ few $10^6 M_{\odot}$) lead to observational biases favoring detection of high Eddington sources. In a similar vein, Hopkins et al. (2009) argue that samples with an implicit high Eddington-ratio selection would favor lower BH masses and hence less massive more disc-dominated host galaxies, as observed for NLS1s.

The existence of a possible NLS1 selection bias implicitely favoring lower BH masses and high accretion rates is not a concern here. This has been in fact our implicit assumption, and such systems are of particular interest in understanding the growth of BH. It is worth

---

[8]At the 2012 Bonn conference titled "Nuclei of Seyfert galaxies and QSOs - Central engine & conditions of star formation"

remembering however that not all NLS1 do have high accretion rates. For a given luminosity, higher Eddington ratios are related to lower BH-masses. Given the observed $M_{BH} - M_{\rm bulge}$ relation, this also means different bulge and host masses, and hence such systems reside more likely in less massive more disc-dominated hosts. That last picture may not fully hold for NLS1 where the M_{BH}-bulge relations are debated (see section 5.5.3) and their bulges may as well be more massive than predicted by the relations. A second argument against this bias is that the distribution of Hubble type in our sample of BLS1s and NLS1s show only a marginal trend towards earlier type galaxies for BLS1s (see Fig. 5.6). We cannot however exclude a possible selection bias favoring low BH masses, high Eddington luminosity ratios, and more discy-dominated galaxies.

Having pointed out the possible role of these selection biases, our conclusions remain unchanged, particularly as NLS1 are often referred to as "more than just Seyfert 1s with narrow lines". Indeed, with respect to their main defining criteria, NLS1s appear to be essentially dominated at all time by secular evolution. And we have also shown that this is consistent with the cosmological context described above, pointing out that a significant fraction of the active galaxy population may evolve similarly.

5.5.2   NLS1s and highly spinning black holes

As discussed in the last section 5.4.3, the radiative efficiency of the AGNs have a direct impact on their black hole growth and their final black hole masses. But radiative efficiency is determined by the supermassive black hole (SMBH) spin, which in turn is influenced by the AGN accretion history. Different scenarios have been studied where SMBH spins evolve through mergers, subsequent prolonged accretion (constant angular momentum axis of the accreting material, e.g. Volonteri et al., 2005, Berti & Volonteri, 2008) or chaotic accretion (random disc orientations with respect to the black hole, e.g. King & Pringle, 2007, King et al., 2008, Berti & Volonteri, 2008). Volonteri et al. (2005) and Berti & Volonteri (2008) have shown that if major and minor BH mergers are the sole source of material, then the distribution of BH spins in a $z = 0$ galaxy population will reflect that of the initial seed BH spin. In contrast, they find that prolonged gas accretion triggered by galaxy mergers tends to spin BHs up, and that galaxies where a significant fraction of the BH growth occurs in this mode could have maximal BH spin. However, in such a case, most distant quasars would have high radiative efficiency and would inefficiently grow their black hole. This would require massive BH seeds, in conflict with the Soltan argument. If instead, the accretion proceeds by short randomly oriented events (King & Pringle, 2007, King et al., 2008), then the spins will tend to be low and lead to high BH masses, resolving the conflict with the Soltan argument. But NLS1 BHs are likely fed via secular rather than merger processes, therefore the angular momentum of the infalling matter could be related to the host structure and hence have a favoured direction. NLS1 SMBHs could be evolving through the prolonged gas accretion scenario. Therefore, NLS1 secular evolution would imply high spins and low BH masses.

Since the publication of our paper, a number of simulations have refined this picture, focussing mostly on the role of secular processes. Dotti et al. (2013) study the orientation and magnitude of BH spins considering different degrees of anisotropy in the fueling through accretion events (to cover the extreme cases between fully coherent and chaotic accretion modes). They found that the largest spins are in the most massive BHs if the degree of anisotropy is sufficiently high. They conclude that a correlation exists between the kinematics of the clouds feeding the BH and its spin but only for the most massive BH, arguing that below

$M_{BH} \lesssim 10^7 M_{\odot}$ the spin alignment timescale is shorter than the spin magnitude evolution. Hence, low mass BH would always be fast rotators. The cosmological consequences in term of BH evolution (with respect to the Soltan argument) and feedback efficiency remains to be studied to further validate their model[9].

Dubois et al. (2014) perform hydrodynamical simulations of the spin evolution, including AGN feedback. Their black hole spins are evolved through accretion of gas, tracking its angular momentum, and coalescences, dictated by their cosmological environments. They find that coherent gas accretion is the main driver of BH growth for midsize BH ($10^6 - 10^8 M_{\odot}$) leading to maximally spinning BH, where more massive BHs have more moderate spins. They also find that despite the interaction between the AGN and the galaxy gas, the overall coherence of the gas in the disk is not strongly perturbed from 1kpc to 10pc. This is further supported by Maio et al. (2013) on sub-pc resolution showing that the impact of star formation processes on the angular momentum cannot induce very strong chaotic trends in the gas flow. Dubois et al. (2014) further test the impact of degree of gas incoherence, finding that fully chaotic accretion results in low spin values. Conversely randomised gas with some level of coherence (angular momentum vectors pointing in the same semi-sphere) lead to high spins. It appears therefore that BH spin evolution is still a matter of debate, but secular processes favoring coherent accretion are definitely promoting high BH spins.

From an observational point of view, it appears to be possible to derive BH spins using the Fe Kα line in the hard X-ray continuum using accretion disk reflection models. While there are several potential reasons that might prevent one from obtaining a good spin constraint for a given source (such as too few photons, or too narrow iron line hampering the fit to pick out the role of relativistic contributors, Brenneman, 2007) several recent works have been able to derive formal constraints on BH spin for a number of Seyfert galaxies (e.g. Brenneman, 2007, Fabian et al., 2009, Miniutti et al., 2009, Ponti et al., 2010). Among these measurements, we find that most of them are for NLS1s, and that the derived spin values are very high. While there are still too few measurements to draw any firm conclusion, these results are already suggestive that NLS1s could have highly spinning BHs owing to the prolonged disk accretion onto their BHs.

The past few years have seen a large number of BH spins to be published. Reynolds (2013a,b) filtered (by applying "quality-control" criteria) and compiled spin constraints on 22 AGN. Those measurements show a clear population of rapidly spinning BH at low masses ($< 4 \times 10^7 M_{\odot}$), among which many are NLS1s. Hence confirming the earlier trend.

Finally, as we have already touched on in section 5.4.3, a high spin leads to a high mass-to-energy conversion or radiative efficiency (because the last stable orbit is closer to the horizon of the BH), and hence to a slow BH growth. Therefore, the high Eddington ratio typically observed in NLS1s could be a signature not just of highly accreting BHs, but also of rapidly spinning BHs. Given that pseudo-bulges are one consequence of secular evolution in a galaxy, and that another consequence is that the SMBH should be rapidly spinning, our result that NLS1 hosts have pseudo-bulges leads to the prediction that a large fraction of NLS1 BHs should have very high spin. Future X-ray missions may be able to test this.

An alternative explanation, possibly valid for some of the most extreme NLS1, resides in different accretion physics. The current best spin measurements are based on the Fe Kα line fitting assuming a disc truncation at the innermost stable circular orbit (ISCO) radius and

---

[9]Indeed, to first order, this is possibly in conflict with the Soltan argument.

hence negligible emission within it. This has been shown to be valid for a thin accretion disk through magnetohydrodynamic simulations giving strong support to the initial hypothesis (Reynolds & Fabian, 2008). In this context, it is interesting to see that several authors have suggested that some NLS1s may display a different kind of accretion disk (Mineshige et al., 2000, Collin & Kawaguchi, 2004), namely a slim disk (Abramowicz et al., 1988). Such a disk is, like the standard disk, optically thick but is also geometrically thick. The presence of slim disk in some NLS1s could explain their particularly strong soft X-ray excess and rapid, large amplitude, variability (Mineshige et al., 2000). At large luminosities, the viscous heating is not solely balanced by radiative cooling, and advection cooling becomes relevant, more so at higher the luminosity. As it increases, the radial velocity becomes larger and the disc thickness increases. The flux emerging from the accretion disk is modified by the advection. Following this heuristic argument, the transition in term of radial velocities at the ISCO radius would be smaller in a slim disk, hence the density and optical thickness would vary less, and therefore a non-negligible emission could be expected from within the last stable orbit. Considering this line of reasoning, the initial hypothesis of ISCO truncation to determine the BH spin would no longer be valid and measurements would artificially over-estimate the BH spin. A quantification of this effect is as yet missing.

As the contribution of advection increases, the radiative efficiency also decreases with increasing accretion rate (e.g., Abramowicz & Fragile, 2013). Hence, NLS1 with slim disk could also have very fast growing BHs with super-Eddington accretion rate, a different scenario to the one suggested in the last section.

5.5.3 Black hole - bulge scaling relation

One question concerning NLS1s that has received much attention is whether they follow the $M_{BH} - \sigma_\star$ relation or are offset under it. The $M_{BH} - \sigma_\star$, or more generally the BH-bulge scaling relations, are often interpreted as physical evidence for the co-evolution of the central BHs with the galactic bulges. The case of NLS1s is rather controversial. On one hand, many studies suggest they may reside below the relation, in which case they could be evolving onto it (e.g. Mathur et al., 2001, Bian & Zhao, 2004, Grupe & Mathur, 2004, Mathur & Grupe, 2005a,b, Zhou et al., 2006). On the other hand, several different studies place them on the relation once contaminating effects have been corrected for, such as [OIII] line[10] broadening due to outflows (see Botte et al., 2005 and Komossa & Xu, 2007), or radiation pressure (as proposed by Marconi et al., 2008).

Current developments regarding the $M_{BH} - \sigma_\star$ relation highlight that it may not be universal (common to all morphological types), and that perhaps one should distinguish between barred and barless galaxies, disks and ellipticals (e.g. Graham, 2008, Hu, 2008, Graham & Li, 2009, Graham et al., 2011), classical bulges and pseudo-bulges (e.g. Nowak et al., 2010, Sani et al., 2011, Kormendy et al., 2011). In fact, barred, disk galaxy bulges and pseudo-bulges appear either to lie below the relation or to scatter around it. Additionally, on a more theoretical side, some authors (Peng, 2007, Jahnke & Macciò, 2011) suggest that the BH-bulge scaling relations could be non-causal (their origin would not invoke a physical coupling between the SMBH and the galaxy) but rather would be naturally produced by the merger-driven assembly of bulge and BH masses, and therefore galaxies with pseudo-bulges would not be expected to obey the same relation (Jahnke & Macciò, 2011).

---

[10]this line is often used as a surrogate of the stellar dispersion $\sigma_\star$, see Nelson (2000).

Our result that NLS1s have pseudo-bulges suggests that we should expect these AGN to lie in the same region as inactive galaxies with pseudo-bulges, that is scattered around and below the $M_{BH} - \sigma_\star$ relation. It is not yet understood how – or whether – black hole and bulge growth are linked when secular processes drive their evolution. Thus, while it is clear that their black holes are still growing, we cannot predict where they will end up on the $M_{BH} - \sigma_\star$ plane.

5.5.4 Evolutionary scenarios

Several authors have suggested different links between NLS1 galaxies and other AGN types in evolutionary sequence contexts. We briefly discuss them in the light of our results.

Mathur (2000) argues that NLS1 galaxies might be in an early stage of evolution owing to their small growing black holes and higher Eddington rates. This proposition is not inconsistent with our results. Nevertheless, it illustrates a different perspective. Either NLS1s would have their nuclear supermassive black holes recently formed and NLS1s would be young objects evolving into BLS1s (Mathur, 2000, Mathur et al., 2012), or NLS1s would not be in any special phase of their evolution but simply have BHs that are growing slowly due to their duty cycle and spin. However, both perspectives agree that NLS1s galaxies have pseudo-bulges and that their black hole growth is driven by secular processes as opposed to mergers at high redshift.

Kawakatu et al. (2007) proposed an evolutionary track from type 1 ULIRG, to NLS1 to BLS1. The connection between ULIRG and NLS1 appears contradictory with our results. Indeed, local ULIRGs are the result of galaxy mergers, while we have argued that, based on the host properties, NLS1s have a secular driven evolution.

Zhang & Wang (2006) study Seyfert 2s with and without a hidden BLR (i.e. presence or absence of BLR in polarized light) and suggest that non-HBLR Seyfert 2s are the counterparts of NLS1s viewed at high inclination angles. In their subsequent paper, Wang & Zhang (2007) propose an evolutionary sequence of the narrow objects to broad line AGN considering time evolution of the black hole mass and the accretion rates. While it is not inconsistent with our results, the distribution of bulge properties in BLS1s suggests that not all BLS1s come from NLS1s that have evolved secularly, but that the BLS1 population should include galaxies that have undergone interactions and mergers. While Wang & Zhang (2007) propose a secular evolution from NLS1s to BLS1s (NLS1s would be an early AGN phase and would evolve to BLS1s during the AGN activity time), Zhu et al. (2009) proposed a similar scenario, but where NLS1s would be produced by mergers of smaller galaxies compared to BLS1s and could evolve to BLS1s only if they encounter more mergers to grow them. This last scenario appears contradictory to the results of the present paper.

While at this point there is no consensus on the cosmic evolution of NLS1s, our results suggest that they are a special case in which the evolution has been dominated at all time by secular processes. Thus, if the BHs in NLS1s continue to grow, they must eventually become broad-line AGN, and thus become part of the BLS1 population. However, our results also show very clearly that not all BLS1s have grown in this way, and that mergers have played a role in the evolution of the BLS1 population. In this respect, perhaps the most enlightening question would be: when NLS1s evolve into BLS1s, will they be distinguishable from systems classified as BLS1s but having undergone galaxy interactions and mergers? Perhaps one can already begin to address this by studying the BLS1s with pure pseudo-bulges, and asking whether they have definable characteristics that differ from the BLS1 population as a whole.

5.6   Conclusions

From a review of the literature, we show that secular evolution in NLS1 galaxies is a powerful and on-going process on all scales, in contrast to BLS1 galaxies. To assess the role of secular processes in the past evolution of NLS1 galaxies, we examine their bulge properties by performing bulge-disk decompositions on NLS1 and BLS1 galaxies with archival HST images. The results indicate that NLS1 host bulges are pseudo-bulges and distinct from the much broader population of BLS1 bulges. From these results, we conclude that NLS1s represent a class of AGN in which the black hole growth is, and has always been, dominated by secular evolution.

Such an evolutionary mode signifies also a different black hole growth mode in NLS1s than in merger-built systems. Interestingly, simulations of prolonged disk-mode gas accretion onto black holes suggest that the most efficient way to spin-up a black hole is through smooth accretion of material. In this light, our results suggest that NLS1 galaxies should possess highly spinning BHs which is indeed what has so far been observed.

Our picture of the NLS1 galaxy phenomenon can be expressed as follows. The activity in NLS1 galaxies is, and always has been, powered by internal secular processes. This has lead to the growth of a pseudo-bulge. It is also characterized by a disk-mode accretion onto the central object, which tends to spin up the black hole. This leads to high radiative efficiency of the accreting material, therefore reducing the actual mass accreted onto the black hole and slowing its growth. The high radiative efficiency could in part explain the high Eddington ratios and small black hole masses of NLS1s.

This picture can be tested by analyzing the angular momentum in NLS1 bulges to assess definitively their pseudo-bulge nature. And studying the kinematics in the central part of NLS1s would help to understand how gas is transported to their central regions, what the mass inflow rates are, and the role played by angular momentum. In parallel, systematic measurements of black hole spins by future X-ray missions would also shed light on the growth of their black holes at the smallest scales.

THE NUCLEAR REGION OF NGC 1365:
THE INNER HUNDREDS OF PARSECS IN THE VICINITY OF
THE CENTRAL BLACK HOLE

"The problem of feeding the monster:
a large (angular momentum) spoon and a small (angular momentum) mouth."
E.S. Phinney

The supply of gas to nuclear and circumnuclear regions of galaxies is an outstanding question in galaxy evolution. The "fueling problem" is often summarized by the question of how to remove the large angular momentum of the gas in the galactic disk and to move it down to sub-parsec scale in the vicinity of a supermassive black hole in order to trigger nuclear activity. Gravitational torques from galaxy-galaxy interactions or large-scale stellar bars are part of the conventional pictures of the fueling problem from kiloparsec scales down to the nuclear and circumnuclear regions (e.g. Shlosman et al., 1990, Phinney, 1994, Wada, 2004, Jogee, 2006).

The gas inflow in large-scale bar galaxies eventually leads to nuclear and circumnuclear starburst activity. The role of this star formation activity on the AGN fuelling is however the topic of an extensive debate. There is currently no consensus on whether the two are effectively linked. Instabilities may be able to drive gas down to parsec scale, in which case star formation does not occur. On the other hand, AGN fuelling could be synchronous to nuclear star formation (e.g. Hobbs et al., 2011), or follow a post-starburst phase (e.g. Davies et al., 2007).

Only nearby galaxies offer the opportunity to test in details the tens to hundreds of parsec scales, and the possible link of nuclear star formation and black hole activity. In this context, detailed studies of single objects can provide first significant insights.

NGC 1365 is a giant isolated strongly barred galaxy. It is undergoing intense starburst activity in its strong bar and spiral structure but as well displays important nuclear activity. The AGN of this nearby galaxy ($z = 0.00546$) is usually classified as a Seyfert 1.5 (Lindblad, 1999) or 1.8 (Véron-Cetty & Véron, 2006). It exhibits a broad Hα line of FWHM~1800km/s and Brγ of FWHM~1000-1300km/s (e.g. Lindblad, 1999, Reunanen et al., 2003, Davies et al., 2005b). The galaxy displays nuclear and circumnuclear activity as recently studied by Alonso-

Herrero et al. (2012) in the far and mid infrared and by Galliano et al. (2012) in the near-infrared. The nuclear star formation activity was previously revealed by, among others, the presence of bright hot spots in the optical, intense Hα emission, supernovae remnants, a large amount of molecular gas, and point-like and diffuse X-ray emission (see Alonso-Herrero et al., 2012, and references therein). These provide an interesting picture of the nuclear region of NGC 1365 with the presence of young star cluster complexes and a CO molecular ring falling between two inner-Lindblad resonances (outer ILR at a radius $R \sim 27''$ and the inner ILR at $R \sim 3''$) (Lindblad et al., 1996b) where the inward flow of gas is slowed down allowing the formation of a massive ring with enhanced star formation between these two resonances (Shlosman et al., 1990). Previous spectroscopic studies (Reunanen et al., 2003, Davies et al., 2005b) however have been unable to detect molecular hydrogen emission in the inner $1''$, thus not able to provide the link to the central AGN.

In the vicinity of the nucleus, an ionization cone, as traced by [OIII], has been observed and results of modelling show the cone is almost parallel to the galaxy's rotation axis. The opening angle of the cone ($\sim 100°$) is also consistent with a direct line of sight to the Seyfert nucleus with possible partial obscuration. The outflow is also almost co-aligned with an observed radio jet originating from the nucleus. Its soft X-ray (0.1-2.5keV) luminosity suggests however that the AGN is of rather low-luminosity (Stevens et al., 1999). X-ray studies have also revealed large absorption variabilities due to obscuring clouds originating from the broad-line region (Risaliti et al., 2009). And more recent results constraining simultaneously the soft and hard X-ray suggest a rapidly spinning black hole (Risaliti et al., 2013).

While there is some confusion about the classification of NGC 1365, building on our results in the previous chapter, there are a number of indications suggesting that NGC 1365 is a NLS1. First, its nucleus does have a narrow BLR component < 2000km/s (H$\alpha \sim 1800$ and Br$\gamma = 1300 \pm 65$km/s), the prime characteristics of NLS1. NGC 1365 has a strong large-scale bar. It displays current intense star formation in its nucleus. The nucleus of NGC 1365 shows as well [OIII] outflows powered by its central AGN, also commonly seen in NLS1 (e.g. Botte et al., 2005, Komossa & Xu, 2007). The AGN is also a rapidly varying X-ray source. In conclusion, from its host properties to its AGN characteristics, many indicators suggest that NGC 1365 is a NLS1, driven by secular evolution and possessing a pseudo-bulge. The high spin measurement and the unique alignment at all scales, that we discuss in more detail in section 6.4, further support this picture.

Those various characteristics and observations make NGC 1365 an interesting object to study the mechanisms able to transport the gas from kiloparsec scales to nuclear and tens of parsec scales and to further understand the triggering of AGN versus the star formation activities.

We study here the physical conditions of the nuclear region of NGC 1365 ($3'' \times 3''$ or $\sim 300 \times 300$ pc) based on near-infrared integral field spectroscopy data. In section 6.1, we present the data reduction of our SINFONI observations. Once reduced, the data are analyzed through a succession of stellar and gas component fitting where we aim at the best extraction possible, see section 6.2. Based on those results, we constrain the stellar, molecular and ionized gas kinematics, the gas excitation mechanisms, and the nuclear stellar population, see section 6.3. The constraints obtained also provide different indirect indicators of the possible feeding mechanisms of the central black hole. We then discuss our results in a broader context and link them to the nuclear and circumnuclear region in section 6.4. We summarize our conclusions in section 6.5.

6.1 Observations and data reduction

The dataset was obtained with the near-infrared integral field spectrograph SINFONI at the ESO/VLT (Eisenhauer et al., 2003) with adaptive optics (visible curvature wavefront sensor, MACAO, Bonnet et al. 2003). The natural guide star used for the wavefront correction was the nucleus itself (it has a 15.7 R magnitude).

The following observing mode was used: the $H+K$ wavelength band ([1.45,2.45]μm with a spectral resolution of ~1500), a field-of-view of $3\times3''$ and spaxels of 50×100mas. Due to the high dispersion in the nuclear regions, the $H+K$ grating (rather than H and K separately) provides sufficient resolution, as experienced by previous observing programs, resulting in more efficient observations. The chosen 100mas pixel scale allows a field-of-view of $3\times3''$ (instead of $0.8\times0.8''$ for the 25mas pixel scale) and requires only 50% additional on-sky observations to enable a good background subtraction using the method of Davies (2007).

The observations were taken during four nights[1] alternating between exposures of 300 seconds[2] of object (O) and sky (B) in the sequence OBOOB. We choose finally to use the total amount of observations, *i.e.* 175 minutes on source, although two nights were graded C by ESO (66 minutes) and do not improve (nor do they degrade) much the resulting sensitivity of the final combined data. In fact, good quality data effectively amounts to 2 hrs.

The data are reduced with the SPRED pipeline (version 1.51, Abuter et al. 2006), and our own routines when necessary. The data reduction are performed as follows. First, the raw data are dark subtracted, flat field and bad pixels corrected. The slitlets are then aligned and calibrated in wavelength and stacked to create the final 35 object cubes. The same operation is performed on the sky cubes, which are then subtracted from the object cubes, using routines for optimum OH lines subtraction (Davies, 2007). This includes the fine tuning of the wavelength shift between object and sky cubes by correlation.

Standard stars (in our case solar type stars) observed at the beginning, middle, or end of the night are used to correct for the atmospheric transmission and telluric absorptions.

6.1.1 Flux calibration

The flux calibration of our data cubes is done using the standard stars of each OBs and their reference H and K magnitude[3] (between 6.5 and 8 mag in H-band). Each standard star observation is reduced in the same way as the object cubes. From the resulting cubes, we separately compute the flux calibration for the H and K band, *i.e.* in the range $\lambda = [1.509, 1.799]$ and $[1.974, 2.384]$ μm respectively. We then take the average of the two, typically consistent within 25%, and use it as our flux calibration for our object cubes. We use the closest in time standard star observation for each object cube. This is done separately for each OB / each standard star. This procedure gives a final flux uncertainty of $\sim 12\%$, taken as the standard deviation of the total flux of the calibrated individual object cubes.

The flux scaling is computed as follows from the standard star. We integrate the counts within a $0.6''$ diameter ($\sim3 \times$ the PSF FWHM), divide by the exposure time, and compare it with a reference flux (based on reference magnitudes from the SIMBAD database). Our flux scalings are typically of order of a few 10^{-17} W m$^{-2}\mu$m^{-1}.

---

[1] end of 2010 and beginning of 2011.

[2] one night had to be splitted into 2×150 seconds exposures to avoid saturation caused by the nucleus, due to "too" good AO performances.

[3] taken from the SIMBAD database, `http://simbad.harvard.edu/simbad/`.

6.1.2   Spatial and spectral resolution

Once the data reduction processes are finished, we measure the final spectral and spatial resolution (also taken into account in the selection of the combined cubes).

Spectral resolution

We estimate the spectral resolution by fitting a single Gaussian to unblended sky lines, both in the H and in the K bands (at 1.613 and 2.197 μm respectively), at every spaxel position. Histograms of the resolution obtained on the reduced sky cube (before *binning and masking*, see also section 6.2.1) are given in appendix in Fig. D.2. The typical spectral resolution are $\sigma_H \sim 102$ km/s and $\sigma_K \sim 62$ km/s, which is consistent with the theoretical estimation, *i.e.* given by $\Delta\lambda = 0.0005\mu m$ per pixels, respectively $\sim$93 and $\sim$68 km/s. We observe a dispersion in spectral resolution of $\sigma \sim 3.5 - 4$km/s. This is further reduced after the binning and masking, with a final dispersion of $\sigma \sim 2.5 - 3.3$ km/s.

Spatial resolution

The spatial resolution is done by estimating the PSF FWHM. For that purpose, we extract a 2D map of the Brγ emission line distribution, which is assumed to be dominated by the unresolved ionised dust around the AGN. As we discuss later, while this holds in the very center, there is a substantial spatially extended emission. The spatial extent is therefore assumed to be given by the quality of the adaptive optics correction, which we wish to estimate. We fit a two components Gaussian, one for the narrow corrected core of the PSF, a second for the wide uncorrected wings of the PSF and the spatially extended emission component, see the discussion in section 6.3.3. The fit is illustrated in appendix in Fig. D.3. The narrow PSF has a FWHM$= 0.16''$ and the broad PSF has a FWHM$= 0.61''$, attesting the good AO performances. This narrow PSF FWHM corresponds to approximately 14 parsecs in the galaxy plane.

6.2   Data Analysis

In this section, we present the procedure used to extract quantitative information from our 3D cube. We discuss first the necessary masking and binning operations needed to ensure a minimum SNR throughout the FoV, the removal of the several Brackett emission lines in the H-band, the stellar kinematics fitting, and the various emission line distributions and kinematics. We describe here the methods used to extract this information. The results obtained and their interpretation are discussed in the next section 6.3.

6.2.1   Masking and Voronoi binning

In order to extract information from our data cube more reliably and uniformly, we mask spaxels of poor SNR, and bin the others to a target SNR. Indeed, kinematics extraction is not linear with SNR but a minimum level is typically required to ensure reliable and unbiased extraction of kinematical information (see Cappellari & Copin, 2003, and references therein). For all those operations, we treat the H and K band separately.

First, we reject spaxels whose continuum SNR is below 10, which corresponds essentially to the edges of the SINFONI field for which there is little overlap between OBs.

In a second step, we concentrate on the stellar absorption strength. The SNR is here estimated by taking the ratio between the maximum depth of the absorption – of the ^{12}CO(2-0) at 2.295μm in the K-band and ^{12}CO(6-3) at 1.62μm in the H-band[4] – and the standard deviation of a featureless continuum range close to the lines. The SNR of those features typically varies between 2 and 8 with a peak around ~ 4. The histogram of the pixels SNR is given in appendix in Fig. D.1. Looking at the spatial distribution of the SNR, it is clear that the center has low SNR due to stellar feature dilution by the strong nucleus continuum emission, this effect is also stronger in the K-band as the dilution is caused by warm dust emission around the AGN of temperature around 1000K (which emission peaks at the end or beyond the K-band).

Based on that observation and the visual inspection of the absence of stellar absorption, we mask the central area. The size of the central mask is adjusted as a function of the binning results and hence the best size is iteratively estimated. The final size is of radius 4.5 pixels for the K-band and 4 pixels for the H-band (the marginal gain is the result of lower dilution, and mitigated by the less pronounced stellar absorption in the H-band and the additionally contaminating Brackett emissions, see next section), which corresponds to ~ 3 times the narrow PSF FWHM.

The data are binned using the 2D Voronoi tessellation binning routine of Cappellari & Copin (2003). The algorithm implemented is a centroidal Voronoi which partitions the 2D image into regions of "equal mass" around generators, where "equal mass" means here of same SNR. Every bin encloses all the points that are closer to its generator than any other. The algorithm of Cappellari & Copin (2003) ensures a minimum scatter in SNR between each bin. Using this routine, the resulting average signal-to-noise ratio is SNR=7, as measured after binning. The binned cube also presents much less SNR scatter, with most of the spaxels having SNR=6-8. We end up with 726 bins in the K-band, and 677 bins in the H-band (applied on the Brackett subtracted cube, see next section).

We apply the same binnings to the noise maps, for which we then divide each bin value by its number of pixels[5].

6.2.2 Removal of the Brackett forest in the H-band

The broad hydrogen brackett AGN emission lines are strong in the vicinity of the nucleus and dominate our H-band wavelength range of interest, therefore hampering stellar absorption identification. Hence, their removal is a prerequisite before any stellar kinematics derivation from the H-band data.

We adopt the following method (similarly to Raimundo et al., 2013).
First, we integrate spatially over a circular aperture of 5 pixels radius where the broad lines

---

[4]we choose this one as it is relatively pronounced, between two Brackett lines – as opposed to the SiI – and will be of interest for studying the dilution of its equivalent width.

[5]assuming a normal distribution of the noise and pixel values for a given bin, the bin variance is given by the pixel variance divied by the number of pixels, and the error on the mean value of the bin is thus futher divided by the number of pixels. Hence, the uncertainty of the bin is the average uncertainty of the pixels divided by the number of pixels in the bin.

are stronger. We fit Lorentzian profiles[6] to the emission lines, *i.e.* the Brackett transitions 10-4 up to 14-4. We fix the relative wavelength positions and widths of the lines, and the relative intensities based on the case B recombination theory[7] (using the results of Hummer & Storey, 1987, for the standard parameters $T = 10^4$K and $n_e(\text{cm}^{-3})=10^4$). To improve the extraction, we simultaneously fit a fourth order polynomial (to take into account the non-stellar continuum and distortion), and a combination of two stellar templates convolved with a Gaussian (to take account for the stellar velocity dispersion). We use a M0 and a K5 star from the Le et al. (2011) late-type stars library that we broaden to the resolution of SINFONI, *i.e.* using a Gaussian kernel of width $\sigma_{\text{kernel}} = \sqrt{\sigma_{\text{SINFONI}}^2 - \sigma_{\text{tpl}}^2}$, where the SINFONI spectral resolution has been measured previously and the template resolution is FWHM=$3.152\times10^{-4}\mu$m.

Following the initial fit on the central aperture, we fix the wavelength position and the velocity dispersion of the Lorentzian profiles ($z = 0.00553536$, FWHM$_{broad}$=1300±65 km/s), hence only one variable remains for the subsequent fit, i.e. the height of the Br$_\zeta$ (Br10; the height of the other lines is fixed by the case B). Therefore the total amount of free parameters is 10, *i.e.* 5 for the continuum, 1 for the Brackett lines, and 4 for the two stellar templates. Note that we subtract in total 11 Brackett lines but we fit only the 5 first ones. Indeed, as the remaining lines are fixed by the case B we consider advantageous to subtract it after but not to fit them since they strongly blend each other (decreasing $\Delta\lambda$ at higher Brackett line transitions).

Hence, the spaxel-by-spaxel fitting determines the line parameters for the Brackett emissions at each spatial position that we use to remove the Brackett lines from the data cube in the *H*-band. We illustrate the fit in Fig. 6.1.

The fit is performed a first time to remove the broad Brackett lines in order to subsequently determine the absorption line SNR and perform the binning. Once the binning is done, we apply it on the original cube and re-perform the Brackett fitting and subtraction.

6.2.3 Stellar kinematics extraction

Using our masked, Voronoi binned, and Brackett subtracted (for the *H*-band) cubes, we determine the stellar velocity and velocity dispersion distributions by fitting the spectra with two sets of stellar templates.

We use the routine pPXF (Cappellari & Emsellem, 2004) which implements a Gauss-Hermite parametrization to fit the line-of-sight velocity distribution. Considering the limited SNR of our data we fit only the two first moments, *i.e.* the velocity offset and the velocity dispersion[8].

As already mentioned in the last section 6.2.2, we use for the *H*-band the late-type stellar library of Le et al. (2011), using here the full set of stellar templates of resolution *R*=5000

---

[6] we use the Lorentzian functional form

$$L(x;\gamma) = \frac{\gamma}{\pi(x^2 + \gamma^2)},$$

for which we have $FWHM = 2\gamma$.

[7] results of large optical depth approximation where any photon emitted from transition to level 1 are immediately absorbed.

[8] hence, we do not use the penalized likelihood, characteristic of pPXF.
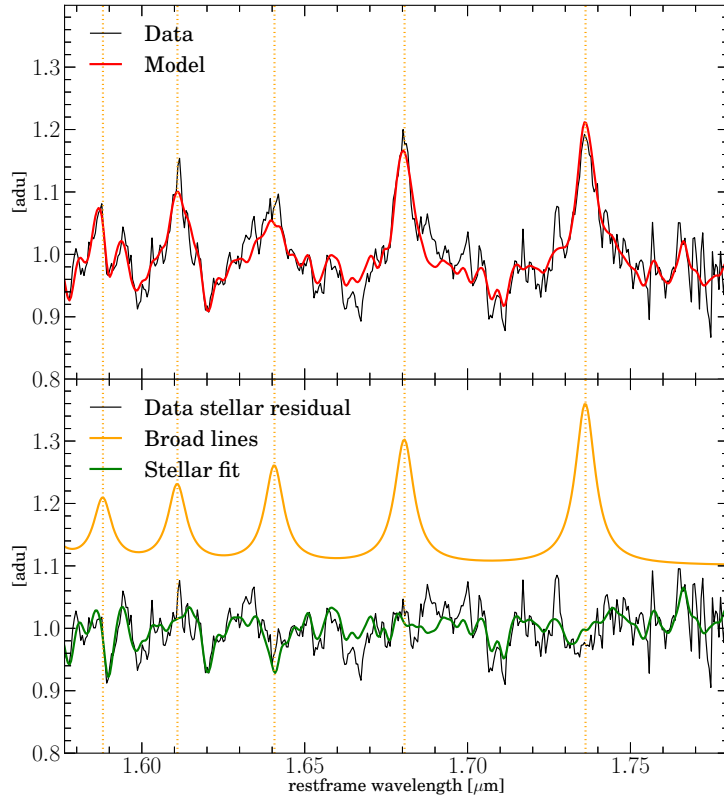
Figure 6.1: Illustration of the Brackett lines extraction on spectral data integrated in a 10 pixels radius central aperture without masking (we choose this aperture for illustration purpose only as it shows both strong Brackett emission and relatively strong absorption features). (Top) data (black) and fit (red), both continuum subtracted. (Bottom) stellar component (black) calculated by subtracting the continuum and the Brackett lines to the data, fitted stellar component (green), fitted brackett lines (orange, shifted for visualisation purpose). While the stellar component fit is not perfect, it grasps the main absorption features and allows a reliable Brackett lines fit.

or FWHM=3.15Å. The library contains a total of 10 late-type stars (from G8 to M0). We exclude two of them with improper sampling for our purpose, *i.e.* having missing spectral data in regions of interest. For the K-band, we use the Gemini near-IR spectral library of late-type stars GNIRS "red" from Weinzirl et al. (2009). We use the spectral range 2.24 - 2.43 μm of resolution R=5900 or FWHM=3.35Å. This library contains a total of 29 late-type stars (from F7 to M3). In addition to the stellar component, we include an additive Legendre polynomial of degree four for the K-band and degree five for the H-band.

Both libraries are appropriately convolved with a Gaussian to the SINFONI resolution before being used for the kinematics fitting. This is performed as previously described in section 6.2.2. We fit the restframe wavelength range [1.56,1.656] μm in the H-band which includes the strong SiI and ^{12}CO (6-3) absorption features and the [FeII] emission line. In the K-band, we fit the range [2.24, 2.378] μm including the three CO bandheads ^{12}CO (2-0), ^{12}CO (3-1), ^{12}CO (4-2). We exclude from the fits the [FeII] emission lines at 1.664μm and a telluric residual in the K-band.
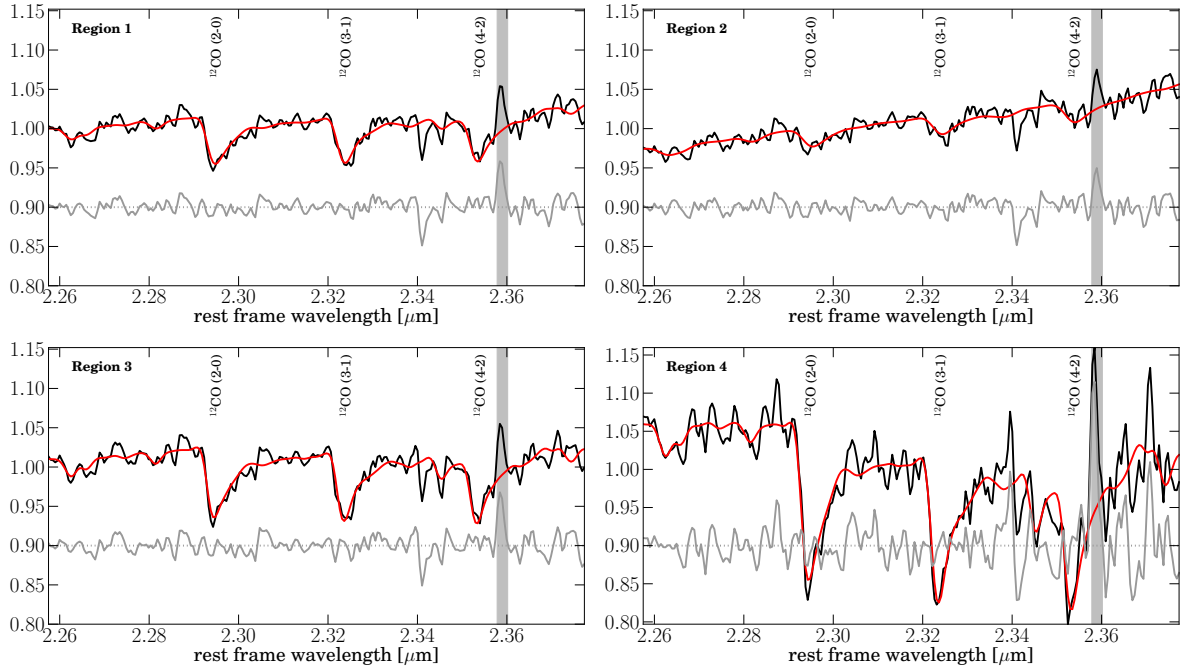
Figure 6.2: Integrated spectra (black), fit (red), residual (grey) in the K-band for four different regions. (Top Left) Region 1 is the full integrated field-of-view. (Top Right) Region 2 is centered on the nucleus with 10×10 pixels (note that a large fraction are masked pixels and not taken into account here), showing the important dilution in the center. (Bottom) Region 3 and Region 4 are 5×5 pixels in the upper left and bottom right of the field, they are dominated by the stellar component. Vertical gray region are excluded from the fit.

In Fig. 6.2 and Fig. 6.3, we plot the results for four different integrated regions: 1) the integrated field-of-view, 2) the central region where the stellar features are strongly diluted by the AGN continuum, 3) and 4) regions of 5×5 pixels dominated by the stellar components. The stellar fit in the H-band uses typically a combination of K5 and M0 stellar templates, where for the K-band more stellar spectra are combined, using K0, K1, K2, K6, and M0 star.

We follow a Monte Carlo approach to derive the final parameters and their respective errors. For each spaxel we generate 100 spectra with additional random noise, and random starting values for the velocity and the velocity dispersion. The additional noise is taken from a Gaussian of dispersion σ given by our binned noise cubes. Our final results and respective errors are the mean and the standard deviation of the Monte Carlo outputs for which we have applied the Chauvenet criterion[9] beforehand. The typical velocity errors are ±14.8 km/s for the H-band and ±11.5km/s for the K-band, and ±21.2 km/s and ±17.2 km/s respectively for the velocity dispersion. So the K-band fit has a slightly lower noise thanks to the strength of its absorption features, while the H-band can marginally push the fitting closer to the central nucleus.

---

[9]this criterion is a mean to identify possible outliers. Typically, considering the sample size, a data point is rejected if it probability is $<1/2$.
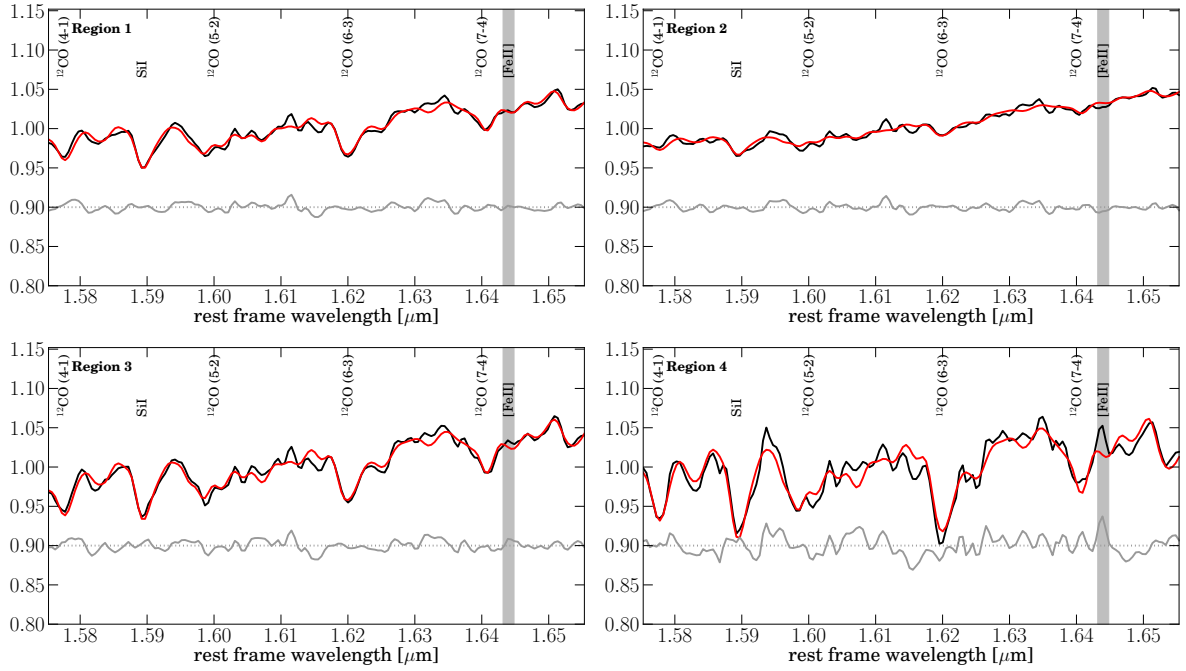
Figure 6.3: *con't* of Fig. 6.2 for the *H*-band.

6.2.4 Gas emission line distributions and kinematics extraction

In addition to the numerous stellar absorption features, there are several emission lines that can be observed. We shall study the Brγ 2.166μm for the ionised gas, H$_2$ (1-0) S(3) 1.9576μm, H$_2$ (1-0) S(1) 2.1218μm, and H$_2$ (1-0) S(0) 2.2233μm for the warm molecular gas, and the forbidden lines [FeII] 1.644μm and [SiVI] 1.9634μm. We aim at extracting fluxes, velocity dispersion and velocity distributions for those lines, allowing us to study the different phases of the interstellar medium and compare them to the stellar component.

Brγ emission line

The Brγ emission in NGC 1365 is not only composed of a broad component originating from the nucleus, but as well of a narrower component of more extended emission. In order to constrain those distributions, we perform a two Gaussian fit of the Brγ emission line. The fit is performed as followed. We performed the fit on both a) the non-binned and not masked cube applying a median spatial filtering of 3 by 3 pixels, and b) the binned and masked *K*-band cube (using the respective noise cubes for the fit). We fit a two Gaussian profile in the range 2.1465 to 2.1875 μm convolved with the instrumental resolution (*i.e.* 62km/s), and additionally fit a linear continuum (subtracted before the Gaussian fit) from 2.105 to 2.227μm excluding the line range and using a pixel rejection based on the Chauvenet criterion (which mitigates the effect, e.g. of the molecular hydrogen emission in the same range). We perform an initial single Gaussian fit on the central region to fix the broad component velocity offset and the width to FWHM=1125 km/s. While it is in agreement with the Brackett width in the *H*-band, it is also partly contaminated by a telluric residual (P-Cygni from 2.16556 to 2.167μm). It is nevertheless sufficient to correctly subtract the broad component and to be

able to fit reliably the narrow component (which is not affected by those features). The fit is then performed on each spaxel. The extracted parameters and their errors are taken as the results of the least-square minimization fit. The typical velocity error using the binned cube is ±34km/s and ±46km/s for the velocity dispersion.

Gas Emission Lines

The other emission lines are extracted by fitting a Gaussian profile convolved to the instrumental resolution, using the code LINEFIT (see e.g. Davies et al., 2009). In total, we fit three molecular lines and two forbidden lines.

For an optimized subtraction, when possible, we use stellar subtracted cubes. Therefore, in addition to the H-band fit, we perform a 'large' K-band fit illustrated in Fig. 6.4. Due to the deep atmospheric features below $\sim 1.98\mu$m, we cannot fit reliably the stellar component in the low K-band. Hence for the lines H_2 1-0 S(3) and [SiVI], we use the initial K-band binned cube. We summarize in Tab. 6.1 the input cubes, the SNR thresholds used to flag well detected lines (more stringent for the low K-band as it is more affected by the atmospheric absorption) and the typical median velocity and velocity dispersion errors. In addition to a Gaussian line, we allow a low order polynomial fit to the continuum.

Formal uncertainties are computed using Monte Carlo simulations by generating 100 spectra and adding perturbation assuming Gaussian noise (the width being determined by the noise level).

Table 6.1: Fitted emission lines with the input data cube, the S/N threshold and the median velocity and velocity dispersion errors. All cubes have been masked following the procedure presented in section 6.2.1.

Line emission	[μm]	input data	S/N	Δv [km/s]	$\Delta\sigma$ [km/s]
[FeII]	1.64400	stellar subtracted cube	3	±16.7	±20.1
H_2 1-0 S(3)	1.95756	original binned cube	5	±34.5	±40.7
[SiVI]	1.9634	original binned cube	5	±43.3	±38.5
H_2 1-0 S(1)	2.12183	stellar subtracted cube	3	±10.8	±13.4
H_2 1-0 S(0)	2.223329	stellar subtracted cube	3	±16.1	±17.46

6.3   Observational results and interpretation

Based on the various diagnostics that we have been able to extract, we shall try and constrain the different kinematic components of the nucleus of NGC 1365 and their physical origins.

6.3.1   Stellar and gas kinematics

We present in Fig. 6.5 the two first moments of the pPXF fits for the H and K bands. The stellar component presents a rotation component as well as a rather uniform velocity dispersion distribution. Both the H-band and the K-band give similar results.

The central part typically shows higher velocity and velocity dispersion. While this could be a real kinematic feature, we argue that this is a bias caused by the dilution of the central part. Indeed, even though the absorption features have in principle a sufficient SNR, the
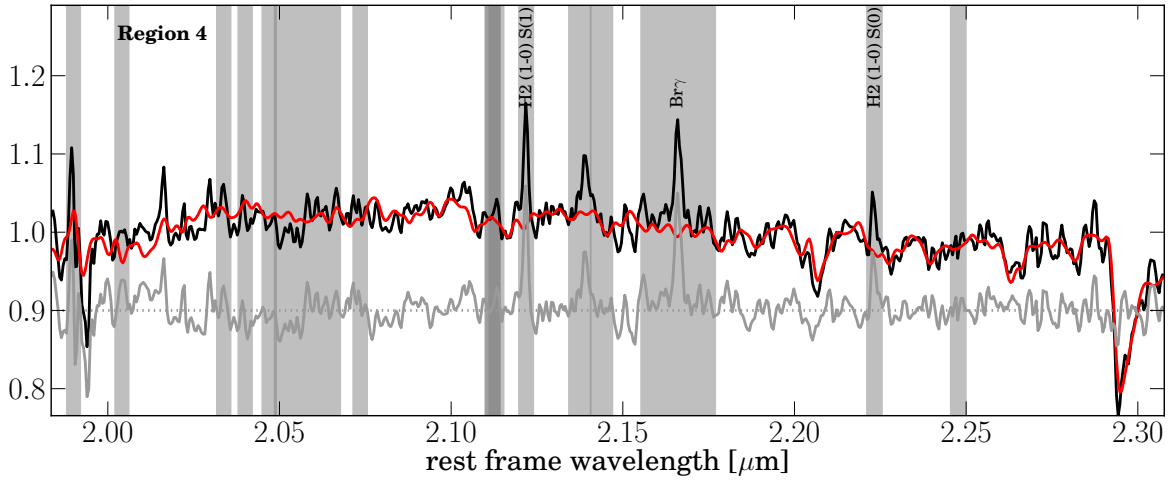
Figure 6.4: Integrated spectra (black), fit (red), residual (grey) in the K-band. This fit is performed to subtract the stellar component and improve the gas emission line fits. See also Fig. 6.2 and Fig. 6.3. The spectra is here integrated over Region 4. The vertical grey regions are excluded from the stellar fit as it is the location of potential emission lines. We include the first CO bandhead in the fit to help constraining the stellar component and as an healthy check.

dilution will tend to smooth the absorption features and lead to larger widths. Concerning the velocity, we note that the most prominent absorption features, typically the CO lines, are rather asymmetric with longer tails toward longer wavelengths. The smoothing caused by the dilution would tend to shift the peak towards longer wavelengths, hence higher velocity. Both effects are stronger in the K-band, as the dilution is stronger and the fit is based only on the asymmetric CO lines.

The typical velocity dispersion varies between 135 and 165km/s. As one moves out of the center, the velocity dispersion tends to slightly increase first and to tentatively decrease at the edge of the field, most notably in the SE (bottom left; clearer in the K-band). If this decrease at the edge of the field is not an artifact, it suggests a ring at radius >140pc from the center of lower velocity dispersion of σ ~105-125km/s. Putatively, this could be attributed to colder regions with more recent star formation than the underlying bulge, as it has been suggested for other Seyfert galaxies (e.g. Riffel & Storchi-Bergmann, 2011, and reference therein). This is also likely in rough agreement with the location of the IILR as proposed by Lindblad et al. (1996b), as we discus further in section 6.4 .

The flux, velocity and velocity distribution maps of the fitted emission lines are given in Fig. 6.8. While we will focus in more detail on their distribution in the next section 6.3.3, we compare here the general gas trends and the stellar kinematics.

It is clear from the kinematic maps that the molecular gas rotates in the same disk as the stars. However, the molecular gas also seems to rotate faster (by $+\sim$ 30 km/s at the edge) and to have a lower velocity dispersion as can be clearly observed in the H_2 (1-0) S(1) map with typical values around 75km/s, or half that of the stellar dispersion. This would indicate that the molecular gas is typically in a somewhat colder disk than obtained from the stellar
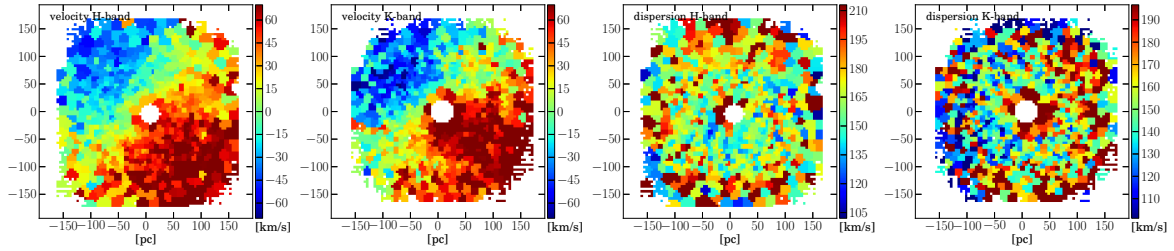
Figure 6.5: Line-of-sight velocity (the two left images) and velocity dispersion (the two right images) distributions, as measured in the H and K-band.

fit.

The low ionization [FeII] and Brγ (Fig. 6.7) lines also seem to follow that trend, where usually [FeII] has a distinct origin. Rotation in the galaxy plane does seem to be the main feature here of both the [FeII] and the narrow Brγ. We discuss their origin in more detail in section 6.3.3.

6.3.2   Disk fitting and radial distribution

The stellar and gas kinematics clearly suggest rotation. In order to constrain the systematic velocity, the inclination angle, and to estimate the bulge mass, we fit velocity maps by an axisymmetric rotating disk model generated by the code DYSMAL (described in Cresci et al., 2009).

The fitted parameters are the total mass, the velocity offset and the inclination angle. The position angle is fixed before hand to 43° based on a manual axis determination (using QFitsView). The kinematic center is fixed to the peak Brackett emission, corresponding to the center of the circular central masks. The mass distribution, described by its Sérsic index n and its effective radius R_e, was initially let as a free parameter but the central obscuration does not lead to an optimum fit, and hence the effective radius obtained was not well constrained and reached approximately 4.5″, *i.e.* two times the size of the field. Therefore from the stellar flux distribution (obtained with the routine STARFIT), we fit a Sérsic profile with GALFIT and obtain $(R_e, n_b) = (0.75″, 0.67)$. We note however that the results from the disk fitting are rather insensitive to this constraint, but only lead to smaller enclosed mass (when free to vary $(R_e, n_b) \sim (4.4″, 0.6)$). We should note that the mass estimation does not represent here the true dynamical mass[10] as we do not include the velocity dispersion in the fit, but should be taken as a lower limit estimation.

We perform this fit for the H and K-band, using the velocity distributions obtained from the stellar fits and the star flux distribution. We also fit the gas emission line H$_2$ (1-0) S(1), using its line velocity and flux distributions. The results are shown in Fig. 6.6. The two stellar fits agree very well and leave no systematic rotation residual in the velocity maps. Residuals

---

[10]we can estimate analytically the dynamical mass based on the rotation velocity and velocity dispersion at the effective radius. Assuming the random motions are isotropic, the mass enclosed within R is

$$M = (V_{\rm rot}^2 + 3\sigma^2)R/G,$$

with $V_{\rm rot}$ and σ the observed rotation velocity and one-dimensional velocity dispersion. For $V_{\rm rot} \sim 94$km/s and $\sigma \sim 151$km/s at the effective radius $R_e \sim 65$pc, we obtain $M[\log M_\odot] = 9.06$.

are typically stronger in the center but the kinematics error bars are also typically higher at those locations.

The residuals of the gas map are somewhat stronger and may be the result of systematic rotation residual (in this case oversubtraction). This could also explain the higher velocity field and higher enclosed mass. We should note that we have used the same Sérsic parameters as for the stellar component, however the molecular gas does not necessarily match the stellar distribution. The residuals could also be partly attributed to the presence of distortion.

Therefore, we have the following results: the systemic velocity (taking only the stellar results) is ~1677 km/s, and the inclination angle is ~50.7°. The position angle was measured to be 43°. Both angles are in agreement from large scale measurements, $i = 41 - 55$° and P.A.=40/220°, see the discussions in Zánmar Sánchez et al. (2008) and section 6.4. The systemic velocity is ~50km/s higher than large scale HI and Hα measurements, see also Zánmar Sánchez et al. (2008) and references therein. We attribute this difference to our smaller field.

The Keplerian enclosed mass[11] is 1.8-2.4×10^8 M$_\odot$ similar to the mass obtained for other Seyfert galaxies, e.g. Riffel & Storchi-Bergmann (2011). The values obtained for the gas have to be taken with an extra caution, considering our comments in the previous paragraph. The obtained free parameters are given in Tab. 6.2.

Table 6.2: Results from the DYSMAL fits for three velocity maps. Note that the velocity offset is taken with respect to an initial redshift $z = 0.005535$ or $v = 1660$km/s. Enclosed masses and inclinations have no fit errors.

	Enclosed mass [log M$_\odot$]	velocity offset [km/s]	inclination [deg]
H-band	8.25	18.15±0.41	50.74
K-band	8.38	16.72±0.36	50.77
H$_2$ (1-0) S(1)	8.53	3.57±0.17	50.74

6.3.3 Gaseous excitation

In order to better understand the physical conditions in the nuclear region, we study in the present section the diagnostics at our disposal: detected molecular and ionised gas emission lines. Their flux distributions and kinematics can help us understand the different excitation and dynamical components.

The molecular hydrogen can be excited either by fluorescence or by thermal processes. The absorption of soft UV radiation can lead to a cascade of radiative decay at the origin of the fluorescent emission. Thermal processes can be provided by shock fronts resulting from supernovae explosions, nuclear outflows or radio jets. The heating can also be provided by X-ray or UV radiation in high density gas, when the collisional timescales become sufficiently short for transitions to thermalize.

We give in Fig. 6.7 and Fig. 6.8 the fluxes and kinematics of the Brγ, the [FeII], the H$_2$(1-0) S(3), the [SiVI], the H$_2$ (1-0) S(1), and the H$_2$ 1-0 S(0) lines. We discuss the different phases of the interstellar medium and their possible excitation mechanisms in the next few sections.

[11]this is the mass supported by ordered rotation.
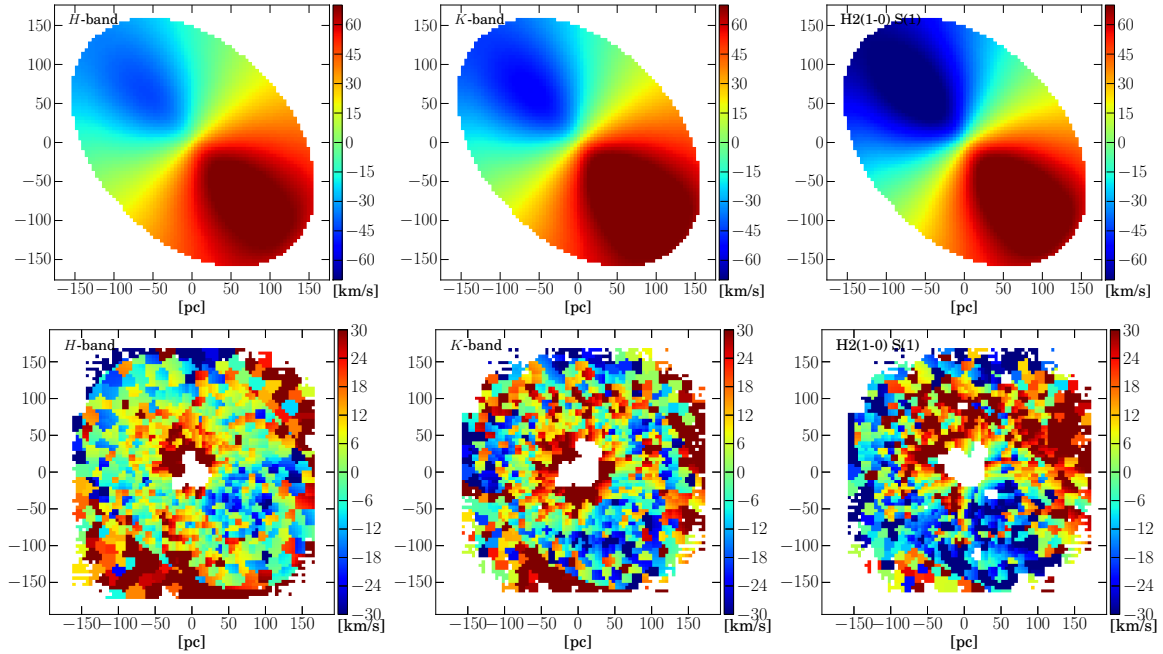
Figure 6.6: DYSMAL models (top) and residuals (bottom). (Left) *H*-band. (Middle) *K*-band. (Right) H2 (1-0) S(1) gas emission line. The two stellar models are very similar to each other and leave no systematic residuals. The gas map fit is subject to more caution. We refer to the discusion in the text.
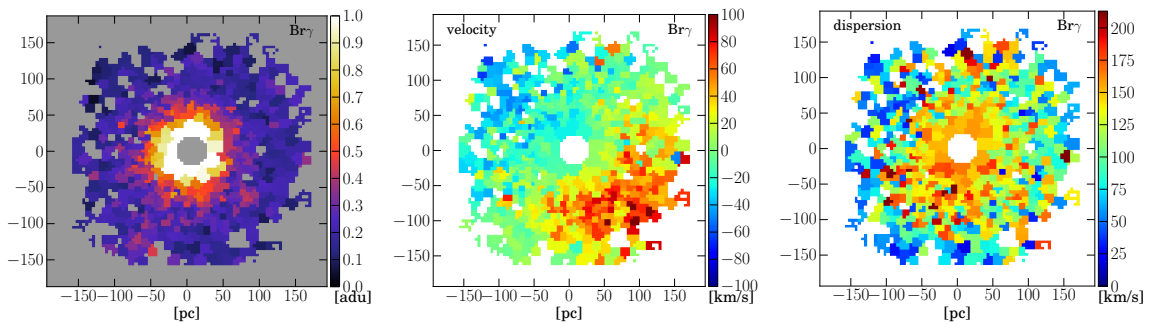

Figure 6.7: Narrow Brγ peak emission, and velocity and velocity dispersion distributions.
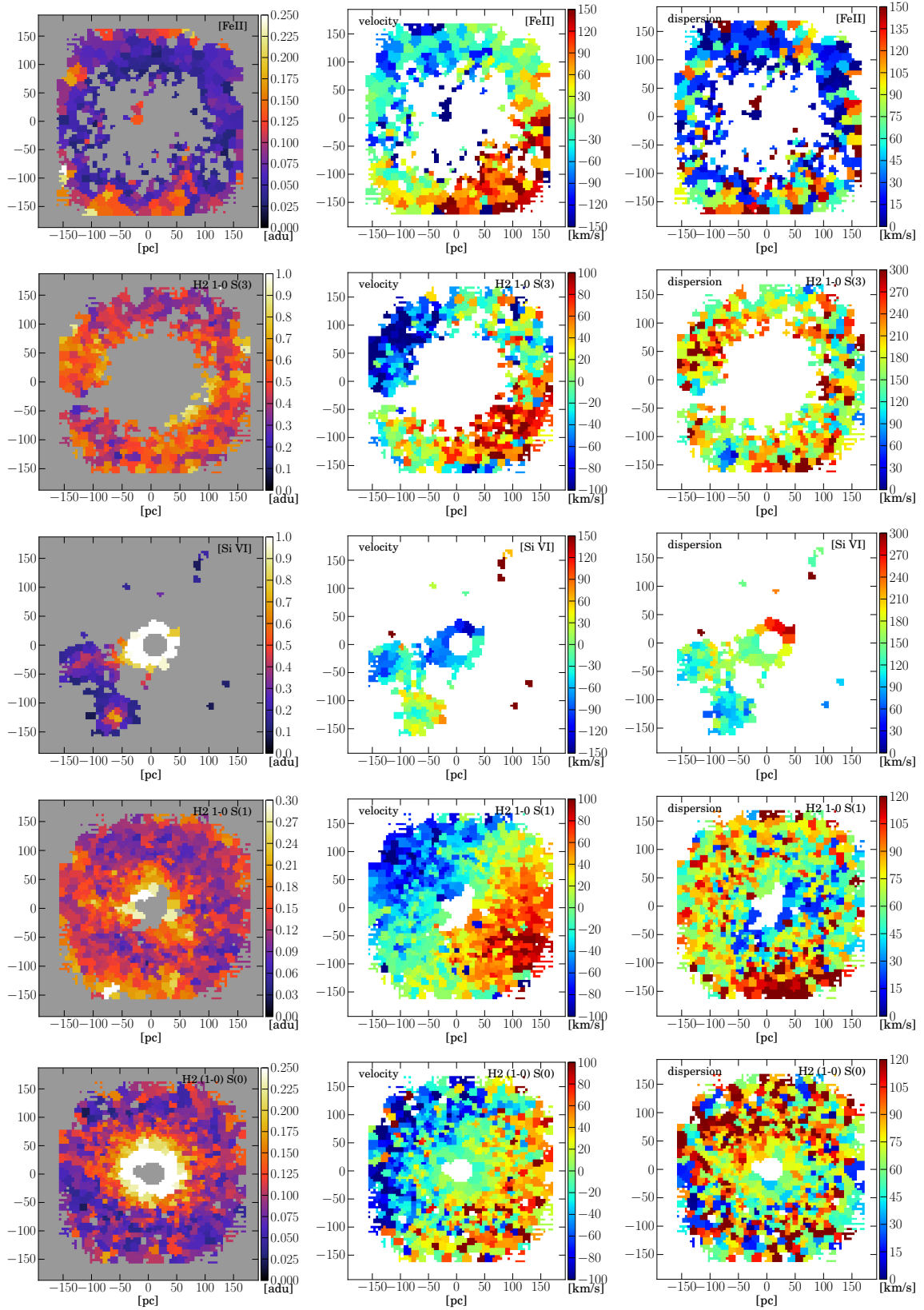
Figure 6.8: Flux, velocity and dispersion for different line maps: the [FeII], the $H_2(1\text{-}0)$ S(3), the [SiVI], the H_2 (1-0) S(1), and the H_2 1-0 S(0). We refer to the text for discussion.

Table 6.3: Lines ratio. Values quoted are median values.

	[FeII]/Brγ	(1-0)S(1)/Brγ	(1-0)S(0)/(1-0)S(1)	(2-1)S(1)/(1-0)S(1)
Full field	0.15 ± 0.03	0.44 ± 0.04	0.73 ± 0.12	< 0.24
Ring 2″-2.5″	0.52 ± 0.07	0.70 ± 0.04	0.67 ± 0.09	< 0.24

The H_2 emission

The molecular gas is rotating in the galaxy plane, similarly to the stellar kinematics. This is clearly seen in the velocity maps of the three fitted lines, H_2 (1-0) S(1), 1-0 S(0) and 1-0 S(3). However, it appears that the rotation velocity is slightly higher (by $\sim$20 to 40 km/s) and the velocity dispersion smaller[12] with respect to the stars. As expected, this shows the gas is in a somewhat cooler dynamical state as observed in a number of galaxy nuclear regions.

The velocity dispersion traced by H_2 (1-0) S(1) appears to be smaller in the center, but this falls below the spectral resolution ($\sim$64km/s) and considering the signal-to-noise, we do not consider it as a robust measurement. We can observe as well a higher dispersion region in the South of the field of view, which matches also a more intense emission region.

The H_2 (1-0) S(1) flux distribution appears to be clumpy and filamentary towards the nucleus, revealing possible higher concentration of gas but as well higher excitation mechanisms as could be provided by star formation. We look at signatures of in- or outflows in the emission line at specific knots but do not find strong asymmetries in the line (we note however that the signal-to-noise may be too small in order to detect such asymmetries).

The relevance of thermal versus non-thermal processes can be studied by the ratios of molecular hydrogen lines. However those ratios not only depend on the excitation mechanisms but on the FUV field intensity, the gas density, the excitation temperature, etc., that can lead to uncertain interpretation.

The line emissions here are very faint, hence we have only access to a limited number of line ratios: we calculate the ratio (1-0) S(0)/(1-0) S(1), and place formal constrains on (2-1) S(1)/(1-0) S(1) for which the line (2-1) S(1) is essentially undetected. The median values and errors for the full field and for a ring from 2″ to 2.5″are given in Tab. 6.3.

As guidelines for our interpretation, we compare the two ratios to five PDR models, relevant for starbursts and AGNs described by Davies et al. (2003). These models consist of static, plane-parallel, semi-infinite clouds exposed to isotropic FUV radiation fields (Sternberg & Dalgarno, 1989, 1995, Sternberg & Neufeld, 1999). Those models are used by Davies et al. (2003, 2005b) to study the molecular excitation in ultraluminous infrared galaxies and in AGNs.

The interpretation of our two measured ratios is inevitably limited. The (1-0)S(0)/(1-0)S(1) ratio is high typical of pure radiative fluorescent excitation in a low-density cool gas (Model 1 Davies et al., 2003). The (2-1)S(1)/(1-0)S(1) constraint however suggests denser gas with the low levels thermalized by collisions and the higher level (e.g. $v = 2$) excited by FUV pumping or thermalized (Model 2 and Model 5 Davies et al., 2003). Considering the low SNR of the emission lines, systematic effect such as stellar or telluric residuals may affect significantly our line ratios. This is also seen, for example, in the different velocity dispersion of the (1-0)S(1) and (1-0)S(0) lines.

While the results are rather inconclusive, the two ratios are consistent with excitation in

---

[12]disregarding 1-0 S(3) which has higher errors bars and is more affected by telluric absorption and could be affected by blending of the coronal line [SiVI].

dense PDRs exposed to high-FUV fields as one might expect of regions efficiently forming massive young stars, Davies et al. (2005b). Shocks, providing a pure thermal excitation, could also locally be relevant.

The Brγ emission

As already mentioned, we detect both a broad (FWHM$\sim$1300km/s from our Brackett lines removal in the H-band and $\sim$1140km/s from the Brγ decomposition) and an extended narrow Brγ component. The first is thought to originate from the broad line region in the vicinity of the AGN and is unresolved. The narrow Brγ however is generally indicative of young stars, although it can also be produced by the AGN and is then associated with the narrow-line region in the form of an outflow.

We have attempted to measure only the narrow Brγ flux, velocity and velocity dispersion distributions. These are presented in Fig. 6.7. However, in the central region, it is difficult to separate from the broad component (see section 6.2.4), and the resulting flux map should be taken as indicative, in particular in the central arcsecond. Similarly the velocity and velocity dispersion seems affected by the central broad component.

The emission distribution is essentially centrally concentrated. But a careful look through the line cube reveals that the emission is often (not always) spatially coincident with the H_2(1-0)S(1) line including its patchy distribution.

The kinematics show that the ionized gas is in rotation in the galaxy plane with similar values to the molecular gas[13]. A similar conclusion is reached for the velocity dispersion (again disregarding the central higher values).

Those two observations provide additional circumstantial evidence for the presence of very young stars hot enough to ionise the gas, or ongoing star-formation.

An additional diagnostic is provided by the 1-0S(1) to the narrow Brγ ratio. High ratios (much higher than unity) typically result from shock-excited regions. Low values, on the other hand, are seen in star-forming regions (Puxley et al., 1990). We obtain values between 0.4 and 0.7 given in Tab. 6.3, typically in the range found by Puxley et al. (1990) in their star-forming galaxy sample. They reproduce these ratios by a model comprising molecular clouds of density 10^3-10^4 cm^{-3} surrounding Strömgren spheres of ionized hydrogen and illuminated by individual hot stars at their centers.

In conclusion, the values obtained are again consistent with photodissociation regions in star-forming complexes.

As a side remark, between the H and K band we detect a strong Paα component associated with the nuclear emission and also coincident with the narrow Brγ (as observed by looking at different channel map with QFitsView). The line is not analyzed further due to the high atmospheric absorption at those wavelength.

---

[13]although an offset is present that may be the result of different systemic velocities, or bias from the broad component subtraction.

The [FeII] emission

The [FeII]$\lambda 1.664\mu m$ is typically interpreted as a tracer of shocks either from radio jets, winds in the ionization cone or supernovae in star-forming regions. It is also possibly generated by X-ray excitation (photo-ionization) from star-forming regions. Nuclear [FeII] is also observed, e.g. in four NLS1 galaxies by Rodríguez-Ardila et al. (2002).

We detect a faint [FeII] emission at the edges of our field, less affected by the non-stellar continuum emission. The [FeII] at 1.644μm is blended with the Br12 at 1.641μm, hence is hardly detected in the center where the Br12 line is broad (even after our Brackett lines removal). However, one can observe a relatively patchy distribution concentrated at some knots usually related to H_2(1-0)S(1) emission. The ionized line also displays a similar rotation component in agreement with the molecular gas. Considering as well the non-detection in the central part, a strong nuclear [FeII] emission is readily rejected.

This faint and limited detection, offset from the nucleus, would suggest a star-formation origin of the [FeII] rather than a nuclear origin. The bright [FeII] spots also correspond to bright H_2 and narrow Brγ spots suggesting the presence of young stars producing a low ionizing continuum (including X-ray excitation). The [FeII] also seems to trace an arm extending toward the nucleus.

The low [FeII]/Brγ ratio of ~ 0.5 (see Tab. 6.3) is consistent with theoretical models of star-forming regions (Reunanen et al., 2003, Colina, 1993). An alternative, or complementary, process is shock excitation at the edges of an outflow. Although geometrically not implausible by comparison to the [OIII] outflow (see later section), the line emission instead seems located in the rotating disk plane favoring star-forming complexes as the main excitation mechanism.

The [SiVI] coronal emission

Coronal lines are forbidden transitions with high ionisation potential (ionization potential >100eV). Those lines form in extreme environments and are therefore usually associated with the AGN, and considered independent from star formation. The location of the coronal-line region is generally seen to coincide with the narrow-line region as traced by [OIII] or Hα although it is seen closer to the AGN and is more compact (Müller-Sánchez et al., 2011, and references therein). As such the excitation mechanisms producing the line can be hard UV to soft X-ray continuum (*i.e.* photoionization by the central source) or fast shocks (*i.e.* shock ionization from radio jets, etc.). The morphology of coronal lines have only been studied in a handful of objects (e.g. Müller-Sánchez et al., 2011, Prieto et al., 2005).

Here, we are able to extract the [SiVI] line at 1.9634μm (excitation potential>166eV; ionization potential>205eV), although in a region strongly affected by atmospheric absorption and with the presence of H_2 (1-0) S(3) at 1.95756μm. The line is detected only at specific locations and is seen to be partly filamentary and located at a few knots (in particular a SE knot), with a possible nuclear enhancement at the base of the radio jet, see Fig. 6.8 and Fig. 6.9. The kinematics field is blueshifted with respect to the gas rotation[14] with values from -30 to -90 km/s, *i.e.* blueshifted by 30 to 60 km/s with respect to the H_2 (1-0) S(1) velocity map. The velocity dispersion off-nucleus appears to be ~ 120 km/s (~ 285km/s FWHM). A visual comparison to the low ionization [FeII] line tells us that the two are essentially not related.

---

[14]we use the same systemic velocity given by $z = 0.005535$.
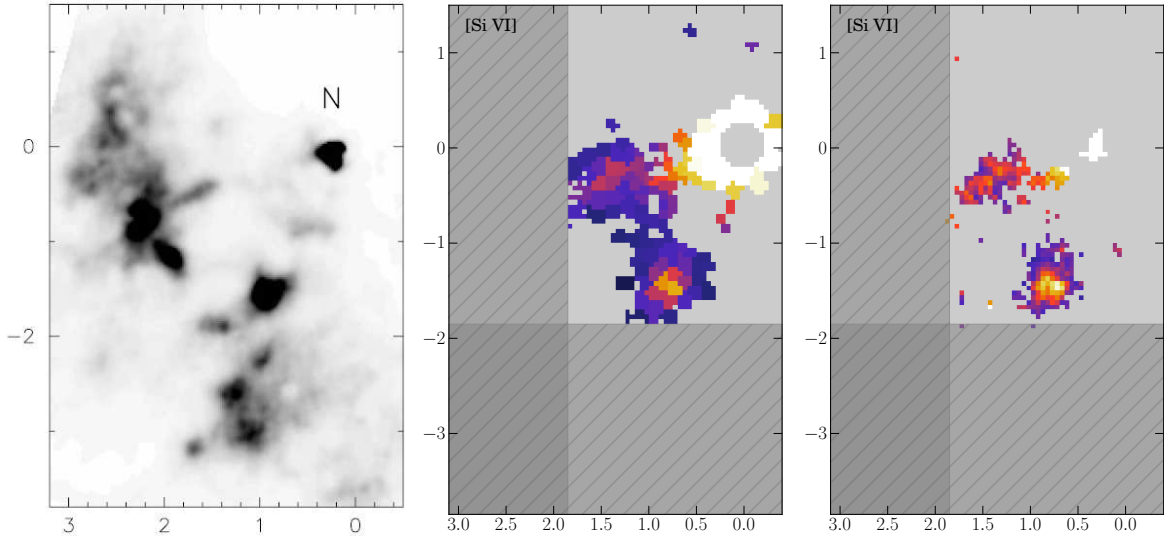
Figure 6.9: (Left) Outflow cone as traced by [OIII] $\lambda5007$ emission. The nucleus is designated by (N). Credit: Lindblad et al. (1996a) and Lindblad (1999). (Middle) [SiVI] map extracted from the binned cube. (Right) [SiVI] map extracted from the unbinned cube with SNR> 3. The latter provides more reliable nuclear constraints and better resolution. The South spot and the filamentary structure are both seen in the [OIII] and the [SiVI] maps. The bright region closer to the nucleus is not clearly seen in the [OIII] map and could be associated with the base of the radio jet. The dark grey areas designate areas outside the field-of-view of SINFONI.

We compare our [SiVI] flux distribution to a HST image of the nucleus and the outflow cone as traced by the [OIII] line (Lindblad, 1999, and reference therein). For a direct visual comparison, we have represented the two distributions with identical spatial scale in Fig. 6.9. The two components appear to coincide very well spatially with a bright knot South and a filamentary structure traced towards the East. This would also suggest that just outside our SINFONI field, one is likely to observe a bright [SiVI] spot at $\sim[2.2, -1]$ arcseconds offset from the nucleus. The kinematics of the [SiVI] seems more blueshifted than the [OIII] line although consistent within our large error bars ($\sim \pm40$km/s; Fig. 21 of Lindblad 1999). In any case, the line is blueshifted with respect to the rotating disk and therefore favours the modeled outflow cone, seen in front of the plane of the galaxy in the SE side (Lindblad, 1999, and reference therein). As the modeled cone has a half opening angle of 50°, one could have possibly expected a highly blueshifted component NW of the nucleus (the measured inclination of the disk is $i = 40 - 50°$) which is not detected probably due to lower gas density out of the disk plane.

On the possibility of nuclear X-ray excitation

In order to evaluate if X-ray heating may account for the 1-0S(1), Brγ and the [FeII] emission, we follow a similar procedure to Zuther et al. (2007) making use of the predictions of Maloney et al. (1996) : we first estimate the effective ionization parameter ξ_{eff}, use the results of Maloney et al. (1996) to obtain the emergent intensities by directly reading off their Fig.6, and compare them to our measured 1-0S(1), Brγ, and [FeII] fluxes. Considering the large

obscuration of the X-ray source, X-ray heating from the central AGN does not seem to be the main excitation mechanism here.

A gas cloud illuminated by a hard X-ray source of luminosity L_X can lead to emergent molecular and ionised gas fluxes. The relevant parameter is the effective (attenuated) ionization parameter given by (Maloney et al., 1996),

$$\xi_{\text{eff}} = 1.26 \times 10^{-4} \frac{f_X}{n_5 N_{22}^{0.9}},$$

where f_X is the incident X-ray flux on a cloud at distance d [pc] from the source, simply calculated by $L_X/4\pi d^2$, n_5 [10^5 cm^{-3}] is the total hydrogen gas density, and N_{22} [10^{22}cm^2] the AGN intrinsic attenuating column density. The BAT 14-195keV X-ray flux F_X is $\sim$7.2 10^{-11} erg/s/cm^2, or $L_X\sim$2.8 10^{42}erg/s, and the column density is $N_H \gtrsim 10^{23}$ cm^{-2} (e.g. Ramos Almeida et al., 2009, Tueller et al., 2010). The intensities are converted to fluxes using the solid angle provided by our pixel scale, *i.e.* 0.05$''^2$ or 5.876 10^{-14}sr. We give – in function of the distance – the effective ionization parameter for a hydrogen gas density of $n = 10^5$cm^{-3}, the predicted (1-0)S(1) and Brγ fluxes, and the observed lines obtained by the average of the flux in rings with radius d and width of 0.2$''$, see Tab. 6.4. We do not compare the [FeII] fluxes since the model essentially predict zero fluxes, in disagreement with what we observe at the edge of the field. Similarly, a lower gas density leads here to an even lower flux prediction.

We conclude that the X-ray source fails to predict correctly the line intensities observed and cannot be the main excitation mechanism. This being due essentially to the high central obscuration.

This thus further support the presence of very young stars or on-going star formation as discussed in the previous paragraphs.

Table 6.4: Comparison of the observed (1-0)S(1) and Brγ fluxes and calculated using the model of Maloney et al. (1996) for an aperture of 0.05$''\times$0.05$''$ for hydrogen density $n = 10^5$cm^{-3}.

	n=10^5cm^{-3}			Observed	
d[pc]	$\log(\xi_{\text{eff}})$	$\log$(1-0S(1))	$\log$(Brγ)	$\log$(1-0S(1))	$\log$(Brγ)
43.5	-3.7	-17.8	-21.7	-17.65	-16.77
87	-4.3	-18.2	–	-17.87	-17.45
130.5	-4.7	-18.5	–	-17.89	-17.71

6.3.4   Stellar population

Based on a few diagnostics such as the CO and Brγ equivalent width (EW)[15], and the narrow Brγ and H$_2$ fluxes, we can investigate the nuclear stellar population.

We present in Fig. 6.10 the ^{12}CO (2-0) and Brγ EW maps. The stellar component is diluted in the center and hence the EW$_{\text{CO}}$ is almost null in the center and increases to its

---

[15]the equivalent width of a line (in emission or absorption) is defined by

$$EW = \int_{\text{line}} \frac{|F_{\text{cont}} - F_{\text{line}}(\lambda)|}{F_{\text{cont}}} d\lambda,$$

where F_{cont} is the continuum emission at the line, F_{line} is the flux of the line.
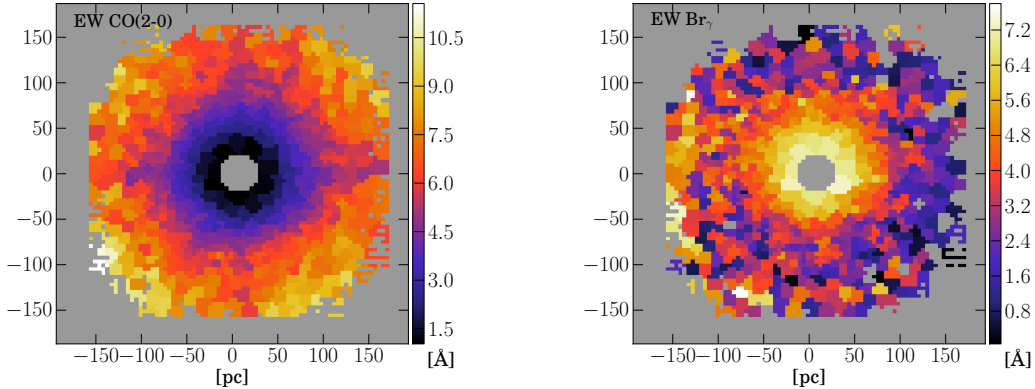
Figure 6.10: (Left) $EW_{CO(2-0)}$ map fainter in the center and converging to its intrinsic value, ~ 9Å, at the edge of the field. Little structure is seen otherwise. (Right) $EW_{Br\gamma}$ map brighter in the center due to the AGN contribution, and converging to ~ 3Å at the edge of the field. Some local increases are also seen and could correspond to more intense star formation, the $EW_{Br\gamma}$ sharply increasing in young star regions.

intrinsic value at the edge of the field. We measure radially the $EW_{CO(2-0)}$, $EW_{CO(6-3)}$, and $EW_{Br\gamma}$, as represented in Fig. 6.11 and fit the radial distributions by Gaussian functions. We obtain an $EW_{CO(2-0);int}$=8.8±0.13Å and $EW_{CO(6-3);int}$=3.5±0.05Å for the stellar absorption lines. The $EW_{Br\gamma}$ is obviously higher in the center and drops to 2.93±0.06Å further out. The map displays also some higher values at the edge of the field, sign of possible more intense star formation.

The obtained CO EW are lower than the typical values of 12Å (2-0) and 4.8Å (6-3) found in the center of Seyfert galaxies (e.g. Hicks et al. 2013, and Burtscher et al. *in prep.*), and expected for an old stellar population as predicted by stellar synthesis code such as STARS (see e.g. Davies, 2007, and references therein). Indeed, the EW are predicted to be almost constant at all ages except for population younger than $\sim$7Myr, where the CO EW sharply drops to zero.

From our two Gaussian decomposition of the Brγ line, we can compare the broad Brackett component - due to the AGN - with the non-stellar continuum responsible for the dilution. This is done by measuring the relative AGN and stellar contributions given by the ratio $f_{stellar}(r) = EW_{meas.}/EW_{intr.}(r)$. The radial profiles are given in Fig. 6.11 where we have adopted a $EW_{intr.} = 9$Å . This intrinsic value leads to a non-stellar continuum distribution in very good agreement with the broad Brackett emission, suggesting the hot dust is indeed spatially unresolved.

To try and understand why the $EW_{CO(6-3);intr.} = 9$Å (rather less than typically found, see Hicks et al., 2013), one can invoke the presence of a young stellar population ($\lesssim$8-10Myr) that would dilute the CO bandheads and produce the spatially extended Brγ. From the EW_{CO}, we can place constraints on the fraction of young stars by

$$f_{young}(age) = \frac{EW_{old} - EW_{meas.}}{EW_{old} - EW_{young}(age)}, \qquad (6.1)$$

where EW_{old}=12Å, and EW_{young}(age) is predicted by STARS (we use numbers for an instan-
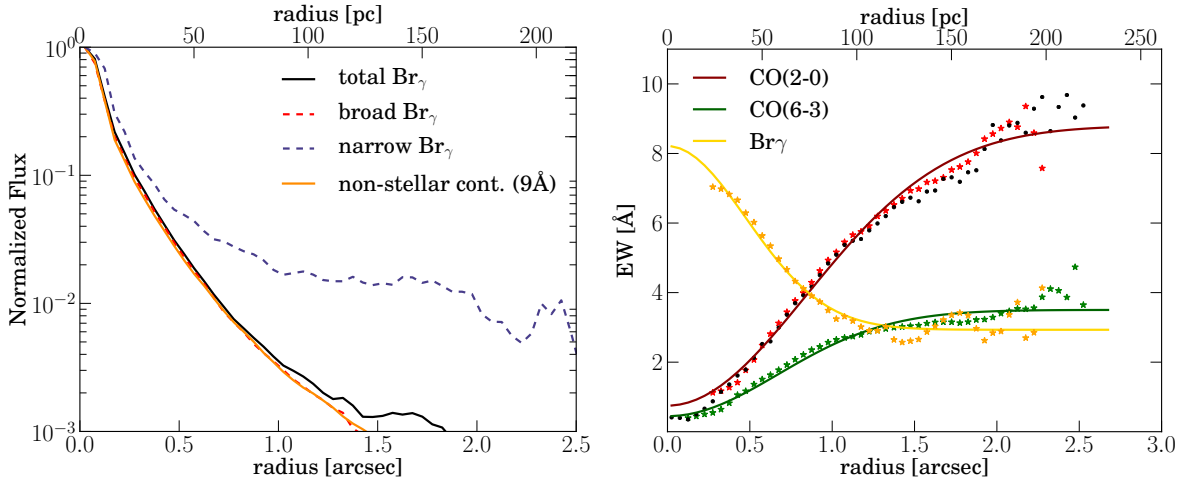
Figure 6.11: (Left) Comparison of the total, narrow and broad radial profiles with the non-stellar continuum radial profile adopting an $EW_{intr.}$=9Å. Each component has been individually normalized. We can clearly see that there is an extended Brγ emission of a non-AGN component. The non-stellar component (derived by adopting an $EW_{intr.}$ = 9Å) is well matched by the broad Brγ component. (Right) Radial profiles of the CO(2-0), CO(6-3), and Brγ equivalent widths, and the respective radial Gaussian fits. The CO absorption features are typically diluted in the center of the field and reach their intrinsic values at the edges, *i.e.* $EW_{CO(2-0);int}$=8.8±0.13Å and $EW_{CO(6-3);int}$=3.5±0.05Å. The narrow component Brγ EW is higher in the center, probably due to improper decomposition there, and converges to $EW_{Br\gamma}$ =2.93±0.06Å further out.

Table 6.5: Derived fluxes at the edge of our field.

Region	$\log(L_K/L_\odot)$	$\log(Q_{Lyc}/ph\ s^{-1})$	$\log(Q_{H_2}/ph\ s^{-1})$	$(Q_{H_2}/Q_{Br\gamma})$
Ring from 1.9″ to 2.5″	7.34	51.29	49.39	0.89

taneous starburst, *i.e.* $\tau = 10^6$yr).

Similarly, we can estimate the K-band continuum provided by the young stars and compare it to the total measured L_K,

$$f_{young}(age) = \frac{L_{K;young}(age)}{L_{K;meas.}}. \tag{6.2}$$

To do so, we estimate first the Lyman ionising continuum ($h\nu > 13.6$eV) photon rate from the Brackett emission taking a photon conversion of 70 (given by the case B recombination theory with T_e=10^{4}K and n_e=10^{4}cm^{-3}, see Hummer & Storey, 1987). From the ionising continuum, STARS predicts the K-band luminosity of the young stars which can then be compared to the measured luminosity. The different values are derived in a ring from 1.9″ to 2.5″ from the center so to be unaffected by the AGN emission. The values are given in Tab. 6.5 (without correction for extinction).

The presence of a spectrally narrow spatially extended Brγ component is another indicator, normally absent in the case of old stellar population, for instantaneous starburst. As discussed in section 6.3.3, there is circumstantial evidence for the presence of young stars at
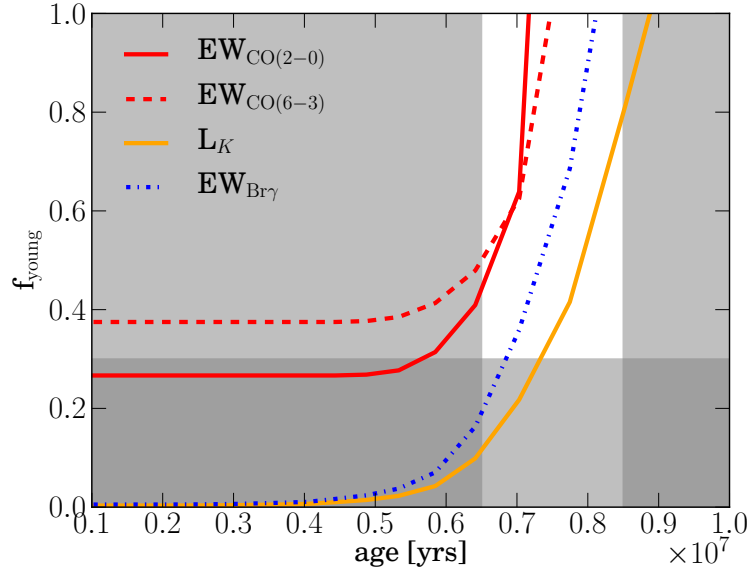
Figure 6.12: Constraints on the fraction of young stars as a function of their age. The old stellar population is assumed to have $EW_{CO(2-0)}$=12Å, $EW_{CO(6-3)}$=4.8Å, and $EW_{Br\gamma}$=0Å. The different curves are thus the constraints derived from equation 6.1 and equation 6.2 based on the following diagnostics : the CO(2-0), CO(6-3) and Brγ equivalent widths, and the K-band continuum. These diagnostics only become consistent to each other within a narrow age range of $\sim 6.5 - 8.5$Myr and for a fraction of those young stars $\gtrsim 30\%$ (the shaded area indicate the age and fraction ranges we can reasonably exclude).

the origin of the Brγ emission – as only those $\lesssim 8$ Myr are hot enough to excite hydrogen sufficiently to emit the Brγ flux. The measured $EW_{Br\gamma}$ provides another constraint on the stellar population and implies a relative narrow range of stellar age. Indeed, at age < 6Myr the $EW_{Br\gamma}$ is > 100Å, and then sharply drops to zero at ages $\gtrsim 10$Myr. The formulation of this constraint is the same as the one posed by the CO bandheads EW, see equation 6.1.

The fraction of young stars, as a function of their age, is represented in Fig. 6.12, assuming that the old stellar population has $EW_{CO(2-0)}$=12Å, $EW_{CO(6-3)}$=4.8Å, and $EW_{Br\gamma}$=0Å. Those constraints do not exactly agree on a precise[16] (age, f_{young}) but they suggest a cluster age of around 6.5-8.5Myr for a large $\gtrsim 30\%$ of the stellar population.

6.4 Discussion: from Nuclear and Circumnuclear Activity Down to the Central Black Hole

Based on optical and radio diagnostics, Sandqvist (1999) presents a schematic overview of the different components in the nuclear region of NGC 1365, reproduced here in Fig. 6.13. This sketch is the combination of (1) radio continuum and CO observations revealing compact

---

[16]the different estimates are also differently affected by unaccounted errors such as imperfect narrow Brγ exctraction, uncertainties on the EW, and on the K-band continuum possibly affected by dilution or absorption by the dust.

radio sources, a radio jet, and a CO ring, of (2) [OIII] HST observations tracing an outflow cone, of (3) HII and star-forming regions, and of (4) hydrodynamical simulations of NGC 1365 predicting the location of an outer and an inner inner lindblad resonance (OILR, IILR). More recently, counterparts of the compact radio sources have been identified in the mid-IR and near-IR (Galliano et al., 2005, 2012) as well as in the far-IR (Alonso-Herrero et al., 2012), revealing young star cluster complexes. Those observations have revealed a bright ring of star formation in the ILR region, suggesting that star formation activity there has been taking place for at least a few million to a few tens of million years. Galliano et al. (2012) suggest that the H_2 emitting gas is predominantly thermally excited in shocks. Gas outflows, as possibly traced by the Brγ emission, would be at the source of this shock excitation. Alonso-Herrero et al. (2012) also suggest that intense star formation is co-located with the CO "twin" peaks, also concluding that most of the star formation is taking place in those dust-obscured regions.

Our SINFONI observations support and complement this picture by providing information on the central few hundreds of parsecs, within the predicted IILR at $R \sim 3''$ (Lindblad et al., 1996b), see Fig. 6.13. Our derived observational constraints suggest that a large fraction of the stellar population ($\gtrsim 30\%$) is young of an age of $\sim$6.5-8.5Myr. This is close to the suggested age of the young star cluster complexes of 5.5-6.5Myr in the ILR found by Galliano et al. (2012). As such it would suggest a common origin. The nuclear molecular and ionised gas emission seems to be dominated by star formation, and is likely thermalized, although we cannot fully exclude fluorescent excitation. High-FUV excitation appears consistent with our observation and shocks could also be a source of excitation. Unfortunately we cannot further constrain the excitation mechanisms on account of the few and faint detected molecular lines. In particular, it is of interest to determine if shock excitation is the source of H_2 emission as observed in the circumnuclear star clusters by Galliano et al. (2012). Such shocks could indeed lead to accretion onto the central black hole.

The molecular hydrogen (as traced by $H_2(1-0)$ S(1)) also appears to be rotating in a, tentatively, cooler disk as the one traced by old stars. The gas distribution displays also filamentary and patchy structure. The higher H_2 luminosity observed at the edges of our field, in particular in the SE and NW, could actually trace the IILR. Owing to the two ILR, an oval ring has apparently formed near the IILR reasonance and possibly fragmented into clumps due to gravitational instability, and by collision could dissipate its orbital energy to feed the nucleus (e.g. Wada, 2004). This would agree with the presence of the CO ring near the IILR, the ring of star formation, and the clumpy structure in our molecular hydrogen map. However, we are not able to measure substantial in- or outflows due to the relative low SNR of the detection.

An exquisite alignment: rotating disk, outflow, "torus", and accretion disk

From our stellar kinematics map and disk fitting, we determine a PA = 43° and $i \sim 50.7°$. The first is in excellent agreement with large scale measurements (e.g. PA=40°, Zánmar Sánchez et al., 2008). On the other hand, the inclination of the galaxy agrees well with photometric measurements ($i = 52 - 55°$, Lindblad, 1978, Zánmar Sánchez et al., 2008), but less with – although not vastly different – Hα kinematics measures ($i = 40 - 41°$, Jorsater & van Moorsel, 1995, Zánmar Sánchez et al., 2008). Regardless of these small differences, the large-scale and the nuclear environment appears well aligned. This alignment is however by itself not particularly unusual.

In the circumnuclear environment, the CO molecular ring has a similar orientation with a PA$\sim$30° (Sandqvist et al., 1995). The nuclear kinematics, as we have seen, is well aligned to the large-scale geometry. This is further confirmed by the [OIII] ionization cone model of Hjelm & Lindblad (1996) which obtain a PA of 126° and $i = 35$°. The position angle is only a few degree different than the stellar rotation axis and only 1° from the radio jet axis (P.A. 125°, Sandqvist et al., 1995, Morganti et al., 1999). The inclination is also in relative good agreement with the galaxy inclination at all scales. While Wilson & Tsvetanov (1994) find in fact a possible trend for ionization cones to align with the disk rotation axis for late-type galaxies, NGC 1365 appears here as an extreme case with its very close alignment. Such an alignment might suggest accretion from the disk, *i.e.* that secular processes have been the dominant process, as discussed for NLS1 in CHAP.5.

Hjelm & Lindblad (1996) also obtain a cone full opening angle of 100°. Alonso-Herrero et al. (2012) fit a clumpy torus model to the SED of NGC 1365 based on near and mid-IR data. Interstingly they obtain an angular opening angle of the torus as measured from its equator $\sigma_{\text{torus}} = 36^{+14}_{-6}$deg, which is compatible to the modeled outflow cone. Finally, Iyomoto et al. (1997) fit the X-ray spectrum of the nucleus, and use the Fe-K emission line to fit an inclined accretion disk. They obtain an inclination of the fitted disk to the plane of the sky of 42^{+15}_{-22}deg. More recently, Risaliti et al. (2013) also contrains the disk parameters, and obtain a disk inclination of 63^{+3}_{-20}. Both are consistent with the large scale inclinations and within their large error bars.

These results at all scales reveal a unique alignement, that one would argue is due to its particularly strong bar which is efficient in driving the gas from the large scale disk down to the nuclear region. It also makes NGC 1365 a prototypical object from which we could learn more on small scales on the structure of the obscuring medium and the accretion around and onto the central black hole.

Accretion on the black hole: mass and spin

Ultimately some gas is accreted onto the black hole. The black hole sphere of influence is given by $R = GM_{BH}/\sigma^2$. Considering a black hole mass of order $M_{\text{BH}} \sim 5 \times 10^6 M_{\odot}$ (see the discussion in the next paragraph), and velocity dispersion $\sigma \sim 100$km/s, one get $R \gtrsim 2$pc$\sim 0.02''$, which is an order of magnitude smaller than the resolution of our data (PSF FWHM is $\sim 0.16''$ with pixel size of $0.05''$). Therefore, tracing the black hole mass influence over the galaxy potential is not trivial, and one can generally only hope to place upper limit. This is further limited in our case by the strong stellar feature dilution, essentially preventing kinematic measurements in the vicinity of the black hole. Following those arguments, we do not try to place formal constraints on the dynamical mass of the black hole. We shall comment nevertheless on estimates found in the literature.

Black hole mass estimations of NGC 1365 varies by approximately an order of magnitude. Assuming a reasonable size of the X-ray source, Risaliti et al. (2009) suggests that the black hole mass must be of order $2 - 3 \times 10^6 M_{\odot}$. From the optical luminosity and the Hβ width, they also estimate a identical black hole mass (using the BLR size - luminosity relation of Kaspi et al., 2005). On the other hand, the $M_{\text{BH}} - \sigma_*$ relation Ferrarese & Merritt (2000) leads to higher estimates $\sim 2 - 4 \times 10^7 M_{\odot}$ (velocity dispersion from this work, and from Oliva et al., 1995). The bulge luminosity to black hole mass gives similar estimates (Risaliti et al., 2009). However, the NGC 1365 presents young star cluster possibly enhancing the bulge luminosity (e.g. Galliano et al., 2012) and biasing these estimates. In addition, NGC
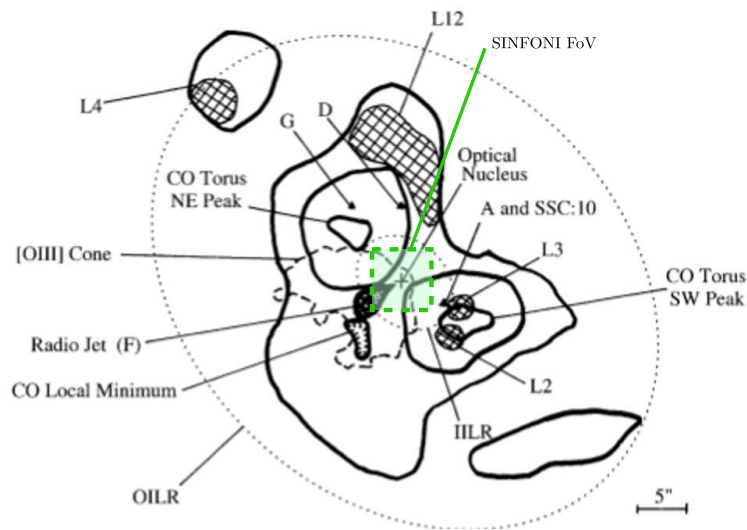
Figure 6.13: Schematic diagram of the nuclear region of NGC 1365. Solid contours: CO distribution; hatched areas: HII and star-forming regions; solid triangles (G,D) : compact radio sources; thick solid contour: radio jet; dashed contour: [OIII] outflow cone; dotted ellipses: approximate positions of Inner and Outer ILR. Credit: Sandqvist (1999). The author uses the denomination of CO "torus". To avoid any confusion with the AGN "torus", we designate it by "CO ring" in the text. The compact radio sources have also been identified in the mid-IR as young star cluster complexes (Galliano et al., 2005) and in the far-IR (Alonso-Herrero et al., 2012). In dashed green, we indicate the approximate SINFONI FoV of our data.

1365 possesses a strong large-scale bar and is likely a NLS1 as we have discussed in the introduction. Its location on the $M_{BH} - \sigma_*$ plane is then possibly not on the relation but more likely below it (see also section 5.5.3). Considering this possible bias, estimations based on BH-bulge relations would overestimate the black hole mass.

Therefore, the currently accepted best estimate is $M_{BH}=2\times10^6 M_\odot$ (Risaliti et al., 2013).

The black hole spin of NGC 1365 is well constrained. This is the result of a combined measurement in the soft X-ray (E<10keV) with XMM-Newton and broadband 3-79keV observations with NuSTAR recently presented by Risaliti et al. (2013). This allows them to break model degeneracy and to favor models including disk reflection scenario from the inner accretion disk rather than models employing multiple variable absorbers instead.

From the relativistic disk reflection, they obtain a spin of $a^* \geq 0.84$ at 90% confidence and with a minimum $\Delta\chi^2$ at $a^* \sim 0.97$. This assumes a truncation of the disk at the innermost stable circular orbit, which has been shown to be valid for thin disk models (Reynolds & Fabian, 2008).

As we have discuss in CHAP.5 section 5.5.2 and later suggested by simulation (Dubois et al., 2014), a prolonged secular evolution could lead to high BH spin. Similarly, the excellent alignment at all scales seen in NGC 1365 can have tentatively lead to its high BH spin.

While the work of Risaliti et al. (2013) provides excellent X-ray constrains and allows them to break down model degeneracies, the high black hole spin measurement should still to be taken with caution, considering as well our discussion in section 5.5.2.

6.5   Conclusions

Our main findings of the inner $D \sim 300$pc region of NGC 1365 are as follows :

- We are able to measure the molecular gas distribution which was undetected in previous spectroscopic studies. The molecular gas is in rotation in the galaxy plane and is likely the source of fuel of the BH as suggested for other active galaxies. The distribution however seems to be more patchy and filamentary than usually observed. This could suggest some sort of fragmentation into clumps due to gravitational instability inside the IILR and could provide the mechanisms for the dissipation of the orbital energy to feed the nucleus. However, considering the low flux detection we are not able to measure in- or outflows.

- We confirm the presence of a rotating disc as suggested from slit spectroscopy of P.A.$\sim$ 43° and inclination angle of $\sim$ 50° in relative agreement with the large scale galaxy rotation (the inclination shows some discrepancy, see the discussion). We do not observe significant asymmetries or trace of stellar bar or spirals and can conclude that there is no substantial warp down to these scales.

- We find evidence for a significant fraction ($\gtrsim$30%) of young stars of age around 6.5-8.5Myr, at the origin of narrow Brγ and [FeII] emissions. This highlights the presence of a nuclear starburst as observed in other AGN possibly at the origin of the nuclear activity.

- We detect the [SiVI] coronal line which shares strong similarity with previous HST image [OIII] line distribution, further highlighting the presence of a nuclear outflow. We also may see the base of the jet. The outflow cone has been previously modeled and is close to the rotation axis of the stellar and gas discs. Hence disc plane and cone are close to orthogonal.

This suggests a smooth prolonged accretion within the galaxy plane down to the black hole. Hence highlighting the importance of secular evolution and putatively leading to a rapidly spinning black hole. We have suggested that those processes play a major role in NLS1 galaxies. And there are evidences suggesting that NGC 1365 is one.

This particular alignment makes also NGC 1365 a prototypical object for which further studies could teach us more on small scales structures and feeding mechanisms onto the central BH.

The presence of a gas rich ring and the low molecular hydrogen intensity in the central few arcseconds suggests that the gas driven in by the bar is currently not reaching the nucleus. This could explain the low AGN luminosity, but the situation could also change in the future, as the gas reservoir in the ring is growing.

THE LASER GUIDE STAR TIP-TILT DETERMINATION CHALLENGE

The use of laser was introduced to compensate the need of a sufficiently bright reference source to achieve the adaptive optics correction, thus limiting the sky coverage of such technique. Nevertheless, laser beacons do not allow an accurate global wavefront tip-tilt determination, and still relies then on the availability of a natural guide star. This indetermination is the consequence of the round trip of the laser beam light. This is sometimes considered to not be a problem since the tip-tilt decorrelation angular distance is much larger and the normalized power spectrum drop off at lower frequencies than for higher modes. Following Rigaut & Gendron (1992), we shall show that those considerations are largely misleading. First, while the tip-tilt is correlated over much higher angular separation, it also carries a much higher wavefront phase variance (see equation 1.7). Hence in an absolute way the angle for which the phase error does not exceed a given value is not much higher than for any other modes, and of order $\sim 10''$ (for $1\mathrm{rad}^2$ phase variance) at visible wavelength[1]. Concerning the brightness of the star, the large correlation time should be regarded as coming from an additional amount of low frequencies in the spectrum. This is readily seen in Fig. 1.1. From this consideration, the tip-tilt correction bandwidth should be kept as high as any other mode. A third argument concerns the gain in collecting surface area. Rigaut & Gendron (1992) shows that in the photon limited regime and for $d > r_0$, the phase error is independent of the aperture diameter in the seeing limited regime (where d is the aperture diameter).

Several techniques have been proposed to solve the tip-tilt indetermination problem. Rigaut & Gendron (1992) proposed the double adaptive optics technique with a second laser beacon in the direction of the tip-tilt star. This allows to benefit from the aperture gain and to reduce the phase error (becoming $\propto d^{-2}$ instead of independent of the aperture). But even with such a solution, the sky coverage in the visible remains limited.

A number of other techniques relies on LGS properties : such as polychromatic laser (e.g. Foy et al., 1995), auxiliary telescopes (e.g. Ragazzoni & Esposito, 1999), etc.. We do not intend to review those possible techniques in detail here. Rather we wish to explore the spatial

---

[1] The isoplanatic angle for tilt is defined as (e.g. Parenti & Sasiela, 1994)

$$\theta_{TA} = \left[0.668 k^2 D^{-1/3} \sec \zeta^3 \int_{\mathrm{path}} C_n^2(z) z^2 dz \right]^{-1/2}.$$

and temporal correlations associated with the upward tip-tilt with respect to the downward tip-tilt, and how such knowledge could help to provide a partial correction. Indeed, while it is generally accepted that the round trip of the laser beam blurs the information, no treatement based on spatial and temporal correlations is known to us. The study below explores shortly such considerations.

The spatial "decorrelation" argument

Spatial correlation of Zernike coefficients   Based on the modified Kolmogorov spectrum (the von Kármán spectrum, see equation 1.7), Takato & Yamaguchi (1995) derive the spatial correlation of Zernike coefficients for phase turbulence with finite outer scale.

If a_j is the j term Zernike coefficient. The correlation between two Zernike coefficients in function of their separation $\vec{s}$ is written as

$$< a_j a_{j'}^*(\vec{s}) > = 2^{14/3} \pi^{8/3} A[(n+1)(n'+1)]^{1/2} R^{5/3} f_{jj'}(s, \theta_0, k_0), \tag{A.1}$$

with R the aperture radius, n and n' the radial degrees of the term j and j' of the Zernike polynomials, $s = |\vec{s}|$ the distance between two apertures normalized by the aperture diameter ($D = 2R$), θ_0 the angle between $\mathbf{s}$ and the direction $\theta = 0$, and $k_0 = 1/L_0$ with L_0 the outer layer of the von Kármán turbulence. A appears in the expression of the power spectrum and is given by

$$A = 0.00969 \left(\frac{2\pi}{\lambda}\right)^2 \int_0^\infty C_n^2(z) dz. \tag{A.2}$$

The function $f_{jj'}$ (for $m, m' \neq 0$, $+$ for j, j' both even and $-$ for j, j' both odd) is given by

$$\begin{aligned} f_{jj'}(s, \theta_0, k_0) &= \pm(-1)^{(n+n'-m+m')/2} \cos((m+m')\theta_0) I_{m+m',n+1,n'+1}(2s, 2\pi R k_0) \\ &+ (-1)^{(n+n'+2m+|m-m'|)/2} \cos((m-m')\theta_0) I_{|m-m'|,n+1,n'+1}(2s, 2\pi R k_0), \end{aligned} \tag{A.3}$$

with the function $I_{\kappa,\mu,\nu}(a, x_0)$ given by

$$I_{\kappa,\mu,\nu}(a, x_0) = \int_0^\infty \frac{x^{-1} J_\kappa(ax) J_\mu(x) J_\nu(x)}{(x^2 + x_0^2)^{11/6}} dx. \tag{A.4}$$

The normalized correlation function is then defined by

$$C_{jj'}(s) = \frac{< a_j a_j'^*(s) >}{< a_j a_j'^*(0) >}, \tag{A.5}$$

where we take $\theta_0 = 0$. For our purpose we are only interested in the tip and tilt, *i.e.* the $j = 2$ and $j = 3$ terms for which we have $n, m = 1, -1$ and $n, m = 1$ for the tip and tilt respectively. Moreover we are interested in the tip-tip and tilt-tilt correlation. In Fig. A.1, we integrate the equation A.5 and represent the results for C_{22} and C_{33} in function of the normalized distance. This is equivalent to the Fig. 3 an 4 of Takato & Yamaguchi (1995). This also illustrates the effect of the outer layer L_0. Typically, higher outer layer leads to higher correlation.

The above formulation describes the one way correlation from a natural guide star. For the LGS, up and down tip-tilt should be taken into account. We analyze this aspect in the next section.
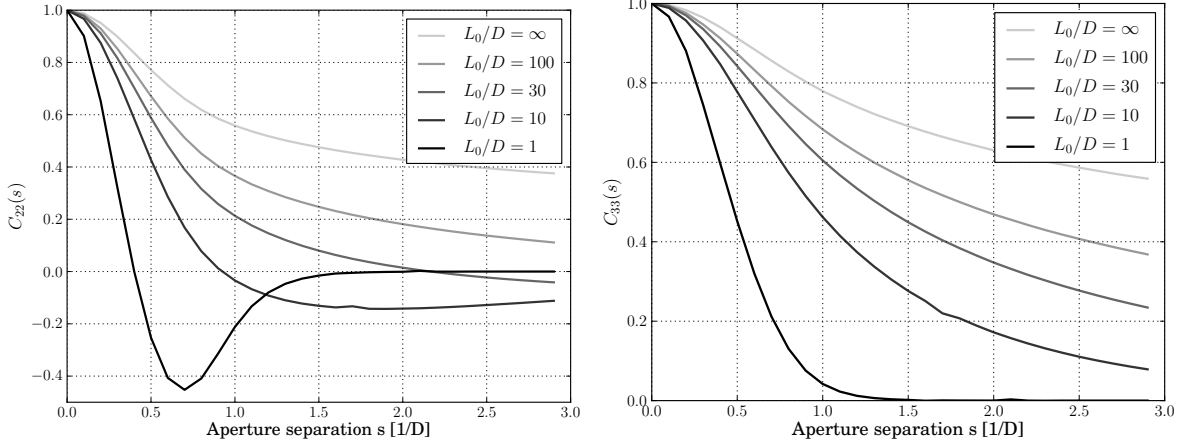
Figure A.1: Illustration of the spatial correlation for the tilt mode, reproducing Fig.3 and Fig.4 of Takato & Yamaguchi (1995). (Left) Tip correlation (X-tilt) along x ($\theta_0 = 0$). (Right) Tilt correlation (Y-tilt) along x ($\theta_0 = 0$) .

LGS up tip-tilt retrieval   Considering an on-axis launch with an aperture d_{launch} and a Shack-Hartmann wavefront sensor sampling the telescope aperture with a subaperture size d_{subap}, each subaperture measures the difference between the up tip-tilt X_1 and the down tip-tilt $X_2, X_3, ...$ sampling a different cone of turbulence. For simplicity, we assume in the following that $d_{launch} = d_{subap}$. Our problem can thus be formulated as follow : we want to retrieve the LGS up tip-tilt X_1 based on the "known" theoretical spatial correlation and our measured differential tip-tilt $X_2 - X_1$, $X_3 - X_1$, etc.

From this formulation, we can express the spatial covariances $Cov(X_i, X_j)$ as a function of the correlation function equation A.5. By doing so we get the following covariance matrix **C**

$$
\begin{cases}
Cov(X_1, X_1) & = \sigma^2 \\
Cov(X_i - X_1, X_i - X_1) & = 2\sigma^2(1 - Corr(X_i, X_0)) \\
Cov(X_i - X_1, X_1) & = \sigma^2(Corr(X_i, X_1) - 1) \qquad i \neq 1 \\
Cov(X_j - X_1, X_i - X_1) & = \sigma^2(Corr(X_j, X_i) - Corr(X_j, X_1) - Corr(X_i, X_1) + 1) \quad i \neq j \neq 1
\end{cases}
$$
(A.6)

where σ is the phase variance of the tip-tilt and is assumed to be the same for X_1, X_2, etc.. This covariance matrix can then be used to estimate the value X_1, *i.e.* the LGS up tip-tilt.

Without discussing here estimation theory, we can express the joint probability distribution function by

$$
\begin{aligned}
\phi(\vec{x}) & = \phi(X_1, X_2 - X_1, ..., X_n - X_1) \\
& = \frac{1}{(2\pi)^{n/2}|C|^{1/2}} \exp\left[-\tfrac{1}{2}(\vec{X} - \vec{\mu})^T \mathbf{C}^{-1}(\vec{X} - \vec{\mu}) \right],
\end{aligned}
$$
(A.7)

with **C**, the covariance matrix formulated above.

This also allow us to formulate the conditional distribution function $\phi(X1|\vec{Y})$, with $Y = X_2 - X_1, X_3 - X_1$, etc.. This CDF width is then used as a proxy for the distribution (and the variance) of $X1$ after having considered the measurements Y, *i.e.* after a potential correction.
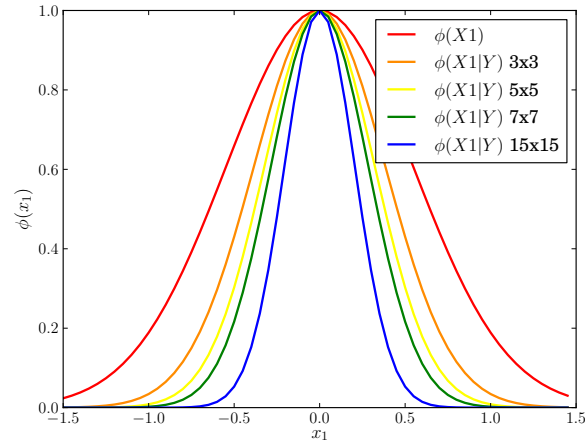
Figure A.2: No correction and use of different grid. Parameters are: $\lambda = 0.5\mu m$, $R = 0.5m$, $L_0 = 100m$. The combination of a relatively small aperture R and large outer layer is not in favor of the best performances.

Grid correction. Based on those considerations, we performed the following numerical computations. We consider grid of measurements (as would be provided by a Shack-Hartmann) of 3×3, 5×5, 7×7, and 15×15. The central aperture measurement of those grid is always 0 (since the correlation is 1), the other apertures depend on the correlation between the up and down beams. Based on these grids, we compute the respective covariance matrix of size $9^2, 25^2, 49^2, 225^2$, and then derive the CDF. The results are presented in Fig. A.2.

The width of the Gaussian we obtain is an indicator of the accuracy of the up tip-tilt retrieval. We see a large reduction of this uncertainty and the possibility to partially retrieve this up tip-tilt. Knowing the upward contribution allows us to know precisely the guide star position on sky and to perform a sensible downward tip-tilt measurement. While we have not study directly their influence, the smaller the aperture R and the larger the outer scale, the less efficient is the up TT retrieval.

The idea presented here is, in fact, very simple and relies on the decorrelation of the downward tip-tilt with subaperture distance, hence an appropriate averaging (taking the correlation function into account) can allow a partial recovery by averaging out the downward contributions.

Cone Effect. Above, we take into account the round trip of the LGS beam but we do not consider the cone effect. This will modify the spatial power spectra and the derived correlation functions.

We propose that the formula of Takato & Yamaguchi (1995) should be modified accordingly by introducing a factor $((H - z)/H)^{5/3}$ in the correlation function and the power spectrum, and to integrate over the altitude z from 0 to H, the laser guide star finite distance.

The temporal "decorrelation" argument

Finally, without developing further the idea, a potential temporal decorrelation between up and down tip-tilt could be of similar interest. Conan et al. (1995), in their wavefront temporal analysis, decompose the temporal power spectra in Zernike coefficients. They also study the

case of laser guide stars and consider (only) their finite distance. In particular, in their Fig. 8, they represent the temporal power spectra of the eight Zernike coefficient for a natural guide star, a sodium (90km) and a Rayleigh (12km) guide stars. In particular they point out a loss of temporal correlation between the LGS wavefront and the natural ones as a consequence of cone effect. It would be therefore of interest to study the temporal decorrelation for a round trip for the tip-tilt Zernike coefficient. The difference in cone effect between the up (small aperture launch optics) and down (large telescope aperture) tip-tilt could present significant temporal decorrelation. This, in turn, may be useful to discrimate the two signals based on their characteristic frequencies.

PNCCD CAMERA SUPPLEMENTS

B.1   Voltages of the pnCCD

We list in Tab. B.1, the different voltages required for the PNCCD, including the "safe" voltage and current ranges for the ARGOS operation. Those limits are implemented in the PNCCD software as hard limits triggering an automatic shutdown if they are exceeded. The high depletion voltage (RK) allows the full depletion of the n-silicon bulk.

B.2   pnCCD performance considerations

B.2.1   Dark current and temperature

We detail here the expectation of a low increase with temperature of noise due to dark current shot noise. The PNCCD noise behavior with temperature is discussed in section 3.3.6.
The relation of the dark current I_d in silicon bulk with temperature is described by (e.g. McLean, 2008)

$$I_d = 2.55 \times 10^{15} A_{pix} I_{d;0}^2 T^{1.5} e^{-\frac{E_g}{2kT}} \quad [\text{e}^-/\text{s/pix}], \tag{B.1}$$

with $I_{d;0}$ the dark current in $[nA/cm^2]$ at room temperature, *i.e.* $T = 300K$, A_{pix} the pixel area in $[cm^2]$, T the operating temperature, E_g the bandgap energy in electronvolts, k the Boltzmann constant (1.38065×10^{-23}J/K or 8.62×10^{-5}eV/K). The bandgap E_g of silicon varies with temperature according to

$$E_g = 1.1557 - \frac{7.021 \times 10^4 T^2}{1108 + T}. \tag{B.2}$$

Using the measurements of PNSENSOR at $-50°$, *i.e.* 0.2e$^-$/px/s, we can estimate the constant factor – $2.55 \times 10^{15} A_{pix} I_{d;0}^2$ – and derive the evolution of the dark current with temperature. We find that at $-35°$C, the dark current amount to $\sim 1.5 e^-$/px/s, and at $-25°$C to $\sim 5.2 e^-$/px/s. Assuming this can be extrapolated to our fast rate of 1000 frames per second, the equivalent shot noise (*i.e.* the square root of the dark current flux) is however negligible in both case, *i.e.* ~ 0.04e$^-$ and ~ 0.07e$^-$ respectively to be added in quadrature to the total variance.

Table B.1: List of the different PNCCD voltage designations, and their allowed voltage and current ranges for the ARGOS operations.

Name	Voltage range [V]	Current range [mA]	Comments
PHI123 (Off.&Amp.)	[15.9-18.1] & [5.9-6.1]	∼0 & [5-15]	image area transfer register voltages
PHI456 (Off.&Amp.)	[15.9-18.1] & [5.9-6.1]	∼ 0 & [5-15]	frame storage area transfer register voltages
RK	[235-290]	∼ 0	depletion voltage
OGR & GRA	[18.9-19.1]	∼ 0	guard rings
VBST	[2.1-2.6]	∼ 0	gate of F2 FET in Fig. 3.4
VSSS	[2.75-2.85]	[40-55]	reference voltage at the current source, at source of F2 (VSSS-Rs) in Fig. 3.4
RFGA (Off.&Amp.)	[3.9-7.7] & [2.9-7.2]	[2-6]	gate of RF in Fig. 3.4
RSTA	[0.75-1.4]	∼ 0	drain of RF in Fig. 3.4
FFDR	[3.9-4.1]	[40-55]	drain of FF in Fig. 3.4
VSS, VDD	[2.75-2.85]	[250-350] & [300-400]	CAMEX
VSST, VDDT	[2.65-2.75]	[150-200]	CAMEX
VSSD, VDDD	[2.65-2.75]	[2-40]	CAMEX
VREF	[1.4-1.6]	∼ 0	CAMEX
+BUFF & −BUFF	[4.95-5.05]	[220-270]	bipolar voltages for the PCB
VCC	[4.95-5.05]	[160-220]	PCB PSU

B.2.2 Bias stability: Allan Variance

We present here another possible tool to analyze the bias stability discussed in section 3.3.4. The Allan variance gives a quantitative measure of how much the average of some data vary with the averaging time τ. It is an analyzing tool of a time sequence and as such may be appropriate for the study of pixel offset fluctuations. It can be written as

$$\text{AVAR}^2(\tau) = \frac{1}{2(n-1)} \sum_i \left(y(\tau)_{i+1} - y(\tau)_i \right)^2,$$ (B.3)

where τ is the averaging time, y_i the average value of the measurement in the bin i and n the total number of bins.

We perform this analysis with the 1st LBT engineering camera by acquiring 50400 frames over 14hrs, but processing only 1/100 of them thus spaced by 0.1 second. The usual practice for the Allan variance is to allow for a minimum of 9 bins to average over, hence the maximum averaging time is here of τ =5600 seconds (∼ 1h30). The results is given below in Fig. B.1. The obtained variance decreases smoothly and we are not able to probe the "lifetime" of the pixel offsets, *i.e.* an up-rise of the Allan variance. More frame should be used with also higher maximum inter-frame time delay[1].

[1]e.g. by acquiring offset maps (created out of a hundred of frames) every 10 minutes for 12hrs. This was
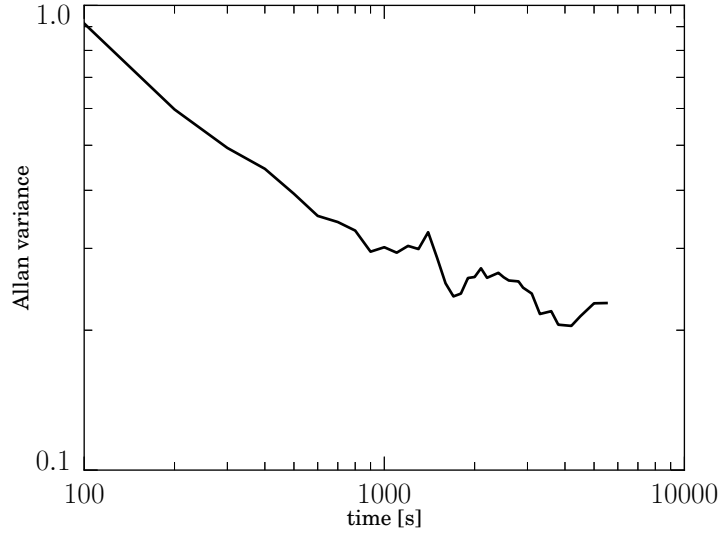
Figure B.1: Allan variance on dark frames images (504 frames in total) acquired over 14hrs. The maximum averaging delay is $\tau = 5600$s.

B.2.3 Noise calculation : comparison of different techniques

The readout noise reported by PNSENSOR is substantially different from ours, as discussed in section 3.3.7. Here we compare different algorithms resulting in different derived noises. We argue that this can account at least partially to the difference between PNSENSOR and our measurements. The following algorithms are considered :

1. The pixel-by-pixel estimated standard deviation over a set of dark frames.

$$s_{i,j} = \sqrt{\frac{1}{N_{frames} - 1} \sum_{k \in \text{frames}}^{N_{frames}} (y_{k;i,j} - \bar{y}_{i,j})^2}, \qquad (B.4)$$

where i and j indicate the pixel coordinates, y the pixel value, $\bar{y}$ the average pixel value over all the frames, and N_{frames} the number of frames used to derive the standard deviation.

2. The algorithm used by PNSENSOR (Andritschke et al., 2008). This implements a sort of outliers rejection : for each pixel-by-pixel a user-supplied number, N_c. of the largest pixel values are excluded, and by symmetry the same amount of the lowest values. Typically the five highest and the five lowest values are rejected for a set of 200 frames. The standard deviation equation B.4 is then computed based on the remaining pixel values.

3. A common way in astronomy to compute a reliable standard deviation is the median absolute deviation, formulated as

$$s_{MAD} = \frac{1}{0.6745} \text{median}_i(|y_i - \text{median}_j(y_j)|). \qquad (B.5)$$

difficult to realize at the time of writing due to laboratory acquisition software limitations.

The factor 0.6745 is included so that this estimator is consistent with σ (or s) for a Gaussian distribution.

4. Finally, we use the Chauvenet criterion, also in common practice in astronomy. A data points is disregarded if the chance that such a measurement falls in a series of N measurements is smaller than $1/2$.

Using these various algorithms, we derive the average noise per CAMEX. We use a set of 200 dark frames in the high gain mode ($\sim 9.5 ADU/e^-$), median dark subtracted and full common-mode corrected, acquired with a chip temperature of $\sim -35°$ C, at 900Hz. The comparison between the four algorithms is given in Tab. B.2.

Table B.2: Derived noise with respect to the different techniques.

Technique	CMX 1	CMX 2	CMX 3	CMX 4
1. Mean standard deviation	2.72	2.73	2.69	2.69
2. Discard 10 extreme values	2.41	2.41	2.37	2.38
3. Median absolute deviation	2.70	2.70	2.66	2.67
4. Use of Chauvenet criterion	2.69	2.69	2.65	2.66

From the values presented in this table, we observe that the technique used by PNSENSOR can underestimate by $\sim 0.3e^-$ the RON compared to the other techniques. In our analyses, we choose to use the more conservative Chauvenet criterion.

B.3   Camera comparison

We compare in section 3.5 the ARGOS PNCCD with two other current state-of-the art alternatives : the OCAM2, an AO development based on an EMCCD, and the sCMOS technology. Here, we provide in Tab. B.3 the key characteristics of the ARGOS PNCCD, the EMCCD-based OCAM2 camera and a sCMOS camera from PCO.EDGE. All three presenting some competitive advantages.

---

[2]at the time of writting a new version going up to 2kHz has been announced.

[3]rs: rolling shutter for which each row start and end its exposure at sligthly offset in time and is typically 2× faster than the global shutter as the duty cycle is 100% instead of 50%; gs: global shutter. The (893Hz/435Hz) is for the image size 320×240.

[4]for a multiplication gain of 500 (this also implies a smaller dynamic range).

[5]Standard silicon $\sim 13\mu$m.

[6]Deep depletion silicon $\sim 40\mu$m.

[7][lp/mm] is the line pairs per millimeter. A rough approximation would gives FWHM$\sim 1/$MTF $= 13\mu$m which is $\sim$2px.

[8]*i.e.* broadband anti-reflective coating.

Table B.3: Comparison of key characteristics between the Argos pnCCD camera, the Ocam2 and CMOS technologies.

Parameters	Argos pnCCD camera	Ocam2 (e2v CCD220)	sCMOS (e.g. pco.edge)
Image area [px]	256×248	240×240	a) 2560×2160 b) 320×240
Image area [mm^2]	11.9×12.2	5.76×5.76	16.6×14.0
Pixel size	$48\ \mu$m	24μm	6.5μm
Frame rate (max.)	1000Hz	1500Hz[2]	a) 100Hz(rs)/50Hz(gs) b) 893Hz/435Hz[3]
Readout noise [e$^-$]	2.5 - 4	<1, 0.3[4]	<2.4e$^-$
Quantum Efficiency at 532nm	>98%	>82%	>50%
Quantum Efficiency at peak	>99%	92-95 %	>59%
Quantum Efficiency [500, 800] nm	>90%	>30%[5] >70%[6]	>30%
Dark current	<0.2e$^-$/px/s at -50°C, 100fps	<0.01e$^-$/px/frms	2 .. 6e$^-$/px/s (+ 0.6/1.8 e$^-$/pixel with gs; DSNU <2e$^-$rms)
PSF FWHM /MTF	<0.5px	0.55px	76.9lp/mm[7]
PRNU	<2.5%	−	<0.5%
Linearity	<2%	<3%	<1%
Transfer to store area	33μs	18μs	−
Latency between exposure and first pixel availability	$< 41\mu s$	58μs	−
Full well capacity	32000e$^-$/ch. (132px)	150e$^-$/px (gain$\times$1000)	30000 e$^-$/px
Detector operating temperature	-40 to -25°C	-45°C	$+5$° C
External synchronization	✓	✓	✓
Camera head size [mm]	$212 \times 120 \times 82$ (larger with the back electronics)	$175 \times 76.2 \times 238.5$ incl. controller and ADCs	$76 \times 70 \times 88.3$ incl. ADCs
Entrance optics	fused silica 3mm window (with 532nm coating)	fused silica 3mm window + saphire window (0.9mm), both BBAR[8] coated at 650nm	

PHOTOMETRIC PROFILE FITTING

C.1 Sérsic light profile

The Sérsic power-law intensity profile is frequently used in the study of galaxy morphology. It has the following functional form (e.g. Caon et al., 1993, Peng et al., 2010)

$$I(r) = I_e \exp\left[-\kappa\left(\left(\frac{r}{r_e}\right)^{1/n} - 1\right)\right], \tag{C.1}$$

where I_e is the surface brightness at the effective radius r_e. The parameter r_e is known as the effective, or half-light, radius, defined such that half of the total flux lies within r_e. The parameter n is the Sérsic index: with $n = 4$ the profile is the de Vaucouleurs profile typical of elliptical galaxies, $n = 0.5$ gives a Gaussian, and $n = 1$ is the exponential profile typical of disks. Finally, the parameter κ is in fact coupled to n and is not a free parameter.

The exponential disk profile is more frequently described by the compact form

$$I(r) = I_0 \exp\left(-\frac{r}{r_s}\right), \tag{C.2}$$

where I_0 is the central surface brightness, $I_0 = I_e e^\kappa$, and r_s the scale radius given by $r_e = 1.678 r_s$, or more generally by $r_e = \kappa^n r_s$.

To calculate the parameter κ, we use the analytic expansion from Ciotti & Bertin (1999) valid for $n > 0.36$,

$$\kappa \approx 2n - \frac{1}{3} + \frac{4}{405n} + \frac{46}{25515n^2} + \frac{131}{1148175n^3} - \frac{2194697}{30690717750n^4} + \mathcal{O}(n^{-5}). \tag{C.3}$$

The value of κ can be analytically derived for a Gaussian and is $\kappa = \ln(2)$. The value for a de Vaucouleurs profile is $\kappa = 7.67$.

C.1.1 Surface brightnesses and luminosity ratios

From the integrated flux of a Sérsic profile (e.g., Peng et al., 2010), assuming a perfect ellipse of axis ratio q,

$$F_{\text{tot}} = 2\pi r_e^2 I_e^2 e^\kappa n \kappa^{-2n} \Gamma(2n) q, \tag{C.4}$$

we derive hereafter a few useful quantities.

The surface brightness at the effective radius is

$$\mu_e \; [\mathrm{mag/arcsec^2}] = m_{\mathrm{tot}} + 2.5 \log\left(2\pi r_e^2\right) + 2.5 \log\left(\frac{e^\kappa n}{\kappa^{2n}}\Gamma(2n)q\right), \qquad (C.5)$$

with r_e expressed in arcseconds, and $m_{\mathrm{tot}} = -2.5\log\left(F_{\mathrm{tot}}/t_{\mathrm{exp}}\right) + \mathrm{magzpt}$ with t_{exp} the exposure time and mag zpt the magnitude zeropoint.

For an exponential profile, equation C.2, the central surface brightness is expressed by

$$\mu_0 \; [\mathrm{mag/arcsec^2}] = m_{\mathrm{tot}} + 2.5 \log\left(2\pi r_s^2 q\right), \qquad (C.6)$$

with r_s expressed in arcseconds.

The mean surface brightness $< \mu_e >$ within R_e can then be expressed in function of μ_e,

$$< \mu_e > \;\; = \mu_e - 2.5 \log\left(\frac{e^\kappa n}{\kappa^{2n}}\Gamma(2n)\right). \qquad (C.7)$$

Those quantities are of interest for the study of bulges and have been discussed in section 5.3.3. The values for our two samples of NLS1s and BLS1s are also given hereafter Tab. C.2 and Tab. C.4.

The bulge-to-disk (B/D) and bulge-to-total (B/T) luminosity ratios are relevant quantities for the study of galaxy morphology. These ratios tend to decrease from early- to late- type spirals (e.g. Masters et al. (2010)). The B/D ratio, where the disk is described by an exponential profile, can be expressed analytically as

$$\frac{B}{D} = \frac{n_b \Gamma(2n_b) e^\kappa}{\kappa^{2n_b}} \left(\frac{q_b R_b^2}{q_d R_d^2}\right) \left(\frac{I_e}{I_0}\right), \qquad (C.8)$$

and the B/T as

$$\frac{B}{T} = \frac{n_b \Gamma(2n_b) e^\kappa / \kappa^{2n_b} q_b R_b^2 I_e}{n_b \Gamma(2n_b) e^\kappa / \kappa^{2n_b} q_b R_b^2 I_e + q_d R_d^2 I_0}, \qquad (C.9)$$

where the subscripts b and d refer to the bulge and the disk respectively. I_e is the effective surface brightness of the bulge and I_0 is the central surface brightness of the disk, R_b is the effective radius of the bulge and R_d the scale radius of the disk, and q_b, q_d are the axis ratios of the respective profiles.

C.2   The NLS1 sample

We give in Tab. C.1 all the resulting values from our multi-components fit described in section 5.3.2 using GALFIT. All the fit are illustrated in Fig. C.1 to Fig. C.3 with the 2D original, model and residual images, and the radial profiles of the data, the different components, the residual, and the χ_ν^2. We indicate by open symbols the radial ranges entirely or partially masked. The radial residual and the radial χ_ν^2, given in the upper panels, also provide indirect information on the fit errors.

In Tab. C.2 we give the surface brightnesses (μ_e, $< \mu_e >$), and the luminosity ratios (B/D and B/T). The surface brightnesses are calculated using equation C.5 and equation C.7. The B/D and B/T using equation C.8 and equation C.9.

Table C.1: Full fit results of the NLS1 sample fits. The index g, b, d designate respectively *gaussian*, *bulge*, and *disk*. The gaussian fit is indended to fit the AGN and any nuclear cluster (see also text CHAP.5). It is sometimes replaced by a simple PSF fit. The GALFIT results includes, m observed magnitude in HST STMAG, R radii, q axis ratios, n bulge Sérsic index, the sky level, and the resulting reduced chi-squared χ_ν^2.

Object Name	m_g [mag]	m_b [mag]	m_d [mag]	R_g [px]	R_b [px]	R_d [px]	q_g	q_b	q_d	n_b	sky [adu]	χ^2
KUG1136	17.75	17.55	15.82	2.38	32.32	107.08	0.98	0.76	0.62	1.21	1.82	1.162
MRK0042	18.27	16.97	15.3	3.14	19.72	141.13	0.81	0.82	0.58	1.27	1.77	0.946
MRK0359	16.93	14.38	12.1	4.83	74.12	462.74	0.79	0.67	0.83	1.41	0.994	1.029
MRK0382	17.28	16.81	15.96	3.96	16.62	96.39	0.76	0.94	0.54	1.36	2.17	1.489
MRK0493	17.9	17.1	15.2	2.97	11.95	131.25	0.92	0.97	0.41	0.74	1.44	1.025
MRK0766	16.61	16.22	14.0	4.8	13.38	105.12	0.96	0.74	0.44	1.88	3.69	1.046
MRK0896	17.5	16.36	14.48	3.98	14.96	113.56	0.75	0.77	0.71	2.06	2.0	1.343
MRK1044	17.07	15.8	14.9	4.59	13.02	77.55	0.81	0.91	0.76	1.45	1.95	1.048
NGC4748	17.17	15.4	13.89	5.53	18.93	141.44	0.61	0.98	0.68	1.93	2.46	0.677

Table C.2: Values calculated from the NLS1 fit results: the surface brightness at the effective radius μ_e, the average surface brightness within the effective radius $< \mu_e >$, the bulge to disk luminosity ratio, and the bulge to total luminosity ratio. See equation C.5, equation C.7, equation C.8, and equation C.9. Magnitudes are in HST STMAG units.

| Object Name	$\mu_{e;b}$ [mag/arcsec^2]	$< \mu_{e;b} >$ [mag/arcsec^2]	B/D	B/T
KUG1136	20.90	20.11	0.20	0.17
MRK0042	19.35	18.54	0.21	0.18
MRK0359	19.47	18.61	0.12	0.11
MRK0382	19.00	18.16	0.46	0.31
MRK0493	18.32	17.76	0.17	0.15
MRK0766	17.84	16.83	0.13	0.11
MRK0896	18.31	17.26	0.18	0.15
MRK1044	17.46	16.58	0.44	0.30
NGC4748	18.09	17.07	0.25	0.20
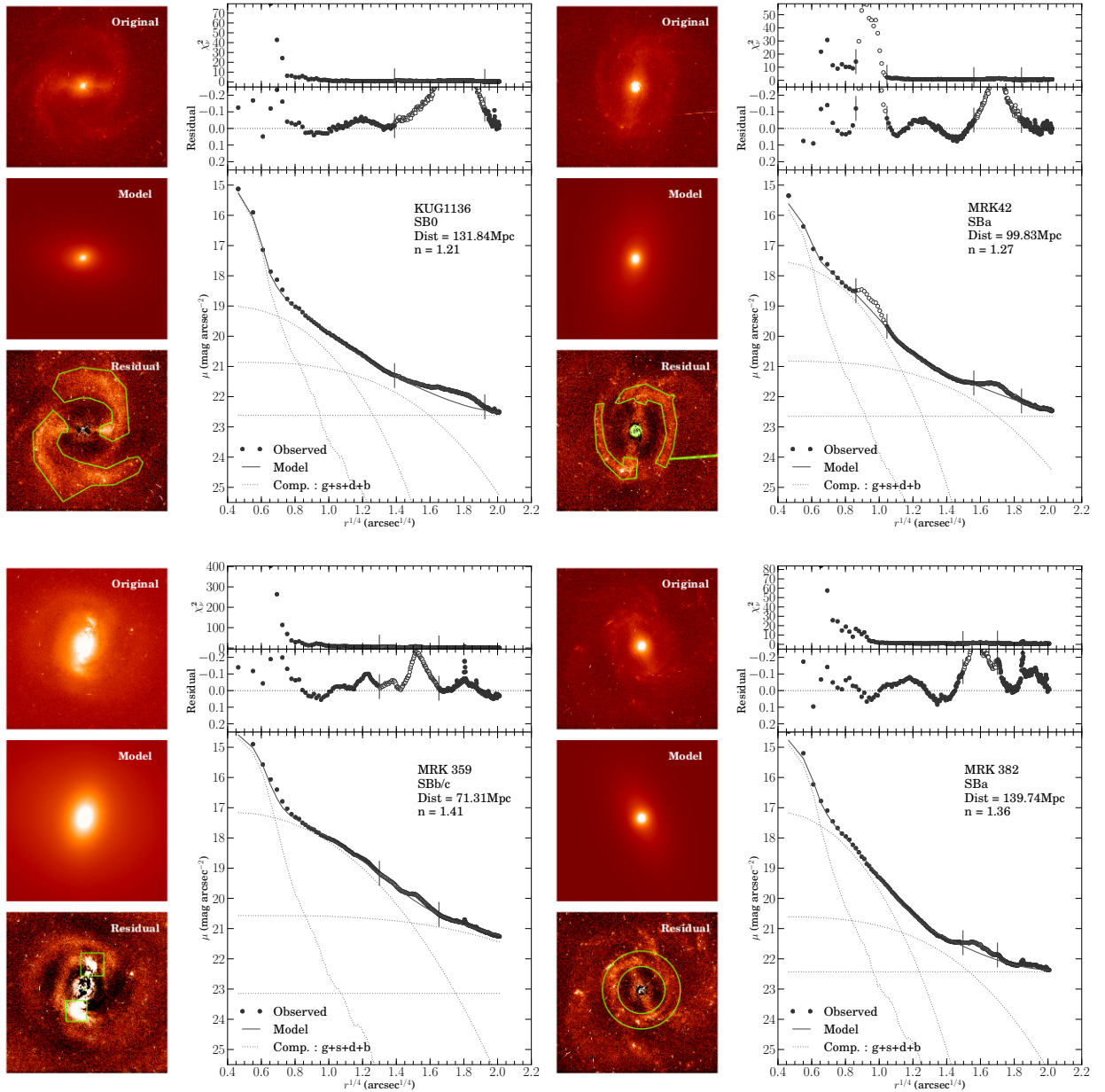
Figure C.1: Bulge-Disk decomposition for the NLS1 sample. The radial ranges of the mask are indicated by open symbols and straight lines in the radial profiles. The upper plot gives the radial distribution of the reduced χ^2, the middle plot is the magnitude difference $\Delta\mu$ between the original and the model images, the bottom plot presents the observed (dots), the total model (solid line), the modelled bulge and the modelled disk (dashed) light distributions. The radius is given in $r^{1/4}$ to emphasize the central region. The left images give the original data, the model, and the residuals. They are not at the same scale but the contrasts have been enhanced
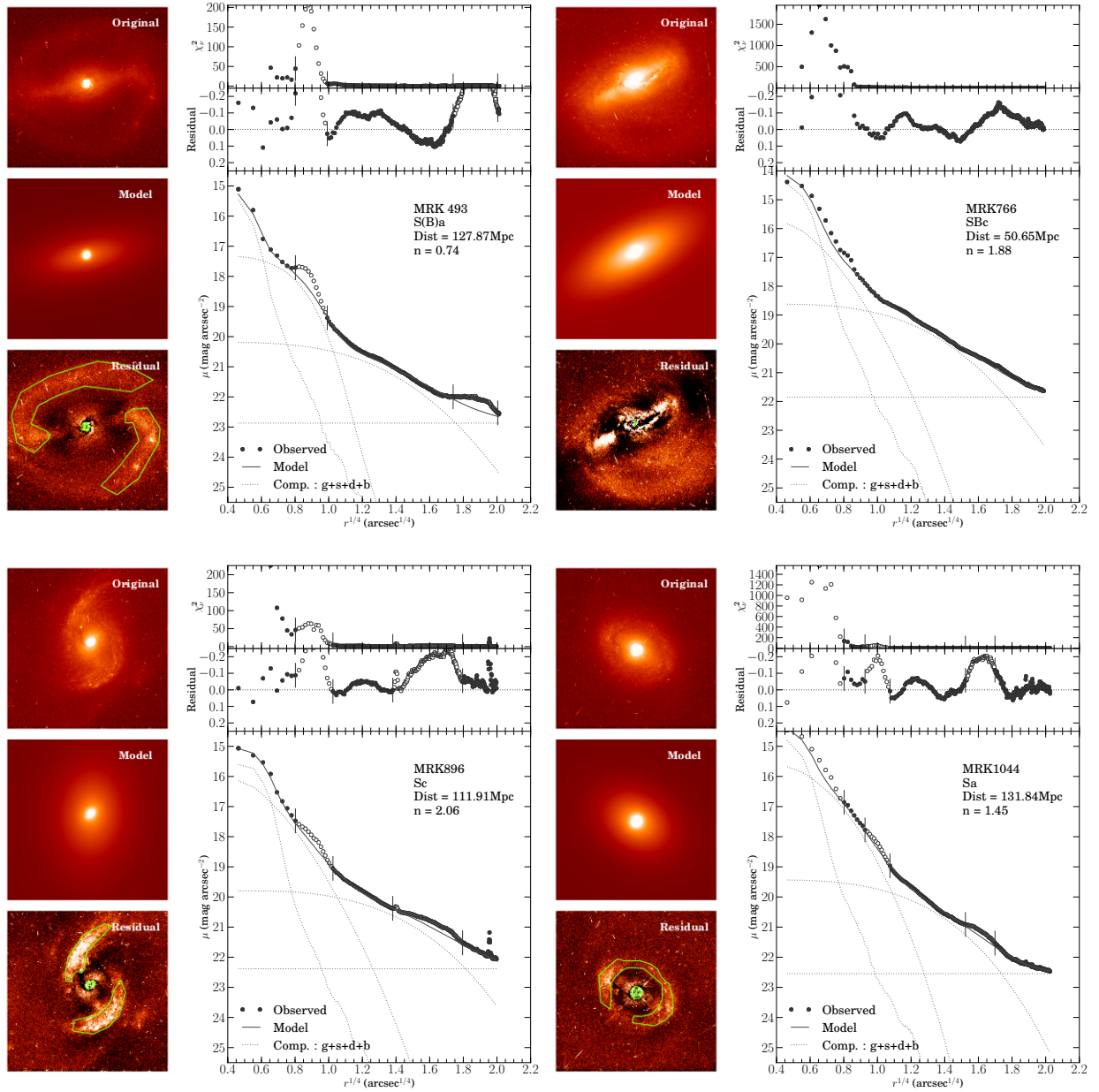
Figure C.2: *con't* of Fig. C.1
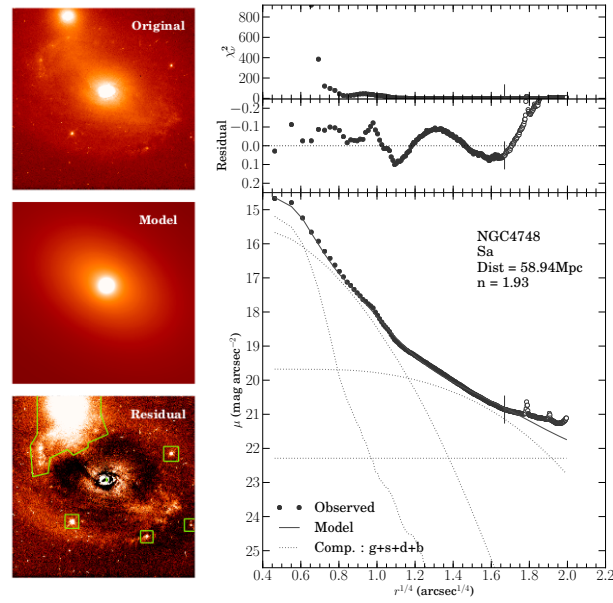
Figure C.3: *con't* of Fig. C.1

C.3 The BLS1 sample

We give in Tab. C.1 all the resulting values from our multi-components fit described in section 5.3.2 for the BLS1s. All the fit are illustrated in Fig. C.4 to Fig. C.6 with the 2D original, model and residual images, and the radial profiles of the data, th e full fit, the components, and the residual and the χ^2.

In Tab. C.4 we give the surface brightnesses (μ_e, $< \mu_e >$), and the luminosity ratios (B/D and B/T). The surface brightnesses are calculated using equation C.5 and equation C.7. The B/D and B/T using equation C.8 and equation C.9.

Table C.3: Full fit results of the NLS1 sample fits. The index g, b, d designate respectively *gaussian*, *bulge*, and *disk*. The gaussian fit is indended to fit the AGN and any nuclear cluster (see also text CHAP.5). It is sometimes replaced by a simple PSF fit. The GALFIT results includes, m observed magnitude in HST STMAG, R radii, q axis ratios, n bulge Sérsic index, the sky level, and the resulting reduced chi-squared χ^2_ν.

Object Name	m_g [mag]	m_b [mag]	m_d [mag]	R_g [px]	R_b [px]	R_d [px]	q_g	q_b	q_d	n_b	sky [adu]	χ^2
ESO438G	15.35	–	14.68	2.55	–	79.68	0.59	–	0.52	–	2.29	1.395
F1146	19.86	15.27	15.49	2.25	30.64	71.07	0.05	0.47	0.65	3.74	12.27	1.541
IC1816	17.64	15.26	12.9	4.09	25.17	277.78	0.66	0.92	0.67	1.98	1.75	0.844
Mrk0279	14.42	14.81	14.2	–	89.75	402.44	–	0.58	0.56	2.18	1.11	0.97
Mrk0290	17.48	16.04	15.93	3.71	17.13	80.31	0.77	0.86	0.88	4.06	1.02	1.109
Mrk0352	17.85	15.6	15.35	3.22	63.22	111.65	0.89	0.98	0.76	4.49	2.02	0.845
Mrk0423	–	15.66	15.32	–	14.45	58.54	–	0.69	0.68	2.13	2.9	1.623
Mrk0530	16.54	14.58	14.03	6.55	39.02	151.24	0.83	0.85	0.65	2.4	3.21	0.751
Mrk0595	19.27	15.21	15.92	2.46	29.64	74.7	0.12	0.66	0.75	3.47	2.43	1.301
Mrk0609	17.25	14.66	15.17	4.88	47.19	80.94	0.93	0.79	0.95	2.28	3.76	2.523
Mrk0704	16.8	15.14	14.83	5.96	44.55	235.63	0.63	0.7	0.5	2.88	4.45	1.252
Mrk0871	17.41	16.92	14.67	3.68	19.37	120.77	0.75	0.52	0.38	1.28	1.59	0.91
Mrk0885	19.41	14.74	13.5	3.16	117.41	393.32	0.91	0.74	0.52	2.62	0.36	0.828
Mrk1126	18.16	15.58	13.67	3.52	25.31	168.19	0.77	0.86	0.66	1.86	1.74	0.472
Mrk1400	20.18	16.45	15.22	4.5	20.8	85.13	0.67	0.61	0.31	1.7	3.29	0.978
NGC5252	19.7	14.62	14.03	3.54	114.3	151.3	0.51	0.53	0.44	3.9	5.21	0.354
NGC5940	17.99	17.59	14.59	3.09	9.58	120.42	0.9	0.89	0.66	1.23	2.76	0.988
NGC6212	19.7	15.25	14.96	3.31	44.63	104.43	0.88	0.75	0.7	1.52	1.56	0.873
IISZ10	20.48	14.3	13.91	5.7	49.88	137.02	0.44	0.91	0.72	1.92	13.9	0.566

Table C.4: Values calculated from the NLS1 fit results: the surface brightness at the effective radius μ_e, the average surface brightness within the effective radius $< \mu_e >$, the bulge to disk luminosity ratio, and the bulge to total luminosity ratio. See equation C.5, equation C.7, equation C.8, and equation C.9. Magnitudes are in HST STMAG units.

Object Name	$\mu_{e;b}$ [mag/arcsec^2]	$< \mu_{e;b} >$ [mag/arcsec^2]	B/D	B/T
ESO438G	–	–	–	–
F1146	18.55	17.19	1.22	0.55
IC1816	18.51	17.48	0.11	0.10
Mrk0279	20.37	19.29	0.57	0.36
Mrk0290	18.76	17.36	0.90	0.47
Mrk0352	21.35	19.90	0.79	0.44
Mrk0423	17.43	16.36	0.73	0.42
Mrk0530	18.80	17.67	0.60	0.38
Mrk0595	18.75	17.43	1.92	0.66
Mrk0609	19.18	18.08	1.60	0.62
Mrk0704	19.53	18.31	0.75	0.43
Mrk0871	18.77	17.95	0.13	0.11
Mrk0885	21.24	20.07	0.32	0.24
Mrk1126	18.74	17.74	0.17	0.15
Mrk1400	18.77	17.82	0.32	0.24
NGC5252	20.91	19.53	0.58	0.37
NGC5940	18.48	17.68	0.06	0.06
NGC6212	19.39	18.49	0.77	0.43
IISZ10	19.01	17.99	0.70	0.41
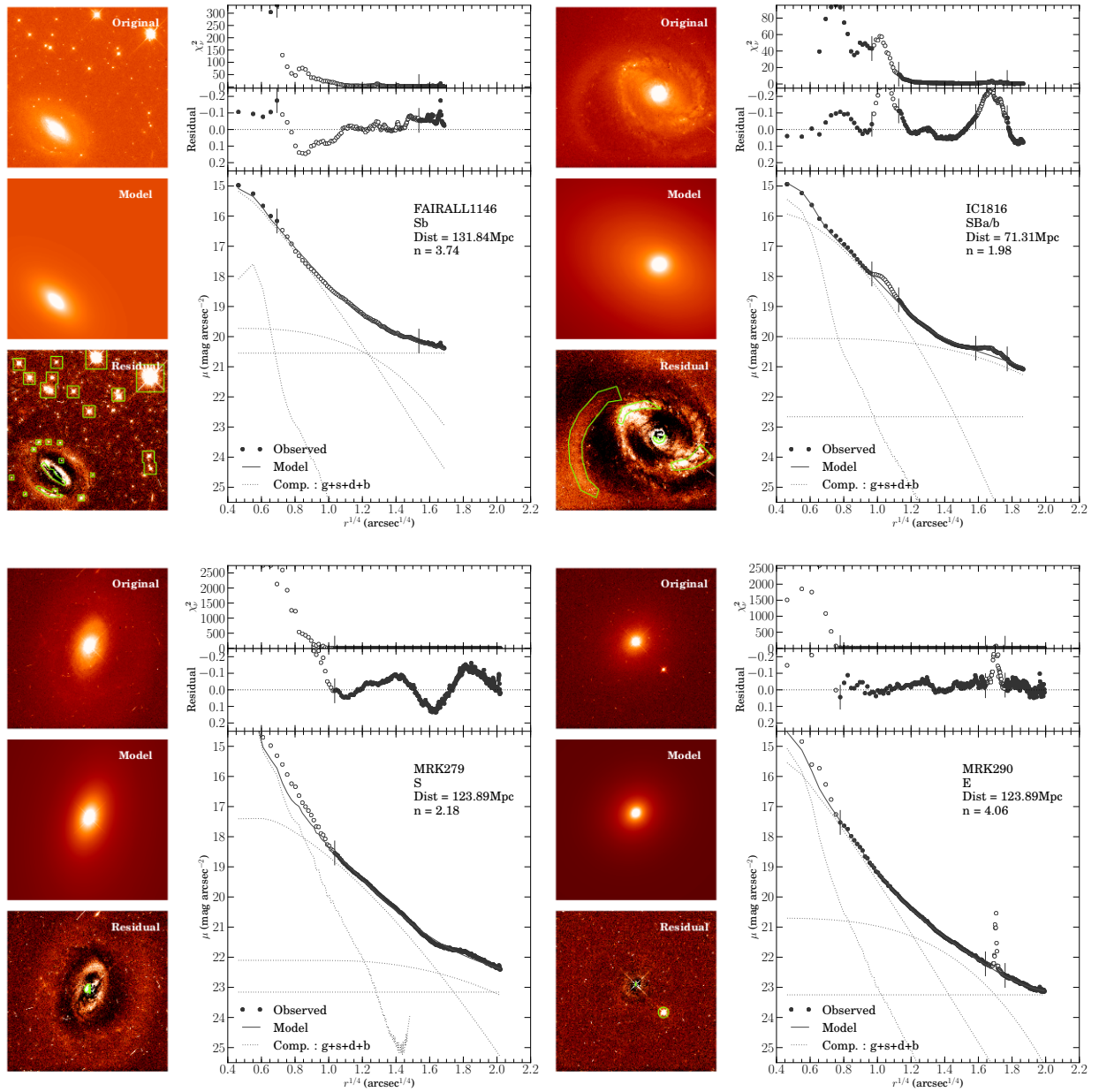
Figure C.4: Bulge-Disk decomposition for the BLS1 sample. See Fig. C.1 for more comments.
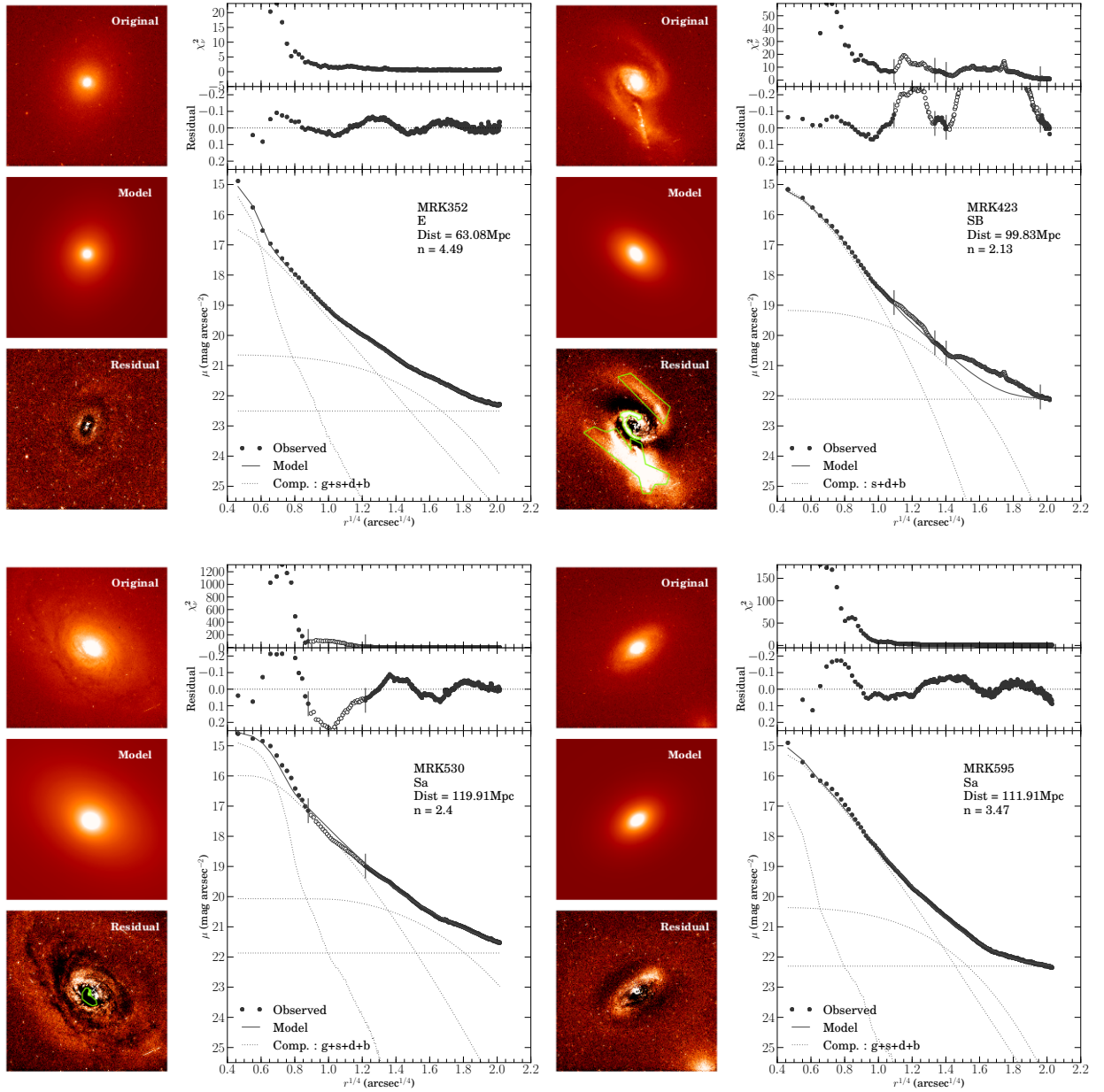
Figure C.5: con't of Fig. C.4.
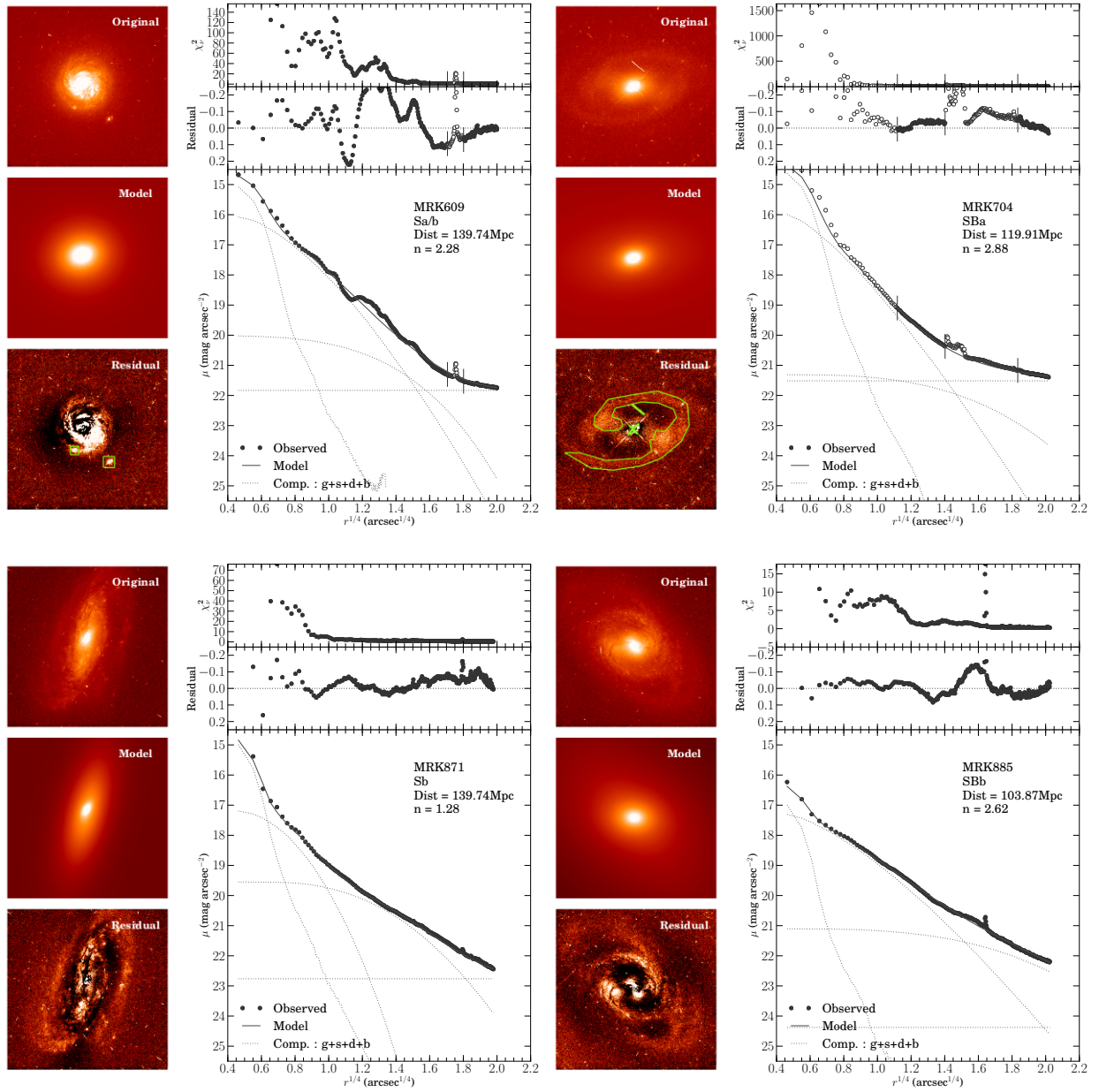
Figure C.6: BLS1s fit atlas (2)
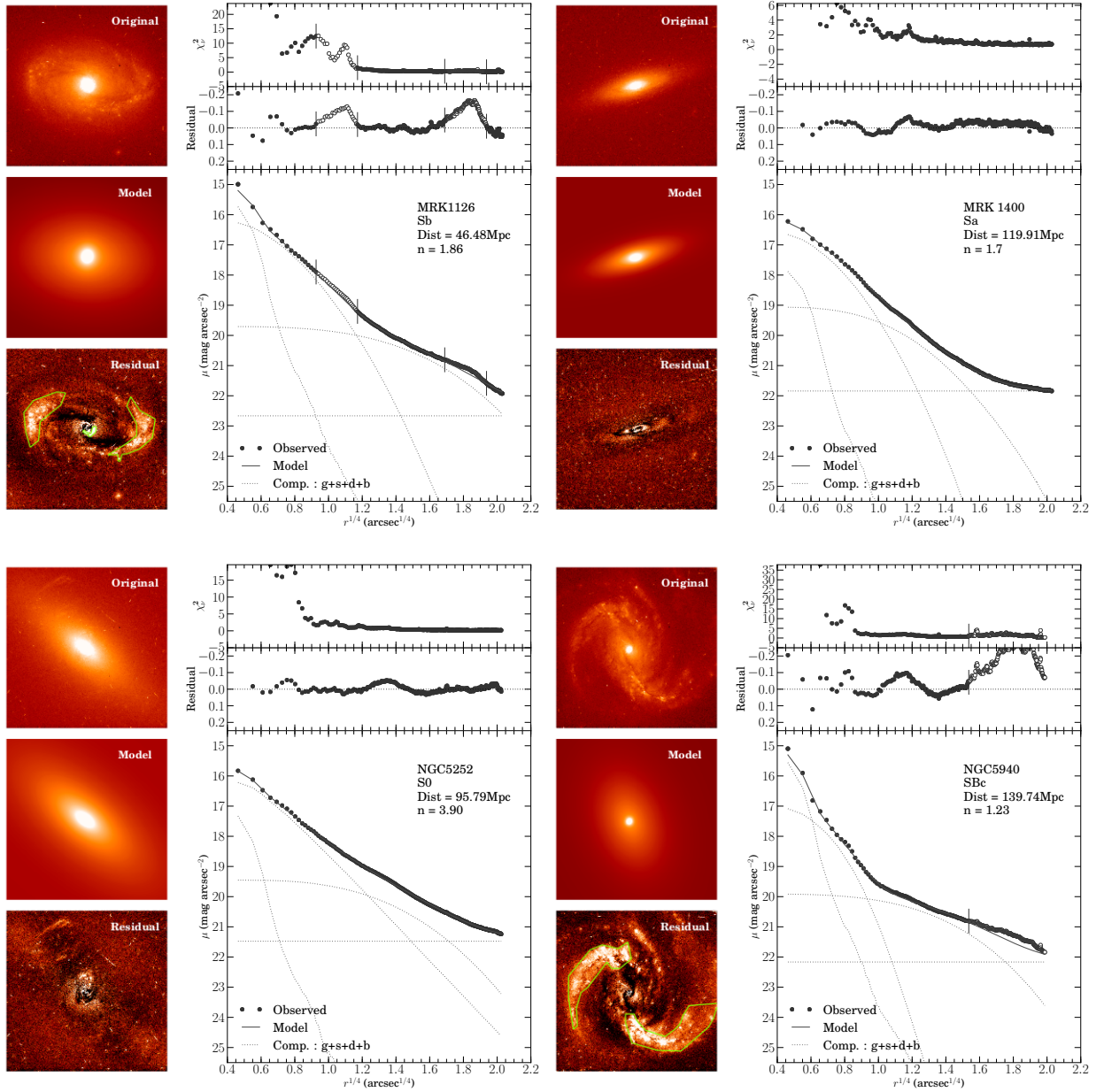
Figure C.7: con't of Fig. C.4.
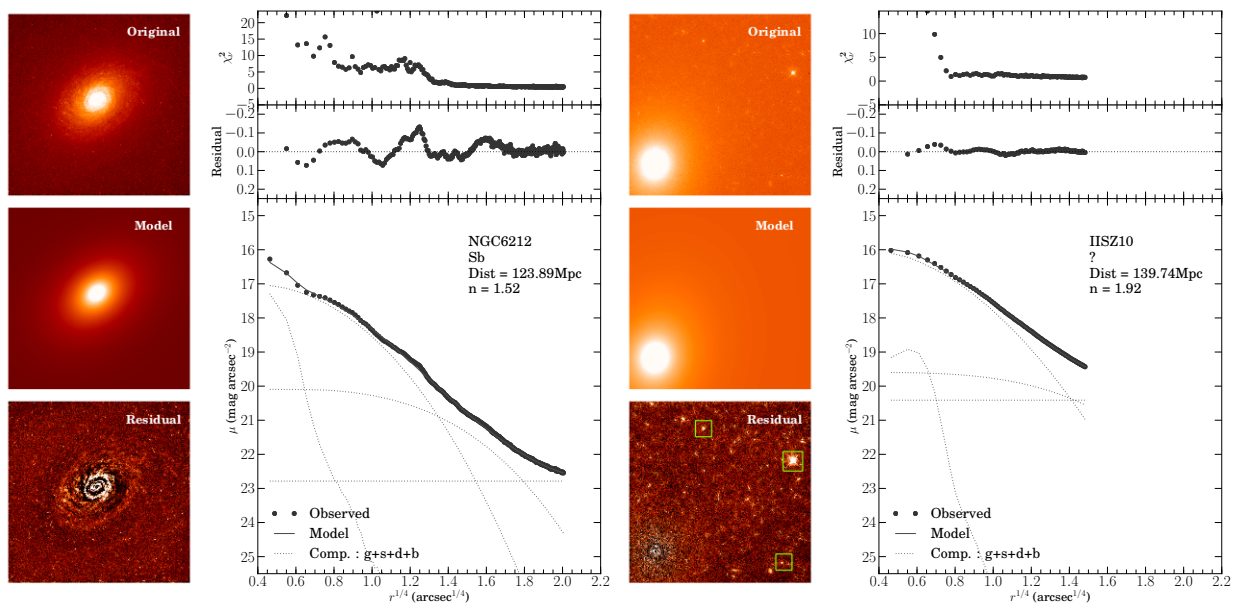
Figure C.8: con't of Fig. C.4.

SUPPLEMENT ON THE DATA ANALYSIS OF THE NGC 1365 SINFONI OBSERVATIONS

We provide further information on the data analysis (section 6.2) of the SINFONI data cube of NGC1365. In particular, we present the SNR before and after Voronoi binning performed on the cube, we give more information on the Brackett emission line fit constraints in the H-band, and finally the spectral and spatial resolution distribution obtained with the cube.

Voronoi SNR improvement

We bin the data using the 2D Voronoi tessellation binning routine of Cappellari & Copin (2003). This is performed in order to increase the SNR and ensure a minimum scatter in the SNR, thus allowing for a more robust kinematics fitting. The SNR is measured based on the depth of absorption lines versus the continuum (see also section 6.2.1). We present in Fig. D.1 the SNR before and after the Voronoi binning in both H and K bands. We can observe the overall increase and the larger uniformity in SNR.

(a) Before binning. (Left) H-band, (Right) K-band.   (b) After binning. (Left) H-band, (Right) K-band.
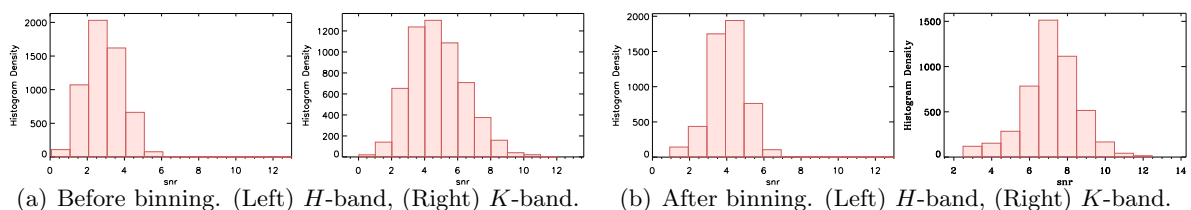
Figure D.1: Signal-to-noise ratio of the stellar absorption features before (a) and after (b) Voronoi binning in the H band (left) and the K band (right). See section 6.2.1 for a discussion.

Brackett emission lines in the H-band

To perform the Brackett emission line removal in the H-band, see section 6.2.2, we fix the relative wavelength positions and widths of the lines, and the relative intensities. To fix the relative wavelength positions, we use the atomic line database NIST[1]. The relative intensities

---

[1]We use the NIST atomic spectra database lines form, see `http://www.nist.gov`.

Table D.1: Fitted Brackett emission lines in the H-band. We assume the case B recombination (Hummer & Storey, 1987) with $T = 10^4 K$ and $n_e(\text{cm}^{-3}) = 10^4$. The lines presented here correspond to transition 20-10 to level 4. We effectively fit only the five first lines, but subtract all the 11 lines from the data cube. The wavelengths are taken from NIST.

Name	Transition	Wavelength (μm)	Intensities $\times 10^{-3}$
Brζ	10-4	1.7362	9.09
Brη	11-4	1.6806	6.79
Brθ	12-4	1.6407	5.21
Brι	13-4	1.6109	4.09
Brκ	14-4	1.5880	3.27
Brλ	15-4	1.5701	2.66
Brμ	16-4	1.5556	2.20
Brν	17-4	1.5439	1.84
Brξ	18-4	1.5342	1.56
Bro	19-4	1.5261	1.33
Brπ	20-4	1.5192	1.16

are fixed based on the case B recombination theory[2], using the results from Hummer & Storey (1987) for the standard parameters $T = 10^4$K and $n_e(\text{cm}^{-3})= 10^4$. The values are given in Tab. D.1.

Spectral and Spatial resolution

To verify the good quality of the data and for later input in the kinematics fitting, we measure the final spectral and spatial resolutions. We refer to section 6.1.2 for the complete discussion.

We plot in Fig. D.2 the spectral resolution distribution, as measured from OH lines, in the H and K band. The spectral resolution are $\sim$102km/s and $\sim$62km/s in the H and K band respectively, with a dispersion in resolution $<$4km/s. The spatial resolution measured from the Brγ emission lines is given in Fig. D.3. We fit a two components Gaussian, one for the narrow corrected core of the PSF, a second for the wide uncorrected wings of the PSF and the spatially extended emission components. The narrow PSF has a FWHM=0.16″, and the broad PSF a FWHM=0.61″.

---

[2]case B theory is based on the assumption that Lyman lines are optically thick, *i.e.* an emitted Lyman photon is immediately re-absorbed and thus does not affect the net recombination rate.
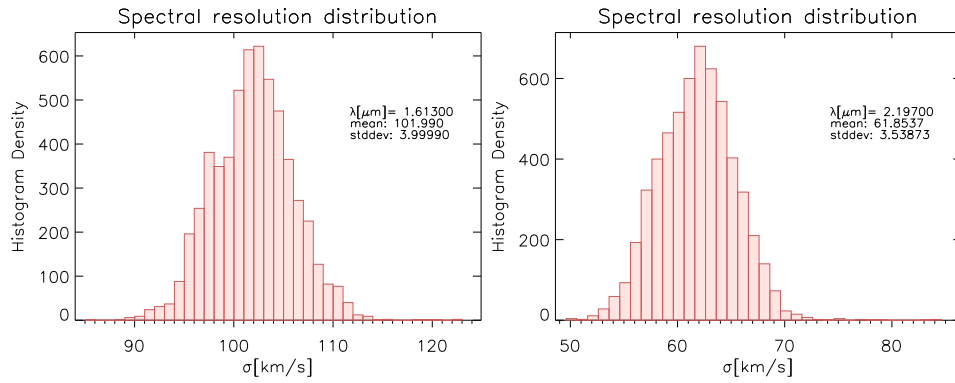
Figure D.2: Measured spectral resolution in the H and K-bands (by Gaussian fitting of unblended sky lines at 1.613 and 2.197μm) as measured on the initial data cube (no binning and masking). Dispersion in resolution is $\sim$3.5-4 km/s.
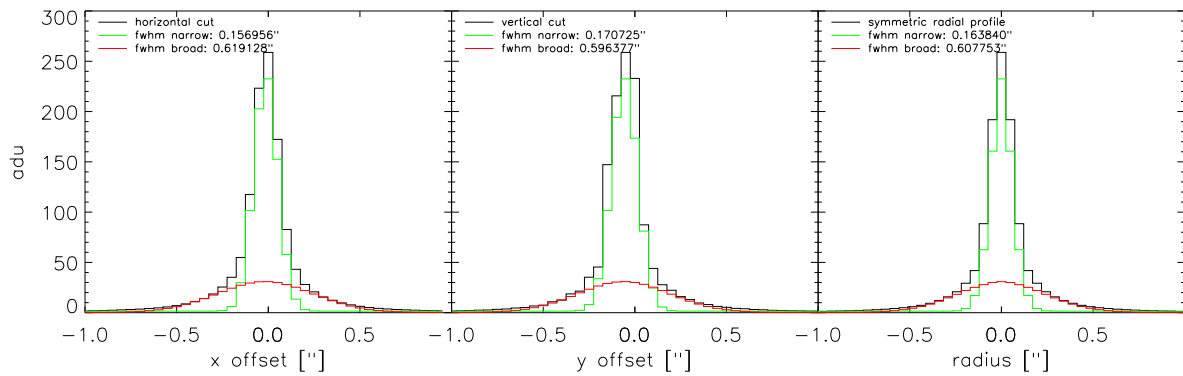

Figure D.3: Horizontal, vertical and symmetric profiles cut of the point spread function as derived from fitting spatially the Brγ line, on the initial data cube (no binning and masking).

LIST OF ACRONYMS AND ABBREVIATIONS

ADC   Analog-to-Digital converter
AGN   Active Galactic Nuclei
AO   Adaptive Optics
APD   Avalanche Photo-Diode
AR   Anti-reflective
ARGOS   Advance Rayleigh Guided adaptive Optics System
ASIC   Application Specific Integrated Circuits
ASM   Adaptive Secondary Mirror
BCU   Basic Computational Device (MICROGATE)
BH   Black-hole
BLS1   Broad-Line Seyfert type 1 (*i.e.* typical Seyfert type 1)
BLR   Broad-Line Region (of AGN)
CAD   Computer-Aided Design
CAMEX   CMOS Amplifier and MultiplEX, readout unit of the PNCCD
CDS   Cross-correlated Double Sampling
CMOS   Complementary metal-oxide semi-conductor
DSP   Digital Signal Processing
ELT   Extremely Large Telescope
EMCCD   Electron-Multiplying Charge-Coupled Device
ESO   European Southern Observatory
EW   Equivalent Width
FDR   Final Design Review
FLAO   First Light Adaptive Optics (at LBT)
FoV   Field-of-View
FWHM   Full Width at Half Maximum
GLAO   Ground-Layer Adaptive Optics
GLAS   Ground-Layer Adaptive-optics System at WHT
GPU   Graphics Processing Unit
GRAAL   GRound layer Adaptive optics Assisted by Lasers (VLT)
HLL   Halbleiterlabor of the Max-Planck-Society (semiconductor laboratory)
HST   Hubble Space Telescope
HVC   High Voltage Controller
INAF   Istituto Nazionale di Astrofisica (Italy)
JFET   Junction gate Field-Effect Transistor
LUCI   Large binocular telescope spectroscopic Utility with Camera and Integral Field unit for Extragalactic Research
LBT   Large Binocular Telescope

LGS	Laser Guide Star
LGSW	LGS Wavefront Sensor
MAD	Multi-Conjugate Adaptive Optics Demonstrator
MAS	Milli-arcseconds
MCAO	Multi-conjugated adaptive optics
MPE	Max-Planck-Institut für extraterrestrische Physik
MPIA	Max-Planck-Institut für Astronomie
MPIfR	Max-Planck-Institut für Radioastronomie
Nd:YAG	neodymium-doped yttrium aluminum garnet crystal
NGS	Natural Guide Star
NFIRAOS	Narrow-Field Infrared Adaptive Optics System (for the TMT)
NIR	Near-Infrared
NLS1	Narrow-Line Seyfert type 1
NLR	Narrow-Line Region (of AGN)
OB	Observation block
PCB	Printed circuit board
PCI	Peripheral Component Interconnect.
PDR	Preliminary Design Review
pnCCD	pnp structured Charge-Coupled Device (PNSENSOR)
pPXF	Penalized Pixel-Fitting routine for stellar kinematics extraction
PRNU	Photo Response Non-Uniformity
PSF	Point-Spread Function
PSU	Power Supply Unit
PtV	Peak-to-Valley
PTC	Photon Transfer Curve
QE	Quantum Efficiency
RMS	Root-Mean Squared
RON	Read-Out Noise
SAM	SOAR Adaptive Module
SED	Spectral energy density
SDRAM	Synchronous dynamic random access memory
SINFONI	Spectrograph for Integral Field Observation in the Near Infrared
SH	Shack-Hartmann
SMBH	Super-Massive Black Hole
SNR	signal-to-noise ratio
SOAR	Southern Astrophysical Research Telescope
TMT	Thirty Meter Telescope
TT	Tip-Tilt
ULIRG	Ultra-luminous infrared galaxy
VLT	Very Large Telescope
WDHS	Wavefront Data Handling System
WFS	WaveFront sensor system
WHT	William Herschel Telescope
YAO	Monte-Carlo AO simulation tool coded in Yorick

BIBLIOGRAPHY

Abraham, R. G., Merrifield, M. R., Ellis, R. S., Tanvir, N. R., & Brinchmann, J. 1999, MNRAS, 308, 569 127

Abramowicz, M. A., Czerny, B., Lasota, J. P., & Szuszkiewicz, E. 1988, ApJ, 332, 646 131

Abramowicz, M. A., & Fragile, P. C. 2013, Living Reviews in Relativity, 16, 1 131

Abuter, R., Schreiber, J., Eisenhauer, F., Ott, T., Horrobin, M., & Gillesen, S. 2006, NewA Rev., 50, 398 137

Acosta-Pulido, J. A., Vila-Vilaro, B., Perez-Fournon, I., Wilson, A. S., & Tsvetanov, Z. I. 1996, ApJ, 464, 177 113

Aller Carpentier, E. 2011, PhD thesis, Universidad Autónoma de Madrid and European Southern Observatory 8

Alonso-Herrero, A., et al. 2012, MNRAS, 425, 311 135, 136, 158, 159, 160

Andrighettoni, M., & Biasi, R. 2011, ARGOS BCU mini-crate System Design, Tech. Rep. LBT-MIC-TRE-00910-0001, Microgate 90, 92, 102, 103

Andritschke, R., Hartner, G., Hartmann, R., Meidinger, N., & Struder, L. 2008, in Nuclear Science Symposium Conference Record, 2008. NSS '08. IEEE, 2166–2172 67, 171

Argos consortium. 2008, LBT LGS Phase A Report, Tech. Rep. 1.0, LBT LGS Consortium 17

—. 2009, Preliminary Design Review, Tech. Rep. ARGOS-PDR-000 to ARGOS-PDR-013, Argos Consortium 17, 20, 21, 24

—. 2010, Final Design Review, Tech. Rep. ARGOS-FDR-000 to ARGOS-FDR-022, Argos Consortium 17, 20, 30, 31, 37, 40, 42

Berti, E., & Volonteri, M. 2008, ApJ, 684, 822 129

Bian, W., & Zhao, Y. 2004, MNRAS, 347, 607 131

Biasi, R. 2012, Present Microgate RTCs and perspectives, Presented at the Real Time Control for Adaptive Optics Workshop 103

Boller, T., Brandt, W. N., & Fink, H. 1996, A&A, 305, 53 108

Bonaglia, M. 2012, PhD thesis, Universitá Degli Studi di Firenze 18, 24

Bonnet, H., et al. 2003, in Society of Photo-Optical Instrumentation Engineers (SPIE) Conference Series, Vol. 4839, Adaptive Optical System Technologies II, ed. P. L. Wizinowich & D. Bonaccini, 329–343 137

Bonnet, H., et al. 2004, The Messenger, 117, 17 9

Boroson, T. A. 2002, ApJ, 565, 78 108

Botte, V., Ciroi, S., di Mille, F., Rafanelli, P., & Romano, A. 2005, MNRAS, 356, 789 131, 136

Brenneman, L. W. 2007, PhD thesis, University of Maryland, College Park 130

Bufton, J. L. 1973, Appl.Optics, 12, 1785 5

Buschkamp, P. 2012, PhD thesis, Ludwig-Maximilians-Universität München 18

Busoni, L., & Puglisi, A. 2013, Procedures to measure the Interaction Matrixes, Tech. Rep. ARGOS-TECH-NOTE 118 v1.0, Argos Consortium 22

Caon, N., Capaccioli, M., & D'Onofrio, M. 1993, MNRAS, 265, 1013 175

Cappellari, M., & Copin, Y. 2003, MNRAS, 342, 345 138, 139, 189

Cappellari, M., & Emsellem, E. 2004, PASP, 116, 138 140

Cassata, P., et al. 2010, ApJ, 714, L79 127

Chanan, G. 2000, in Proceedings: Summer School on Adaptive Optics, Santa Cruz, CA, ed. C. for Adaptive Optics (CfAO) 9

Ciotti, L., & Bertin, G. 1999, A&A, 352, 447 175

Cisternas, M., et al. 2011, ApJ, 726, 57 126

Colina, L. 1993, ApJ, 411, 565 152

Collin, S., & Kawaguchi, T. 2004, A&A, 426, 797 131

Conan, J.-M., Rousset, G., & Madec, P.-Y. 1995, Journal of the Optical Society of America A, 12, 1559 4, 166

Conselice, C. J., et al. 2004, ApJ, 600, L139 127

Crenshaw, D. M., Kraemer, S. B., & Gabel, J. R. 2003, AJ, 126, 1690 109, 110, 113, 114, 127

Cresci, G., et al. 2009, ApJ, 697, 115 146

Davies, R., Hippler, S., & Ragazzoni, R. 2005a, Sterne und Weltraum, 44, 100000 13

Davies, R., & Kasper, M. 2012, ARA&A, 50, 305 2, 14

Davies, R. I. 2007, MNRAS, 375, 1099 137, 155

Davies, R. I., Maciejewski, W., Hicks, E. K. S., Tacconi, L. J., Genzel, R., & Engel, H. 2009, ApJ, 702, 114 144

Davies, R. I., Müller Sánchez, F., Genzel, R., Tacconi, L. J., Hicks, E. K. S., Friedrich, S., & Sternberg, A. 2007, ApJ, 671, 1388 135

Davies, R. I., Sternberg, A., Lehnert, M., & Tacconi-Garman, L. E. 2003, ApJ, 597, 907 150

Davies, R. I., Sternberg, A., Lehnert, M. D., & Tacconi-Garman, L. E. 2005b, ApJ, 633, 105 135, 136, 150, 151

Demerlé, M., Madec, P. Y., & Rousset, G. 1994, in NATO ASIC Proc. 423: Adaptive Optics for Astronomy, ed. D. M. Alloin & J. M. Mariotti, 73 99

Deo, R. P., Crenshaw, D. M., & Kraemer, S. B. 2006, AJ, 132, 321 109, 110, 111, 113

Dotti, M., Colpi, M., Pallini, S., Perego, a., & Volonteri, M. 2013, ApJ, 762, 68 129

Downing, M., Finger, G., Baade, D., Hubin, N., Iwert, O., & Kolb, J. 2008, in Society of Photo-Optical Instrumentation Engineers (SPIE) Conference Series, Vol. 7015, Society of Photo-Optical Instrumentation Engineers (SPIE) Conference Series 36, 82

Downing, M., et al. 2010, in Society of Photo-Optical Instrumentation Engineers (SPIE) Conference Series, Vol. 7742, Society of Photo-Optical Instrumentation Engineers (SPIE) Conference Series 82

Dubois, Y., Volonteri, M., & Silk, J. 2014, MNRAS, 570 130, 161

Eisenhauer, F., et al. 2003, in Society of Photo-Optical Instrumentation Engineers (SPIE) Conference Series, Vol. 4841, Society of Photo-Optical Instrumentation Engineers (SPIE) Conference Series, ed. M. Iye & A. F. M. Moorwood, 1548–1561 137

Elberich, M., & Connot, C. 2012, Bonn Tip-Tilt Unit, Tech. Rep. v1.4, MPIfR 86, 93

Elmegreen, B. G., Elmegreen, D. M., & Hirst, A. C. 2004, ApJ, 612, 191 127

Esposito, S., et al. 2010, in Society of Photo-Optical Instrumentation Engineers (SPIE) Conference Series, Vol. 7736, Society of Photo-Optical Instrumentation Engineers (SPIE) Conference Series 8

Fabian, A. C., et al. 2009, Nature, 459, 540 130

Feautrier, P., et al. 2011, PASP, 123, 263 81

Ferrarese, L., & Merritt, D. 2000, ApJ, 539, L9 159

Fisher, D. B., & Drory, N. 2008, AJ, 136, 773 109, 112, 113, 119, 120, 121, 122, 123, 124

—. 2010, ApJ, 716, 942 112

Forster, K. 1999, PhD thesis, Columbia University 121

Foy, R., Migus, A., Biraben, F., Grynberg, G., McCullough, P. R., & Tallon, M. 1995, A&AS, 111, 569 14, 163

Fried, D. L. 1994, in NATO ASIC Proc. 423: Adaptive Optics for Astronomy, ed. D. M. Alloin & J. M. Mariotti, 25 2

Fusco, T., Nicolle, M., Rousset, G., Michau, V., Beuzit, J.-L., & Mouillet, D. 2004, in Society of Photo-Optical Instrumentation Engineers (SPIE) Conference Series, Vol. 5490, Society of Photo-Optical Instrumentation Engineers (SPIE) Conference Series, ed. D. Bonaccini Calia, B. L. Ellerbroek, & R. Ragazzoni, 1155–1166 98

Gadotti, D. A. 2009, MNRAS, 393, 1531 109, 112, 122, 123

Galliano, E., Alloin, D., Pantin, E., Lagage, P. O., & Marco, O. 2005, A&A, 438, 803 158, 160

Galliano, E., Kissler-Patig, M., Alloin, D., & Telles, E. 2012, A&A, 545, A10 136, 158, 159

Gässler, W., et al. 2012, in Society of Photo-Optical Instrumentation Engineers (SPIE) Conference Series, Vol. 8447, Society of Photo-Optical Instrumentation Engineers (SPIE) Conference Series 33

Gatti, E., & Rehak, P. 1984, Nuclear Instruments and Methods in Physics Research, 225, 608 39

Genel, S., Bouché, N., Naab, T., Sternberg, A., & Genzel, R. 2010, ApJ, 719, 229 126

Genel, S., et al. 2008, ApJ, 688, 789 126

Glindemann, A., Hippler, S., Berkefeld, T., & Hackenberg, W. 2000, Experimental Astronomy, 10, 5 2, 4, 9

Goodrich, R. W. 1990, ApJ, 355, 88 121

Graham, A. W. 2008, ApJ, 680, 143 131

Graham, A. W., & Li, I.-h. 2009, ApJ, 698, 812 131

Graham, A. W., Onken, C. A., Athanassoula, E., & Combes, F. 2011, MNRAS, 412, 2211 131

Graham, A. W., & Worley, C. C. 2008, MNRAS, 388, 1708 122

Greene, J. E., & Ho, L. C. 2004, ApJ, 610, 722 123

Greene, J. E., Ho, L. C., & Barth, A. J. 2008, ApJ, 688, 159 123

Grupe, D. 2004, AJ, 127, 1799 108

Grupe, D., & Mathur, S. 2004, ApJ, 606, L41 131

Hardy, J. W. 1998, Adaptive Optics for Astronomical Telescopes (Oxford University Press) 2, 5, 10

Hart, M., Milton, N. M., Baranec, C., Powell, K., Stalcup, T., McCarthy, D., Kulesa, C., & Bendek, E. 2010, Nature, 466, 727 15

Hartmann, R. 1999, Nuclear Instruments and Methods in Physics Research A, 439, 216 55

Hartmann, R., Buttler, W., Gorke, H., Herrmann, S., Holl, P., Meidinger, N., Soltau, H., & Strüder, L. 2006, Nuclear Instruments and Methods in Physics Research A, 568, 118 40

Hartmann, R., Gorke, H., Meidinger, N., Soltau, H., & Strueder, L. 2005, in Society of Photo-Optical Instrumentation Engineers (SPIE) Conference Series, Vol. 5903, Society of Photo-Optical Instrumentation Engineers (SPIE) Conference Series, ed. R. K. Tyson & M. Lloyd-Hart, 210–218 40

Hartmann, R., et al. 2008, in Society of Photo-Optical Instrumentation Engineers (SPIE) Conference Series, Vol. 7015, Society of Photo-Optical Instrumentation Engineers (SPIE) Conference Series 42, 62

Hicks, E. K. S., Davies, R. I., Maciejewski, W., Emsellem, E., Malkan, M. A., Dumas, G., Müller-Sánchez, F., & Rivers, A. 2013, ApJ, 768, 107 155

Hjelm, M., & Lindblad, P. O. 1996, A&A, 305, 727 159

Ho, L. C. 2008, ARA&A, 46, 475 127

Ho, L. C., Filippenko, A. V., & Sargent, W. L. W. 1997, ApJ, 487, 591 111

Hobbs, A., Nayakshin, S., Power, C., & King, A. 2011, MNRAS, 413, 2633 135

Hopkins, P. F., Hickox, R., Quataert, E., & Hernquist, L. 2009, MNRAS, 398, 333 128

Hu, J. 2008, MNRAS, 386, 2242 131

Hummer, D. G., & Storey, P. J. 1987, MNRAS, 224, 801 140, 156, 190

Ihle, S., et al. 2008, in Nuclear Science Symposium Conference Record, 2008. NSS '08. IEEE, 3351–3356 37, 38, 64

Iyomoto, N., Makishima, K., Fukazawa, Y., Tashiro, M., & Ishisaki, Y. 1997, PASJ, 49, 425 159

Jahnke, K., & Macciò, A. V. 2011, ApJ, 734, 92 131

Janesick, J. R. 2001, Scientific charge-coupled devices (SPIE Press) 56

Jogee, S. 2006, in Lecture Notes in Physics, Berlin Springer Verlag, Vol. 693, Physics of Active Galactic Nuclei at all Scales, ed. D. Alloin, 143 128, 135

Jogee, S., et al. 2004, ApJ, 615, L105 127

Jorsater, S., & van Moorsel, G. A. 1995, AJ, 110, 2037 158

Kajisawa, M., & Yamada, T. 2001, PASJ, 53, 833 127

Kasper, M. 2000, PhD thesis, Rupertus Carola University of Heidelberg 9, 11, 97, 98

Kasper, M., Looze, D., Hippler, S., Davies, R., & Glindemann, A. 1999, in Conf. Wavefront Sensing, Canterbury 98

Kaspi, S., Maoz, D., Netzer, H., Peterson, B. M., Vestergaard, M., & Jannuzi, B. T. 2005, ApJ, 629, 61 159

Kawakatu, N., Imanishi, M., & Nagao, T. 2007, ApJ, 661, 660 132

King, A. R., & Pringle, J. E. 2007, MNRAS, 377, L25 129

King, A. R., Pringle, J. E., & Hofmann, J. A. 2008, MNRAS, 385, 1621 129

Kolmogorov, A. N. 1962, Journal of Fluid Mechanics, 13, 82 2

Komossa, S. 2008, in Revista Mexicana de Astronomia y Astrofisica, vol. 27, Vol. 32, Revista Mexicana de Astronomia y Astrofisica Conference Series, 86–92 108

Komossa, S., & Xu, D. 2007, ApJ, 667, L33 131, 136

Kormendy, J., Bender, R., & Cornell, M. E. 2011, Nature, 469, 374 131

Kormendy, J., & Kennicutt, Jr., R. C. 2004, ARA&A, 42, 603 109, 112, 125

Lardière, O., Conan, R., Bradley, C., Jackson, K., & Hampton, P. 2009, MNRAS, 398, 1461 97

Laurikainen, E., Salo, H., Buta, R., & Knapen, J. H. 2007, MNRAS, 381, 401 119

Le, H. A. N., Kang, W., Pak, S., Im, M., Lee, J.-E., Ho, L. C., Pyo, T.-S., & Jaffe, D. T. 2011, ArXiv e-prints 140

Lindblad, P. A. B., Lindblad, P. O., & Athanassoula, E. 1996a, in Lecture Notes in Physics, Berlin Springer Verlag, Vol. 474, Lecture Notes in Physics, Berlin Springer Verlag, ed. A. Sandqvist & P. O. Lindblad, 83 153

Lindblad, P. A. B., Lindblad, P. O., & Athanassoula, E. 1996b, A&A, 313, 65 136, 145, 158

Lindblad, P. O. 1978, in Astronomical Papers Dedicated to Bengt Stromgren, ed. A. Reiz & T. Andersen, 403–408 158

Lindblad, P. O. 1999, A&A Rev., 9, 221 135, 153

Maciejewski, W. 2004a, MNRAS, 354, 883 111

—. 2004b, MNRAS, 354, 892 111

Maio, U., Dotti, M., Petkova, M., Perego, A., & Volonteri, M. 2013, ApJ, 767, 37 130

Maiolino, R., & Rieke, G. H. 1995, ApJ, 454, 95 121

Malkan, M. A., Gorjian, V., & Tam, R. 1998, ApJS, 117, 25 109, 111, 113, 114

Maloney, P. R., Hollenbach, D. J., & Tielens, A. G. G. M. 1996, ApJ, 466, 561 153, 154

Marchetti, E., et al. 2007, The Messenger, 129, 8 15

Marconi, A., Axon, D. J., Maiolino, R., Nagao, T., Pastorini, G., Pietrini, P., Robinson, A., & Torricelli, G. 2008, ApJ, 678, 693 128, 131

Marinova, I., & Jogee, S. 2007, ApJ, 659, 1176 128

Márquez, I., et al. 2004, A&A, 416, 475 113

Martini, P., Regan, M. W., Mulchaey, J. S., & Pogge, R. W. 2003, ApJ, 589, 774 110, 111

Masciadri, E., Stoesz, J., Hagelin, S., & Lascaux, F. 2010, MNRAS, 404, 144 5

Masters, K. L., et al. 2010, MNRAS, 404, 792 122, 123, 176

Mathur, S. 2000, MNRAS, 314, L17 132

Mathur, S., Fields, D., Peterson, B. M., & Grupe, D. 2012, ApJ, 754, 146 112, 123, 125, 132

Mathur, S., & Grupe, D. 2005a, A&A, 432, 463 131

—. 2005b, ApJ, 633, 688 131

Mathur, S., Kuraszkiewicz, J., & Czerny, B. 2001, NewA, 6, 321 131

McLean, I. S. 2008, Electronic Imaging in Astronomy (Springer Berlin Heidelberg) 62, 80, 169

Meidinger, N., et al. 2012, in Society of Photo-Optical Instrumentation Engineers (SPIE) Conference Series, Vol. 8453, Society of Photo-Optical Instrumentation Engineers (SPIE) Conference Series 42

Mineshige, S., Kawaguchi, T., Takeuchi, M., & Hayashida, K. 2000, PASJ, 52, 499 131

Miniutti, G., Panessa, F., de Rosa, A., Fabian, A. C., Malizia, A., Molina, M., Miller, J. M., & Vaughan, S. 2009, MNRAS, 398, 255 130

Morganti, R., Tsvetanov, Z. I., Gallimore, J., & Allen, M. G. 1999, A&AS, 137, 457 159

Müller-Sánchez, F., Prieto, M. A., Hicks, E. K. S., Vives-Arias, H., Davies, R. I., Malkan, M., Tacconi, L. J., & Genzel, R. 2011, ApJ, 739, 69 152

Nelson, C. H. 2000, ApJ, 544, L91 131

Nicolle, M., Fusco, T., Rousset, G., & Michau, V. 2004, Optics Letters, 29, 2743 97

Noll, R. J. 1976, Journal of the Optical Society of America (1917-1983), 66, 207 3, 23

Nowak, N., Thomas, J., Erwin, P., Saglia, R. P., Bender, R., & Davies, R. I. 2010, MNRAS, 403, 646 131

Oesch, P. A., et al. 2010, ApJ, 714, L47 127

Ohta, K., Aoki, K., Kawaguchi, T., & Kiuchi, G. 2007, ApJS, 169, 1 109, 110

Oliva, E., Origlia, L., Kotilainen, J. K., & Moorwood, A. F. M. 1995, A&A, 301, 55 159

Orban de Xivry, G. 2010, Requirements for the ARGOS BCU, Tech. Rep. 1.3, MPE 88

—. 2013, ARGOS PNCCD Unit User Manual, Tech. Rep. 1.0, MPE 54

Orban de Xivry, G., Davies, R., Schartmann, M., Komossa, S., Marconi, A., Hicks, E., Engel, H., & Tacconi, L. 2011, MNRAS, 417, 2721 xv, 17, 107

Orban de Xivry, G., & Rabien, S. 2012, in Society of Photo-Optical Instrumentation Engineers (SPIE) Conference Series, Vol. 8447, Society of Photo-Optical Instrumentation Engineers (SPIE) Conference Series 17, 103

Orban de Xivry, G., et al. 2010, in Society of Photo-Optical Instrumentation Engineers (SPIE) Conference Series, Vol. 7736, Society of Photo-Optical Instrumentation Engineers (SPIE) Conference Series 17

Ordavo, I., et al. 2011, Nuclear Instruments and Methods in Physics Research A, 654, 250 41, 52

Osterbrock, D. E., & Martel, A. 1993, ApJ, 414, 552 113

Parenti, R. R., & Sasiela, R. J. 1994, Journal of the Optical Society of America A, 11, 288 2, 5, 7, 11, 14, 23, 163

Parry, O. H., Eke, V. R., & Frenk, C. S. 2009, MNRAS, 396, 1972 126, 127

Peng, C. Y. 2007, ApJ, 671, 1098 131

Peng, C. Y., Ho, L. C., Impey, C. D., & Rix, H.-W. 2010, AJ, 139, 2097 113, 115, 175

Peterson, B. M., et al. 2004, ApJ, 613, 682 108

Pettazzi, L., Fedrigo, E., & Clare, R. 2012, Impact of Latency and Jitter on the Optics Systems Performance of Adaptive for ELTs, Presented at the Real Time Control for Adaptive Optics Workshop 101

Phinney, E. S. 1994, in Mass-Transfer Induced Activity in Galaxies, ed. I. Shlosman, 1 135

Pinotti, E., et al. 1993, Nuclear Instruments and Methods in Physics Research A, 326, 85 39, 41

Pogge, R. W. 2011, in Narrow-Line Seyfert 1 Galaxies and their Place in the Universe 108

Ponti, G., et al. 2010, MNRAS, 406, 2591 130

Prieto, M. A., Marco, O., & Gallimore, J. 2005, MNRAS, 364, L28 152

Primot, J., Rousset, G., & Fontanella, J. C. 1990, Journal of the Optical Society of America A, 7, 1598 9

Puxley, P. J., Hawarden, T. G., & Mountain, C. M. 1990, ApJ, 364, 77 151

Ragazzoni, R. 1996, Journal of Modern Optics, 43, 289 7

Ragazzoni, R., & Esposito, S. 1999, MNRAS, 307, 55 14, 163

Raimundo, S. I., Davies, R. I., Gandhi, P., Fabian, A. C., Canning, R. E. A., & Ivanov, V. D. 2013, MNRAS, 431, 2294 139

Ramos Almeida, C., et al. 2009, ApJ, 702, 1127 121, 154

Reunanen, J., Kotilainen, J. K., & Prieto, M. A. 2003, MNRAS, 343, 192 135, 136, 152

Reynolds, C. S. 2013a, Space Sci.Rev. 130

—. 2013b, Classical and Quantum Gravity, 30, 244004 130

Reynolds, C. S., & Fabian, A. C. 2008, ApJ, 675, 1048 131, 161

Riffel, R. A., & Storchi-Bergmann, T. 2011, MNRAS, 417, 2752 145, 147

Rigaut, F. 1994, in NATO ASIC Proc. 423: Adaptive Optics for Astronomy, ed. D. M. Alloin & J. M. Mariotti, 163 12

Rigaut, F. 2002, in European Southern Observatory Conference and Workshop Proceedings, Vol. 58, European Southern Observatory Conference and Workshop Proceedings, ed. E. Vernet, R. Ragazzoni, S. Esposito, & N. Hubin, 11 12

Rigaut, F., & Gendron, E. 1992, A&A, 261, 677 163

Risaliti, G., et al. 2009, MNRAS, 393, L1 136, 159

—. 2013, Nature, 494, 449 136, 159, 161

Roddier, F. 1988, Appl.Optics, 27, 1223 8

Rodríguez-Ardila, A., Viegas, S. M., Pastoriza, M. G., & Prato, L. 2002, ApJ, 565, 140 152

Rousset, G. 1999, in Adaptive Optics in Astronomy, ed. F. Roddier (Cambridge University Press), 91 97

Ryan, C. J., De Robertis, M. M., Virani, S., Laor, A., & Dawson, P. C. 2007, ApJ, 654, 799 108, 109, 112, 123

Sakamoto, K., Okumura, S. K., Ishizuki, S., & Scoville, N. Z. 1999, ApJ, 525, 691 111

Sandqvist, A. 1999, A&A, 343, 367 157, 160

Sandqvist, A., Joersaeter, S., & Lindblad, P. O. 1995, A&A, 295, 585 159

Sani, E., Lutz, D., Risaliti, G., Netzer, H., Gallo, L. C., Trakhtenbrot, B., Sturm, E., & Boller, T. 2010, MNRAS, 403, 1246 111

Sani, E., Marconi, A., Hunt, L. K., & Risaliti, G. 2011, MNRAS, 413, 1479 131

Sheth, K., Regan, M. W., Scoville, N. Z., & Strubbe, L. E. 2003, ApJ, 592, L13 128

Sheth, K., Vogel, S. N., Regan, M. W., Thornley, M. D., & Teuben, P. J. 2005, ApJ, 632, 217 111

Sheth, K., et al. 2008, ApJ, 675, 1141 128

Shlosman, I., Begelman, M. C., & Frank, J. 1990, Nature, 345, 679 135, 136

Shlosman, I., Peletier, R. F., & Knapen, J. H. 2000, ApJ, 535, L83 110

Sternberg, A., & Dalgarno, A. 1989, ApJ, 338, 197 150

—. 1995, ApJS, 99, 565 150

Sternberg, A., & Neufeld, D. A. 1999, ApJ, 516, 371 150

Stevens, I. R., Forbes, D. A., & Norris, R. P. 1999, MNRAS, 306, 479 136

Strüder, L., Holl, P., Lutz, G., & Kemmer, J. 1987, Nuclear Instruments and Methods in Physics Research A, 257, 594 37

Strüder, L., et al. 2001, A&A, 365, L18 37, 38, 39

Takato, N., & Yamaguchi, I. 1995, Journal of the Optical Society of America A, 12, 958 164, 165, 166

Tatarskii, V. I. 1961, Wave Propagation in Turbulent Medium (McGraw-Hill) 2

Thomas, S., Fusco, T., Tokovinin, A., Nicolle, M., Michau, V., & Rousset, G. 2006, MNRAS, 371, 323 96, 97, 98

Tran, H. D. 2010, ApJ, 711, 1174 113

Tueller, J., et al. 2010, ApJS, 186, 378 154

Valencia-S., M., et al. 2013, ArXiv e-prints 128

van den Bergh, S., Cohen, J. G., Hogg, D. W., & Blandford, R. 2000, AJ, 120, 2190 127

Véron-Cetty, M.-P., & Véron, P. 2001, A&A, 374, 92 108

—. 2006, A&A, 455, 773 135

—. 2010, A&A, 518, A10 113, 114

Véron-Cetty, M.-P., Véron, P., & Gonçalves, A. C. 2001, A&A, 372, 730 109, 113, 114

Volonteri, M. 2010, A&A Rev., 18, 279 128

Volonteri, M., Madau, P., Quataert, E., & Rees, M. J. 2005, ApJ, 620, 69 128, 129

Wada, K. 2004, Coevolution of Black Holes and Galaxies, 186 135, 158

Wang, J.-M., & Zhang, E.-P. 2007, ApJ, 660, 1072 132

Wang, L. 2012, Studying GPU based RTC for TMT NFIRAOS, Presented at the Real Time Control for Adaptive Optics Workshop 103

Weinzirl, T., Jogee, S., Khochfar, S., Burkert, A., & Kormendy, J. 2009, ApJ, 696, 411 119, 121, 126, 127, 141

Williams, R. J., Pogge, R. W., & Mathur, S. 2002, AJ, 124, 3042 108, 127

Wilson, A. S., & Tsvetanov, Z. I. 1994, AJ, 107, 1227 159

Winick, K. A. 1986, Journal of the Optical Society of America A, 3, 1809 96

Wizinowich, P. 2013, PASP, 125, 798 14

Xompero, M., Andrighettoni, M., Zanotti, D., & Riccardi, A. 2008, Required sequence of operations for the optical WF reconstruction process and proposed implementation, Tech. Rep. LBT-ADOPT-486f015e, INAF-Arcetri 21, 85

Zánmar Sánchez, R., Sellwood, J. A., Weiner, B. J., & Williams, T. B. 2008, ApJ, 674, 797 147, 158

Zhang, E.-P., & Wang, J.-M. 2006, ApJ, 653, 137 127, 132

Zhou, H., Wang, T., Yuan, W., Lu, H., Dong, X., Wang, J., & Lu, Y. 2006, ApJS, 166, 128 108, 127, 131

Zhu, L., Zhang, S. N., & Tang, S. 2009, ApJ, 700, 1173 132

Ziegleder, J. 2013, CCD Power Supply DSV7K User Manual, Tech. Rep. 2.3, MPE 49

Zuther, J., Iserlohe, C., Pott, J.-U., Bertram, T., Fischer, S., Voges, W., Hasinger, G., & Eckart, A. 2007, A&A, 466, 451 153

ACKNOWLEDGEMENTS